University of Szeged
Albert Szent-Györgyi Medical School
Doctoral School of Multidisciplinary Medical Science

Photonic application of proteins

PhD thesis

Szilvia Krekic

Supervisors:
András Dér PhD; DSc, scientific adviser
Zsuzsanna Heiner PhD, scientific adviser

Biological Research Centre, Institute of Biophysics
Biomolecular Electronics Research Group

Szeged

2023

Table of Contents

List of publications i
List of abbreviations ii
1. Introduction 1
1.1. Photoactive Yellow Protein 2
1.2. Z-scan 5
1.3. Broadband Vibrational Sum-Frequency Generation Spectroscopy 6
1.4. Optical switching 9
1.4.1. Integrated optical interferometric light modulation 9
1.4.2. Ultrafast all-optical switching using transient grating spectroscopy 10
2. Aims of this work 11
3. Materials and Methods 12
3.1. Film preparation 12
3.2. Kinetic absorption spectroscopy 14
3.3. OWLS measurements 15
3.4. Z-scan 15
3.5. Broadband Vibrational Sum-Frequency Generation Spectroscopy 17
3.6. Optical switching 19
3.6.1. Switching with an IO Mach–Zehnder interferometer 19
3.6.2. Ultrafast switching demonstrated with transient grating technique 20
4. Results and Discussion 22
4.1. Photocycle of the glycerol-doped Photoactive Yellow Protein film 22
4.2. Determining the linear and nonlinear refractive index of PYP films 24
4.2.1. Linear refractive index 24
4.2.2. Nonlinear refractive index 24
4.3. Investigation of oriented PYP films 26
4.3.1. VSFG spectra of the PYP 26
4.3.2. VSFG spectra of PEI and PEI+PGA at the air-water interface 28
4.3.3. PYP adsorption at the air-polyelectrolyte interfaces 30
4.4. Optical switching 34
4.4.1. All-optical switching demonstrated with IO Mach–Zehnder interferometer 34
4.4.2. All-optical switching demonstrated with transient grating 39
5. Conclusions 43
6. Acknowledgements 46
7. References 47
8. Annex 50

List of publications

List of full papers directly related to the subject of the thesis

I. **Krekic, S.**; Nagy, D.; Taneva, S. G.; Fábián, L.; Zimányi, L.; Dér, A. Spectrokinetic Characterization of Photoactive Yellow Protein Films for Integrated Optical Applications. *Eur. Biophys. J.* **2019**, *48* (5), 465–473. https://doi.org/10.1007/s00249-019-01353-8. IF: 2.012

II. **Krekic, S.**; Zakar, T.; Gombos, Z.; Valkai, S.; Mero, M.; Zimányi, L.; Heiner, Z.; Dér, A. Nonlinear Optical Investigation of Microbial Chromoproteins. *Front. Plant Sci.* **2020**, *11*, 1567. https://doi.org/10.3389/fpls.2020.547818. IF: 5.753

III. Petrovszki, D.; **Krekic, S.**; Valkai, S.; Heiner, Z.; Dér, A. All-Optical Switching Demonstrated with Photoactive Yellow Protein Films. *Biosensors* **2021**, *11* (11), 432. https://doi.org/10.3390/bios11110432. IF: 5.743

IV. **Krekic, S.**; Mero, M.; Dér, A.; Heiner, Z. Ultrafast all-optical switching using doped chromoprotein films. *J. Phys. Chem. C* **2023**, *127* (3), 1499–1506. https://doi.org/10.1021/acs.jpcc.2c06232. IF: 4.177*

V. **Krekic, S.**; Mero, M.; Kuhl, M.; Balasubramanian, K.; Dér, A.; Heiner, Z. Photoactive yellow protein adsorption at hydrated polyethyleneimine and poly-L-glutamic acid interfaces. Submitted to *Molecules* on April 7, **2023**. https://doi.org/10.26434/chemrxiv-2023-zmtk4. IF: 4.927*

Cumulative impact factor of papers directly related to the subject of thesis: 22.612

List of full papers not related to the subject of the thesis

I. Szekeres, G. P.; **Krekic, S.**; Miller, R. L.; Mero, M.; Pagel, K.; Heiner, Z. The interaction of chondroitin sulfate with a lipid monolayer observed by using nonlinear vibrational spectroscopy. *Phys. Chem. Chem. Phys.*, **2021**, *23*, 13389-13395. https://doi.org/10.1039/D1CP01975A. IF: 3.945

Cumulative impact factor of other full papers: 3.945

**IF based on data for 2021*

List of abbreviations

BB-VSFG	Broadband Vibrational Sum Frequency Generation
bR	Bacteriorhodopsin
CA	Closed aperture
CW	Continuous wave
GL-PYP	glycerol-doped PYP film
IO	Integrated optics
LbL	Layer-by-layer method
MEM	Maximum entropy method
MZI	Mach-Zehnder Interferometer
NLO	Nonlinear optical
OA	Open aperture
OMA	Optical Multichannel Analyzer
OWLS	Optical Waveguide Lightmode Spectroscopy
PAS	Per–Arnt–Sim
PEI	Polyethylenimine
PGA	Poly-L-glutamic acid
PLL	Poly-L-lysine
PMT	Photomultiplier tube
PYP	Photoactive Yellow Protein
RH	Relative humidity
TG	Transient grating

1. Introduction

The need for faster information transfer and data processing continues to grow every year, which pushes towards innovations that would go around the currently faced problems with miniaturization and heat effects. The implementation of photonic devices is one of the possible solutions to these emerging problems, because they are ideally all-optical, meaning their speed of operation is limited by the optical processes present in the circuit, omitting electronic components. All-optical integrated photonics (IO) is the equivalent of currently prevalent integrated electronics; however, every process is solely optical. The key building blocks of photonic devices are nonlinear optical (NLO) materials which possess properties that can modify light propagation, or can store optical information. Photonic devices have started to take their hold in diverse fields such as optical communication, data processing and storage, holography, quantum computing, etc., and the possibilities to make them even more easily accessible and widespread are highly researched. One of the most challenging components of this research is finding or developing materials that possess optimal NLO properties for applicational purposes. Several materials are currently being tested for all-optical operations [1–4], however, many of them are yet to be implemented in application. The application of biomaterials with π-conjugated electron systems has also been recently considered, since opposed to many other materials in development, they are readily available. Chromoproteins are one class of these materials. Various organisms contain chromoproteins functioning as light detectors and energy converters, and have been perfected for these purposes through millions of years of evolution – making them in theory an ideal candidate for a similar filled purpose in IO. However, before photonic application, we need to consider the material's mechanical stability or the NLO properties which change corresponding with their environment. This makes a full NLO characterization and optimization unavoidable.

In the past, the protein bacteriorhodopsin (bR) has been extensively investigated for IO purposes [5–15], and it has proved to be a good candidate for future IO applications; however, utilizing bR also comes with some disadvantages originating from the fact that it only maintains its original structure and functions while embedded in the cell membrane. This makes the technical applicability of the bR limited, and prompts the investigation of other light-sensitive proteins. The photoactive yellow protein (PYP) is a promising candidate for IO. PYP's IO characterization and possible application serves as the topic of this PhD thesis and will be further detailed in the next chapters.

1.1. Photoactive Yellow Protein

The photoactive yellow protein (PYP) is a relatively small (molecular weight of 14 kDa; consists of 125 amino acids), water soluble protein found in purple sulfur bacteria. First found in *Halorhodospira halophila* in 1985, PYP has a major role in bacterial phototaxis, as it makes bacteria avoid blue light [16–18]. PYP belongs to the Per–Arnt–Sim (PAS-) domain superfamily, which is a signal transduction α/β pathway structure, commonly found in prokaryotic and eukaryotic organisms. PAS domains serve as building blocks of sensory and signaling proteins and play an integral part in protein-protein interactions taking place during signaling. Based on structural investigations, PYP displays the same α/β fold structure, with a central β-sheet with five strands and helical connectors on both sides, which can be seen in Figure 1 [19]. Additionally, on either side of the β-sheet, the protein has two hydrophobic cores – the larger one of the two has the chromophore binding pocket, while the smaller one contains the N-terminus [18,20–22]. PYP serves as the structural prototype of the PAS domain superfamily [23].

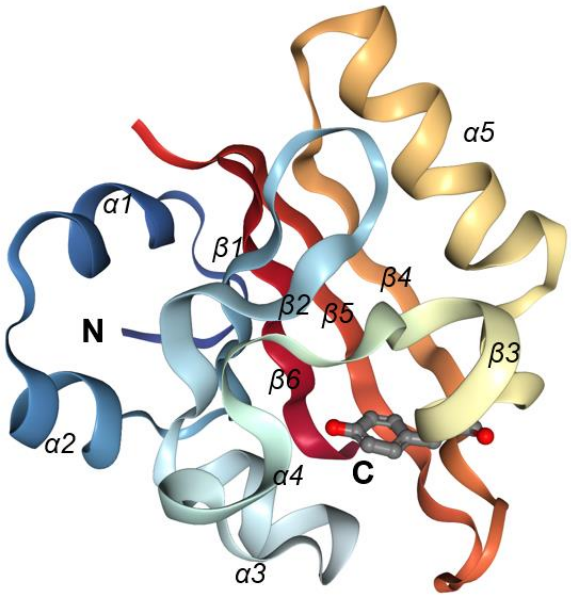

Figure 1. Structure of the PYP. Image created on RCSB Protein Data Bank (https://www.rcsb.org) of PDB ID ID7E [24]**.**

The protein's distinct color comes from the p-coumaric acid chromophore, which is deprotonated in the ground state and lies in trans configuration [22,25]. During light-excitation, the chromophore goes into reversible trans-cis isomerization around its thiol-ester bound attached to the cysteine-69 [22,26,27], which is also responsible for the negative phototaxis detected in PYP-containing bacteria [21]. After this trans-cis isomerization, PYP goes through

several quasi-stable intermediates before re-isomerization, and return to the ground state. This reaction scheme is also called the protein's photocycle [16,28], and is a main factor when considering PYP for IO applications. Generally, the photocycle consists of three main intermediates which differ spectrally – the dark state or ground state (pG) of PYP has an absorption maximum at 445 nm, which when excited, transitions first into a red-shifted intermediate (pR), followed by a blue-shifted one (pB). However, these intermediates can be further classified into multiple substates (pR_1, pR_2, pB_1, pB_2) via spectrally "silent" transitions. Recently, additional fast-rising intermediates have been also detected at the beginning of the photocycle (pR_0) [29]. Furthermore, the photocycle of the protein can also be influenced by numerous factors, such as pH, humidity, or even the excitation wavelength used [30–32].

The processes taking place during light absorption of PYP correspond to the classic scheme of photoexcitable disordered systems, where energy absorption is followed by thermal relaxation [33–35] - in the case of PYP light absorption and light-induced conformational change is followed by the protein's relaxation back to its pG ground state. The primary reaction occurring between atoms and molecules when light excitation is present is described by a rate constant. The rate constant is proportional to the light intensity applied (I) and the reaction's efficiency factor (σ), which includes the absorption cross sections and the quantum efficiencies. Thermal relaxation processes are generally light-independent [7,33–35]. The PYP's photocycle can be seen in Scheme 1A, where the arrows correspond to the transitions between intermediates, however, for the purposes of the detailed experiments the full photocycle can be simplified to that of Scheme 1B.

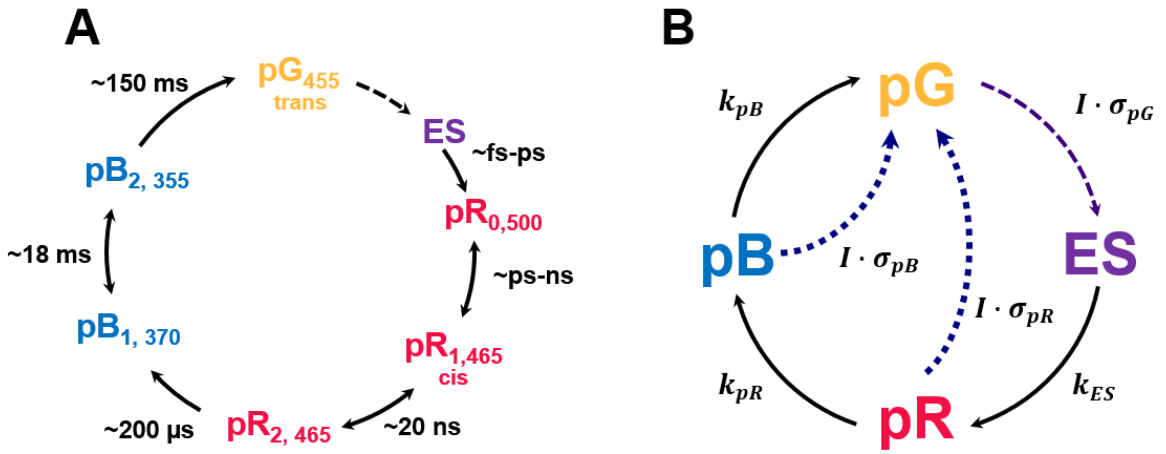

Scheme 1. The full (A) and simplified (B) schematic diagram of the PYP's photocycle.

For the simplified photocycle case, the differential equation system describing the kinetics of the concentrations of the photocycle intermediates can be written as such:

$$\frac{d[pG]}{dt} = -I \cdot \sigma_{pG} \cdot [pG] + I \cdot \sigma_{pR} \cdot [pR] + \left(I \cdot \sigma_{pB} + k_{pB}\right) \cdot [pB] \quad (1a)$$

$$\frac{d[ES]}{dt} = I \cdot \sigma_{pG} \cdot [pG] - k_{ES} \cdot [ES] \quad (1b)$$

$$\frac{d[pR]}{dt} = k_{ES} \cdot [ES] - \left(I \cdot \sigma_{pR} + k_{pR}\right) \cdot [pR] \quad (1c)$$

$$\frac{d[pB]}{dt} = k_{pR} \cdot [pR] - \left(I \cdot \sigma_{pB} + k_{pB}\right) \cdot [pB] \quad (1d)$$

Using chromoproteins in film form are more convenient for practical implementation, and also because generally in dried films the light-induced refractive index changes are orders of magnitude larger than in solutions, where the refractive index of water dominates over that of the protein's [36]. However, certain negative drawbacks also need to be considered, such as the PYP's dependence on the environment. Generally, in high relative humidity (RH, ~80-90%), photocycles are close to the native ones, but as RH drops to moderate values (30-50% to 80%), transitions that follow large conformational changes are held back due to the decreased conformational flexibility, thus slowing down the photocycle [32]. At even lower RH, the photocycle of PYP does not take place [30]. Additionally, applicability is also highly dependent on the NLO material's light-induced refractive index change. Humidity has an impact on refractive index change (Δn) of proteins, thus previously done experiments implementing bR used high to moderate RH environment to maximize Δn but still maintain fast photocycle kinetics [37,38]. While the photocycle does slow down, PYP does have fast intermediates at the beginning of its photocycle when in crystalline form [39–41] which, theoretically the same way as it is for bR [42], are unaffected by humidity. Additionally, the intermediates are also light-sensitive, and are known to be able to transition back to pG by light excitation without going through the entirety of the photocycle, effectively shortcutting it [43].

Due to its size and water-solubility, PYP is a promising biomaterial for IO applications, since it can be more conveniently combined with passive IO components than the more robust, membrane-bound bR [16,17,44], however, for application purposes, the refractive index changes accompanying the absorption changes of intermediates is the most important factor. The refractive index change in function of wavelength can be calculated using the Kramers-

Kronig relations. The complex refractive index is defined as the sum of the real part of the refractive index (n) and the extinction coefficient (κ):

$$n' = n + i\kappa. \tag{2}$$

A material's extinction coefficient is related to its absorption coefficient (α(ω)) in such way:

$$\alpha(\omega) = \frac{4\pi}{\lambda_0}\kappa(\omega), \tag{3}$$

where λ_0 is the applied light's wavelength. One of the Kramers-Kronig relations defines that a material's real part of the refractive index is determined by the extinction coefficient at all frequencies [45,46]:

$$n(\omega) - 1 = \frac{c}{\pi} P \int_0^{\infty} \frac{\kappa(\omega')}{\omega'^2 - \omega^2} d\omega, \tag{4}$$

in which P is the integral's principal value. The absorption and refractive index changes in the function of λ can be seen in Figure 2 from the data provided in [47] and [48] for PYP in solution. Applying Equations 2-4, the data displayed in Figure 2B can be calculated from Figure 2A.

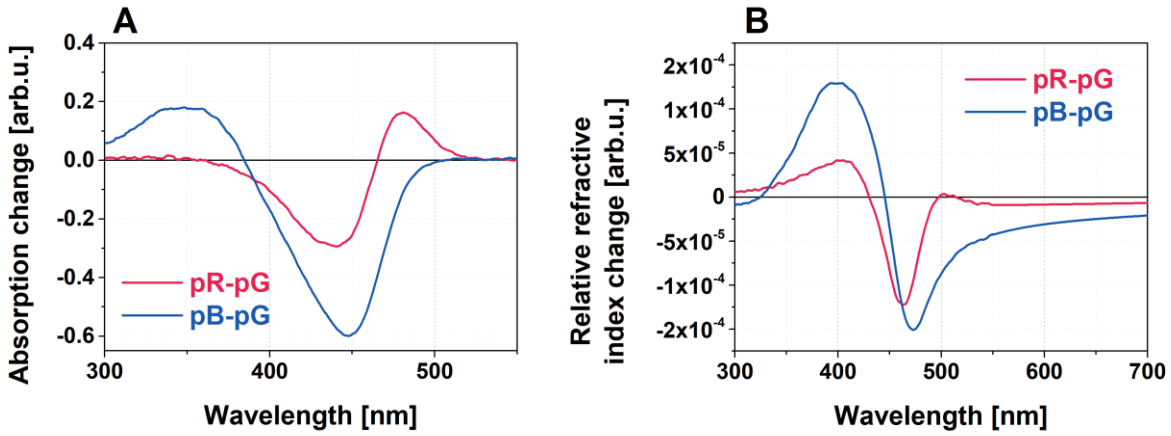

Figure 2. (A) Absorption difference spectra of the pR (red line) and pB (blue line) intermediates compared to the pG ground state of PYP. (B) Refractive index change of the pR (red line) and pB (blue line) intermediates compared to the pG ground state of PYP.

1.2. Z-scan

The single-beam Z-scan technique, first employed in [49], is a popular way to characterise the nonlinear optical properties of both organic and inorganic materials, due to the setup's simplicity. During Z-scan measurement, the investigated sample is moved along the optical axis through the focus of a Gaussian laser beam, while the transmitted power or energy in function of sample position (z) is measured through an aperture placed behind the focus in the far field.

The Z-scan can either be done with open or closed aperture (OA and CA, respectively) – an OA measurement gives us information of the nonlinear absorption coefficients, while a closed, or small aperture trace yields the sign and magnitude of the nonlinear refractive index n_2. The form of the CA Z-scan trace is signature of the technique, and can be explained as the following. The measurement is started while the sample is far away from the focus when the irradiance is low on the sample, and nonlinearity does not occur. If at this point the sample is moved towards the focus, the irradiance will increase, and self-lensing will occur. In case of positive self-lensing, the sample prior to the focus will de-focus the beam, which will lead to a decrease of transmittance measured at the detector due to the beam expanding at the CA, and most of it being cut off. If the sample is moved further along the optical axis, there is a null-point at the focus where the transmittance is equal to the transmittance measure in the far-field. Passing the focal plane, the measured transmittance will increase because of the collimation of the beam after the sample, which also makes the beam narrower at the CA. The scan ends when the sample is moved away from the focal plane to the far field, where irradiance is low again and transmittance becomes linear. The entirety of the measurement will yield first a decrease (or valley) in the transmittance trace, followed by an increase (peak), which is the characteristic of a sample with positive n_2 value. In case of a peak forming first, followed by a valley in transmittance, we are dealing with a sample with negative nonlinear refractivity. This is a clear and simple indicator of the sample's n_2 before even analysis of the measured data. If there is no nonlinear absorption present in the sample (such as multiphoton or saturable absorption), the peak's and valley's transmittance are the same magnitude. The difference between magnitudes can be attributed to the nonlinear absorption happening in the sample, which can be measured by removing the aperture and performing an OA scan. By performing both CA and OA scans, the sample's nonlinear optical properties can be thoroughly investigated.

To characterize the nonlinear refractive index of PYP films, Z-scan technique was applied in both CW and pulsed laser beams with various wavelengths, average- and peak intensities. The Z-scan technique requires the knowledge of the material's linear refractive index, thus, to gain this information for the analysis of Z-scan measurements, optical waveguide lightmode spectroscopy (OWLS) was also performed on a selected wavelength.

1.3. Broadband Vibrational Sum-Frequency Generation Spectroscopy

Vibrational sum-frequency generation (VSFG) spectroscopy is a second-order laser spectroscopic method. It is a powerful surface-sensitive tool for the study of orientation,

structure and dynamics of molecules located on interfaces between two centrosymmetric or random-oriented media. A VSFG setup consists of a narrow-bandwidth visible (VIS) pulse and a narrow-bandwidth infrared (IR) pulse which spatially and temporally overlap on the sample, and through second-order nonlinear process interact and produce an SFG signal with at the sum frequency ($\omega_{SFG} = \omega_{VIS} + \omega_{IR}$). The generated signal's electric field is dependent on the incoming laser beams' electric fields and the second-order susceptibility tensor ($\chi^{(2)}$) through

$$E_{SFG}^{i} \propto \sum_{jk} \chi_{ijk}^{(2)} \otimes E_{VIS}^{j} E_{IR}^{k} \tag{5}$$

where i, j, k are Cartesian coordinate directions of the electrical field components of the visible (E_{VIS}) and infrared (E_{IR}) pulses, while $\chi_{ijk}^{(2)}$ is an element of $\chi^{(2)}$. The intensity of the sum-frequency signal (I_{SFG}) is the square of Equation (5), and thus also proportional to the incident electric fields (I_{VIS} and I_{IR}):

$$I_{SFG} \propto \left|\chi_{eff}^{(2)}\right| I_{VIS} I_{IR}, \tag{6}$$

$\chi_{eff}^{(2)}$ is the linear combination of $\chi_{ijk}^{(2)}$ second-order susceptibility tensor elements.

$\chi^{(2)}$ is only non-zero when the investigated sample is not centrosymmetric - which is the case for interfaces - and can be further broken down into non-resonant ($\chi_{NR}^{(2)}$) and resonant factors ($\sum_q \chi_q^{(2)}$) as so [50]:

$$\chi^{(2)} = \chi_{NR}^{(2)} + \sum_q \chi_q^{(2)} = \chi_{NR}^{(2)} + \sum_q \frac{A_q}{\omega_{IR} - \omega_q + i\Gamma_q}. \tag{7}$$

In the above equation A_q is the amplitude, ω_q is the resonant frequency of the q^{th} vibrational mode and Γ_q is the damping factor. The IR pulse ω_{IR} is tuned so it is resonant with the vibrational transition of the molecules located on the investigated surface, while the VIS pulse is used to upconvert this signal into the visible region. The signal is enhanced when $\omega_{IR} = \omega_q$. From Equation (7) we can see that the measured VSFG signal provides information of the amplitude and spectral width of certain molecular vibrations, and from this we can determine the molecules' orientation on the investigated surface. By implementing tunable femtosecond IR laser pulses, the technique transitions into Broadband VSFG (BB-VSFG), where whole vibrational regions can be measured with single-shot acquisition, while also improving the stability of the measurements by using a higher repetition rate laser system [51]. Additionally, BB-VSFG - opposed to scanning VSFG - can also give us the opportunity to conduct ultrafast

time-resolved vibrational studies. Measurements are done by changing the polarization of the incident beams and the detected signals. Generally, the IR and VIS pulses are linearly S or P polarized, while the VSFG signal is also detected through polarization filters, which overall enables eight polarization combinations – 5 achiral (PPP, SSP, PSS, SPS, SSS) and 3 chiral (SPP, PSP and PPS). In the abbreviations for the polarization combinations, the first polarization belongs to the VSFG signal, the second to the VIS, while the third to the IR. Measuring in either achiral or chiral polarization combination yields different information of the sample. From measuring in achiral polarization-combinations we can investigate the surface's achiral properties - such as the water structure -, while with chiral polarizations-combinations we can reveal the secondary structures present on the surface [52]. VSFG spectroscopy previously has been used to study biomolecules on interfaces, as the technique can cover a wide range resonance wavelengths. The main spectrum of interest ranges from 1600− 1700 cm^{-1}, which covers the vibrational amide I modes of protein backbones, 2800-3800 cm^{-1} for C-H, O-H, and N-H stretching modes, as well as the Amide A and B vibrational modes above 3000 cm^{-1} [52–54]. By investigating the amide I region in unison with the N-H stretch region, we can get information of the protein's secondary structures. With applying chiral VSFG in the 3100-3500 cm^{-1} region we can get an idea of the N-H stretch vibrations coming from the H-bonds from the protein's backbone while distinguishing it more from any signal coming from achiral O-H stretching modes surrounding it [54]. By combining the chiral amide I and N-H stretching vibrational modes, it's possible to establish signature vibrations for specific secondary structures of proteins, as both of these signals are highly specific to certain structures [52,55]. The amide is a C=O stretching vibration mode, which specifically refers to the peptide bond. If it is not in a peptide bond, it is found above 1690 cm^{-1}. Similarly to this, N-H is also different if it is in a peptide bond, however, if a H-bridge is formed with the peptide bond then we are talking about a secondary structure. The typical vibrational resonances obtained for various secondary structural motifs are summarized in Table 1, based in Figure 10 of [52] .

secondary structure	*Chiral vibrational resonance at the air/water interface (cm^{-1})*	
	amide I	*N-H stretch*
α-helix, e.g., rhodopsin	–	3282
parallel β-sheet, e.g., human islet amyloid peptide	1622, 1660	–
antiparallel β-sheet, e.g.,tachyplesin I	1634	3175, 3274
disordered, random coil	–	–

Table 1. Characteristic vibrational wavenumbers of the amide I and N-H stretching modes of different model peptides' and protein's secondary structures in chiral, PSP polarization scheme [52]**.**

Polyelectrolyte multilayers were created by layer-by-layer method, and PYP monolayer was created on the topmost differently charged layers via surface adsorption. VSFG spectroscopy were applied in various polarization combinations to characterize the homogeneity and the orientation of the protein film. IO requires for the structures to be of optical quality and as small and compact as possible. VSFG spectroscopy gives us the opportunity to easily verify the structure and homogeneity of these layers, and their readiness to apply in further IO measurements, such as all-optical switching.

1.4.Optical switching

All-optical switching utilizes a material's light-induced refractive index change to modify another light's signal. All-optical switching can be performed many ways, however, in the current thesis, two interferometric methods were used to demonstrate the optical switching capabilities of PYP.

1.4.1. Integrated optical interferometric light modulation

Interferometric light-modulation can be achieved, e.g., by implementing a Mach-Zehnder interferometer (MZI) as an IO passive device. The MZI is one of the simplest IO passive devices, and consists of bifurcated linear IO waveguide structure with two arms. If a transparent NLO material is adsorbed on one (or both) arms, it alters the effective refractive index of the structure, and it creates a phase difference at the output of the device. The phase difference

manifests as intensity change at the output, and the momentarily measured intensity (I_{out}) corresponds to equation (8):

$$I_{out} = I_1 + I_2 + 2\sqrt{I_1 I_2}\cos(\Delta\varphi). \tag{8}$$

In the above equation I_1 and I_2 are intensities of light propagating through the arms of the MZI, while $\Delta\varphi$ is the phase difference between the two beams.

The IO switching experiment was based on the principle of using PYP as an adlayer on the both arms of the MZI, and thus making it an active IO structure. By utilizing the PYP's refractive index change during its photocycle, excitation of the different intermediates leads to different phase shifts in the arms, resulting a change in the output intensity. With this, either constructive or destructive interference can be achieved.

1.4.2. Ultrafast all-optical switching using transient grating spectroscopy

Transient grating (TG) spectroscopy is a time-resolved four-wave mixing technique, where ultrashort laser pulses with the same frequency are spatially and temporarily intersected on a sample. This creates a sinusoidal distribution of excited states - an interference pattern - in the active material, which then acts as a Bragg diffraction grating. This grating is then probed by a third ultrashort pulse, which arrives at a specific incident angle on the sample. The measured intensity corresponds to the diffraction the pulse undergoes, while the time dependence of it gives information about the dynamic changes happening in the sample [56–58]. We can use the principle of TG spectroscopy to demonstrate optical switching in the sense that if there is no diffraction grating present in the sample, the optical switch is in OFF position, however, if there is a grating present the switch is in ON position.

TG spectroscopy can be applied on PYP films based on the refractive index and absorption change of the protein during its photocycle. A Bragg grating in the sample can be achieved due to the protein entering its photocycle where the interference maxima are present, but staying in ground state where there's an interference minimum.

2. Aims of this work

In this work, the structure and NLO properties of PYP films were investigated in consideration if the protein could be used as an IO active component in the future. Preliminary experiments were also done to demonstrate the switching capabilities of glycerol-doped PYP (GL-PYP) films under various circumstances. The thesis constitutes of four sections detailing the different properties, and preliminary switching application of PYP:

1. First, to investigate the possibility of utilizing protein films in IO, my aim was to study certain photocycle intermediates of PYP. Therefore, the photo-induced changes of PYP films were monitored at different RH, to find the optimal environment. To counteract the possible negative effects of humidity on the photocycle, the kinetics of doped PYP films were also investigated.

2. After characterizing the kinetics of the photocycle of PYP, the linear and non-linear refractive index of GL-PYP films had to be determined. The NLO refractive index of PYP films was investigated with the Z-scan technique as a function of excitation laser pulse parameters, i.e., average and peak intensities, and repetition rate of the pulses.

3. To investigate the potential miniaturization of PYP films, along with their adsorption to solid substrates, the structure of PYP monolayers on top of a single and multilayers of polyelectrolytes was planned to be investigated by applying vibrational sum-frequency generation spectroscopy at different RH environments, in order to create homogeneous protein monolayers for further IO applications.

4. After studying the structural, kinetic, and material properties of PYP films, the final goal was to demonstrate IO switching utilizing the PYP's slow intermediate states by using a Mach- Zehnder interferometer with GL- PYP on the MZI's arms. Then, employing the fast, sub-10 ps, transitions at the beginning of the photocycle of PYP, the aim was to demonstrate ultrafast all-optical switching on GL-PYP samples with a transient grating setup.

3. Materials and Methods

3.1. Film preparation

During measurements two different types of films were implemented. For the experiments involving the measurement of the proteins' photocycle kinetics and nonlinear refractive index, glycerol was added as a doping material, while for the vibrational spectroscopy measurements, the used multilayer structure was built by the layer-by-layer deposition technique.

One of the major requirements for the optimization of protein films for IO applications is that the films need to have a high optical quality. Due to crack formation when drying the PYP films, glycerol was added, which helped to maintain the homogeneity of the films while also stabilizing the relative humidity inside the samples. This approach maintains the relative humidity inside the sample at around 80-85% (which was estimated based on OWLS experiments conducted on bR), enabling the PYP's photocycle to take place, which is not possible at low-humidity environments. To create the samples, the PYP suspensions were mixed with an 87% glycerol solution so as the glycerol constituted 2% of the mixture. The mixtures were sonicated for 1-2 minutes, pipetted onto the surface of interest depending on the conducted measurement, then left to dry for at least 12 hours under an extractor fume hood. For the Z-scan and fast optical switching measurements, the films were sandwiched between two 200μm-thick microscope cover slips, with a 200μm-thick spacer used between the glass slabs, maintaining the film thickness at 200 μm. For the OWLS, absorption kinetics experiments and the optical switching demonstrated on PYP by CW lasers, the protein-glycerol mixtures were prepared the same way, however, sandwiching was not applied. The environment's relative humidity was kept at 33% during each experiment, while the temperature was kept at 23°C.

For the VSFG measurements, the PYP monolayer was adsorbed on top of a polyelectrolyte multilayer which was prepared by the spray-assisted layer-by-layer (LbL) assembly technique. The polyelectrolyte multilayer was an important prerequisite to achieve a homogenous sample surface to which the PYP can adsorb on. The chosen polyelectrolytes were the positively charged Polyethylenimine (PEI, branched type) and Poly-L-lysine (PLL); and the negatively charged Poly-L-glutamic acid (PGA), which were all purchased from Sigma-Aldrich and have a molecular weight of 600,000-1,000,000 (branched PEI solution, concentration of ~50% in H_2O), 50,000-100,000 (PGA sodim salt), and >30,000 (PLL hydrochlorid). The prepared PEI stock solution had a concentration of 5 mg/ml, while the PGA and PLL solutions' concentration was 1 mg/ml. Measurements were done on six different kinds of surfaces - PEI

and PEI+PGA 'monolayer' surfaces, a multilayer finishing off with a PGA surface (PEI+(PGA+PLL)$_{6.5}$), and all of these surfaces with and PYP adsorbed on top. A schematic of the sample preparation procedure can be seen on Figure 3.

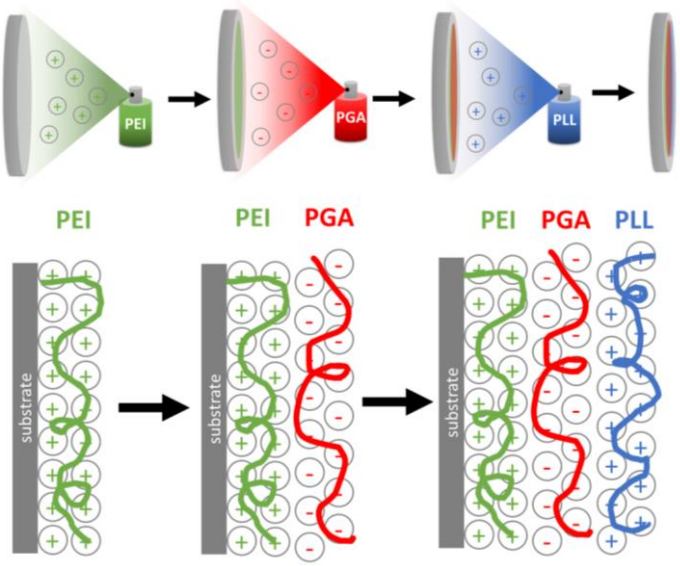

Figure 3. Schematic illustration of LbL assembly on CaF_2 substrate using oppositely charged Polyethylenimine (PEI), Poly-L-glutamic acid (PGA), and Poly-L-lysine (PLL).

The stock solutions were sprayed on CaF_2 windows – first PEI was applied to the entirety of the window to provide a basis for the subsequent layers. The PEI solution was left to set for a minute then the residue was washed away with distilled water. This was followed by spraying PGA, which was left to set for 20 seconds followed by washing of the residue. The PLL was then layered on top of the PGA with the same method, and the layer building continued with layering PGA and PLL on top of each other for up to six and a half pairs of layers, ending with a PGA layer. The PYP stock solution of 0.28 mM was then evenly distributed on top of the final layer of PEI or PGA and left to dry for 5 minutes before washing the residue away. The schematic representation of the polyelectrolyte multilayer preparation can be seen on Figure 3. Measurements were done on polyelectrolyte multilayers finished off with PGA layers to ensure a homogeneous base for the PYP, as created surfaces are more homogenic with higher layer counts [59,60]. Measurements on PYP were done at high (~80%) RH values, however, additional measurements were done at 3% and 100% in the amide region to monitor structural change on the surface due to shift in humidity. In case of sample reuse, the samples were put in a 100% relative humidity environment for an hour before measurements to ensure proper hydration.

3.2. Kinetic absorption spectroscopy

To consider the PYP for integrated optical applications, information about the protein's photocycle is essential. The photocycle kinetics of PYP in solution has already been investigated (overview in[18]), however, the information we have of PYP films is scarce, and GL-PYP films have not yet been investigated previously in the literature. For this purpose, we have conducted measurements with optical multichannel analyzer on PYP films without glycerin in both low and high humidity environments to map the photocycle of the pure protein in film form, however, due to cracking of the protein films, this thesis focuses more on the kinetics of the GL-PYP film. To investigate this, one-wavelength measurements were done on doped films to monitor how the photocycle changes in the presence of added glycerol.

Time-resolved absorption spectra were measured with a home-built pump-probe apparatus. The timescale was from milliseconds to seconds to investigate the accumulating intermediates and their decay during the proteins' photocycle. The applied pump source was Surelite II Nd:YAG laser with an OPO extension (Continuum, USA) with a wavelength of 445 nm for the excitation of the initial state of PYP. The pulse energy was 2.80 mJ. The probe light was an unpolarized beam from a 35-W high-pressure Xenon lamp (Hamamatsu, Japan), which was filtered by narrow-band interference filters at specifically chosen wavelengths to monitor certain photocycle intermediates. The pump and probe beams spatially overlapped on the sample. The transmitted probe beam was sent to Hamamatsu PMT through a HR-320 monochromator (ISA Jobin–Yvon, France). A repetition rate of 0.1 Hz was used to ensure that both proteins return to the ground state before the next excitation. The output signals of the PMT were observed with a homemade current-voltage converter and recorded by a National Instruments oscilloscope card. Ten traces were averaged in total.

To measure the difference spectrum of the formed protein state after excitation, light-excitation experiments were carried out with illuminating the samples with a CW laser for an extended amount of time. We have used the same experimental setup as for the absorption kinetics measurements in the previous paragraph, however, the probe light's intensity was filtered by neutral density (ND) filters before reaching the sample. An iStar gated ICCD detector (Andor Technology, United Kingdom) was equipped to the measuring spectrograph. A 410-nm 40mW laser diode was used for the PYP film, which was illuminated for 10 seconds before the start of each measurement. Ten spectra were averaged.

3.3. OWLS measurements

For the experiments, grating-coupled Si(Ti)O_2 slab waveguides created on a glass substrate ($n_s = 1.53$) were used with a grating width of 1 mm, line density of 2400 mm^{-1}, and refractive index between 1.78-1.80 (n_f, MicroVacuum Ltd.). The waveguides were put on a rotational table (DPS, Ealing Electro Optics). The applied probe beam was from a 543-nm He-Ne laser (λ_0, Melles Griot) and the angle of incidence of it on the sample was measured with high precision and with an accuracy of 10^{-4}. The intensity of the coupled light was measured by a photomultiplier tube (PMT, Hamamatsu, Japan) at the end of the waveguide, then amplified by a voltage converter and recoded by a digital oscilloscope (LeCroy 9310-L). During this measurement, only two discrete modes of electromagnetic waves (adhering to highly selective resonance conditions) can propagate inside the guiding layer - the transversal electric, "TE" and transversal magnetic, "TM", modes. By measuring the incidence angles' peak positions and by using the mode equations of the three-layer waveguide (Equations (9) from [61]), the adlayer's refractive index (n_a) can be calculated:

$$\frac{2\pi}{\lambda_0} d_f \sqrt{n_f^2 - N_{TE}^2} = \arctan \sqrt{\frac{N_{TE}^2 - n_s^2}{n_f^2 - N_{TE}^2}} + \arctan \sqrt{\frac{N_{TE}^2 - n_a^2}{n_f^2 - N_{TE}^2}} \tag{9a}$$

$$\frac{2\pi}{\lambda_0} d_f \sqrt{n_f^2 - N_{TM}^2} = \arctan \left[\frac{n_f^2}{n_s^2} \sqrt{\frac{N_{TM}^2 - n_s^2}{n_f^2 - N_{TM}^2}} \right] + \arctan \left[\frac{n_f^2}{n_a^2} \sqrt{\frac{N_{TM}^2 - n_a^2}{n_f^2 - N_{TM}^2}} \right] \tag{9b}$$

In Equation (9), d_f is the thickness of the guiding layer, N_{TE} and N_{TM} are the effective refractive indices of the TE and TM guiding modes, respectively.

3.4. Z-scan

For the pulsed Z-scan measurement, the setup described in [62] was used by applying laser pulses in the visible spectral range (cf. Figure 4).

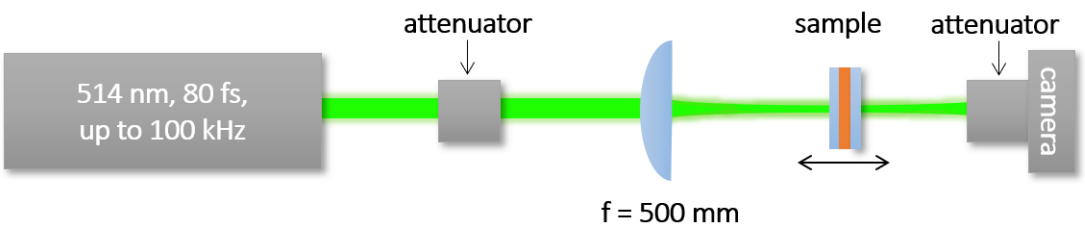

Figure 4. Schematics of the pulsed-mode Z-scan setup.

The utilized laser source was a commercial Yb:$KGd(WO_4)_2$ laser oscillator-amplifier system operating at a central wavelength of 1028 nm with adjustable laser repetition rates up to 100 kHz. After frequency-doubling the fundamental pulses, the sample was probed by linearly polarized 82-fs, 514-nm pulses. To reduce the peak power of the pulses reaching the sample, the pulses were reflected off an uncoated wedge, sent through neutral density filters, a half-wave plate and a thin film polarizer. After attenuation, an f = 500-mm singlet lens was used to focus the pulses onto the sample. The used Gaussian beam radius was measured to be 37 μm, while the measured M^2 values were ≤1.1 both in the horizontal and vertical planes. The pulsed Z-scan setup was additionally used for the CW measurements done at 405 nm using single longitudinal mode, TEM_{00}-spatial-mode, temperature-stabilized diode laser. In this case, the Gaussian beam waist radius was measured to be 36.6 μm. All measurements were detected using a beam profiling camera, and instead of using apertures usually applied in classic Z-scan setups, the OA and CA Z-scan traces were extracted from the measured beam profiles using image processing. The OA traces were determined by adding the signal counts of all pixels of the camera, while the CA traces were obtained by adding the signal counts in a predefined 2D pixel area centered on the center of gravity of the beam profile.

To remove the effect of absorptive nonlinearities present in the pulsed Z-scan measurement, at each z position a 2D Gaussian spatial distribution was fitted on the obtained beam profiles in order to extract the position dependent beam waists, $w_x(z)$ and $w_y(z)$, and amplitudes, A(z). This was followed by the correction of amplitudes, assuming that the background-subtracted total signal count (E, energy) remains constant, i.e., independent of the sample position z. E is defined at a position where the nonlinear absorption is negligible,

$$E = A(|z| \gg z_0)\frac{w_x((|z| \gg z_0)w_y((|z| \gg z_0)\pi}{2} = const. \tag{10}$$

The corrected amplitudes constitute the corrected CA trace with an infinitesimally small aperture, and which can be fitted with the expression valid for negligible nonlinear absorption, cubic nonlinearity, thin-samples, and a peak on-axis phase shifts below π, defined in [49]:

$$T(x, \langle\Delta\phi_0\rangle) = 1 - \frac{[4x\langle\Delta\phi_0\rangle]}{[(x^2+9)(x^2+1)]}. \tag{11}$$

In equation 11, $x = \frac{z}{z_0}$ is the sample position z normalized by the Rayleigh range z_0, and $\langle\Delta\phi_0\rangle$ is the time-averaged, peak, on-axis phase shift. The nonlinear refractive index, n_2, is calculated from

$$n_2 \cong \frac{\langle \Delta\phi_0 \rangle (F\lambda w_0^2)}{L_{eff} P}, \tag{12}$$

where λ is the center wavelength, w_0 is the Gaussian beam waist, $L_{eff} = (1 - e^{-\alpha L})/\alpha$ is the effective sample thickness, and α is the linear absorption coefficient, while L is the sample thickness. F is $\sqrt{2}/4$ or 1/4 and $P = E_p/1.064 \cdot \tau_P$, or $P = E \cdot T_{rep}$ for peak or average power, respectively, in the case of temporally Gaussian pulses (τ_P is the pulse duration at full width of half-maximum, and T_{rep} is the laser repetition period). $\langle \Delta\phi_0 \rangle$ can be obtained when fitting Equation (11) on the measured CA traces, and it is the time-averaged peak on-axis phase shift. The sample holder was made of BK7, which while being empty was measured to have a nonlinear refractive index value of $n_2 = \sim 3 \cdot 10^{-16}$ cm^2/W at 514 nm, which is congruent with that of previously published in the literature [63–65].

3.5. Broadband Vibrational Sum-Frequency Generation Spectroscopy

The BB-VSFG measurements were done at Dr. Zsuzsanna Heiner's laboratory at the Humboldt University of Berlin. A detailed account of the whole home-built laser setup can be found in [51,66,67], however, a brief overview will be given here of the experimental setup. The used pump laser source was a Yb:$KGd(WO_4)_2$ laser oscillator-amplifier system with a center wavelength of 1028 nm, repetition rate of 100 kHz and a maximum output power of 6 W. The pulses were split into two – one beam was used to generate the tunable MIR via optical parametric amplification either in the 2725-3825 cm^{-1} or in the 1400-1700 cm^{-1} spectral range; while the second beam was used to generate the quasi-monochromatic VIS pulses with a center wavelength of 514 nm. A home-made purging system was used along the MIR beam's path to minimize the absorption by atmospheric water vapor and CO_2. The applied VIS laser pulses' energy was at 4 μJ, while for the MIR at 1267, 2980, and 3455 cm^{-1} had been 0.2, 0.7, and 0.7 μJ respectively, which was measured incident on the sample. An f=300 mm singlet lens was used to focus the VIS pulses on the target, while f = 50 mm singlet lens was applied to focus the MIR pulses and temporally and spatially overlap them with the VIS pulses on the sample. The angles of incidence for the pulses were 68° and 57°, respectively for the VIS and MIR pulses. The VSFG spectra were collected by an imaging spectrometer with a Peltier-cooled CCD (Horiba, Ltd., Japan). The spectral resolution was ~3 cm^{-1} which was limited by the spectral width of the VIS pulses and the resolution of the spectrograph. The polarizations of the incident light beams were controlled by zero-order half-waveplates, while a polarizer with a

half-wave plate was applied for the VSFG signal at the entrance of the spectrometer. VSFG spectra were collected in four different spectral ranges - the C-H, N-H and O-H stretching regions and the amide I region -, in two achiral (PPP and SSP) and three chiral (SPP, PSP, PPS) polarization combinations. The acquisition times ranged from 10 s to 120 s depending on the spectral region and polarization combination. All measurements were done in a near total-reflection-geometry and were carried out using a home-built container seen in Figure 5.

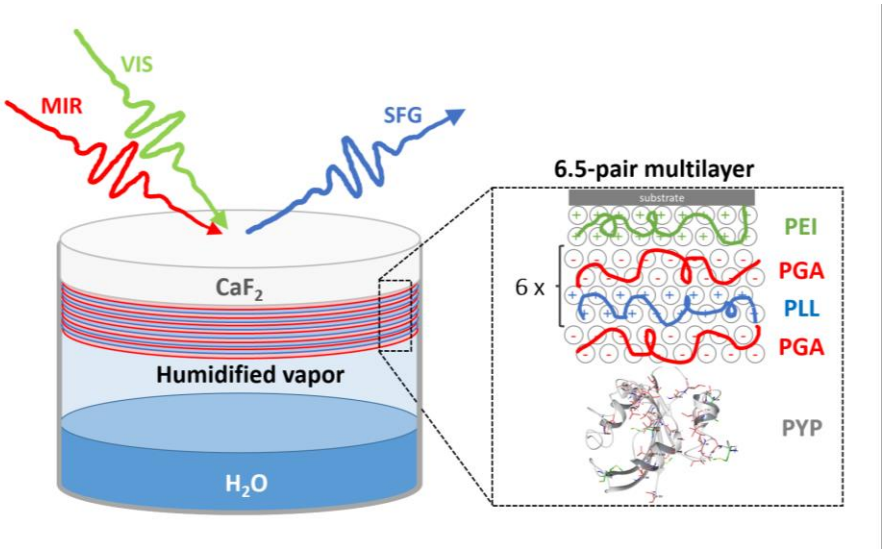

Figure 5. Schematics of the near total-reflection-geometry used in VSFG measurements.

The CaF_2 plates on which the samples were created were turned to face the inside of the container in which water was left in the bottom to maintain high relative environmental humidity throughout the measurements. The temperature was also kept at 23°C, and each measurement was repeated at least three times. The spectra were calibrated with a 50-µm-thick polystyrene film, which was inserted into the MIR beam's path. The background's contribution was removed from the spectra by subtracting a spectrum measured without the MIR's contribution. The spectra were converted into count-per-second by dividing the background corrected spectra by the acquisition time. A non-resonant spectrum was measured on a silver surface which was used to normalize the sample's VSFG spectra. This was followed by multiplying the VSFG spectra by the MIR's intensity measured at the sample's surface to get an absolute comparison of different spectral regions.

The spectra were finally fitted with Lorentzian peak profile to accurately determine the position of the vibrational bands:

$$I_{VSFG}(\omega) \propto \left| P_{NR} e^{i\phi} + \sum_{i=1}^{v} \frac{Q_v}{\omega - \omega_v - i\Gamma_v} \right|^2 . \qquad (13)$$

In equation (13), $P_{NR}e^{i\phi}$ is the nonresonant contribution of the SFG signal, while Q_υ, ω_υ, and Γ_υ is the υ^{th} vibrational mode's strength, central frequency, and damping factor.

The fits were done by using global fitting method, simultaneously fitting all chiral and all achiral VSFG spectra, which minimized the error that would occur if the spectra would have been fitted separately. The spectra were fitted by a sum of Lorentzian functions based on Equation 13 (depending on surface and chirality). The fitted equation permits constructive and destructive interference between peaks, which depend on the phase of the Lorentzian oscillator. All fits were done using the Igor Pro 8 software.

3.6. Optical switching

3.6.1. Switching with an IO Mach–Zehnder interferometer

A beam from a green laser diode (532 nm, 50 mW, Roithner, Austria) was used as a probe light and was coupled into a single mode home-build MZI by a single-mode optical fiber (S630-HP, Thorlabs GmbH, Germany), which was positioned at the MZI's input by a micro-positioner (DC-3K, Märzhäuser Wetzlar GmbH & Co. KG, Germany) and was fixed with photopolymer glue (OP-66-LS, Dymax Europe GmbH, Germany). An additional single-mode optical fiber was used for outcoupling of the light from the interferometer. The GL-PYP stock solution was pipetted onto both arms of the interferometer in ~1 mm diameter patches and was left to dry before conducting the measurements. To excite different intermediates in the PYP's photocycle two CW lasers were used at 445 nm and 405 nm, with an intensity of 4.44 mW and 21.7 mW at the sample, respectively. The duration of the excitation was varied between 2 and 14 seconds, depending on measurements, and only one protein patch was excited at a time. To tune the bias point of the MZI, a heating wire was implemented in the vicinity of one of the MZI's arms, and the voltage switched on it was varied between 0–4.6 V by a variable DC power supply (VLP 2403pro, Konrad Electronics, Germany).

To measure the MZI's transfer characteristics, the optical fiber at the output was coupled into a PMT (H5783-01, Hamamatsu, Japan) from which the signal was transmitted to and recorded by a digital oscilloscope (LeCroy 9310-L, LeCroy, USA). During measurements, the environment's temperature was 23 °C, with a relative humidity of 33%. The schematic representation of the measuring setup can be seen in Figure 6.

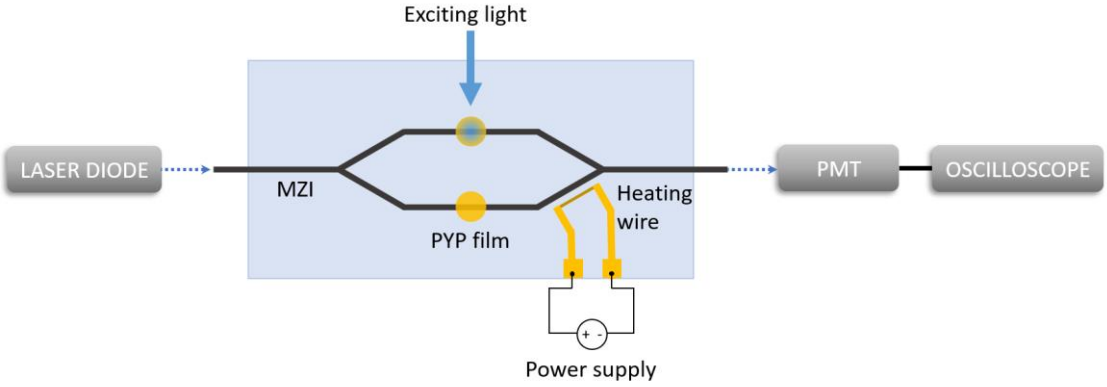

Figure 6. Schematic representation of the measuring IO device, the MZI with the PYP adlayer and the heating wire for bias-point adjustment.

3.6.2. Ultrafast switching demonstrated with transient grating technique

For the ultrafast TG experiments, the same 6 W Yb:$KGd(WO_4)_2$ laser system was used as for the VSFG spectroscopy and Z-scan measurements but with minor modifications. An average power of 4 W (i.e., 40 μJ) was used to generate the probe pulses at 514 nm, while the remaining 2 W was used for pumping an optical parametric amplifier (Orpheus, Light Conversion, Lithuania) to generate either 450 nm or 480 nm laser pulses that were used as a pump beams during measurement. The pulse durations were 160 fs in both of the pump and probe pulses. Before each experiment, temporal pulse characterization was performed using the same TG setup with a 1-mm thick fused silica plate, applying the transient-grating frequency-resolved optical gating (TG-FROG) technique [68,69]. The schematics of the setup and experimental method can be seen in Figure 7.

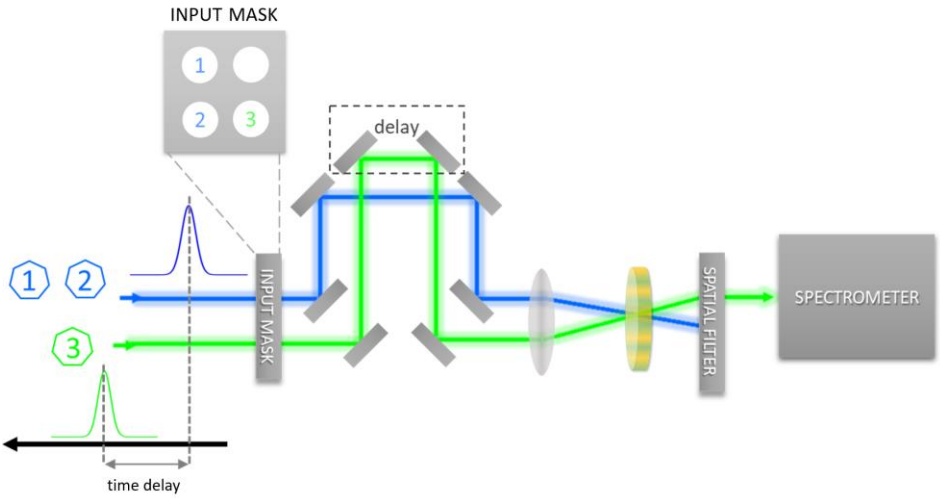

Figure 7. The TG setup's schematic diagram.

During experiments, a simplified version [69] of the folded BOXCARS geometry was used [70,71]. The beams were expanded and spatially filtered by an input mask, generating flat-top beams with a diameter of 2 mm, pulse energies between 1-12.5 nJ at repetition rate of 1 Hz. The two pump beamlets (1 and 2 on Figure 7) were derived from the expanded input beam, and then were focused on the sample by a 50 mm achromat lens to generate the grating. The pump beamlets were spatially and temporally overlapping in the sample, while the third beamlet (probe, 3 on Figure 7) was delayed with respect to the excitation pulses by using a translational stage with 20 fs step sizes, and had a pulse energy of 3 nJ at the sample. The time-dependent diffracted probe signal was spatially separated by the incident beams by an output mask and was detected using a miniature fiber optic spectrometer (Ocean Optics, USB2000+, USA). The diffracted signal could only be detected at the direction corresponding to the phase matching equation $\vec{k} = \overrightarrow{k_1} - \overrightarrow{k_2} + \overrightarrow{k_3}$ (where $\vec{k}_{1-3}$ are the wave vectors of beamlet 1-3, respectively). The 450-nm and 480-nm pump wavelengths were chosen specifically to overlap with the ground state of PYP and were used to test the hypothesis that the photocycle kinetics differ depending on excitation wavelength. To create a mixture of excited states that also functions as quasi-steady state, an additional CW excitation was applied on to the sample with the wavelength of 405 nm, with various excitation intensities.

During the TG measurements, a single shot spectrum without averaging was recorded from -0.8 to 10 ps, which provided the time-dependent TG signals. A background spectrum was measured at -1.8 ps and was subtracted from the data. The zero time position was determined by increasing the pump intensity and substituting the protein sample for an uncoated glass substrate and generating a non-resonant Kerr-type diffraction signal in the bulk substrate. Due to the applied spectral bandwidth of the pump and probe pulses being relatively narrow, a limited range of pixels were used and summed up at each delay position to generate the diffraction signal.

4. Results and Discussion

4.1. Photocycle of the glycerol-doped Photoactive Yellow Protein film

To consider the PYP films for IO application, an extensive knowledge of the protein's photocycle is required. To characterize certain intermediates, and to consider the possible transitions between them due to photoexcitation while the photocycle is already in progress, flash-photolysis experiments were performed. Previously, PYP films without any ballast material have been investigated, and it was concluded that while the photocycle does take place similarly to that of the protein-in-solution sample at high humidities (absorption spectra of intermediates of undoped PYP films presented in Figure 8A and kinetics in Figure 8B), this is not the case when the environment's humidity drops below 50%. Moreover, pure protein films tend to set on a solid substrate with surface cracking, leading to an optically inadequate film that is not utilizable in the long run for IO.

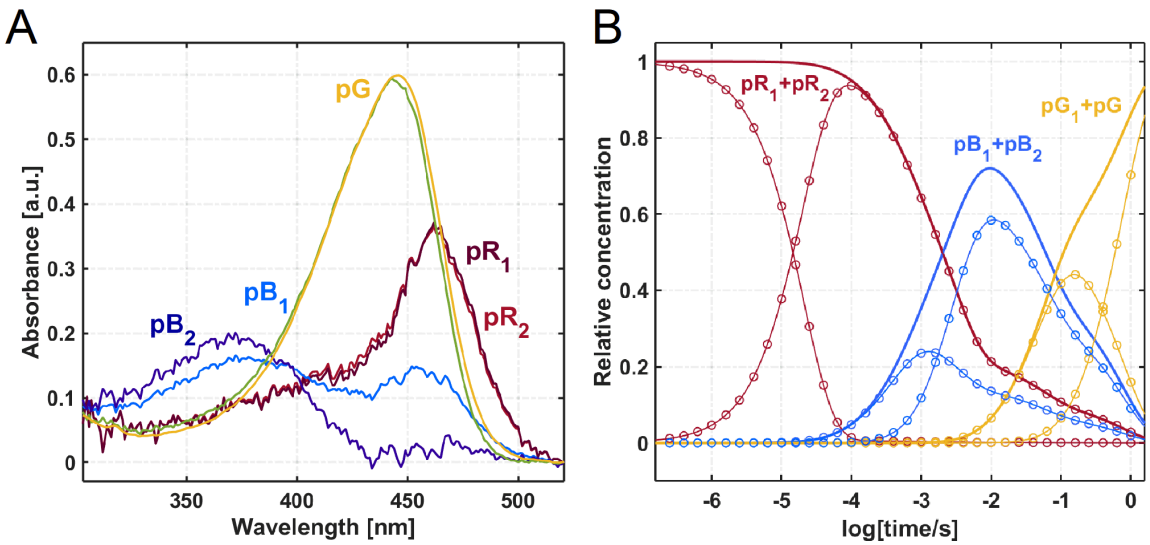

Figure 8. Intermediate spectra (A) and kinetics (B) of undoped PYP films in 85% RH environment.

To address the issues present in an undoped film, we have added glycerol to the PYP solutions, however, this can cause changes in the photocycle of the protein, which needs to be monitored. To do this, absorption kinetic experiments were performed by selecting specific wavelengths corresponding to photocycle intermediates and detecting the absorption changes over time after excitation. One of the chosen wavelengths was 430 nm to monitor the changes in the ground state's concentration. The chosen 430 nm is slightly blue-shifted from the initial state's maximum, to limit backscattering of the exciting light. Additionally, 360 nm was chosen to follow the concentration changes of the pB intermediates, while 470 nm was chosen for the

pR intermediates. We have found that the GL-PYP films' photocycle – opposed to the pure PYP film's one – does take place even in low RH environments, and has a rate-limiting step of ca. 6 s (Figure 9A). There were spectral changes taking place in the protein sample at wavelengths corresponding to the pR and pB intermediates, which should not have been possible in case of the absence of the photocycle.

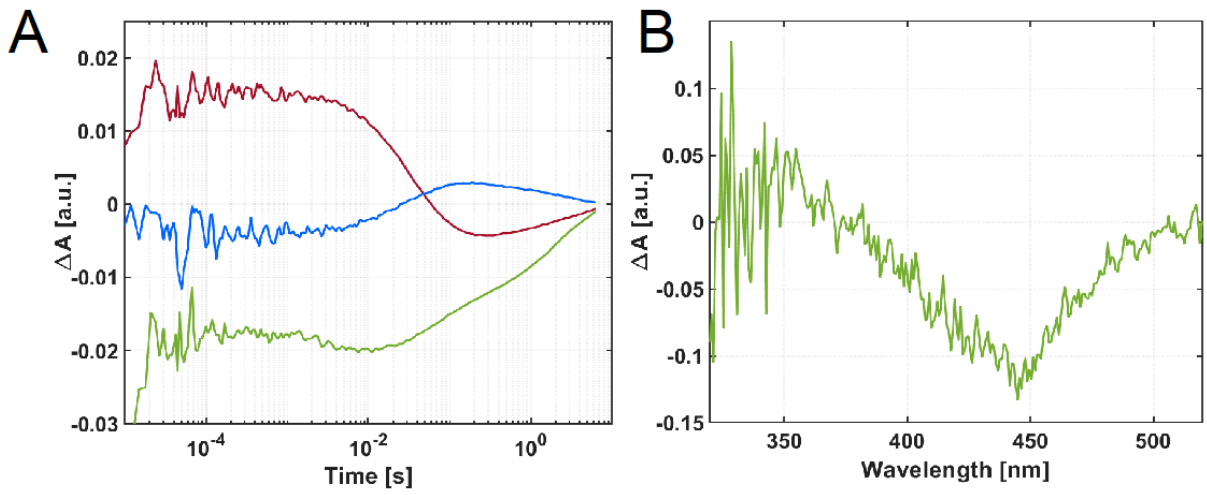

Figure 9. (A) Absorption kinetics measurements and (B) intermediate accumulation measurements taken on a GL-PYP film. In subfigure (A), the blue line corresponds to the absorption difference spectrum measured at 360 nm, the green line at 430 nm, and the red line at 470 nm. In subfigure (B), the absorption difference spectrum is shown after exciting the sample for 10 s with a CW laser of 410 nm at 40 mW.

Based on the glycerol concentration present in the sample, it is estimated that the water activity inside the sample to be equivalent of a glycerol-devoid PYP film placed in a 80% environment [72], however, when comparing the PYP films' photocycle in high RH environment, the GL-PYP film has a significantly slower photocycle [73]. This can be attributed to viscosity effects [74], opposed to water-structure mediated kosmotropic effects [75], which would be expected to accelerate the photocycle due to destabilization of open conformations - such as the pB intermediate [47,76].

According to the accumulation measurements, after 10 s continuous illumination, the majority of the protein is in the pB state (Figure 9B), hence we can assume that PYP is driven to a steady state of pB and the initial states. The ratio of the intermediates in this steady-state is dependent on and adjusted by the average exciting light intensity applied during Z-scan and switching experiments, and specific simplified photocycle schemes will be discussed in further chapters relative to these parameters.

Due to the photocycle pathway not changing significantly (other than kinetically) between PYP in solution compared to the GL-PYP film in high RH environment, we can assume the spectra presented in [47] hold true for the above investigated GL-PYP sample. This is also accurate when comparing the measured absorption difference spectrum of the pB intermediate in Figure 9B and the difference spectrum subtracted from [47], which is previously shown in Figure 2A (blue line).

4.2. Determining the linear and nonlinear refractive index of PYP films

4.2.1. Linear refractive index

To successfully access the Δn and n_2 values of PYP from the Z-scan experiments, the linear refractive index values of GL-PYP films need to be determined. By applying the OWLS method, high-resolution scans were done by measuring the angle of incidence in the range where light could be coupled inside the waveguide. The measurements were first conducted with a bare waveguide, then followed by coating the same waveguide with the PYP film. The recorded signals were fitted with Gaussians to obtain the TM and TE modes. By fitting first only the bare waveguide, the guiding layer's thickness and refractive index was determined, which was then used to calculate the PYP adlayer's refractive index. The protein film was always prepared in a way to make sure its thickness was an order of magnitude larger than the guiding light's penetration depth [61]. The measured and calculated values of the bare waveguide and the GL-PYP film can be seen in Table 2.

	TM position [°]	**TE position [°]**	**Refractive index**	**Thickness**
Bare waveguide	15.777	19.164	1.799	195.26 nm
GL-PYP	18.672	20.595	1.460	>5 μm

Table 2. The measured TM and TE incident angles and the calculated refractive index values and sample thicknesses.

4.2.2. Nonlinear refractive index

Based on the findings in the previous chapter (Chapter 4.1), excitation of the initial ground state of PYP has negligible linear absorption at 514 nm, therefore, using this wavelength at low excitation intensities would not trigger the protein's photocycle during Z-scan

measurements. If the photocycle is initiated at high (≥ 1 kHz) repetition rates, it would lead to the accumulation of the pR intermediate state.

OA and CA Z-scan traces were recorded using 514-nm pulsed excitation at 1 kHz and 100 kHz repetition rates, of which the CA traces can be seen in Figure 10A and B at different average and peak intensities. The peak-to-valley configuration of the CA traces indicates a negative n_2 value, meaning a defocusing nonlinearity, which is in agreement with our group's previously measured negative Δn value at 633 nm for undoped PYP films, and also corresponds to previously recorded data in the literature between 470 nm and 570 nm [77]. We have found that the nonlinear response is driven by the average intensity rather than the peak intensity. As shown in Figure 10C, the magnitude of the nonlinear refraction at an average intensity of ~4.6 W/cm^2 at 1 kHz and 100 kHz only varies within ~30%, despite peak intensities being a factor of thousand different. This suggests that the excitation mechanism is not two-photon absorption but a weak linear absorption process, which agrees with the OA measurements, which also show no sign of nonlinear absorption (cf. Figure 10C open symbols).

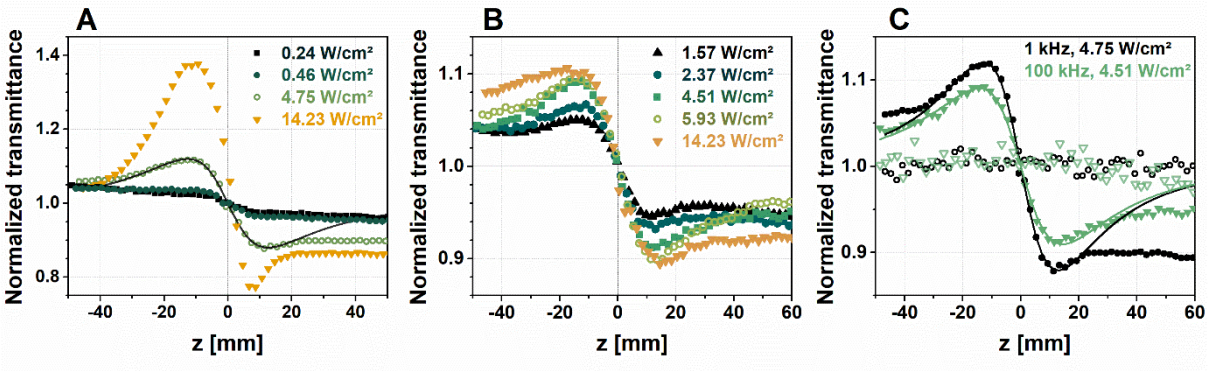

Figure 10. Closed-aperture Z-scan measurements done on PYP using fs 514 nm laser pulses at repetition rates of (A) 1 kHz and (B) 100 kHz at various average excitation intensities. (C) shows the comparison of closed-aperture traces (filled symbols) and the open-aperture traces (hollow symbols) at the repetition rate of 1 kHz and 100 kHz.

The nonlinear refractive indices which were calculated from the traces above can be seen in Figure 11A and B. The absolute value of the nonlinear refractive index is inversely proportional to the average intensity. In case of average intensity being in the range of 0.1 to 1 W/cm^2, n_2 values fall between the range of 10^{-3} to 10^{-4} cm^2/W. These results correspond to n_2 data extracted from [78] article's Δn numbers, which yield a nonlinear refractive index value of $-2\cdot10^{-2}$ to $-9\cdot10^{-3}$ cm^2/W, obtained for an average intensity between $3\cdot10^{-3}$ and $2\cdot10^{-2}$ W/cm^2 at 475-nm CW-laser excitation. The measured n_2 values of PYP are several orders of magnitude higher than compared to values previously reported for NLO materials [4,63,79].

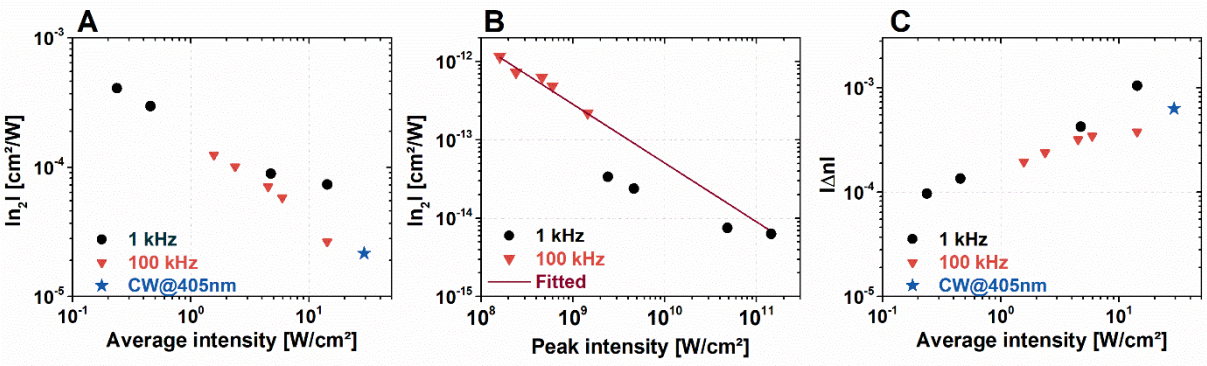

Figure 11. Absolute value of the nonlinear refractive index of PYP at 514 nm as a function of (A) average and (B) peak intensity. (C) shows the absolute value of the measured refractive index change as the function of average intensity.

When plotting the nonlinear refractive index values as a function of peak intensity, we have found that n_2 values at different repetition rates follow different power laws (Figure 11B) – the line fitted on the values corresponding to 100 kHz clearly do not fit to the data of the 1-kHz measurements. However, we have found that, at both repetition rates, the n_2 values depend less on the peak intensity than they do on average intensity, with n_2 being in the range between 10^{-12} and 10^{-14} cm^2/W with peak intensities of 10^8–10^{11} W/cm^2. The Δn values increase as a function of average intensity at both repetition rates, following a weak power law, maintaining Δn values at same order of magnitude throughout the applied average intensity range (cf. Figure 11C). The obtained Δn values are in agreement with those found in literature for CW excitation at 475 nm, in the case where the photocycle can be unambiguously initiated [78].

4.3. Investigation of oriented PYP films

In this chapter, the focus is kept on the secondary structure of the PYP on top of the charged polyelectrolyte layers. Information on secondary structure can be deducted from chiral VSFG spectra, and for this reason, while measurements have been done and are shown occasionally in multiple polarization combinations to observe layer homogeneity, this chapter will be mostly focused on detailing the findings in the chiral SPP and PSP polarizations.

4.3.1. VSFG spectra of the PYP

To monitor the adsorption of the protein on positively and negatively charged polyelectrolyte films, first a hydrated PYP film was created on top of a plasma-treated CaF_2 window/slab. The slabs were kept at constant humidity and temperature during measurements. The measured VSFG spectra at 80% RH can be seen in Figure 12, for wavenumbers between 2800 and 3500

cm^{-1} to see the C-H, O-H, and N-H regions; and between 3000 and 3800 cm^{-1} for the N-H and O-H region. The VSFG spectra of the thin protein films were measured at both chiral and achiral polarization combinations.

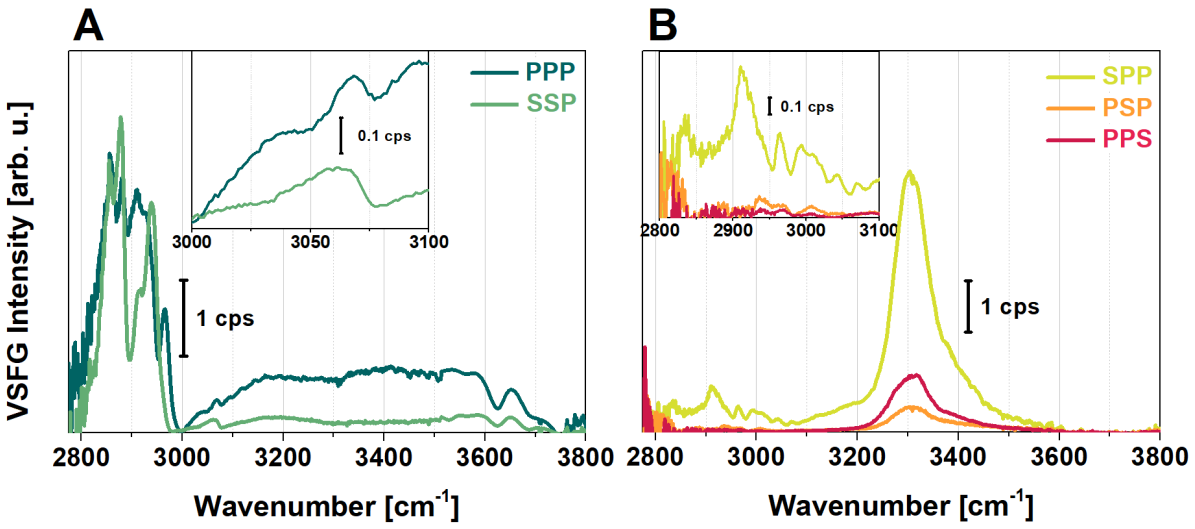

Figure 12. Achiral (SSP, PPP) and chiral (SPP, PSP, PPS) VSFG spectra of hydrated thin film of PYP on CaF_2 in the C-H and N-H/O-H stretching regions. Inset shows only the chiral spectra in the C-H stretching region. The spectra were interlinked from two measurement sets between 2800-3600 and 3500-3800 cm^{-1}.

Looking at the achiral polarizations, there are three intense bands visible for the C-H stretching, which can be assigned to the C_α-H, CH_2 and CH_3 vibrational modes. The CH_3 symmetric and asymmetric stretching modes, which appear at 2883 and 2958 cm^{-1}, respectively, are the most intense out these bands. The Fermi resonance of the methyl group (a resonance between the symmetric methyl stretching and the symmetric bending overtone) also has a strong band at 2945 cm^{-1}. The obtained high intensity of the vibrational modes of the methyl group correlates with their high number in the side chains of the protein, possessing a highly ordered arrangement at the air-protein interface. The high conformational order of the methyl groups is due to their hydrophobic nature leading them to point more upwards in the direction of the vapor. The contribution of the symmetric (2850 cm^{-1}) and asymmetric (2930 cm^{-1}) stretching, and the Fermi resonance (2910 cm^{-1}) of the methylene group is relatively small. These observations are in good agreement with previous studies of various proteins at hydrophilic silica surfaces [80] or at the air-water interface [81,82]. Interference effects are also visible between the aromatic C-H stretching and NH_3^+ modes of the side chains (Figure 12A).

For chiral polarization combinations (SPP, PSP, and PPS, Figure 12B) four stretching modes are present in the measurements at 2945, 2970, 2984, and 2998 cm^{-1}. In SPP polarization

additionally the methylene stretching band is also visible at 2910 cm^{-1}, which may be a contribution from the C_β-H_2 methylene groups of sidechains.

Between 3000 and 3100 cm^{-1}, we can see chirality coming from the side chains of rings and NH_3^+ groups in the PYP. We can see interference effects stemming from the ring's C-H stretching and side-chain's NH_3^+ modes interfering with the vibration of Amide B's. In chiral polarizations at 3300 cm^{-1}, we can see bands belonging to N-H stretching, which are almost nonexistent at achiral polarizations. This corresponds to previously obtained N-H stretching spectra [52]. Around 3200 and 3400 cm^{-1}, the chiral O-H stretching vibrations are visible and are coupled with the chiral N-H stretching modes of the protein backbone. This indicates that the secondary structure of PYP at the air-water interface is well-ordered and the interfacial water molecules that are H-bonded to the backbone are following the ordering of the N-H dipoles. Previous studies concluded that this water reorientation occurs within an interaction distance of about < 10 Å at the air-water interface. What we see here is likely the well-ordered β-sheet part of PYP, since the chirality of the C_α-H group governs the symmetry of the N-H moiety [55]. This β-scaffold motif stands at the end of the protein from the 88th to the 125th amino acid, where most of the side chains (22 out of 38) are polar or charged. This chiral feature was previously assigned in the literature to the C-H and N-H groups of the backbone of an antiparallel β-sheet also influencing the orientation of nearby water molecules [83]. On the measured homodyne VSFG spectra an analysis based on the maximum entropy method (MEM) [84,85] was performed by Dr. Zsuzsanna Heiner, from which we can assume that the anti-parallel β-sheet part of PYP, i.e., β-scaffold, is more likely oriented parallel with the surface.

4.3.2. VSFG spectra of PEI and PEI+PGA at the air-water interface

To get an idea of the surfaces the PYP will be adsorbed on, first measurements were done on PEI and PEI+PGA polyelectrolyte layers. For more comprehensive information, each of the normalized VSFG spectra was fitted by a sum of Lorentzian functions based on Equation (13), where the number and sign of the amplitudes of the resonances were taken from the MEM analysis. A global fitting procedure was employed on the VSFG spectra in SPP and PSP chiral polarizations. The resulting curves are also shown in Figure 13 A-B.

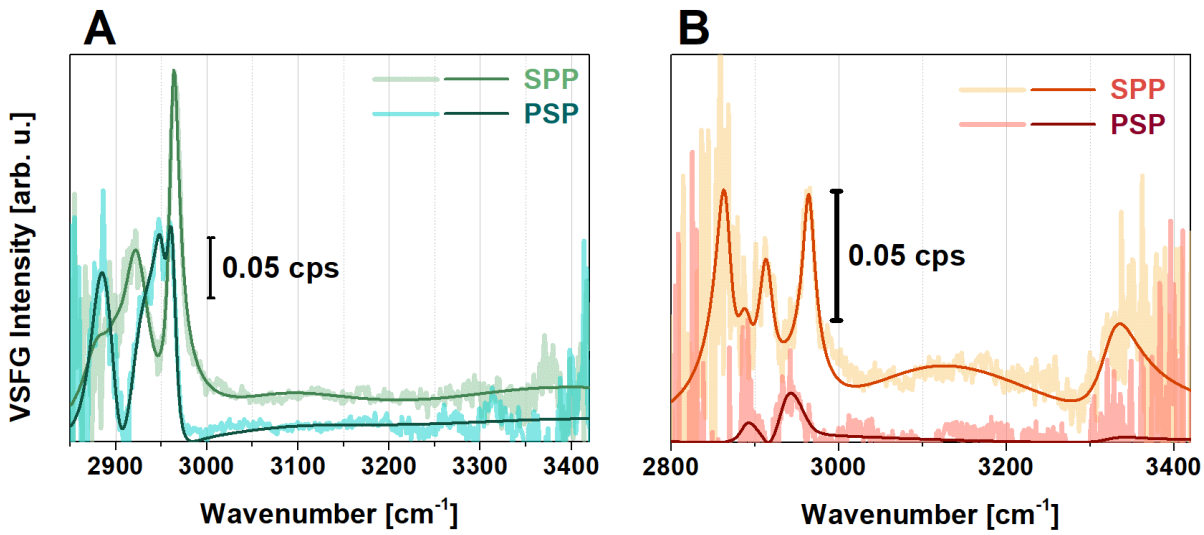

Figure 13. Obtained and fitted chiral VSFG spectra of PEI on CaF_2 (A) green/blue curves, and PGA on PEI-CaF_2 (B) orange/red curves. The fitted curves based on Equation (13).

In the chiral VSFG spectra of PEI (Figure 13A), C-H stretching bands appear at 2890, 2900, 2925, and 2950 cm^{-1}. This suggests secondary structural elements present in the chain of the hydrated layer, i.e., double helix conformational parts [86]. N-H and O-H stretching modes with small amplitudes are observed at around 3070, 3270, and 3320 cm^{-1}, which resonances can be linked to the chiral C-H groups. The lower N-H stretching frequency indicates a strong N-H···N hydrogen bond.

At chiral polarizations for PGA, C-H vibrational bands at 2900, 2934, and 2960 cm^{-1} are observed. We can attribute the first and the last vibrational bands to the C_α-H stretching mode controlling the chirality in amino acids. This doublet was previously also obtained in the Raman spectra of alcohols [87]. Above 3000 cm^{-1} both in SPP and PSP polarizations we can see a broad bandwidth very weak signal, which suggests the PGA does not form in a well-ordered β-sheet or α-helical arrangement since there is no characteristic chiral N-H stretch at ~3300 cm^{-1} present. This absence of chiral N-H stretch only occurs for random coil or disordered structures, which implies the PGA possibly depositing in a random coil structure atop of PEI [52]. The overall VSFG signal decreased when PGA was adsorbed on PEI which is most likely due to destructive interference between the methylene modes of PEI and PGA.

The homogeneity of the created multilayers can be improved by creating several pairs of oppositely charged layers [59,88]. For this reason, VSFG spectra was measured of the topmost layer of PGA changed when 0.5 versus 6.5 pairs of layers were built up with the LbL technique, using PLL between PGA layers. In each of the applied polarization combinations (PPP, SSP, SPP) a much higher signal was observed for 6.5-pair layers due to the higher surface

homogeneity. Importantly, the red-shifted O-H stretching in each polarization shows a higher signal which can be attributed to a well-ordered interfacial water structure near the charged side chains of amino acids. The results can be seen in Figure 14.

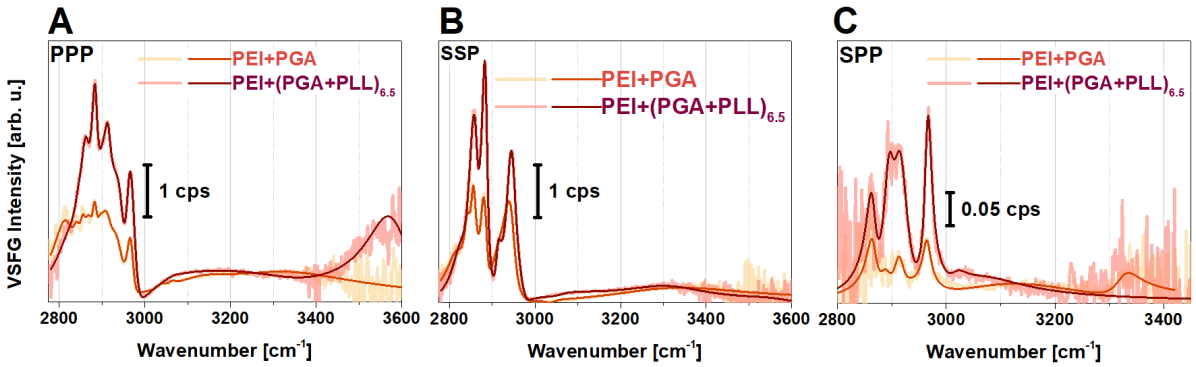

Figure 14. Achiral (A and B) and chiral (C) VSFG spectra of one pair of PEI+PGA (orange) and PEI+(PGA+PLL)$_{6.5}$ (dark red) multilayers in the C-H, N-H, and O-H stretch region. The topmost layer contains PGA in each case.

4.3.3. PYP adsorption at the air-polyelectrolyte interfaces

Finally, the VSFG spectra of PYP adsorbed on clean CaF_2, on PEI and PEI+PGA layers was measured. The measurements were done in the 2800 to 3600 cm^{-1} range in SPP polarization combination. The findings are summarized in Figure 15.

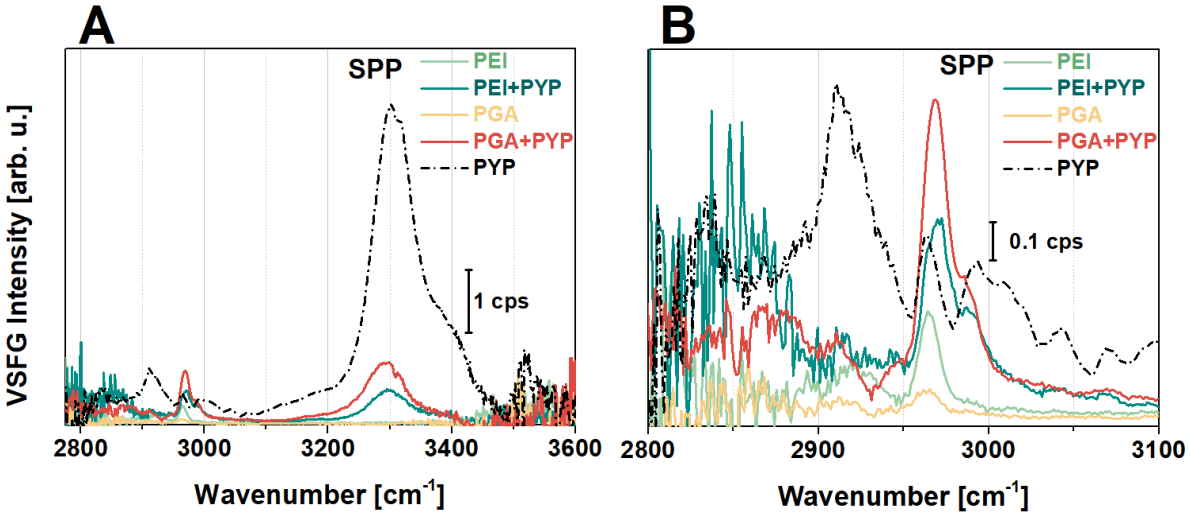

Figure 15. VSFG spectra of PYP adsorbed on PEI or PGA single polyelectrolyte layers prepared by LBL method. For comparison, the corresponding spectrum of PYP film (black dash-dotted line) is shown. (A) shows the spectra in the 2800-3600 cm^{-1} range, while (B) is a zoomed in figure of the 2800-3100 cm^{-1} VSFG spectra.

The VSFG spectra measured for PYP and PYP adsorbed on either PEI or PGA surfaces is different, however, only small differences in VSFG spectra were observed for the PYP

adsorbed on PEI or PGA. In chiral polarization, vibrational bands at 3030, 3050, and 3070 cm^{-1} appear clearly without interference for each PYP sample. Looking at the zoomed-in spectra in Figure 15B we can see that by adsorbing the PYP on both PEI and PGA, characteristic bands of C_α-H and CH_3 groups emerge at 2943, 2958, 2976, and 2990 cm^{-1}. The vibrational bands corresponding to C_α-H and N-H stretching modes are red-shifted for PGA+PYP versus PEI+PYP, indicating stronger interaction, i.e., shorter bond lengths. At 2990 cm^{-1}, the sign of the vibrational mode is opposite, positive for PEI+PYP and negative for PGA+PYP. These bands all come from various amino acids in PYP. The C_α-H stretching can be attributed to the valley at 2958 cm^{-1} and the local peak at 2976 cm^{-1}. These bands show opposite signs in the imaginary χ^2 spectra (figure not shown) which suggests that the C_α-H stretch exhibits the same chirality and orientation as the N-H stretch at ~3300 cm^{-1}. From this we can conclude that these chiral vibrational modes can be connected to the antiparallel β-sheets with hydrogen bonds between C═O···H–N which are lying on the plane of the surface. The spectral shoulder located at 2990 cm^{-1} is usually connected to a C_α-H bond from other amino acids, most often assigned to lysine [55,82], which is the amino acid that is in highest number in the structure of the β-scaffold motif of PYP. The PYP's β-sheet structure is also supported by the well-ordered N-H stretching and the presence of a strong chiral amide I vibrational mode, as seen in Figure 16.

Additionally, the VSFG spectra of the 6.5 pair polyelectrolyte layers were investigated in the amide I region due to their improved structural homogeneity and thus larger observable VSFG signal. The results for these measurements in the SPP polarization combination can be seen in Figure 16, with and without PYP, between 1500 and 1700 cm^{-1}. This region is suitable for both observing the amide I, II modes as well as side-chain vibrations.

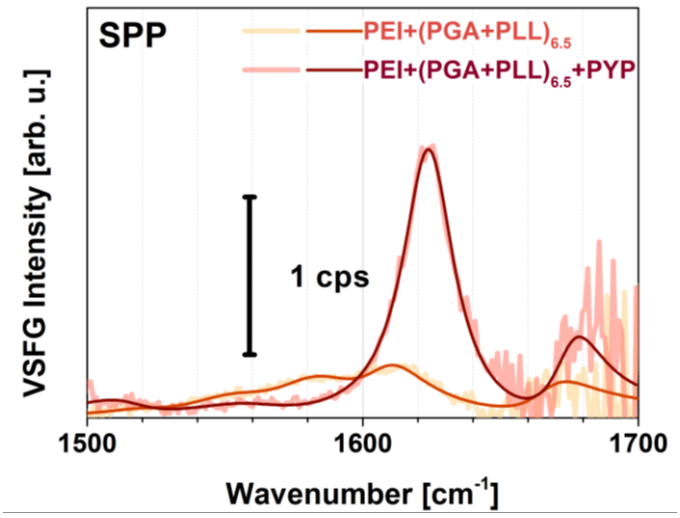

Figure 16. Chiral (B) spectra of $(PGA\text{-}PLL)_{6.5}$ (orange) and $(PGA\text{-}PLL)_{6.5}$+PYP (dark red) in the amide I region.

The symmetric and asymmetric bending mode of the NH_3^+ group are presented on both surfaces with and without PYP at 1527 and 1625 cm^{-1}, respectively. However for the PGA layer, these modes probably appear from the PLL layer under the PGA. For PGA, the band appearing at 1583 cm^{-1} can be assigned to the asymmetric COO^- stretching. For the PYP spectrum, we can see the ring mode near 1517 cm^{-1} which is very characteristic for protein absorption spectra. The band at 1590 belongs to the COO^- stretching of glutamate/aspartate side chains, and it is red-shifted during the interaction of PYP with PGA-surface. Since the stretching frequency of the COO^- moiety very sensitive to the environment, the shift can range between ± 40-60 cm^{-1} [89]. At 1610 cm^{-1} there is a band present for both surfaces due to a bifurcated H-bonding to −COOH groups on the protonated glutamic side chain. This shows very strong H-bonding [90,91]. Previously Raman optical activity spectroscopy studies of polylysine, polyglutamic acid, and some proteins presented a negative and positive signal pair at 1610 and 1626 cm^{-1}, respectively, which was attributed to β-sheet structures [92], and was later linked to the formation of β_2-fibrils [93]. The fitting parameters based on equation (13) of both surfaces are summarized in Table 3.

	wavenumbers (cm^{-1}), spectral widths (cm^{-1}), and amplitudes					
Surface	*PEI+(PGA+PLL)$_{6.5}$*			*PEI+(PGA+PLL)$_{6.5}$+PYP*		
Band assignments						
δ_S NH_3^+ (Lys)	1521	14.6	1	1516	14.5	3.6
Amide II / ν_{AS} COO^- (Glu, Asp)	1554	20	4.1	1554	19.1	4.2
ν_{AS} COO^- (Glu, Asp)	1583	20	7.1	1588	21.6	3.3
-COOH / δ NH_2 (Gln, Asn) / ν C-C (Tyr, Trp)	1609	14.4	4.8	1612	15.8	9.3
Amide I B_2 mode for β-sheet	-	-	-	1626	10.7	-17.5
Amide I B_1 mode for β-sheet, ν C=O (Glu, Asp)	1668	13.9	4.1	1682	7.7	-5.7

Table 3. Chiral vibrational mode assignments and corresponding wavenumbers, spectral widths, and amplitudes of vibrational resonances obtained for PEI+(PGA+PLL)$_{6.5}$ and PEI+(PGA+PLL)$_{6.5}$+PYP in the spectral region between 1500 and 1700 cm^{-1} at a relative humidity of 80%.

As previously discussed, the PYP's structure changes when the sample is exposed to different RH environment. To further monitor this in terms of the protein present in a multilayer structure, the chiral spectra of the PYP adsorbed on PEI+(PGA+PLL)$_{6.5}$ multilayer structure in the spectral range from 1500 to 1700 cm^{-1} were investigated in high (100%), medium-high

(80%), and low (3%) RH environment. The measurements and the corresponding fits can be seen on Figure 17.

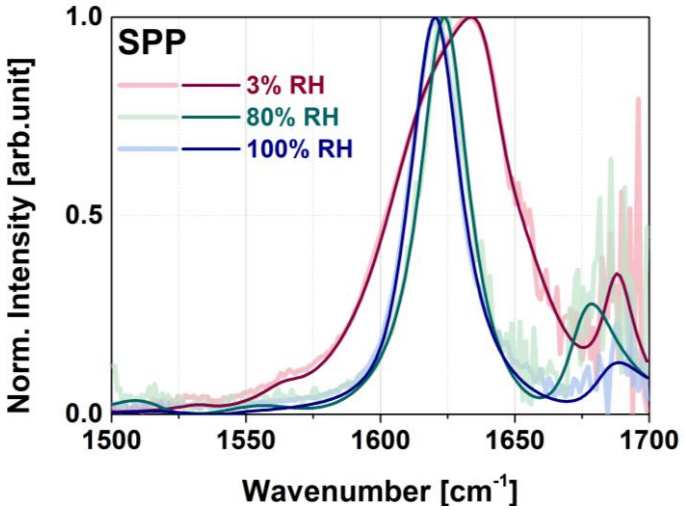

Figure 17. Normalized chiral VSFG spectra of PEI+(PGA+PLL)6.5+PYP multilayer in different relative humidity environment, red corresponding to low (3%), dark green to medium-high (80 %), and blue to high (100%) relative humidity, respectively. The measurements were normalized to 1 to enable comparison between measurements done on different days.

During lowering humidity, the PYP loses its hydrogen shell and partially its tertiary structure as denaturation occurs. This can be observed by the change of orientation of α-helixes and β-sheets, and the weakened H-bond structure with the shift in frequency peaks. At high RH, the characteristic amide I B_1- and B_2-modes are very narrow (8 and 11 cm^{-1} wide respectively), indicating a narrow orientational distribution of the peptide bonds β-scaffold part of PYP. At high RH B_2-mode of the β-sheet structure is found at the lowest frequency from the three RH at 1621 cm^{-1}, which can be explained by the strong H-bonds present. When the humidity decreases, the peak of the B_2-mode shifts to 1626 cm^{-1} at RH of 80%, then to 1640 cm^{-1} at RH of 3%, the latter being almost the highest frequency possible for the B_2 band. As the humidity lowers, no broadening of the chiral B_1 and B_2 vibrational modes were observed, but a new peak arises at 1654 cm^{-1} which we assigned to the amide I mode for an α-helix secondary structure. Yan and co-workers obtained no chiral amide I signal for rhodopsin, pHLIP, and LKα14 model systems [54] which suggests that the chiral amide I mode is silent for helical structures, however, Ishibashi's group found a small but significant chiral amide I band for BSA with a secondary structural content of 67% α-helix and 10% β-turn [81]. The band assignments are summarized in Table 4.

	wavenumbers (cm^{-1}), spectral widths (cm^{-1}), and amplitudes								
Relative humidity	***3%***			***80%***			***100%***		
Band assignments									
ν C-C (Tyr, Trp, Phe)	1510	30	-2	1516	14.5	3.6	1522	16	2.8
δ_S NH_3^+ (Lys)	1533	9.4	-2.2	1521	14.6	1			
Amide II / ν_{AS} COO^- (Glu, Asp)	1564	12.7	-3.9	1554	19.1	4.2	1545	8	-0.5
ν_{AS} COO^- (Glu, Asp)	1590	24.5	-9	1588	21.6	3.3	1590	13.9	-0.8
-COOH / δ NH_2 (Gln, Asn) / ν C-C (Tyr, Trp)	1610	25	-60.1	1612	15.8	9.3	1605	12.5	-6.6
Amide I B_2 mode for β-sheet	1640	10.3	9	1626	10.7	-17.5	1621	11.9	39.4
Amide I for a-helix	1654	24.7	52.7	-	-	-	-	-	-
Amide I B_1 mode for β-sheet, ν C=O (Glu, Asp)	1688	7.6	10	1682	7.7	-5.7	1685	11.3	8.9

Table 4. Chiral vibrational mode assignments and corresponding wavenumbers, spectral widths, and amplitudes of PEI+(PGA+PLL)$_{6.5}$+PYP in a relative humidity of 3%, 80%, and 100% in the spectral region between 1500 and 1700 cm^{-1}.

4.4.Optical switching

4.4.1. All-optical switching demonstrated with IO Mach–Zehnder interferometer

All-optical switching on the GL-PYP film was first demonstrated by monitoring the intensity changes at the MZI's output when the sample was excited by light. The probe light was chosen to be a 532-nm He-Ne CW laser beam during all of the measurements to not influence the sample, as this wavelength has no overlap with the ground state's and the excited states' absorption spectra, while still staying in the high-refractive index region (see Figure 2B). The exciting light was first chosen to be a 405 nm CW laser beam, which illuminated the sample for 2 seconds, then was turned off for 2 more, alternately. The changes detected at the MZI's output indicate all-optical switching taking place. The bias point was adjusted to zero before the measurement by tuning, and then keeping the heating voltage at constant 4 V to prevent heat-induced fluctuations. Based on the simplified reaction scheme detailed in Chapter 4.1. and shown in Scheme 1B, a steady-state equilibrium forms between the ground state and the pB intermediate forms after 2 s of illumination, also inducing refractive index change of the adlayer. After suspending the light-excitation for 2 seconds, most of the protein returns to the ground state, which may be re-excited again, yielding the same signal as previously (Figure 18).

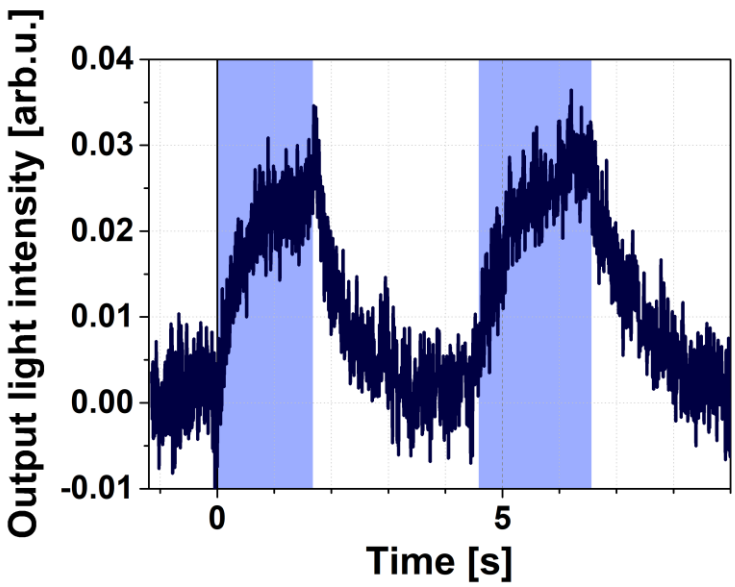

Figure 18. Optical switching demonstrated by measuring the MZI's output when exciting the PYP on one arm at 445 nm, 4 mW. The probe light was 532 nm. The blue color blocks indicate the time period when the light excitation happened.

As indicated in Chapter 4.1, light-induced shortcut in the PYP's photocycle at the pB intermediate gives way to another mode of all-optical switching. To demonstrate this, the PYP film was first excited for 3 second with a 4-mW 445-nm light, which was followed by a 6-second break in excitation, then another 3 of illumination by the 405-nm, 27-mW light (Figure 19A). While the latter excitation yielded a larger signal, at 445 nm, the PYP has higher absorption cross section, which overcompensates for the difference in applied CW intensities. The protein in both cases gets excited from the ground state to the pB intermediate. The bias voltage was kept at 2.1 V during this measurement.

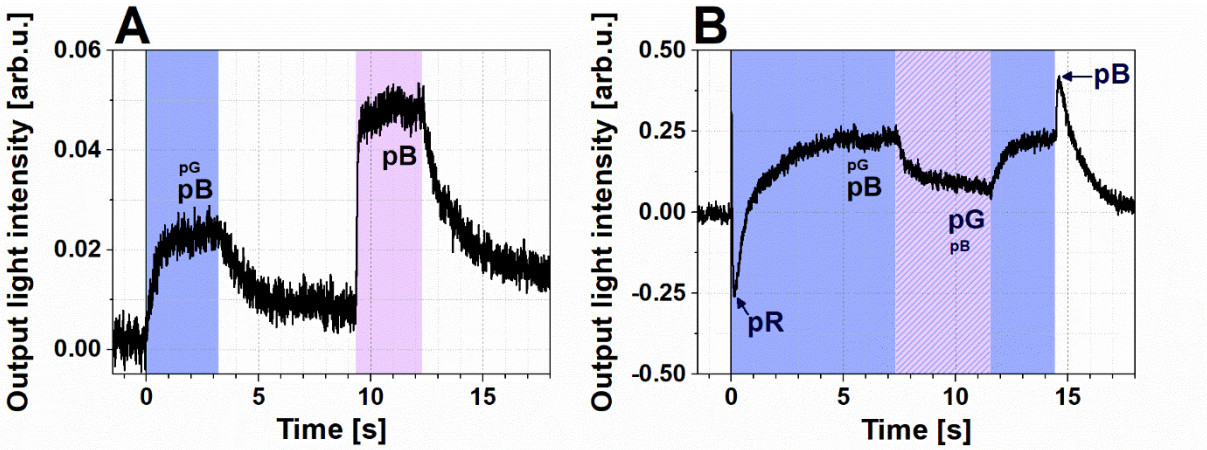

Figure 19. MZI's output intensity measured while (A) first 445-nm, 4-mW excitation beam was applied to the PYP film, followed by a cease in excitation, then another illumination at 405 nm (27 mW) for 3 seconds. The bias voltage was 2.1 V during the measurement; (B) The measured output light intensity of the MZI while a strong (44mW) 445-nm continuous light excited the sample for the duration of 14 s. During excitation, another, 405-nm continuous light was exciting the sample for 4 s. The applied probe light in the MZI was 532 nm during both (A) and (B) measurements. The color blocks indicate the time periods while the 405-nm (blue) and 445-nm (purple) excitation was applied to the sample. The states of the photocycle most prevalent and the extents of contribution to the effect are indicated by the size of the caption.

To demonstrate further switching effects, first, the PYP film was illuminated for 7 seconds with 445 nm, at 44 mW, driving most of the molecules to the pB state (Figure 19B). (Substituting the low, 4-mW intensity with a 44-mW high intensity illumination at 445 nm, a higher level steady-state was formed in the sample.) Then, a 405-nm, 27-mW light-beam illumination was superimposed on the same excitation area, for ca. 5 seconds, driving part of the PYP population to the pG state. Subsequently, the two illuminations were terminated in two steps, in opposite order.

When applying low-intensity excitations, the PYP's photocycle scheme can be further simplified by only keeping the rate-limiting transitions, and the pG ground state and the pB state. For the reactions occurring during illumination, we can apply quasi-first-order rate constants, namely $I_{455} \cdot \sigma_{pG}$ for the 445 nm, and $I_{405} \cdot \sigma_{pB}$ for the 405 nm CW excitation, where I_{455} and I_{405} are the applied light intensities, while σ_{pG} and σ_{pB} include the absorption cross sections and the quantum efficiencies of the light-induced photocycle reactions at the applied CW excitation wavelength. When only 445-nm excitation is applied, the pG and pB states' equilibrium concentration can be written as such:

$$[pB] = pG_0 \cdot I_{455} \cdot \frac{\sigma_{pG}}{I_{455} \cdot \sigma_{pG} + k_{pB}} \quad \text{and} \quad (14a)$$

$$[pG] = pG_0 \cdot \frac{k_{pB}}{I_{455} \cdot \sigma_{pG} + k_{pB}}, \quad (14b)$$

in which [pG] and [pB] are the concentrations of assigned the photocycle states, k_{pB} is the rate constant of the thermally induced decay of pB, while $pG_0 = [pG] + [pB]$ and $\frac{d[pG]}{dt} = \frac{d[pB]}{dt} = 0$.

In the case of both blue and violet lights exciting the sample, the photocycle scheme develops as follows: the transition from pG to pB is now driven by the sum of the two rate constants $I_{455} \cdot \sigma_{pG} + I_{405} \cdot \sigma_{pG405}$, where σ_{pG405} is the absorption cross-section of the pG intermediate at 405 nm. The rate constant of the pB to pG transition will be modified to $I_{455} \cdot \sigma_{pB445} + I_{405} \cdot \sigma_{pG}$. Since $\sigma_{pG405} < \sigma_{pG}$ and $\sigma_{pB445} \ll \sigma_{pB}$ (based on Figure 8A), and while both excitation light intensities are of the same order of magnitude, the PYP states' concentration can be estimated as such:

$$[pB] = pG_0 \cdot I_{455} \cdot \frac{\sigma_{pG}}{I_{455} \cdot \sigma_{pG} + I_{405} \cdot \sigma_{pB} + k_{pB}} \text{ and} \quad (15a)$$

$$[pG] = pG_0 \cdot \frac{I_{405} \cdot \sigma_{pB} + k_{pB}}{I_{455} \cdot \sigma_{pG} + I_{405} \cdot \sigma_{pB} + k_{pB}}. \quad (15b)$$

If the PYP's ground state is exited with high-intensity light (such as the applied light at $I_{455} \cdot \sigma_{pG} \gg k_{pB}$), pG and pB states form a steady-state equilibrium (described by equation (14a)), with pB state being present predominantly in the sample. Based on the findings in Chapter 4.1., the steady state forms in seconds, and as excitation stops, the PYP returns to the ground state. When violet light is also applied, the pB state is targeted as well, introducing a shortcut reaction to the pG state, shifting the concentration contribution of the intermediates and establishing a new steady-state, which can be defined by equations (15a) and (15a).

The refractive index changes in the samples on the arms of the MZI, following light-excitation with either or both blue and violet light, influence the intensity measured at the output. The two different steady-states induce two distinctive refractive indices, and the corresponding difference is detectable and utilizable for optical switching. Different routes are contributing to the negative and positive peaks in Figure 19B – the building negative peak corresponds to the accumulation to the pR during illumination with 445 nm light, before it transitions further into the pB state [16]; while the positive peak following the ceasing of

excitation corresponds to the transition to the pB state, without any short-cutting of the photocycle induced with background illumination.

Since only steady-state concentrations are considered during the measurements, the complex differential equation system (Equation (1a)) describing the PYP's photocycle was not solved, however, some general assumptions can be made for the purpose of explaining the experimental results found in this chapter. First, the time constant of the relaxation is determined by the slowest transition in the photocycle after illumination ceases on the sample, which is the decay from pB to pG. By fitting exponentials only on the measured data descripting $pB \rightarrow pG$ in Figure 18 and Figure 19, we can get an idea of the time-constant of thermal relaxation, which was calculated to be 1.2 ± 0.2 s, and aligns with measurements done on film samples not containing glycerol. Secondly, for the intermediate transitions that are driven by light, the observed data points are always a result of several virtual rate constants ($k_{virtual} = I_{PUMP} \cdot \sigma + k_{thermal}$) and correlate with the applied exciting light intensity. By fitting exponentials on the rising parts of measured signals, we get shorter time constants compared to that of the thermal relaxation's namely $\tau_{445} = 600 \pm 100$ ms for exciting with 445 nm, 4 mW CW, and $\tau_{405} = 200 \pm 40$ ms for 405 nm and 27 mW excitation, however, for the latter case the intensity overcompensates the smaller absorption cross section. Light-induced back-reactions can occur due to introduction of an additional exciting light, or exciting more than one intermediate at high light intensities, which further complicate the photocycle. In this case, the applied 445-nm beam excited both the pG and pR intermediates due to their overlapping spectra, thus shortcutting the photocycle and driving back a large amount of the population to the ground state before reaching the pR state. Because of this, the pB's formation is considerably slowed down even at high illumination intensities, however, when the 445 nm excitation is switched off there is a 40 ms rise in the signal. The rise can be attributed to the excited molecules which decay to the pB state in the lack of back-reaction in the photocycle.

From the results discussed in this chapter, it can be established that the PYP could be utilized in future IO applications, due to the demonstrated controllability of the photocycle by various illuminations. The intensity changes measured at the output of the MZI, cover the full dynamic range of the device, proving the GL-PYP films' IO switching ability.

4.4.2. All-optical switching demonstrated with transient grating

This chapter was reused with permission from J. Phys. Chem. C 2023, 127, 3, 1499–1506. Copyright 2023 American Chemical Society.

The first measurements were done with a pump wavelength of 450 nm, which is chosen because of the absorption of the PYP's ground state is at its peak here. The probe wavelength was chosen to be 515 nm, which was selected to monitor the fastest known intermediate of the PYP, pR, that has an absorption maximum near 500 nm. The measured diffraction signal can be seen in Figure 20 (blue line), and is collected up to 10 ps time delay. The signal maximum is at 140 fs, which decays to 50% of its value by 520 fs, and 10% by 1.6 ps. We have measured no recovery during the duration of the experiment.

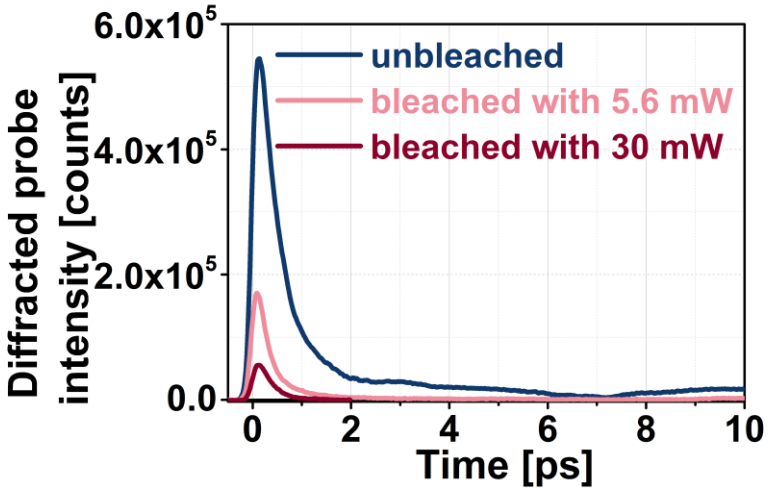

Figure 20. Diffracted probe intensity as a function of time. Probe wavelength was 514 nm, while pump wavelength corresponded to 450 nm with a pulse duration of 160 fs. Reprinted with permission from J. Phys. Chem. C 2023, 127, 3, 1499–1506. Copyright 2023 American Chemical Society.

Ground state bleaching was achieved by exciting the sample with an additional 405-nm CW light. This decreased the population of the PYP residing in the ground state, however, it also had an increase on the populations in other intermediates, such as $pR_{0,1,2}$ and $pB_{1,2}$, but mainly the $pB_{1,2}$ states accumulate due to their longer decay time (cf. Scheme 1). The chosen 405-nm excitation overlaps with the pB states' absorption spectra (based on [47] and Figure 8 in Chapter 4.1), and therefore can re-excite the sample, driving a portion of the PYP back to the ground state [43]. The diffracted probe light's intensity has decreased with the increase of intensity of the applied CW excitation, however, there was still a detectable signal in all cases. At the highest applied bleaching intensity, at an average of 30 mW, the detected diffracted

signal was decreased by 91% of the original signal. By modifying the CW wavelength to be on the red-shifted side of the pG absorption spectrum, the diffraction intensity is expected to diminish to zero. These results demonstrate that sub-picosecond all-optical switching based on the NLO properties of PYP films is achievable and the efficacy of switching is controllable by modifying the steady state of intermediates in the sample.

At 514 nm, only the pG and pR intermediates were expected to contribute to the absorption change within the detected 10 ps timeframe [29,31,94,95], however, during modelling only assuming these two intermediates, the model did not reproduce the measured kinetics data. By adding a Franck-Condon and one or more excited state, similarly as it was detailed in [29] and [96], the model in Figure 21A is proposed for the early photocycle.

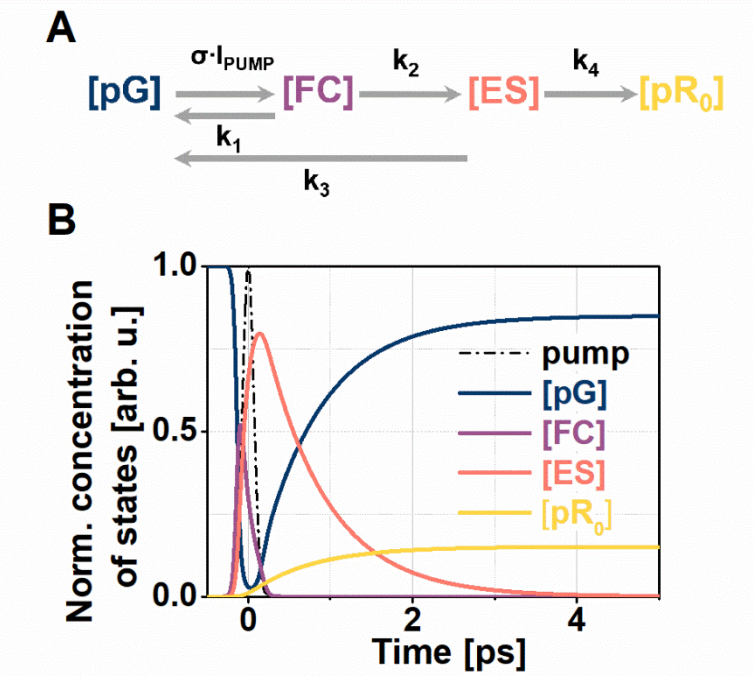

Figure 21.(A) Kinetic scheme for the rate equations describing the beginning of the PYP's photocycle. (B) Simulation of the normalized intermediate concentrations present in the sample (pG, FC, ES and pR_0) as a function of time after exciting with a 450-nm pump pulse (temporal shape can be seen with dash-dot line).
Reprinted with permission from J. Phys. Chem. C 2023, 127, 3, 1499–1506. Copyright 2023 American Chemical Society.

In this model [pG] and [pR_0] are the concentrations of intermediates, [FC] is the concentration of the Franck-Condon state, and [ES] is the concentration of one or more excited state. σ_{pG} is the absorption cross-section of the ground state, I_{PUMP} represents the applied pump beam's intensity, while $k_{1\text{-}4}$ are the rate constants. Thus, the differential equations proposed for the start of the photocycle can be written as such:

$$\frac{d[pG]}{dt} = -I_{PUMP} \cdot \sigma_{pG} \cdot [pG] + k_1 \cdot [FC] + k_3 \cdot [ES] \quad (16a)$$

$$\frac{d[FC]}{dt} = I_{PUMP} \cdot \sigma_{pG} \cdot [pG] - (k_1 + k_2) \cdot [FC] \quad (16b)$$

$$\frac{d[ES]}{dt} = k_2 \cdot [FC] - (k_3 + k_4) \cdot [ES] \quad (16c)$$

$$\frac{d[pR_0]}{dt} = k_4 \cdot [ES] \quad (16d)$$

During modeling, the detected diffracted probe intensity ($\eta(t)$) was assumed to be proportional to the sum of the squares of the peak change in the real and the imaginary parts of the complex refractive index across the induced excited-state concentration grating. These were then assumed to be in proportion with the concentration of the intermediate state normalized to the initial concentration of the ground state [56,57], such as:

$$\eta(t) \propto \left[a_i \sum_i \Delta n_i(t)\right]^2 + \left[a_i \sum_i \Delta \kappa_i(t)\right]^2 \propto \left[a_i \sum_i {N_i(t)}/{N_0}\right]^2 \quad . \quad (17)$$

In equation (17), $\Delta n_i(t)$, $\Delta \kappa_i(t)$ are the change in real and the imaginary parts of the complex refractive index of intermediate i. i can be any state that contributes to the detected signal at the probe wavelength, while $N_i(t)$ is the said intermediate's concentration. N_0 corresponds to the pre-excitation concentration of pG, while a_i is a constant. The diffracted signal's change in time was modelled by solving the coupled differential equations for the concentrations, employing the least squares method, and thus summing up of normalized concentration-squared values for each time delay. The absorption cross-section at 450 nm was assumed to be $\sigma = 1.682 \cdot 10^{-16}$ cm^2 [96]. The obtained rate constants are k_1=1/40 fs^{-1}, k_2=1/100 fs^{-1}, k_3=1/880 fs^{-1}, and k_4=1/5360 fs^{-1}. In Figure 21B, the so-obtained time-dependent concentrations are plotted, while the comparison of the measured and modelled diffracted probe signals can be seen in Figure 22A and B, with light blue circles (measured) and dark blue line (modelled). Based on the findings, the proposed Figure 21A is a valid model for the early stages of the PYP's photocycle, when the protein is located in hydrated glycerol films and is excited at 450 nm.

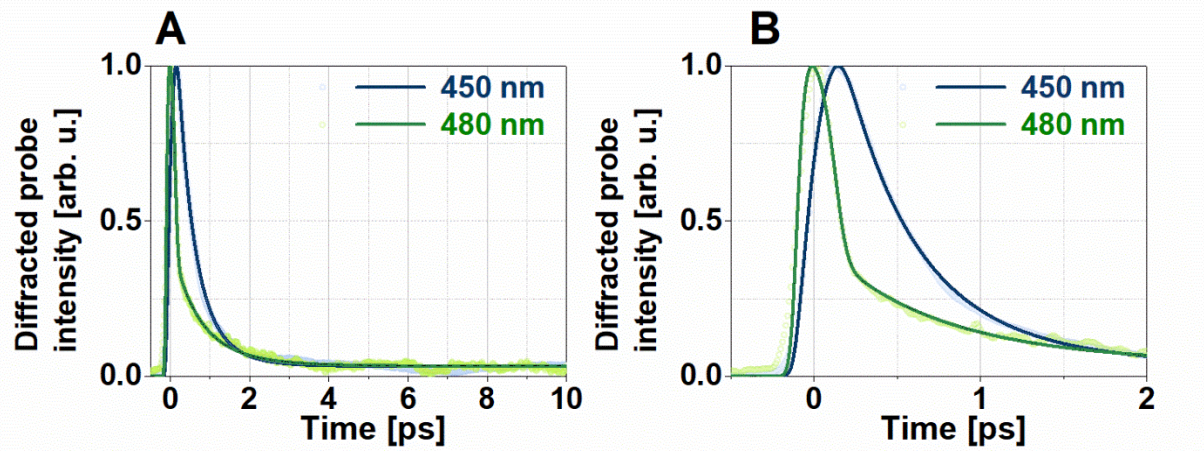

Figure 22. (A) The measured and the model-calculated diffracted probe intensity. as a function of time at an excitation wavelength of 450 nm (blue) or 480 nm (green), and probe wavelength of 514 nm. (B) Zoomed in version of Figure 22A showing the time delay only up to 2 ps.
Reprinted with permission from J. Phys. Chem. C 2023, 127, 3, 1499–1506. Copyright 2023 American Chemical Society.

Shifting excitation wavelength to 480 nm, which is on the red side of the absorption peak of the ground state, led to considerable shortening of the switching time. The detected signal's peak value dropped to 50% at 160 fs, compared to the 450 nm excitation, which reached the same intensity at 520 fs. The diffraction signal also reached its peak at 20 fs which is drastically shortened when compared to 140 fs corresponding to the 450-nm pump. The measured, normalized signal is shown for up to 10 ps in Figure 22A, and up to 2 ps in Figure 22B, plotted in light green circles.

The modelling of the time-dependent diffraction signal was done with the same Figure 21A model which yielded k_1=1/20 fs^{-1}, k_2=1/170 fs^{-1}, k_3=1/1500 fs^{-1}, and k_4=1/4040 fs^{-1} as rate constants. This values imply a faster response from the Franck-Condon state at 480 nm, which can be contributed to higher stimulated-emission cross section, and following emission, resulting in the protein's faster decay to its ground state, in correspondence to previous observations [94]. The measured diffracted signal intensity and the model fit can be seen in Figure 22A and B, plotted with dark green.

5. Conclusions

IO is a relatively new field of study which, analogously to integrated electronics, aims for the miniaturization of optical structures for the purpose of information transfer and data processing, but in an optical manner. By circumventing electronical components, all-optical IO aims to narrow a circuit's speed down to solely depend on the active material's NLO properties and its changes. Currently the biggest challenge in IO is finding or developing materials that possess adequate NLO properties - such as large light-induced refractive index change, sensitivity, speed, re-excitability - that can be utilized as active components, but also are stable enough for long term usage. Previously, several materials – both organic and inorganic – have been proposed for this purpose, however, none are yet considered ideal for a variety of reasons. Biological materials have also been considered for IO purposes, from which the protein bacteriorhodopsin and more recently the photoactive yellow protein have garnered the most interest.

The goal of this thesis was the investigation of photoactive yellow films in the aspect of future integrated optical application. To investigate the topic thoroughly, in the first part of the thesis, doped PYP films were investigated using a variety of spectroscopical methods, to monitor the changes during the photocycle. It was previously demonstrated that at high relative humidities, undoped PYP films have a similar photocycle to that of the protein in solution, however, for the PYP to be applicable in IO further down the line, it needs to be doped for it to remain optically homogenous, at the same time allow high protein concentration. Glycerol was chosen as the doping agent when creating PYP films, since optical homogeneity could be maintained. To get a full picture of the differences between the PYP in solution and the GL-PYP film, the NLO properties of GL-PYP films were investigated by monitoring the absorption kinetics from 10 μs to 10 s. It was shown that the photocycle of GL-PYP films have a similar progression through intermediates to that of the PYP in solution, however, the time frame in which the entire photocycle takes place is longer (>10 s). Intermediate-accumulation measurements were performed on the films, to measure the predominant intermediate the protein is in when light excitation is performed for a longer time period. This yielded the result that the protein accumulates predominantly in the pB state when continuously illuminated. It was found that the GL-PYP film was appropriate for IO application, as it allows for high protein concentration, optical quality, and stability.

To further map out the PYP's optical properties, its linear and nonlinear refractive indices were investigated with Z-scan technique at different intensities, to account for different possibilities during excitation. At low intensities (<0.1 W/cm^2) Δn was measured to be $\sim 10^{-4}$, which is comparable to the Δn of the best solid-state materials. The high n_2 value of $\sim 4 \cdot 10^{-4}$ cm^2/W lends possibility to future utilization of the protein in IO, where high Δn and n_2 values are necessary.

Miniaturization is the main issue in currently used integrated electrical devices, and IO faces the same upcoming problems as well. While applying proteins provides a good alternative, the passive structures need to also be scalable, which poses the question if we can create PYP films that are as close to monolayer thickness as possible. To investigate this possibility, PYP was absorbed onto polyelectrolyte multilayers created by PEI, PGA and PLL with the LbL technique, and characterized by chiral and achiral VSFG spectroscopy. While the initial reason to investigate the PYP on top of polyelectrolyte layers was more in terms of IO applicability, valuable fundamental-research results were also obtained. A thorough analysis was done of PEI and PGA monolayers, as well as changes occurring when building polyelectrolyte multilayers, such as higher homogeneity and hence signal intensity. The VSFG spectra of PYP were investigated when PYP was adsorbed on top of polyelectrolyte single and multilayers. The measurements were done in the 1400-1750 cm^{-1} and 2800-3800 cm^{-1} region. The chiral spectra revealed details about the β-scaffold of PYP, and when compared to polyelectrolyte layers, the signal of C_α-H and C-H vibrational bands, which are characteristic of proteins, also appear in achiral polarization combinations, making achiral signals also surface specific. The homodyne N-H stretch signal shows a red shift for negatively charged PGA+PYP compared to the positively charged PEI+PYP layer. The relative red shift in the PGA-PYP case suggests that PYP keeps its tertiary structure to a higher degree when interacting with PGA than with PEI. The changes in the amide I and II bands in the 1400-1700 cm^{-1} range suggest that PYP loses its external hydrogen shell at low humidity, in spite of a stable beta-sheet secondary structural motif. At the same time, some minor denaturation is also detectable.

IO switching on the GL-PYP was demonstrated with two techniques, utilizing different parts of the protein's photocycle. First, switching using a MZI was demonstrated by continuously illuminating the sample on the interferometer's arms, thus influencing the intensity at the output of the interferometer. By using two different excitation wavelengths simultaneously, the PYP molecules were first pushed to be in the pB intermediate state by CW excitation at 445 nm, followed by shortcutting the whole photocycle by illuminating the sample

by a 405-nm CW laser, which targeted the accumulated pB intermediate. The second excitation not only returns the protein to the ground state faster than the regular decay of the pB state, but enables an extra control of light-switching with the PYP.

Ultrafast all-optical switching was demonstrated on GL-PYP films by using TG setup in a BOXCARS geometry. The temporal evolution of the laser-induced concentration grating in the films was monitored for up to 10 ps, while employing pump laser pulses of different wavelengths. The excitation wavelength has a drastic effect on the switching time, due to the varying contribution of stimulated emission from the Franck-Condon to the ground state. The time-dependent diffracted probe intensity was modelled with coupled rate equations. From this, it was established that the early stages of the PYP's photocycle model were needed to be extended to obtain a better fit between experiment and theory. Based on this result, creating all-optical logic components is possible by PYP films on a sub-ps timescale, which would enable THz switching speed. Different CW laser intensities at 405 nm were used to bleach the sample and investigate its effect on the photocycle's dynamics.

Based on the findings summarized in this thesis, GL-PYP films are valid options as active materials in IO applications. Producing PYP is cheap, and thin films made of it possess a high enough light-induced refractive index change; meanwhile being small enough and water-soluble to be easily combined with nanostructured materials. Doping the PYP film with glycerol also maintains high optical quality and protein concentration in the films, preventing cracking formation and enabling the photocycle to take place even in low humidity environments, due to the glycerol's water retention. The comprehensive investigation of the GL-PYP's NLO properties was performed by characterizing absorption kinetics, linear and nonlinear refractive indices, and it's IO switching capability. The investigation of PYP's monolayer structure on PEI and PGA was also performed.

For further practical applications, high-repetition-rate switching experiment should be performed. It can be done, e.g., by utilizing the photosensitivity of the primary intermediates of the photocycle, and driving the protein back to the ground-state conformation, similarly as demonstrated in some switching experiments done with MZI. Another way to accomplish high-repetition-rate switching by PYP could utilize the chemical modification of the chromophore by removing the p-coumaric acid via hydroxylamine treatment, and subsequently reconstitute the protein-pigment complex by non-isomerizable analogues, similarly to what was shown in bR [97–100].

6. Acknowledgements

I would like to express my gratitude towards my supervisors, Prof. Dr. András Dér and Dr. Zsuzsanna Heiner. I want to thank Prof. Dr. András Dér for giving me the opportunity to work in the Biomolecular Electronics Research Group at the Institute of Biophysics of the Biological Research Centre and for guiding me throughout my undergraduate and doctoral years; and want to express my gratefulness to Dr. Zsuzsanna Heiner for allowing me to visit her group at the Photonics Application Lab at Humboldt University of Berlin, as during the time I had spent there I was able to learn so much of VSFG spectroscopy and how to properly build up a research project from start to finish. I want to thank them both for teaching me how good research is done and I appreciate all their contribution of time, ideas, support, and motivation which have made my PhD possible.

I would like to sincerely thank Dr. Mark Mero and Dr. Sándor Valkai for all their help and insight during experiments and writing manuscripts.

Many thanks for all the support I have received from the current and former members of the Biomolecular Electronics Research Group and Photonics Application Lab.

I would also like to acknowledge funding by the German Academic Exchange Service (DAAD) and the Eotvos Hungarian State Scholarship of Tempus Public Foundation funded by the Hungarian Government.

I would also like to thank my family and friends for all their encouragement and love during these years. I would like to dedicate this work to my mother who always stood by me and encouraged me from the beginning to pursue knowledge and science.

Thank you.

7. References

[1] C. Monat, Y. Su, APL Photonics 5 (2020) 020402.

[2] D.J. Blumenthal, APL Photonics 5 (2020) 020903.

[3] H. Chen, C. Wang, H. Ouyang, et al., Nanophotonics 9 (2020) 2107–2124.

[4] B.J. Eggleton, B. Luther-Davies, K. Richardson, Nat. Photonics 5 (2011) 141–148.

[5] P. Ormos, L. Fábián, L. Oroszi, et al., Appl. Phys. Lett. 80 (2002) 4060–4062.

[6] A. Mathesz, L. Fábián, S. Valkai, et al., Biosens. Bioelectron. 46 (2013) 48–52.

[7] L. Fábián, Z. Heiner, M. Mero, et al., Opt. Express 19 (2011) 18861.

[8] L. Fábián, E.K. Wolff, L. Oroszi, et al., Appl. Phys. Lett. 97 (2010) 142.

[9] J.A. Stuart, D.L. Marcy, R.R. Birge, NATO Sci. Ser. SUB Ser. I LIFE Behav. Sci. 335 (2001) 16–29.

[10] A. Dér, L. Keszthelyi, Bioelectronic Applications of Photochromic Pigments, IOS Press, Szeged, Hungary, 2001.

[11] N. Hampp, T. Juchem, NATO Sci. Ser. SUB Ser. I LIFE Behav. Sci. 335 (2001) 44–53.

[12] S. Roy, M. Prasad, J. Topolancik, et al., J. Appl. Phys. 107 (2010) 053115.

[13] C.P. Singh, S. Roy, Opt. Commun. 218 (2003) 55–66.

[14] Y.-T. Li, Y. Tian, H. Tian, et al., Sensors 18 (2018) 1368.

[15] N. Vsevolodov, Biomolecular Electronics: An Introduction via Photosensitive Proteins, Springer Science & Business Media, Berlin, Germany, 2012.

[16] T.E. Meyer, E. Yakali, M.A. Cusanovich, et al., Biochemistry 26 (1987) 418–423.

[17] T.E. Meyer, Biochim. Biophys. Acta - Bioenerg. 806 (1985) 175–183.

[18] K.J. Hellingwerf, J. Hendriks, T. Gensch, J. Phys. Chem. A 107 (2003) 1082–1094.

[19] G.E.O. Borgstahl, D.W.R. Williams, E.D. Getzoff, Biochemistry 34 (1995) 6278–6287.

[20] W.D. Hoff, I.H. van Stokkum, H.J. van Ramesdonk, et al., Biophys. J. 67 (1994) 1691–1705.

[21] W.W. Sprenger, W.D. Hoff, J.P. Armitage, et al., J. Bacteriol. 175 (1993) 3096–3104.

[22] M. Baca, G.E.O. Borgstahl, M. Boissinot, et al., Biochemistry 33 (1994) 14369–14377.

[23] J.-L. Pellequer, K.A. Wager-Smith, S.A. Kay, et al., Proc. Natl. Acad. Sci. 95 (1998) 5884–5890.

[24] D.M.F. Van Aalten, L. Joshua-Tor, W. Crielaard, et al., Protein Sci. 9 (2000) 64–72.

[25] M. Kim, R.A. Mathies, W.D. Hoff, et al., Biochemistry 34 (1995) 12669–12672.

[26] J.J. Van Beeumen, B. V. Devreese, S.M. Van Bun, et al., Protein Sci. 2 (1993) 1114–1125.

[27] W.D. Hoff, P. Düx, K. Hård, et al., Biochemistry 33 (1994) 13959–13962.

[28] T.E. Meyer, G. Tollin, J.H. Hazzard, et al., Biophys. J. 56 (1989) 559–564.

[29] P.E. Konold, E. Arik, J. Weißenborn, et al., Nat. Commun. 11 (2020) 4248.

[30] M.A. Van Der Horst, I.H.M. Van Stokkum, N.A. Dencher, et al., Biochemistry 44 (2005) 9160–9167.

[31] L.T. Mix, E.C. Carroll, D. Morozov, et al., Biochemistry 57 (2018) 1733–1747.

[32] B. Borucki, C.P. Joshi, H. Otto, et al., Biophys. J. 91 (2006) 2991–3001.

[33] I. Abdulhalim, Appl. Phys. Lett. 66 (1995) 3248.

[34] I. Abdulhalim, J. Appl. Phys. 77 (1995) 1897–1901.

[35] I. Abdulhalim, M. Gelbaor, M. Klebanov, et al., Opt. Mater. Express 1 (2011) 1192.

[36] Z. Heiner, K. Osvay, Appl. Opt. 48 (2009) 4610–4615.

[37] A. Dér, L. Keszthelyi, Bioelectronic Applications of Photochromic Pigments, IOS Press, 2001.

[38] N. Vsevolodov, Biomolecular Electronics: An Introduction via Photosensitive Proteins, Springer Science & Business Media, 2012.

[39] J. Tenboer, S. Basu, N. Zatsepin, et al., Science 346 (2014) 1242–1246.

[40] S. Yeremenko, I.H.M. Van Stokkum, K. Moffat, et al., Biophys. J. 90 (2006) 4224–4235.

[41] F. Schotte, H.S. Cho, V.R.I. Kaila, et al., Proc. Natl. Acad. Sci. U. S. A. 109 (2012) 19256–19261.

[42] A. Colonna, G.I. Groma, M.H. Vos, Chem. Phys. Lett. 415 (2005) 69–73.

[43] C.P. Joshi, B. Borucki, H. Otto, et al., Biochemistry 44 (2005) 656–665.

[44] D. Oesterhelt, W. Stoeckenius, Nat. New Biol. 233 (1971) 149–152.

[45] H.M. Nussenzveig, Math. Sci. Eng. Ed. HM Nussenzveig (Amsterdam Elsevier) (1972) 3–53.

[46] E.A. Moore, L.E. Smart, Solid State Chem. An Introd. 41 (2020) 283–314.

[47] P. Khoroshyy, A. Dér, L. Zimányi, J. Photochem. Photobiol. B Biol. 120 (2013) 111–119.

[48] L. Fábián, S. Krekic, R. Tóth-Boconádi, et al., in: AIP Conf. Proc., 2017, p. 040001.

[49] M. Sheik-Bahae, A.A. Said, T.H. Wei, et al., IEEE J. Quantum Electron. 26 (1990) 760–769.

[50] Y.R. Shen, Principles of Nonlinear Optics, Wiley-Interscience, New York, NY, USA, 1873.

[51] Z. Heiner, V. Petrov, M. Mero, APL Photonics 2 (2017) 66102.

[52] E.C.Y.Y. Yan, L. Fu, Z. Wang, et al., Chem. Rev. 114 (2014) 8471–8498.

[53] K. Meister, A. Paananen, H.J. Bakker, Phys. Chem. Chem. Phys. 19 (2017) 10804–10807.

[54] E.C.Y. Yan, Z. Wang, L. Fu, J. Phys. Chem. B 119 (2015) 2769–2785.

[55] X.H. Hu, L. Fu, J. Hou, et al., J. Phys. Chem. Lett. 11 (2020) 1282–1290.

[56] J.C. Dainty, Opt. Acta Int. J. Opt. 33 (1986) 1336–1337.

[57] K.A. Nelson, R. Casalegno, R.J.D. Miller, et al., J. Chem. Phys. 77 (1982) 1144–1152.

[58] H. Ohmori, L. Nagy, M. Dorogi, et al., Eur. Biophys. J. 37 (2008) 1167–1174.

[59] C. Picart, G. Ladam, B. Senger, et al., J. Chem. Phys. 115 (2001) 1086–1094.

[60] K. Nagy, A.M. Pilbat, G. Groma, et al., J. Biol. Chem. 285 (2010) 38811–38817.

[61] J.J. Ramsden, J. Stat. Phys. 73 (1993) 853–877.

[62] M. Mero, L. Wang, W. Chen, et al., in: Proc.SPIE, 2019, p. 58.

[63] R. Adair, L.L. Chase, S.A. Payne, J. Opt. Soc. Am. B 4 (1987) 224.

[64] E.T.J. Nibbering, M.A. Franco, B.S. Prade, et al., Opt. Commun. 119 (1995) 479–484.

[65] R.W. Boyd, in: R.W.B.T.-N.O. (Second E. Boyd (Ed.), Nonlinear Opt., Elsevier, San Diego, 2003, pp. 189–235.

[66] F. Yesudas, M. Mero, J. Kneipp, et al., J. Chem. Phys. 148 (2018) 1–7.

[67] Z. Heiner, L. Wang, V. Petrov, et al., Opt. Express 27 (2019) 15289.

[68] J.N. Sweetser, D.N. Fittinghoff, R. Trebino, Opt. Lett. 22 (1997) 519.

[69] M. Li, J.P. Nibarger, C. Guo, et al., Appl. Opt. 38 (1999) 5250.

[70] A.C. Eckbreth, Appl. Phys. Lett. 32 (1978) 421–423.

[71] J.A. Shirley, R.J. Hall, A.C. Eckbreth, Opt. Lett. 5 (1980) 380.

[72] M.J. Wheeler, S. Russi, M.G.M.W. Bowler, et al., Acta Crystallogr. Sect. F Struct. Biol. Cryst. Commun. 68 (2012) 111–114.

[73] S. Krekic, D. Nagy, S.G. Taneva, et al., Eur. Biophys. J. 48 (2019) 465–473.

[74] D. Beece, S.F. Bowne, J. Czégé, et al., Photochem. Photobiol. 33 (1981) 517–522.

[75] Z. Násztor, F. Bogár, A. Dér, Curr. Opin. Colloid Interface Sci. 23 (2016) 29–40.

[76] H. Kamikubo, N. Shimizu, M. Harigai, et al., Biophys. J. 92 (2007) 3633–3642.

[77] K. Lee, Y. Kim, J. Jung, et al., Sci. Rep. 8 (2018) 3064.

[78] J. Vanhanen, V.P. Leppanen, T. Haring, et al., Opt. Commun. 155 (1998) 327–331.

[79] R.A. Ganeev, I.A. Kulagin, A.I. Ryasnyanskiĭ, et al., in: Opt. Spectrosc. (English Transl. Opt. i Spektrosk., SPIE, 2003, pp. 561–568.

[80] J. Kim, G.A. Somorjai, J. Am. Chem. Soc. 125 (2003) 3150–3158.

[81] M. Okuno, T.A. Ishibashi, J. Phys. Chem. C 119 (2015) 9947–9954.

[82] E.A. Perets, P.E. Videla, E.C.Y. Yan, et al., J. Phys. Chem. B 123 (2019) 5769–5781.

[83] E.A. Perets, D. Konstantinovsky, L. Fu, et al., Proc. Natl. Acad. Sci. U. S. A. 117 (2020) 32902–32909.

[84] A.G.F. De Beer, J.S. Samson, W. Hua, et al., J. Chem. Phys. 135 (2011) 224701.

[85] M. Sovago, E. Vartiainen, M. Bonn, J. Phys. Chem. C 113 (2009) 6100–6106.

[86] T. Hashida, K. Tashiro, Polymer (Guildf). 48 (2007) 7614–7622.

[87] L. Chen, W. Zhu, K. Lin, et al., J. Phys. Chem. A 119 (2015) 3209–3217.

[88] I. V. Panayotov, P.Y. Collart-Dutilleul, H. Salehi, et al., Macromol. Biosci. 14 (2014) 1771–1782.

[89] A. Barth, Prog. Biophys. Mol. Biol. 74 (2000) 141–173.

[90] A. Fulara, W. Dzwolak, J. Phys. Chem. B 114 (2010) 8278–8283.

[91] A. Xie, L. Kelemen, J. Hendriks, et al., Biochemistry 40 (2001) 1510–1517.

[92] I.H. McColl, E.W. Blanch, A.C. Gill, et al., J. Am. Chem. Soc. 125 (2003) 10019–10026.

[93] F. Tobias, T.A. Keiderling, Langmuir 32 (2016) 4653–4661.

[94] H. Kuramochi, S. Takeuchi, K. Yonezawa, et al., Nat. Chem. 9 (2017) 660–666.

[95] P. Changenet-Barret, P. Plaza, M.M. Martin, et al., Chem. Phys. Lett. 434 (2007) 320–325.

[96] C.N. Lincoln, A.E. Fitzpatrick, J.J.V. Thor, Phys. Chem. Chem. Phys. 14 (2012) 15752–15764.

[97] Y. Imamoto, T. Ito, M. Kataoka, et al., FEBS Lett. 374 (1995) 157–160.

[98] Y. Kim, P. Ganesan, J. Jo, et al., J. Phys. Chem. B 122 (2018) 4513–4520.

[99] M. Sheves, N. Friedman, A. Albeck, et al., Biochemistry 24 (1985) 1260–1265.

[100] D. Oesterhelt, M. Meentzen, L. Schuhmann, Eur. J. Biochem. 40 (1973) 453–463.

8. Annex

I. **Krekic, S.**; Nagy, D.; Taneva, S. G.; Fábián, L.; Zimányi, L.; Dér, A. Spectrokinetic Characterization of Photoactive Yellow Protein Films for Integrated Optical Applications. *Eur. Biophys. J.* **2019**, *48* (5), 465–473. https://doi.org/10.1007/s00249-019-01353-8. IF: 2.012

European Biophysics Journal (2019) 48:465–473
https://doi.org/10.1007/s00249-019-01353-8

ORIGINAL ARTICLE

Spectrokinetic characterization of photoactive yellow protein films for integrated optical applications

Szilvia Krekic[1] · Dávid Nagy[1] · Stefka G. Taneva[2] · László Fábián[1] · László Zimányi[1] · András Dér[1]

Received: 5 November 2018 / Revised: 19 February 2019 / Accepted: 4 March 2019 / Published online: 23 March 2019
© The Author(s) 2019

Abstract
In this paper, the photocycle of the dried photoactive yellow protein film has been investigated in different humidity environments, in order to characterize its nonlinear optical properties for possible integrated optical applications. The light-induced spectral changes of the protein films were monitored by an optical multichannel analyser set-up, while the accompanying refractive index changes were measured with the optical waveguide lightmode spectroscopy method. To determine the number and kinetics of spectral intermediates in the photocycle, the absorption kinetic data were analysed by singular value decomposition and multiexponential fitting methods, whose results were used in a subsequent step of fitting a photocycle model to the data. The absorption signals of the films were found to be in strong correlation with the measured light-induced refractive index changes, whose size and kinetics imply that photoactive yellow protein may be a good alternative for utilization as an active nonlinear optical material in future integrated optical applications.

Keywords Photoactive yellow protein · Integrated optics · Biophotonics · Kinetic absorption spectroscopy · Optical waveguide lightmode spectroscopy

Introduction

In the past few decades, there has been an ever increasing demand for faster information transmission and data processing. Achieving greater speed in state-of-the-art electronic devices requires further miniaturization of integrated electronic circuits and integrating more and more components on a small silicone chip. However, scaling down the structure causes several problems (heat damage, crosstalk, quantum effects, etc.), limiting the size of the components. The empirical law proposed by Moore (1965), stating that the number of electronic components integrated on a silicon wafer of unit area is doubling in every 18 months, has been valid until recent times, but cannot be sustained for much longer (see Waldrop 2016 as a quick overview).

One of the several alternative solutions investigated is integrated optics (IO), which comprises similar elements to integrated electronics; however, in IO the information transmission and processing is done solely by optical means. Analogously to their electronic counterparts, IO circuits also comprise passive and active elements, corresponding to the wires, resistors and capacitors, on the one hand, and the transistors, on the other. The theory of integrated optics and the technology for manufacturing passive IO elements (i.e. miniature waveguides) are well established, and the main challenge is to find or develop materials with suitable nonlinear optical (NLO) properties that can function as active elements in IO circuits.

In recent works, cost-effective organic materials have been proposed to be tested as active IO components, as alternatives to the currently used semiconductor materials (Haque and Nelson 2010). The design and application of organic, pi-conjugated molecular materials generated the most interest (Hales et al. 2010; Hu et al. 2008; Service 1995), but their naturally occurring, stable counterparts, such as chromoproteins, have also been successfully tested (as a recent review, see Fábián et al. (2015)). One of the most

Special Issue: Regional Biophysics Conference 2018.

✉ Szilvia Krekic
krekic.szilvia@brc.mta.hu

[1] Institute of Biophysics, Biological Research Centre, Hungarian Academy of Sciences, Temesvári krt. 62, P.O. Box 521, Szeged 6701, Hungary

[2] Institute of Biophysics and Biomedical Engineering, Bulgarian Academy of Sciences, Acad. G. Bonchev Str., bl. 21, Sofia 1113, Bulgaria

researched biological materials in the field is the light-sensitive protein bacteriorhodopsin (bR) (Oesterhelt and Stoeckenius 1971, 1973), due to its relatively large light-induced refractive index change (Ormos et al. 2002) and mechanical stability (Hristova et al. 1984). In previous works of our group, the usability of bR in IO circuits has been investigated extensively, demonstrating the ability of fast optical switching and light modulation (Dér et al. 2007; Fábián et al. 2010, 2011; Mathesz et al. 2013). In our current work, similarly to bR, the expedience of the photoactive yellow protein (PYP) in IO circuits has been investigated.

PYP is a small, water-soluble cytoplasmic protein that was first extracted from the purple halophilic bacterium *Halorhodospira halophila* (Meyer 1985; Meyer et al. 1987). The chromophore of the PYP is *p*-coumaric acid, which is responsible for the colour of the protein that, when excited by light, undergoes a reversible trans–cis isomerization around its thiol-ester linked bond attached to cysteine-69 (Baca et al. 1994; Hoff et al. 1994a; Van Beeumen et al. 1993). The photoexcitation is also linked to the negative phototaxis detected in bacteria where the PYP is present as photoreceptor (Sprenger et al. 1993). Upon photoisomerization PYP undergoes a cyclic reaction series between quasi-stable intermediate states, accompanying transient protonation and conformational changes before returning to its original state ("pG"). The intermediate states of the photocycle may also differ spectrally. The pG initial or dark state has an absorption maximum at 446 nm, while during the photocycle, two spectrally distinct states are present: the red-shifted pR, followed by the blue-shifted pB. Since the first study of the photocycle (Meyer et al. 1987, 1989), the kinetic and spectral properties of the intermediates have been investigated with numerous methods under various environmental conditions, resulting in several distinctive photocycle schemes and rate coefficients, including spectrally "silent" transitions, too (Borucki et al. 2006; Cusanovich and Meyer 2003; Groot et al. 2003; Hellingwerf et al. 2003; Hoff et al. 1994b; Ihee et al. 2005; Imamoto and Kataoka 2007; Joshi et al. 2005; Kim et al. 2012; Pande et al. 2016; Ujj et al. 1998; van der Horst et al. 2005; Yang et al. 2017). A recent work suggests that the protein's photodynamics also depend on the wavelength of the excitation light (Mix et al. 2018). Taking into account all internal and external factors, the photocycle can occur multiple ways.

When considering PYP for IO applications, the most important features are the fast spectral transitions of the protein at the beginning of its photocycle and the accompanying refractive index changes. Contrary to bR that is available in large membrane fragments, or in a detergent-solubilized form, PYP is water-soluble per se, which offers unique opportunities for its combination with passive IO elements. These properties make PYP a good candidate for using it as an active element of IO structures. For such applications, dry samples are preferred, because of their higher mechanical stability and larger photoinduced refractive index changes.

In our current work, we investigated the photocycle of dry PYP films and determined the accompanying light-induced refractive index changes at various relative humidities in order to evaluate their potential IO adaptability. For the photocycle measurements, we used an optical multichannel analyser (OMA) set-up, while the refractive index change measurements were performed with the optical waveguide lightmode spectroscopy (OWLS) method. Our results show that PYP films of controlled relative humidity are good candidates for utilization as active elements in IO devices.

Materials and methods

Sample preparation

PYP was a kind gift of Dr. John Fitch. The lyophilized protein was dissolved in 10 mM Tris buffer, pH 8.2, up to a protein concentration of 50 µM. In both experiments, 15 µl protein solution was homogeneously dried on a glass slab forming an approximately 5 mm diameter patch. For kinetic absorption spectroscopy, the glass slab with the dried protein film was placed into a plastic cuvette. Saturated salt solutions were introduced in the bottom of the cuvette, without contact with the PYP film, to maintain the desired humidity. For the low-relative humidity (20%) experiments, we used potassium acetate, while high-relative humidity (85%) was achieved by using potassium chloride.

For the OWLS experiments, the protein solution was dried on the top of a slab optical waveguide directly over the grating coupler. The waveguide and the rotational table of the experimental set-up were placed inside a glass case, where the environment's humidity was also controlled with the same salt solutions as used in the absorption kinetics experiments. An additional experiment was performed in an environment where the relative humidity was kept at 75% using sodium chloride.

Samples were prepared 1 day before the experiments to attain the desired humidity and hydration state of the protein.

Kinetic absorption spectroscopy

Excitation of the protein film was done by a Surelite I Nd-YAG laser with an OPO extension (Continuum, USA). 5-ns pulses, with 5 mJ/cm^2 at a wavelength of 450 nm, were used, while the white measuring light was provided by a 35-W high-pressure Xenon lamp (Hamamatsu, Japan), which was chopped by a Uniblitz digital shutter to avoid excess exposure of the sample. The shutter was open for 20 ms, and a new recording was done every 6 s to ensure that the protein returned to its dark state between consecutive actinic

pulses. The excitation pulse and the measuring light crossed the sample perpendicular to each other. Absorption difference spectra were detected with an Andor iStar gated ICCD detector (Andor Technology, UK) which was attached to a HR-320 spectrograph (ISA Jobin–Yvon, France). The length of the gate pulse of the detector was adjusted depending on its time delay after the laser pulse, and 10–30 spectra were averaged at each delay.

Data analysis

The data analysis of the OMA experiments was based on the analysis and results in our previous article (Khoroshyy et al. 2013).

The measured time-resolved difference spectra were collected in a $\boldsymbol{D}_{m\times n}$ matrix, where m is the number of data points on the wavelength scale and n is the number of different time delays after the pulsed excitation. Using the Beer–Lambert law, the matrix consisting of the difference spectra can be written as the product of the intermediate difference spectra and the transpose of their time-dependent concentrations.

Singular value decomposition (SVD) was performed on the data matrix to determine the number of spectrally distinguishable intermediates, which is equal to the rank of the matrix, and to reconstruct the data matrix with reduced noise from the significant spectral and kinetic eigenvectors. Assuming first-order transitions between the intermediates, their concentrations are composed of the linear combinations of time-dependent exponentials. As a consequence, the temporal SVD eigenvectors are also linear combinations of the same exponential functions. Multiexponential least squares fit of the temporal eigenvector matrix yielded amplitudes and phenomenological rate coefficients. The data matrix itself was then reconstructed as the linear combination of the obtained time-dependent exponentials.

A spectrotemporal least squares model fit was performed to the matrix $\boldsymbol{D}^{e}$, i.e. the spectra that were reconstructed from the exponential fit of the significant SVD kinetic vectors. The fitting parameters consisted of the spectra of the photocycle intermediates and the rate coefficients of our photocycle scheme obtained by Khoroshyy et al. (2013) for the PYP in solution, and the protein fraction entering into the photocycle. The spectral fitting parameters were permitted to moderately vary relative to the input spectra, with the constraint of no negative absorption, to allow spectral differences between the photocycle intermediates observed in aqueous solution or in the dry, rehydrated sample. As the result of the fit, we could determine the spectra of the different intermediates in the photocycle and the molecular rate coefficients represented in our scheme and also calculate the concentration matrix, i.e. the kinetics of the intermediates. These data were then used in the interpretation of the refractive index changes during the photocycle measured by optical waveguide lightmode spectroscopy.

Optical waveguide lightmode spectroscopy

To determine the relative refractive index change of the PYP intermediates at different time delays after excitation, we used the optical waveguide lightmode spectroscopy (OWLS) method, which uses the principle that only such discrete modes can propagate in an optical waveguide that meet the criteria of the (1) and (2) mode equations.

$$\frac{2\pi}{\lambda_0} d_{\mathrm{F}} \sqrt{n_{\mathrm{F}}^2 - N_{\mathrm{TE}}^2} = \arctan \sqrt{\frac{N_{\mathrm{TE}}^2 - n_{\mathrm{S}}^2}{n_{\mathrm{F}}^2 - N_{\mathrm{TE}}^2}} + \arctan \sqrt{\frac{N_{\mathrm{TE}}^2 - n_{\mathrm{A}}^2}{n_{\mathrm{F}}^2 - N_{\mathrm{TE}}^2}} + m\pi \tag{1}$$

$$\begin{aligned} \frac{2\pi}{\lambda_0} d_{\mathrm{F}} \sqrt{n_{\mathrm{F}}^2 - N_{\mathrm{TM}}^2} = {} & \arctan \left[\frac{n_{\mathrm{F}}^2}{n_{\mathrm{S}}^2} \sqrt{\frac{N_{\mathrm{TM}}^2 - n_{\mathrm{S}}^2}{n_{\mathrm{F}}^2 - N_{\mathrm{TM}}^2}} \right] \\ & + \arctan \left[\frac{n_{\mathrm{F}}^2}{n_{\mathrm{A}}^2} \sqrt{\frac{N_{\mathrm{TM}}^2 - n_{\mathrm{A}}^2}{n_{\mathrm{F}}^2 - N_{\mathrm{TM}}^2}} \right] + m\pi. \end{aligned} \tag{2}$$

In the above equations, λ_0 is the vacuum wavelength of the light propagating inside the guiding layer with a refractive index of n_{F} and thickness of d_{F}, while the substrate's refractive index is n_{S}. The m is the mode order which was zero in all of our experiments. The propagating modes are also dependent on the refractive index of the adlayer (n_{A}), which is the material that is above the guiding layer. In our experiments, the PYP film was the adlayer. The propagation properties of the guided modes can be represented by the effective refractive indices, which are N_{TE} for the transversal electric (s-polarized) and N_{TM} for the transversal magnetic (p-polarized) modes.

Our experimental set-up was arranged in a way that the change of the effective refractive index of the guided mode could be easily determined by measuring the incident angle of the light coupled into the waveguide. The arrangement consisted of a slab optical waveguide fixed on a high-resolution ($\sim 10^{-3\circ}$) rotational table. As a probe we used a HeNe laser (632.8 nm), which was incident on the integrated grating coupler. This wavelength stands outside of the absorption bands of all the intermediate states, so no absorption change interferes with the measurement of the refractive index change. The incoupled light intensity was measured by two photodiodes that were attached to the two ends of the waveguide.

The change in the adlayer's refractive index alters the coupling conditions in Eqs. (1) and (2). Based on the measured angle shifts of the incoupling peak, the refractive index change could be determined up to a precision of 10^{-5}.

We measured the light-induced refractive index change of the dried PYP film with both continuous and pulse excitations. For the CW excitation, a diode laser of 410 nm was used. The pulse excitation was done by a XeCl excimer laser-pumped Coumarin 450 dye laser (wavelengths of 308 and 451 nm, respectively).

Results and discussion

Kinetic absorption spectroscopy

The absorption difference spectra were measured in the case of both high humidity and low humidity, but extensive data were only measured when the protein was in a state of high hydration. Our analysis is demonstrated on the high-humidity environment case.

Difference spectra were recorded in the range of 250 ns to 1 s in 34 logarithmically equidistant time delays after excitation. SVD yielded a rank of 2, based on the singular values and the autocorrelation of the spectral and kinetic eigenvectors. The first 2 eigenvectors accounted for 96.72% of the variance of the data matrix. Similar experiments on PYP in solution, in the presence or absence of various salts, typically yielded a rank of 3 (Khoroshyy et al. 2013). As it became clear from the analysis, the difference is not due to a reduced number of intermediates, but to the lack of significant spectral difference between certain intermediates in the hydrated PYP film. Global multiexponential fit was done on the two weighted kinetic eigenvectors. For an adequate fit, 5 exponentials were required, similarly to the case of PYP aqueous solutions (Khoroshyy et al. 2013). The significant $\boldsymbol{U}$ spectral eigenvectors and the corresponding $\boldsymbol{V}$ vectors are shown in Fig. 1, together with the multiexponential fit of the latter.

The five exponential amplitude spectra (B-spectra) corresponding to the multiexponential fit (Fig. 2) are by and large similar to those obtained for PYP in solution (cf. Fig. 3A in Khoroshyy et al. 2013). This indicates that not only the number of distinguishable photocycle intermediates (5) but also their spectral characteristics and the photocycle scheme are similar. The corresponding phenomenological rate coefficients are, however, different: $4.8 \cdot 10^4$, $7.0 \cdot 10^2$, $1.44 \cdot 10^2$, 57 and 1.7 s^{-1}, as compared to $3.43 \cdot 10^5$, $4.0 \cdot 10^3$, $6.78 \cdot 10^2$, 2.28 and 0.18 s^{-1} in 0.66 M NaCl, pH 8.2, 22 °C. Since the phenomenological rate coefficients are functions of the molecular rate coefficients, the latter are also expected to be different in the dried, hydrated PYP sample compared to the aqueous sample.

Due to the overall similarity of the two data sets, we fitted the photocycle scheme published in Khoroshyy et al. (2013) (Fig. 3) to the present data. As in our earlier publication, pR_O

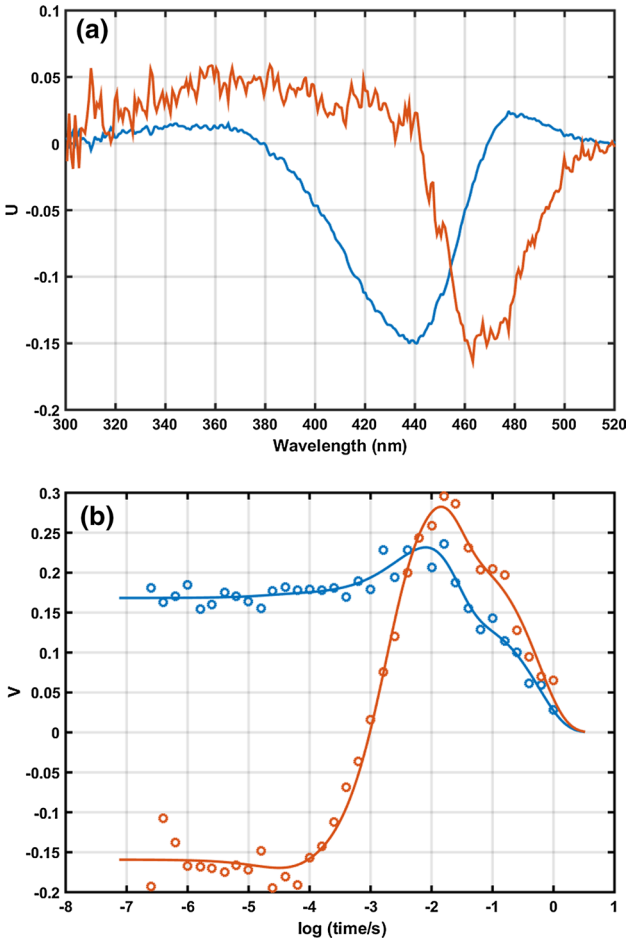

Fig. 1 The two significant spectral eigenvectors **a** U_1: blue, U_2: red; and the two significant kinetic eigenvectors **b** V_1: blue symbols, V_2: red symbols from the SVD analysis. Lines in **b** show the result of the multiexponential fit to the kinetic eigenvectors

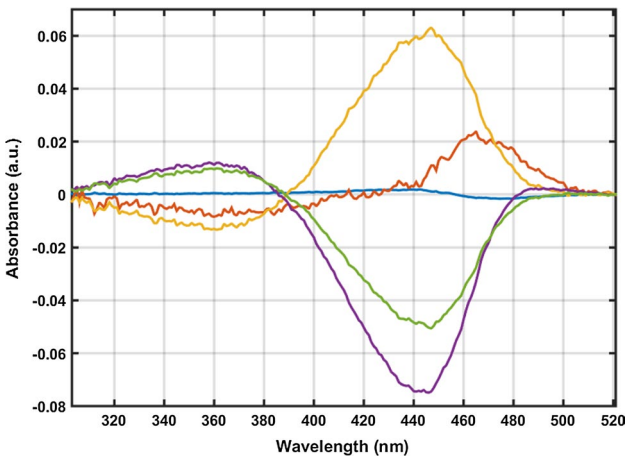

Fig. 2 Consecutive exponential amplitude spectra (B-spectra) of the multiexponential fit: blue, first component corresponding to the first (fastest) time-dependent exponential (rate coefficient k_1), red (k_2), yellow (k_3), purple (k_4), green (k_5)

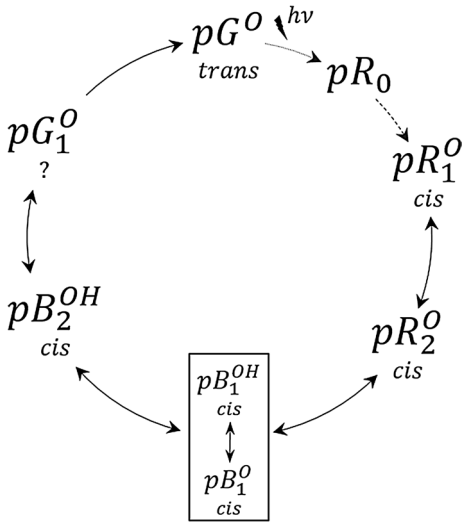

Fig. 3 The photocycle scheme. pR and pB intermediates are red- and blue-shifted, respectively, relative to the initial pG states. Trans and cis refer to the isomerization state of the p-coumaric acid chromophore of PYP, and O and OH refer to the deprotonated and protonated states of the chromophore, respectively

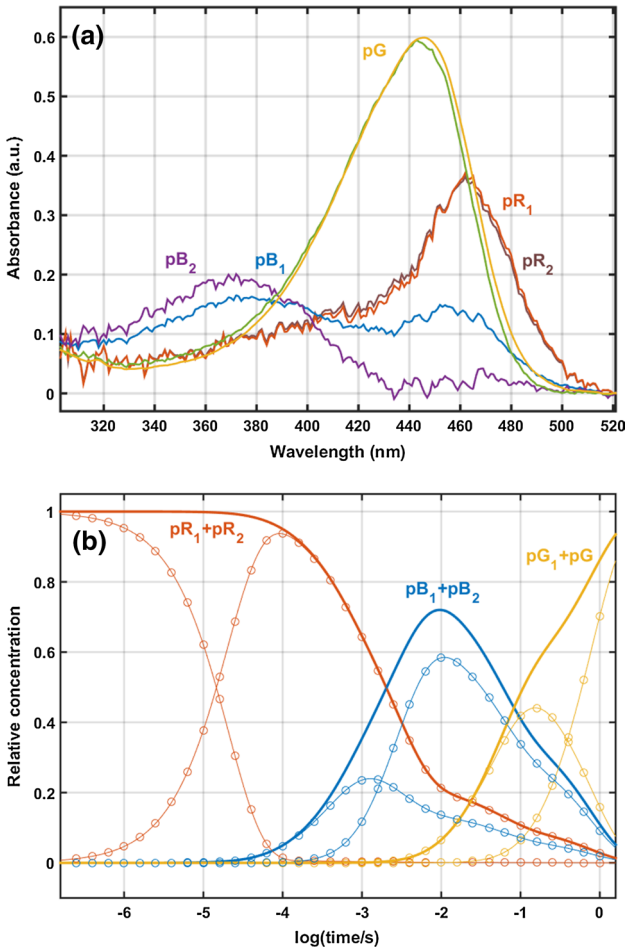

Fig. 4 The intermediate spectra obtained from the global spectrotemporal model fit (**a**) and the time-dependent relative concentrations of the intermediates (**b**). In **b,** thin lines show the kinetics of the consecutive individual intermediates and thick lines the total time evolution of the spectrally similar intermediates

was not resolved in this experiment and not included in the photocycle fit.

The fit yielded the spectra and the kinetics of the photocycle intermediates (Fig. 4a, b) and the molecular rate coefficients of the forward and reverse transitions in the scheme. The obtained intermediate spectra are similar to those published earlier (Khoroshyy et al. 2013, Fig. 4b) with two very similar pR spectra, with pB_1 appearing as a mixture, indicating a rapid equilibrium between the protonated and deprotonated forms of the chromophore, with a distinct pB_2 form and a spectrally silent pG_1 as the final intermediate before the recovery of the dark state, pG. A detailed description of the photocycle intermediates is presented in Khoroshyy et al. (2013). Briefly, the gradual conformational change (opening) of the protein starts already during the pR_1 to pR_2 transition, with a very minor spectral change not clearly resolved in this study. The blue shift of the spectrum is known to be due primarily to the protonation of the chromophore. It has also been shown (Khoroshyy et al. 2013) that the main conformational change appears during the pR_2 to pB_1 transition. The existence of the pG_1 intermediate with a spectrum similar to that of pG, the initial form, is supported by the biphasic recovery of the initial form (decay of pB) without a clear spectral signature. The pG_1 to pG transition is expected to complete the recovery of the initial conformation of the protein without affecting the immediate surroundings of the chromophore. The main difference as compared to the aqueous sample is that pB_2 is not blue-shifted relative to pB_1. The approximately 15 nm blue shift in solution has been explained by the completion of the major conformational change in the photocycle, resulting in stronger hydrogen bonding or hydration of the chromophore (Hendriks et al. 2003). This transition has not been observed in PYP crystals (Yeremenko et al. 2006), and it appears to be absent in the dried, partially hydrated PYP film, too. The absence of this conformational change in the present experiment is the probable reason for the faster recovery of the dark state, already reflected in the one order of magnitude faster fifth phenomenological exponential component, 1.7 s^{-1} vs. 0.18 s^{-1}. Table 1 lists the molecular rate coefficients obtained for the dried, partially rehydrated sample and the aqueous sample in 0.66 M NaCl, pH 8.2, 22 °C (Khoroshyy et al. 2013). Comparison of the rate coefficients shows that while transitions up to the pB_2 intermediate are faster in the aqueous sample, those after the pB_2 intermediate are up to an order of magnitude slower.

Table 1 Molecular rate coefficients obtained from the global spectrotemporal fit of the photocycle scheme (Fig. 3) to the present data (rehydrated) and to the 0.66 M NaCl, pH 8.2 data (Khoroshyy et al. 2013) (aqueous)

Transition	Rate coefficient (s^{-1})	
	Rehydrated	Aqueous
pR1 to pR2	$4.8 \cdot 10^4$	$3.7 \cdot 10^5$
Reverse	$2.7 \cdot 10^2$	$1.6 \cdot 10^2$
pR2 to pB1	$6.7 \cdot 10^2$	$2.2 \cdot 10^3$
Reverse	$1.0 \cdot 10^3$	$1.8 \cdot 10^3$
pB1 to pB2	$7.8 \cdot 10^2$	$1.0 \cdot 10^3$
Reverse	$1.6 \cdot 10^2$	$2.2 \cdot 10^2$
pB2 to pG1	16	2.9
Reverse	7.9	0.19
pG1 to pG	2.9	0.21

Light-induced refractive index change of the photoactive yellow protein

With the pulsed excitation, the refractive index change of the sample was determined by monitoring the outcoupled light intensity at an incident angle of the measuring beam (HeNe, $\lambda = 632.8$ nm) tuned slightly off-resonance, to the half-maximum of the peak intensity. Measurements were taken on both sides of the resonance peak, and the absolute values were averaged. The experiments were performed at low- (20%) and high- (75%, 85%) relative humidity environments. For each different environment, the change in refractive index was monitored at two timescales (50 ms and 2 s full scales) after excitation. An additional measurement was taken on the sample at 85% relative humidity and 500 µs time scale, for the comparison of the OMA and OWLS results regarding the fast transition in the first part of the photocycle.

At low humidity (20%, data not shown) and 50 ms after excitation, the decay of the signal (guided light intensity change after the excitation of the PYP layer) was still in progress, and the calculated relative refractive index change was $\sim 10^{-5}$, which is comparable to the accuracy of our OWLS set-up. By 2 s after excitation, the measured intensity change was negligible. Comparing the OWLS results to the measured kinetics of the PYP, we concluded that the experienced refractive index change at low humidities stems from the heat jump induced by the exciting light, rather than the protein entering the photocycle. This observation is in agreement with the results of van der Horst et al. (2005).

At high humidities (both at 75% and 85%, Fig. 5), after 50 ms from the excitation a quasi-steady state is formed, whose refractive index is different from that of the ground state. The measured kinetics and concentrations at 85% relative humidity (shown in Fig. 4b) imply that at 50 ms after

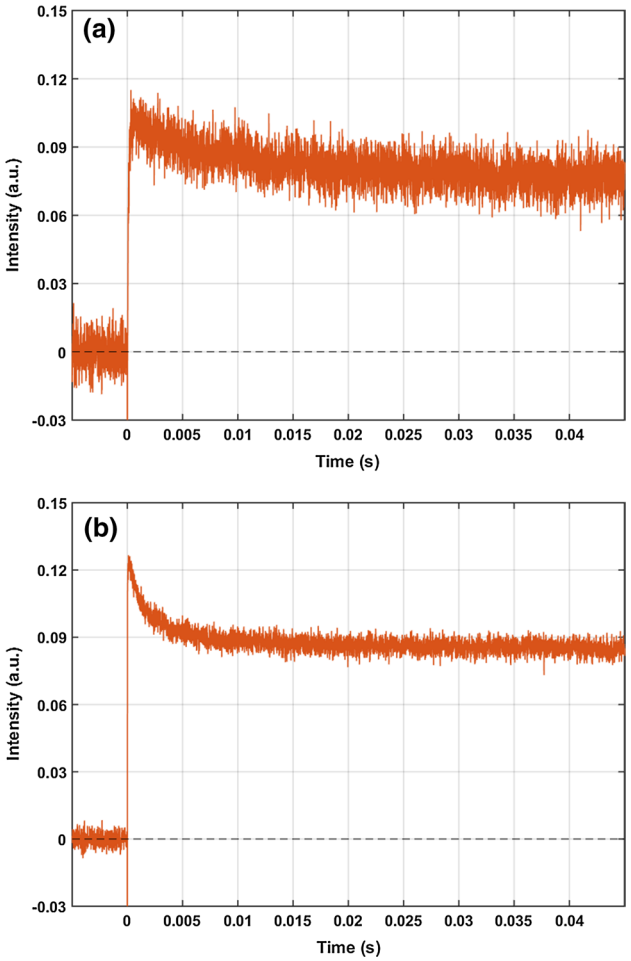

Fig. 5 The measured OWLS data at 75% RH (**a**) and 85% RH (**b**). The data indicated are measured at the right side of the incoupling peak

the excitation the mixture of two pB states dominates the photocycle, while the pR and pG_1 conformations are present only in lesser amounts. The calculated refractive index change for the pB mixture state is $\Delta n = -3 \cdot 10^{-4}$. At 2 s after excitation, a small residual refractive index signal was present (Fig. 6c), which is likely due to a temperature artefact. At lower, 75% RH, the results were similar to those obtained at 85% RH.

At 85% relative humidity, an additional experiment was done on the 500-µs timescale, to compare the kinetic coefficients obtained from the OWLS and OMA experiments. The 500-µs timescale OWLS data were fitted with two exponentials, the second of them corresponding to the second phenomenological rate constant from the OMA results (Fig. 6a), while the first rate constant was found slightly slower than its absorption kinetic counterpart ($2.4 \cdot 10^4\ s^{-1}$). For the traces of 50-ms timescale, two exponentials were used, whose kinetic constants corresponded to the second and third phenomenological rate coefficients ($7.0 \cdot 10^2$, $1.44 \cdot 10^2\ s^{-1}$,

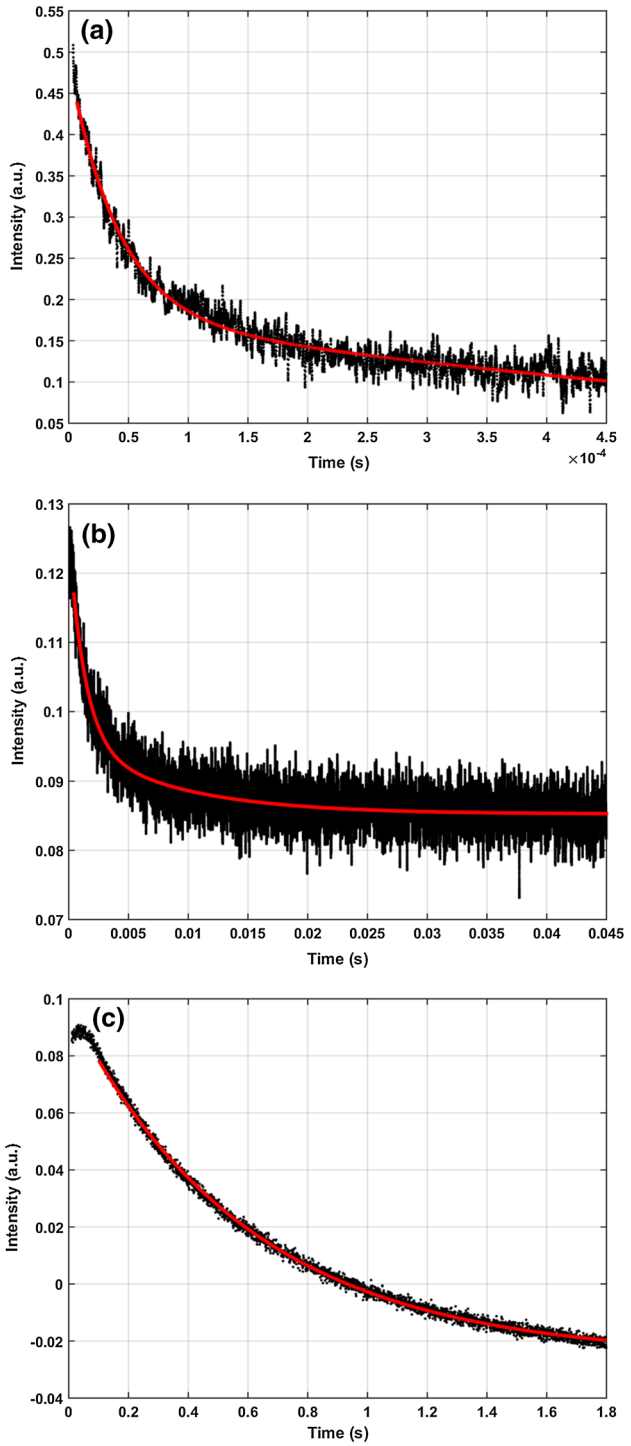

Fig. 6 Exponential fit on the data measured in 85% RH environment on a 500-µs (**a**), 50-ms (**b**) and 2-second (**c**) timescale

respectively, Fig. 6b), while the 2-s timescale data could be fitted with one exponential with a rate constant of 1.7 s^{-1} (Fig. 6c), which corresponds to the last phenomenological rate coefficient obtained from the OMA's multiexpoential fit.

A global multiexponential fit to the OWLS and OMA data on the 500-µs, 50-ms and 2-s timescales showed a similar correlation between the kinetics of the curves measured by the two methods, with a goodness of fit of R^2 0.96, 0.83 and 0.99, respectively, for the three timescales. These results confirm that the refractive index changes of the films are due to conformational changes in the protein molecule following light excitation.

At 85% relative humidity, an additional experiment with a blue-light CW excitation was also performed, where a refractive index change $\Delta n_{\mathrm{pB-pG}} = -5 \cdot 10^{-4}$ was observed at 632.8 nm (data not shown), and was attributed to a dynamic equilibrium between the pG and pB states. This value is slightly higher than the corresponding refractive index change observed during the photocycle ($-3 \cdot 10^{-4}$), which might be explained by the < 1 quantum efficiency of the photocycle for a short flash, similarly to the BR-M transition in bacteriorhodopsin, where stationary excitation of the film yielded higher concentrations of the M form (Dér et al. 2007). Based on the amplitude ratios of the kinetic OWLS traces (Fig. 6a, b), the transient refractive index changes corresponding to the pR_1 and pR_2 states are estimated to be even higher (about 10 and 5 times, respectively), which are comparable to the maximum values obtained for bR films.

Conclusions

The photocycle of dried PYP films was examined at different relative humidities. For determining the kinetics of the photocycle, we used an optical multichannel analyser setup and compared the data to those of light-induced relative refractive index change measurements by optical waveguide lightmode spectroscopy.

At low humidity (20%), no regular photocycle takes place in the protein, and the small spectral changes observed are probably due to a temperature jump effect caused by the pumping laser.

At high humidities (75% and 85% RH), the photocycle is similar to the one measured in solution, but the rate-limiting steps are faster. In previous publications, a number of different photocycle schemes have been proposed for PYP in solution. According to our analysis, the simple, unbranched photocycle scheme containing multiple red- and blue-shifted intermediates (pR_1, pR_2, pB_1, pB_2 and pG_1) with reversible transitions between most of the states, as established by (Khoroshyy et al. 2013), could adequately account for the photocycle of PYP in dried film at high RH (85%). With the time resolution of the experiments, the formation of pR_2 from the pR_1 state is the fastest transition with a phenomenological rate constant greater than $4.8 \cdot 10^4$ s^{-1}. The spectra of the two pR states are similar to each other; however, they have sharper maxima than their counterparts in solution.

The decay of pR and the formation of pB states are slower in the dried protein, with the pB states being less blue-shifted, and pB_1 having spectral features resembling a mixture of, presumably, protonated and deprotonated chromophores. The refractive index change of blue-shifted intermediates is calculated to be $\Delta n = -3 \cdot 10^{-4}$, while the faster phases of the OWLS signal indicate refractive index changes in the 10^{-3} regime, similar to the highest values of bR-based films.

The above results are expected to serve with essential information for future biophotonic devices utilizing the nonlinear optical properties of PYP or other chromoproteins. Note that optical film preparation at controlled pH and relative humidity is solved for chromoproteins like bR (see examples in Dér and Keszthelyi 2001 and references therein). According to our experience, optical-quality films of PYP, prepared at pre-adjusted pH, and stored under controlled relative humidity conditions, keep their functionality for at least 6 months. PYP could substitute or complement bR in such applications where, for example, shorter-wavelength operations are needed. Another distinct feature of PYP is that, contrary to bR, it is inherently water soluble in its monomeric form that allows its penetration into nanometric holes of porous silicon or other porous materials, making unique hybrid nonlinear optical structures possible. Most of all, applications in holography or integrated photonics are envisaged.

Acknowledgements Open access funding provided by MTA Biological Research Centre (MTA SZBK). This work was supported by grants from the Hungarian Ministry for National Economy (Economic Development and Innovation Operational Programme, GINOP-2.3.2-15-2016-00001) and by the National Research, Development and Innovation Office (NKFIH K-124922 and K-108697). The authors are indebted to Dr. John Fitch for generously providing photoactive yellow protein.

Open Access This article is distributed under the terms of the Creative Commons Attribution 4.0 International License (http://creativecommons.org/licenses/by/4.0/), which permits unrestricted use, distribution, and reproduction in any medium, provided you give appropriate credit to the original author(s) and the source, provide a link to the Creative Commons license, and indicate if changes were made.

References

Baca M, Borgstahl GEO, Boissinot M, Burke PM, Williams DR, Slater KA, Getzoff ED (1994) Complete chemical structure of photoactive yellow protein: novel thioester-linked 4-hydroxycinnamyl chromophore and photocycle chemistry. Biochemistry 33:14369–14377. https://doi.org/10.1021/bi00252a001

Borucki B, Joshi CP, Otto H, Cusanovich MA, Heyn MP (2006) The transient accumulation of the signaling state of photoactive yellow protein is controlled by the external pH. Biophys J 91:2991–3001. https://doi.org/10.1529/biophysj.106.086645

Cusanovich MA, Meyer TE (2003) Photoactive yellow protein: a prototypic PAS domain sensory protein and development of a common signaling mechanism. Biochemistry 42:4759–4770. https://doi.org/10.1021/bi020690e

Dér A, Keszthelyi L (2001) Bioelectronic applications of photochromic pigments. IOS Press, Amsterdam

Dér A, Valkai S, Fábián L, Ormos P, Ramsden JJ, Wolff EK (2007) Integrated optical switching based on the protein bacteriorhodopsin. Photochem Photobiol 83:393–396. https://doi.org/10.1562/2006-06-21-RA-944

Fábián L, Wolff EK, Oroszi L, Ormos P, Dér A (2010) Fast integrated optical switching by the protein bacteriorhodopsin. Appl Phys Lett 97:023305. https://doi.org/10.1063/1.3462940

Fábián L et al (2011) Protein-based ultrafast photonic switching. Opt Express 19:18861–18870. https://doi.org/10.1364/OE.19.018861

Fábián L, Mathesz A, Dér A (2015) New trends in biophotonics. Acta Biol Szeged 59(Suppl. 2):189–202

Groot ML, van Wilderen LJGW, Larsen DS, van der Horst MA, van Stokkum IHM, Hellingwerf KJ, van Grondelle R (2003) Initial steps of signal generation in photoactive yellow protein revealed with femtosecond mid-infrared spectroscopy. Biochemistry 42:10054–10059. https://doi.org/10.1021/bi034878p

Hales JM et al (2010) Design of polymethine dyes with large third-order optical nonlinearities and loss figures of merit. Science 327:1485–1488

Haque SA, Nelson J (2010) Toward organic all-optical switching. Science 327:1466–1467

Hellingwerf KJ, Hendriks J, Gensch T (2003) Photoactive yellow protein, a new type of photoreceptor protein: will this "yellow lab" bring us where we want to go? J Phys Chem A 107:1082–1094. https://doi.org/10.1021/jp027005y

Hendriks J, van Stokkum IHM, Hellingwerf KJ (2003) Deuterium isotope effects in the photocycle transitions of the photoactive yellow protein. Biophys J 84:1180–1191. https://doi.org/10.1016/S0006-3495(03)74932-7

Hoff WD et al (1994a) Thiol ester-linked p-coumaric acid as a new photoactive prosthetic group in a protein with rhodopsin-like photochemistry. Biochemistry 33:13959–13962. https://doi.org/10.1021/bi00251a001

Hoff WD et al (1994b) Measurement and global analysis of the absorbance changes in the photocycle of the photoactive yellow protein from *Ectothiorhodospira halophila*. Biophys J 67:1691–1705

Hristova SG, Varo G, Der A (1984) Long time stability of purple membranes from *Halobacterium halobium*. Acta Biochim Biophys Acad Sci Hung 19:215–219

Hu X, Jiang P, Ding C, Yang H, Gong Q (2008) Picosecond and low-power all-optical switching based on an organic photonic-bandgap microcavity. Nat Photonics 2:185

Ihee H et al (2005) Visualizing reaction pathways in photoactive yellow protein from nanoseconds to seconds. Proc Natl Acad Sci USA 102:7145–7150. https://doi.org/10.1073/pnas.0409035102

Imamoto Y, Kataoka M (2007) Structure and photoreaction of photoactive yellow protein, a structural prototype of the PAS domain superfamily. Photochem Photobiol 83:40–49. https://doi.org/10.1562/2006-02-28-ir-827

Joshi CP, Borucki B, Otto H, Meyer TE, Cusanovich MA, Heyn MP (2005) Photoreversal kinetics of the I1 and I2 intermediates in the photocycle of photoactive yellow protein by double flash experiments with variable time delay. Biochemistry 44:656–665. https://doi.org/10.1021/bi0481141

Khoroshyy P, Dér A, Zimányi L (2013) Effect of Hofmeister cosolutes on the photocycle of photoactive yellow protein at moderately alkaline pH. J Photochem Photobiol B 120:111–119. https://doi.org/10.1016/j.jphotobiol.2012.12.014

Kim TW et al (2012) Protein structural dynamics of photoactive yellow protein in solution revealed by pump-probe X-ray solution scattering. J Am Chem Soc 134:3145–3153. https://doi.org/10.1021/ja210435n

Mathesz A et al (2013) High-speed integrated optical logic based on the protein bacteriorhodopsin. Biosens Bioelectron 46:48–52. https://doi.org/10.1016/j.bios.2013.02.022

Meyer TE (1985) Isolation and characterization of soluble cytochromes, ferredoxins and other chromophoric proteins from the halophilic phototrophic bacterium *Ectothiorhodospira halophila*. Biochem Biophys Acta 806:175–183. https://doi.org/10.1016/0005-2728(85)90094-5

Meyer TE, Yakali E, Cusanovich MA, Tollin G (1987) Properties of a water-soluble, yellow protein isolated from a halophilic phototrophic bacterium that has photochemical activity analogous to sensory rhodopsin. Biochemistry 26:418–423. https://doi.org/10.1021/bi00376a012

Meyer TE, Tollin G, Hazzard JH, Cusanovich MA (1989) Photoactive yellow protein from the purple phototrophic bacterium, *Ectothiorhodospira halophila.* Quantum yield of photobleaching and effects of temperature, alcohols, glycerol, and sucrose on kinetics of photobleaching and recovery. Biophys J 56:559–564. https://doi.org/10.1016/S0006-3495(89)82703-1

Mix LT et al (2018) Excitation-wavelength-dependent photocycle initiation dynamics resolve heterogeneity in the photoactive yellow protein from *Halorhodospira halophila*. Biochemistry 57:1733–1747. https://doi.org/10.1021/acs.biochem.7b01114

Moore GE (1965) Cramming more components onto integrated circuits. Electronics 38:114–117

Oesterhelt D, Stoeckenius W (1971) Rhodopsin-like protein from the purple membrane of *Halobacterium halobium*. Nat New Biol 233:149

Oesterhelt D, Stoeckenius W (1973) Functions of a new photoreceptor membrane. Proc Natl Acad Sci 70:2853–2857

Ormos P, Fábián L, Oroszi L, Wolff EK, Ramsden JJ, Dér A (2002) Protein-based integrated optical switching and modulation. Appl Phys Lett 80:4060–4062. https://doi.org/10.1063/1.1481197

Pande K et al (2016) Femtosecond structural dynamics drives the trans/cis isomerization in photoactive yellow protein. Science 352:725–729. https://doi.org/10.1126/science.aad5081

Service RF (1995) Two steps for light-altering polymers. Science (New York, NY) 268:1570

Sprenger WW, Hoff WD, Armitage JP, Hellingwerf KJ (1993) The eubacterium *Ectothiorhodospira halophila* is negatively phototactic, with a wavelength dependence that fits the absorption spectrum of the photoactive yellow protein. J Bacteriol 175:3096–3104. https://doi.org/10.1128/jb.175.10.3096-3104.1993

Ujj L, Devanathan S, Meyer TE, Cusanovich MA, Tollin G, Atkinson GH (1998) New photocycle intermediates in the photoactive yellow protein from *Ectothiorhodospira halophila*: picosecond transient absorption spectroscopy. Biophys J 75:406–412. https://doi.org/10.1016/S0006-3495(98)77525-3

Van Beeumen JJ et al (1993) Primary structure of a photoactive yellow protein from the phototrophic bacterium *Ectothiorhodospira halophila*, with evidence for the mass and the binding site of the chromophore. Protein Sci 2:1114–1125. https://doi.org/10.1002/pro.5560020706

van der Horst MA, van Stokkum IHM, Dencher NA, Hellingwerf KJ (2005) Controlled reduction of the humidity induces a shortcut recovery reaction in the photocycle of photoactive yellow protein. Biochemistry 44:9160–9167. https://doi.org/10.1021/bi050237d

Waldrop MM (2016) The chips are down for Moore's law. Nat News 530:145–147

Yang C, Kim SO, Kim Y, Yun SR, Choi J, Ihee H (2017) Photocycle of photoactive yellow protein in cell-mimetic environments: molecular volume changes and kinetics. J Phys Chem B 121:769–779. https://doi.org/10.1021/acs.jpcb.6b13076

Yeremenko S, van Stokkum IHM, Moffat K, Hellingwerf KJ (2006) Influence of the crystalline state on photoinduced dynamics of photoactive yellow protein studied by ultraviolet-visible transient absorption spectroscopy. Biophys J 90:4224–4235. https://doi.org/10.1529/biophysj.105.074765

Publisher's Note Springer Nature remains neutral with regard to jurisdictional claims in published maps and institutional affiliations.

II. **Krekic, S.**; Zakar, T.; Gombos, Z.; Valkai, S.; Mero, M.; Zimányi, L.; Heiner, Z.; Dér, A. Nonlinear Optical Investigation of Microbial Chromoproteins. *Front. Plant Sci.* **2020**, *11*, 1567. https://doi.org/10.3389/fpls.2020.547818. IF: 5.753

frontiers in Plant Science

ORIGINAL RESEARCH
published: 21 October 2020
doi: 10.3389/fpls.2020.547818

Nonlinear Optical Investigation of Microbial Chromoproteins

Szilvia Krekic[1,2], Tomás Zakar[3†], Zoltán Gombos[3‡], Sándor Valkai[1], Mark Mero[4], László Zimányi[1], Zsuzsanna Heiner[5] and András Dér[1]**

[1] Institute of Biophysics, Biological Research Centre, Szeged, Hungary, [2] Doctoral School of Multidisciplinary Medical Sciences, University of Szeged, Szeged, Hungary, [3] Institute of Plant Biology, Biological Research Centre, Szeged, Hungary, [4] Max Born Institute for Nonlinear Optics and Short Pulse Spectroscopy, Berlin, Germany, [5] School of Analytical Sciences Adlershof, Humboldt-Universität zu Berlin, Berlin, Germany

OPEN ACCESS

Edited by:
Michael Hippler,
University of Münster, Germany

Reviewed by:
Heiko Lokstein,
Charles University, Czechia
Dimitris Petroutsos,
UMR 5168 Laboratoire de Physiologie Cellulaire Vegetale (LPCV), France

***Correspondence:**
Zsuzsanna Heiner
heinerzs@hu-berlin.de
András Dér
der.andras@brc.hu

†Present address:
Tomás Zakar,
Institute of Photonics and Electronics, The Czech Academy of Sciences, Prague, Czechia

‡Deceased

Specialty section:
This article was submitted to Plant Physiology, a section of the journal Frontiers in Plant Science

Received: 31 March 2020
Accepted: 22 September 2020
Published: 21 October 2020

Citation:
Krekic S, Zakar T, Gombos Z, Valkai S, Mero M, Zimányi L, Heiner Z and Dér A (2020) Nonlinear Optical Investigation of Microbial Chromoproteins. Front. Plant Sci. 11:547818. doi: 10.3389/fpls.2020.547818

Membrane-bound or cytosolic light-sensitive proteins, playing a crucial role in energy- and signal-transduction processes of various photosynthetic microorganisms, have been optimized for sensing or harvesting light by myriads of years of evolution. Upon absorption of a photon, they undergo a usually cyclic reaction series of conformations, and the accompanying spectro-kinetic events assign robust nonlinear optical (NLO) properties for these chromoproteins. During recent years, they have attracted a considerable interest among researchers of the applied optics community as well, where finding the appropriate NLO material for a particular application is a pivotal task. Potential applications have emerged in various branches of photonics, including optical information storage and processing, higher-harmonic and white-light continuum generation, or biosensorics. In our earlier work, we also raised the possibility of using chromoproteins, such as bacteriorhodopsin (bR), as building blocks for the active elements of integrated optical (IO) circuits, where several organic and inorganic photonic materials have been considered as active components, but so far none of them has been deemed ideal for the purpose. In the current study, we investigate the linear and NLO properties of biofilms made of photoactive yellow protein (PYP) and bR. The kinetics of the photoreactions are monitored by time-resolved absorption experiments, while the refractive index of the films and its light-induced changes are measured using the Optical Waveguide Lightmode Spectroscopy (OWLS) and Z-scan techniques, respectively. The nonlinear refractive index and the refractive index change of both protein films were determined in the green spectral range in a wide range of intensities and at various laser repetition rates. The nonlinear refractive index and refractive index change of PYP were compared to those of bR, with respect to photonics applications. Our results imply that the NLO properties of these proteins make them promising candidates for utilization in applied photonics, and they should be considered as valid alternatives for active components of IO circuits.

Keywords: Z-scan, bacteriorhodopsin, photoactive yellow protein, nonlinear refractive index, saturable absorption, photo-induced refractive index change

INTRODUCTION

Ubiquitous applications of photonics and optoelectronics are now penetrating into diverse areas from everyday life to the most advanced scientific disciplines, such as optical communication, data processing and storage, quantum computing, holography, just to mention a few. Key elements of photonic devices are the so-called nonlinear optical (NLO) materials, which can actively modify light propagation or store optical information. Examples for the use of NLO materials in photonics ranges from all-optical signal processing (Willner et al., 2014), to all-optical switching (Chai et al., 2017), optical filtering (Dini et al., 2016), with the list of applications continuously growing. To this end, one of the biggest challenges is finding materials with optimal NLO characteristics that could be applied in photonic devices. The development and characterization of NLO materials (such as nonlinear crystals or chalcogenide glasses) (Adair et al., 1989; Eggleton et al., 2011) is in current progress, because the diverse applications require special solutions. E.g., several aspects must be taken into account when selecting a material for an IO application, such as mechanical stability, re-excitability, sensitivity, but most importantly, the material has to have a large refractive index change induced by an outer stimulus of an electric field or light. Amongst others, the application of molecules possessing π-conjugated electron systems have been most favored, since they show a high (third-order) optical polarizability, usually without two-photon losses (Hales et al., 2010; Haque and Nelson, 2010; Hu et al., 2017). However, various problems concerning their robustness and incorporation into solid matrices for practical applications are still to be solved. On the other hand, natural π-conjugated materials, such as chromoproteins are readily available (Clays et al., 2001; Fábián et al., 2011). Chromoproteins have been perfected by evolution for billions of years for utilizing light as a source of energy or information. Their protein matrix stabilizes their chromophores, and fine-tunes their optical properties. At the same time, the application of proteins as NLO materials in photonics also raises non-trivial technical problems. Building up stable hybrid structures of the protein and the passive substrate (such as a thin film of chromoprotein on a photonic circuit), and a thorough characterization of their NLO properties is inevitable, as well as their optimization for a particular application, such as IO switching, or other optical information processing tasks.

One of the most investigated candidates in the field is the protein bacteriorhodopsin (bR), while other proteins, such as photoactive yellow protein (PYP) have recently also been considered as IO active materials (Krekic et al., 2019). Their molecular and bulk optical properties (e.g., linear and nonlinear polarizabilities, and their refractive index and its light-induced changes) are of high interest from the point of view of potential optoelectronic applications of chromoproteins, in general.

Bacteriorhodopsin is a membrane protein (embedded in quasi-crystalline lipid-protein patches, the so-called purple membranes) first discovered in the archaeon *Halobacterium salinarum* (Oesterhelt and Stoeckenius, 1971; Lanyi, 2004). It consists of seven-transmembrane alpha helices to which an all-trans retinal is covalently attached through a protonated Schiff base. bR is widely known to be the simplest light-driven proton pump (Oesterhelt and Stoeckenius, 1973), hence considered as a model for more complicated systems. One of the protein's most important characteristics is its photocycle. Upon light absorption, bR enters a reaction cycle, going through quasi-stable intermediate states (K, L, M, N, O) in a matter of milliseconds in solution, before returning to the initial state. Each of the intermediary states possesses characteristic absorption spectra, distinct from the initial state's spectrum. The difference in absorption spectra between the intermediate states and the initial state indicates a difference in refractive indices according to the Kramers–Kronig relations (Nussenzveig, 1972; Wooten, 2013).

Photoactive yellow protein is a water-soluble protein present in purple sulfur photosynthetic bacteria (Meyer, 1985), much smaller than bR-containing purple membrane patches (Oesterhelt and Stoeckenius, 1971; Meyer, 1985). This makes PYP a promising candidate for incorporation into IO passive structures (e.g., in porous silicon), where membrane-bound bR cannot be used due to its larger particle size. When excited with blue light, PYP enters its photocycle (Meyer et al., 1987), which standardly consists of four intermediates (pR_1, pR_2, pB_1, pB_2) and takes place in a matter of milliseconds in solution.

To fully consider a protein in IO applications, a conclusive optical characterization is needed. The utility of NLO materials for optical communication is highly dependent on the magnitude of the refractive index change that can be induced in the material at hand. The larger the associated change in the complex refractive index, the larger the amplitude and phase modulation effect will be. When combining NLO materials with passive components, the size and energy consumption also depend on the NLO response, hence a larger refractive index change is preferred (Miller, 2010; Sasikala and Chitra, 2018).

In dried films of chromoproteins the light-induced refractive index changes are orders of magnitude higher than in suspensions, where, due to the overwhelming excess of water (ca. 55 M water to a few 100 μM of protein in the densest suspensions), the refractive index of water is dominating (Heiner and Osvay, 2009). Hence, as far as photonic applications of bR utilizing light-induced optical changes are concerned, dried films (usually under controlled humidity), are used (Dér and Keszthelyi, 2001; Vsevolodov, 2012 and references therein). Exceptions are only the few applications that are based on absorption instead of refractive index changes (Stuart et al., 2001). From the point of view of technical applications, on the other hand, using dried films is convenient due to their form and stability. Combining dried films of proteins with IO passive structures is a solvable task (see the section "Materials and Methods"), and in such samples proteins maintain their optical properties for a long time (several decades) (Váró and Keszthelyi, 1983; Dér and Keszthelyi, 2001; Vsevolodov, 2012).

One should note, however, that the photocycles of both pigments do depend on the relative humidity of the films (Váró and Keszthelyi, 1983; van der Horst et al., 2005). The general rule of thumb is that at high-enough relative humidity (>80–90%), the photocycles are close to the native ones, while at moderate relative humidity (between ca. 30–50% to 80%), such transitions that accompany large-scale conformational changes (e.g., the

ones following M formation in the bR, or those after pB_1 in PYP) are hindered, hence the rate-limiting steps become slower. The reason for this phenomenon is that protein conformational flexibility is decreasing by lowering relative humidity (Fitter et al., 1999). Further lowering relative humidity values leads to more serious truncation of the photocycles (Váró and Keszthelyi, 1983; van der Horst et al., 2005). Technical applications (considered so far for bR only) normally use the higher end of moderate humidity range, as a reasonable trade-off between maximizing $\boldsymbol{\Delta n}$ and having a decent photocycle kinetics (Dér and Keszthelyi, 2001; Vsevolodov, 2012). Proteins in this range show an overall slower photocycle than native proteins, which might appear to be less favorable for some photonic applications, however, both proteins have fast (sub-picosecond to picosecond) transitions in the beginning of their photocycles, which are unaffected by humidity in bR (Colonna et al., 2005), and probably in PYP, too (see fast kinetics detected in crystallized PYP (Yeremenko et al., 2006; Schotte et al., 2012; Tenboer et al., 2014), but yet to be characterized in PYP dry samples). On the other hand, the first intermediate states of both the bR and PYP photocycles can be driven back by fast, light-induced reactions to the ground state (Balashov, 1995; Joshi et al., 2005; Tóth-Boconádi et al., 2006, 2010), allowing a rapid, light-controlled manipulation of refractive index kinetics of the films. The lifetime of various types of dried bR films is known to be in the range of several decades, appropriate for technical applications (Dér and Keszthelyi, 2001).

In the past decades, several research articles have demonstrated the dried bR film's large light-induced refractive index change ($\boldsymbol{\Delta n}$), and its utilization in optical switching experiments and light modulation (Ormos et al., 2002; Fábián et al., 2011; Mathesz et al., 2013). bR also shows a large hyperpolarizability, important in frequency-doubling experiments, investigated by NLO techniques (Naskali et al., 2014). The nonlinear refractive index value $\boldsymbol{n_2}$ of bR-containing samples has been extensively investigated previously under various experimental conditions, in most of the cases using the so-called Z-scan technique (Song et al., 1993; Aranda et al., 1995; Jeganathan et al., 2017). The spectro-kinetic properties and light-induced refractive index changes have also been discussed (van der Horst et al., 2005; Krekic et al., 2019), which further encourages investigation of the protein's NLO properties. There have been a few publications dealing with the nonlinear refractive index of different PYP samples, e.g., embedded in thick polyacrylamide matrices (Vanhanen et al., 1998; Leppanen et al., 1999) or adsorbed to poly-methyl-methacrylate microspheres (Lee et al., 2018), however, the results are hard to reconcile due to the different samples and the various methods applied (Z-scan, Michelson-interferometer, and hyperspectral quantitative phase imaging). No experiments were done so far on a thin-film PYP sample and with a pulsed Z-scan setup.

The single-beam Z-scan technique is a popular method for the characterization of the optical nonlinearities of a wide variety of materials (Sheik-Bahae et al., 1990), including organic and even protein samples. During a Z-scan, the sample is moved through the laser focus and the power or energy transmitted through an aperture placed behind the focus is measured as a function of the sample position, z. When the aperture is small, a closed-aperture trace is obtained, yielding the magnitude and sign of $\boldsymbol{n_2}$. When the aperture is removed or open, an open-aperture trace is measured, providing the magnitude of nonlinear absorption coefficients. While the experimental realization of the technique is simple, determining all the NLO mechanisms causing a particular Z-scan trace is often not possible without performing additional measurements. For example, the photocycle of bR and the related complex kinetics make the interpretation of the associated Z-scan data difficult (Kir'Yanov et al., 2000).

Here, we report on the NLO properties of a new type of thin bR and PYP films, in the light of possible optoelectronic applications of these proteins. The films were experimentally characterized through OWLS, absorption kinetics and Z-scan measurements. The linear and nonlinear refractive index, and the formation and decay times of the respective intermediate states in the photocycle of the two proteins were determined. The nonlinear refractive index was measured using the Z-scan technique with both 543-nm or 405-nm continuous wave (CW) and 514-nm pulsed laser illumination at varying repetition rates and a wide range of intensities. The determined $\boldsymbol{\Delta n}$ and $\boldsymbol{n_2}$ values of bR are compared to previously published data, as well as to the results obtained for PYP, where prior data on NLO properties are scarce. The results are considered to have important implications from the perspective of photonic applications – the future utilization of these biomaterials in film format for integrated optical switching and signal processing experiments. Compared to non-organic NLO materials currently used and researched for such purposes, biological materials, such as bR and PYP, offer a readily available, cost-effective alternative, which is also more versatile depending on the form and environment of the protein building blocks.

MATERIALS AND METHODS

Sample Preparation

Bacteriorhodopsin was prepared according to the standard procedure: purple membranes separated from strain R1M1 of *Halobacterium salinarum* were prepared as described in Oesterhelt and Stoeckenius (1971). Purple membranes contain 25% lipids and 75% bR, as the sole protein constituent in the preparation (Oesterhelt and Stoeckenius, 1974). (For the sake of simplicity, we refer to this membrane-bound form of the protein as bR, throughout the text.) Wild-type PYP apoprotein was overexpressed in *Escherichia coli (BL21DE3)* strain, isolated, and then reconstituted with freshly synthetized pCA (coumaric acid) anhydride in 4 M urea buffer (Mihara et al., 1997; Kamikubo et al., 2007). The holoprotein was purified by column chromatography (DEAE Sepharose CL6B) and concentrated/washed by 10 kDa centrifugal filters several times.

An important requirement for photonic applications is the optical quality of the films. Layering and subsequent drying of protein suspensions normally leads to highly cracked samples, inappropriate for technical applications. To prevent cracking, some ballast materials, such as gelatin or PVA are used at

relatively high concentrations (Vsevolodov, 2012), and the relative humidity is often fixed at the desired values by sandwiching and sealing the sample between glass plates (Hampp and Juchem, 2001). In our experiments, we chose to add low amounts of glycerol to the sample before drying. These treatments completely prevented crack formation, at the same time, kept the sample sufficiently humid without sandwiching, even at low relative humidity values, such as 33% humidity, the standard laboratory environment. According to our estimate based on optical multichannel analyzer experiments on bR (data not shown), the humidity inside the sample corresponded to a ca. 80–85% relative humidity value. During the Z-scan measurements and the absorption kinetic experiments, we controlled the environment to avoid any errors arising from the difference in humidity.

Each of the protein suspensions was first mixed with an 87% glycerol solution. For bR samples, glycerol constituted 10% of the mixture, while for PYP the ratio was lowered to 2% to achieve optimal homogeneity and viscosity of the film. The mixtures were first sonicated for 1–2 min to remove any microbubbles, then pipetted to a 200-μm thick microscope cover slide to form an approximately 5 mm diameter patch. The films were then left to dry under an extractor fume hood for at least 12 h. Before measurements, the protein films were sandwiched using an additional microscope cover slip. The cover slips were made of BK7 glass. For the pulsed-laser measurements, a sample thickness of 200 μm was achieved by embedding a 200-μm thick spacer between the glass slabs. Similarly, for the 405-nm CW measurement on PYP, a sample thickness of 200 μm was used. For the 543-nm CW experiment on bR, a thinner sample was made to accommodate the lowered average power of the applied laser. The environment's relative humidity was 33% during each experiment, while the sample temperature was kept at 23°C.

For the OWLS measurements, the protein-glycerol mixtures were prepared using the same methods as for the Z-scan measurements. The mixtures were pipetted to an optical slab waveguide, and left to dry for at least 12 h before measurements.

For the single-wavelength absorption kinetics experiments, the protein-glycerol mixtures, pipetted onto glass slabs, were left to dry for at least 12 h, and the slabs were then placed into cuvettes in which we set the relative humidity at 33% with a saturated solution of magnesium chloride.

OWLS Measurements

Throughout the experiments, grating-coupled (coupler grating width 1 mm, line density 2400 mm^{-1}) slab waveguides [MicroVacuum Ltd., material $Si(Ti)O_2$, n_f between 1.78 and 1.80, thickness between 195 nm and 205 nm] on glass substrate (n_s = 1.53) were used. The waveguides were mounted on a high-precision rotational turntable (DPS, Ealing Electro Optics), by which the angle of incidence of a measuring light beam (He-Ne laser, Melles Griot, 543 nm) could be adjusted with an accuracy of 10^{-4} degrees. The intensity of the coupled light was detected at the end of the waveguide by a photomultiplier tube (PMT, Hamamatsu, Japan), whose signal was amplified by a laboratory-built current-voltage converter and recorded by a digital oscilloscope (LeCroy 9310-L). Under such conditions, only two discrete modes (transversal electric, "TE" and transversal magnetic, "TM") of the guided light can propagate, with highly selective resonance conditions. From the peak positions, the refractive index of the adlayer can be determined using the mode equations of the three-layer waveguide (Ramsden, 1993).

Absorption Kinetics Measurements

Time-resolved absorption spectra of the protein samples were obtained with a home-built pump-probe apparatus on the time scale of milliseconds to seconds. The pump source was a Surelite II Nd:YAG laser with an OPO extension (Continuum, United States) and was aligned to 514 nm and 445 nm for exciting the initial state of bR and PYP, respectively. The pulse energies were 2 mJ and 2.80 mJ. The source of the unpolarized probe light was a 35-W high-pressure Xenon lamp (Hamamatsu, Japan), filtered by narrow-band interference filters at selected wavelengths. The pump and probe beams spatially overlapped on the sample, and the transmitted probe light was directed to a Hamamatsu PMT through a HR-320 monochromator (ISA Jobin–Yvon, France). The applied repetition rate of the excitation laser was chosen to be 0.1 Hz to ensure that both proteins return to the initial state during each measuring cycle. The output signals of the photomultiplier were amplified by a home-made current-voltage converter, and recorded by a National Instruments oscilloscope card. In total, 10 traces were averaged.

Light-excitation experiments were also done to measure the difference spectrum of the protein state formed after illuminating the samples with a CW laser beam for a longer period. The experimental setup was the same as in the absorption kinetics measurements, except that the measuring light was filtered by a gray-colored glass filter before reaching the sample. The measuring light was detected with a spectrograph equipped with an iStar gated ICCD detector (Andor Technology, United Kingdom). For the light-excitation of the bR film, a Nd:YAG laser (DHOM-M-532-500 mW) was used with an average power of 5 mW at 532 nm wavelength, while for PYP, 40 mW at 410 nm was applied. The samples were illuminated for 10 s before the start of the measurements. 10 spectra were averaged, and each measurement lasted for 1.30 s to complete.

Z-Scan Measurements

We utilized the Z-scan technique to characterize the nonlinear refractive index of dry bR and PYP films. Both CW and pulsed laser beams were employed to interrogate the samples. The setup used with CW illumination is shown in **Figure 1A**. The closed-aperture (CA) Z-scan traces were recorded by a PMT placed behind a circular aperture in the far-field, while the open-aperture (OA) traces were measured without an aperture in the laser beam. The light source was a 543-nm He-Ne laser delivering an average power of 0.75 mW. The power of the He-Ne laser beam was adjusted using a half-wave plate and a polarizer. A quarter-wave plate was placed between the polarizer and the sample to suppress back-reflection toward the laser. Accordingly, the laser beam incident on the samples was circularly polarized in the CW experiments.

The setup used with pulsed excitation was a modified version of the scheme described in detail elsewhere (Mero et al.,

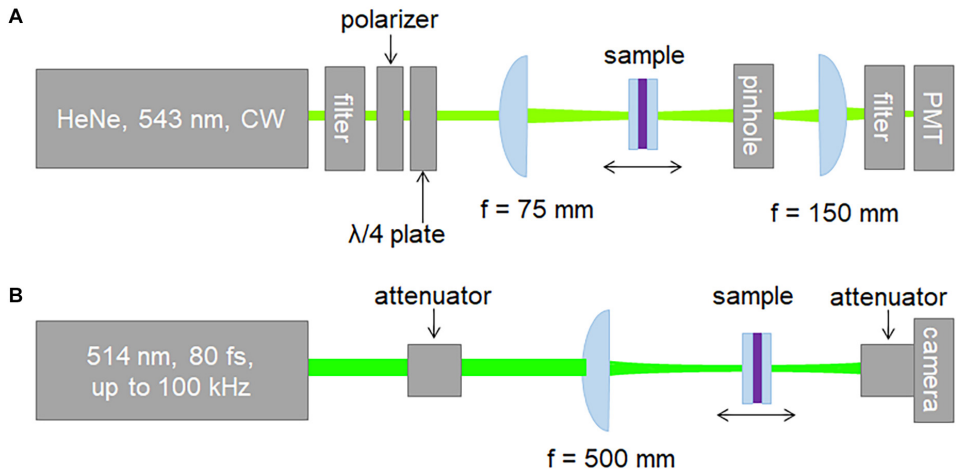

FIGURE 1 | Schematics of the experimental **(A)** CW and **(B)** pulsed-mode Z-scan setup.

2019) and is shown in **Figure 1B**. Briefly, the laser source was a commercial Yb:KGW laser oscillator-amplifier system delivering 1.028-μm pulses at adjustable repetition rates up to 100 kHz. The fundamental pulses were frequency-doubled yielding linearly polarized 82-fs, 514-nm pulses for probing the samples. The temporal intensity profile of the second-harmonic pulses was characterized using the self-diffraction frequency-resolved optical gating (SD-FROG) technique. To reduce the peak power, the pulses were attenuated by reflecting them off an uncoated wedge and sending them through neutral density filters. Further adjustment of the peak power was achieved using a half-wave plate and a thin film polarizer. An f = 500-mm singlet lens was used to focus the pulses on the sample leading to a Gaussian beam waist radius of 37 μm measured with a beam profiling camera. The minor astigmatism of the laser beam was eliminated by an appropriate tilt of the focusing lens. The M^2 values in the horizontal and vertical planes were measured to be ≤1.1. The pulsed Z-scan setup was also used to conduct CW Z-scan measurements at 405 nm, using a single longitudinal mode, TEM_{00}-spatial-mode, temperature-stabilized diode laser (not shown in **Figure 1B**). In this case, the focusing conditions were changed leading to a Gaussian beam waist radius of 36.6 μm. In contrast to the standard implementation of the Z-scan measurement scheme relying on single-pixel detectors, we employed a beam profiling camera. The open- and closed-aperture Z-scan traces were extracted from the measured beam profiles using image processing. Namely, the OA traces were determined by adding the signal counts of all pixels of the camera. The CA traces can be obtained by adding the signal counts in a predefined 2D pixel area centered on the center of gravity of the beam profile, which mimics a real hard aperture in the laser beam.

For samples with absorptive nonlinearities, the CA traces become distorted compared to those containing only refractive nonlinearities. Elimination of such distortive effects on the CA traces is often possible by dividing the CA traces by the OA traces. This procedure in turn allows the use of simple fit functions applicable to purely refractive cubic nonlinearities and a straightforward extraction of the nonlinear refractive index of the sample even in the presence of nonlinear absorption. However, we found that this procedure is not applicable for our protein samples exhibiting strong nonlinear absorption. Relying on 2D camera-based detection in our Z-scan measurements, we developed a novel procedure to remove the distortions in CA traces even in the presence of massive nonlinear absorption (see section "Procedure for Separating Refractive Nonlinearities in Closed-Aperture Z-Scan Traces"). This procedure is also useful to significantly reduce the noise in CA traces for samples exhibiting spatial inhomogeneity.

After the removal of nonlinear absorption effects, we fitted the CA traces with the expression valid for a cubic nonlinearity, negligible nonlinear absorption, thin-samples, and a peak, on-axis phase shifts below π, according to Sheik-Bahae et al. (1990):

$$T(x, \langle \Delta\phi_0 \rangle) = 1 - [4x\langle \Delta\phi_0 \rangle] / \left[(x^2+9)(x^2+1)\right]. \quad (1)$$

In Eq. 1, $\boldsymbol{x = \frac{z}{z_0}}$ is the sample position $\boldsymbol{z}$ normalized by the Rayleigh range $\boldsymbol{z_0}$, while $\langle \boldsymbol{\Delta\phi_0} \rangle$ is the time-averaged, peak, on-axis phase shift. The $\boldsymbol{n_2}$ values were calculated according to the formula,

$$n_2 \cong \langle \Delta\phi_0 \rangle (F\lambda w_0^2)/(L_{eff}P), \quad (2)$$

where $\boldsymbol{\lambda}$ is the center wavelength, $\boldsymbol{w_0}$ is the Gaussian beam waist, $\boldsymbol{L_{eff} = (1 - e^{-\alpha L})/\alpha}$ is the effective sample thickness, $\boldsymbol{\alpha}$ is the linear absorption coefficient and $\boldsymbol{L}$ is the sample thickness. $\boldsymbol{P}$ is the laser power inside the material. For temporally Gaussian pulses $\boldsymbol{P = E_P/1.064 \cdot \tau_P}$, or $\boldsymbol{P = E/T_{rep}}$, when peak or average power is considered, respectively. Here $\boldsymbol{\tau_P}$ is the pulse duration at full-width of half-maximum, and $\boldsymbol{T_{rep}}$ is the laser repetition period. The factor $\boldsymbol{F}$ is $\sqrt{2}/4$ or $1/4$ when the peak or average power aspect of the illumination is considered to be relevant, respectively. In Eq. 2, $\langle \boldsymbol{\Delta\phi_0} \rangle$ is the time-averaged peak on-axis phase shift obtained from fitting the expression in Eq. 1 to experimentally measured CA traces. We note that we tested the accuracy of the pulsed Z-scan setup by measuring the $\boldsymbol{n_2}$ value of a BK7 sample (an empty substrate without a protein film)

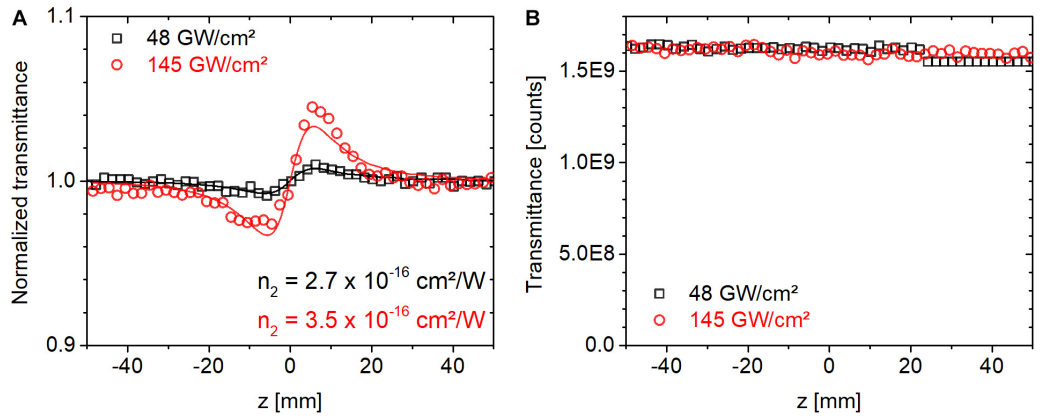

FIGURE 2 | (A) Closed and **(B)** open-aperture Z-scan traces measured for a BK7 substrate using 514-nm ultrafast laser pulses at a repetition rate of 1 kHz at peak on-axis intensities of 48 and 145 GW/cm^2.

and we obtained a value of $\sim 3 \times 10^{-16}$ cm^2/W at 514 nm in agreement with the literature (Adair et al., 1987; Nibbering et al., 1995; Boyd, 2003). **Figure 2** shows the corresponding closed and open-aperture traces. We note that the fluctuations in **Figure 2B**, characterized by a standard deviation of 0.6%, are indicative of camera noise, as BK7 exhibits negligible nonlinear absorption at our applied peak intensities. We found that camera noise had a larger impact on the open-aperture traces than the closed-aperture traces as a result of a drift of the baseline values, which strongly affects the total signal count from the entire CMOS chip.

RESULTS AND DISCUSSION

OWLS Measurements

High-resolution scans by the angle of incidence were carried out in the range of effective coupling, with the bare waveguide and, subsequently, waveguides coated with the biofilms. The recorded traces were fitted by Gaussians, in order to obtain the positions of the TE and TM modes. First, the actual refractive index and thickness values of the guiding layer were determined, then, using these data, the refractive index of the biofilms was obtained, making sure that the thickness of the adlayer was at least an order of magnitude larger than the penetration depth of the guided light (Ramsden, 1993). The measured and calculated values are summarized in **Table 1**. These refractive index data of the biofilms were used for the determination of their Δn and n_2 values from the Z-scan experiments. Adding glycerol to the protein solutions before drying them modifies the refractive indices of the thin film samples, which must be taken into account during the evaluation of the Z-scan data.

Absorption Kinetics Spectroscopy

The absorption kinetics data of both bR and PYP were measured at 33% ambient relative humidity. The photocycles of both bR and PYP are sensitive to environmental parameters, such as temperature or pH, and they are vastly different in the proteins' dry state at different relative humidity values. Therefore, we conducted all our measurements under the same relative humidity, for which we arbitrarily chose a value of 33% as stated in Materials and Methods. In the current study, glycerol was added to the protein suspensions before drying, which further modifies the photocycle, via changing the microviscosity of the medium (Beece et al., 1981), controlling water activity inside the films and enhancing hydrophobic interactions at the protein surface (Draheim and Cassim, 1985). To accurately determine the intermediates which the measured n_2 values belong to, and to see how the distinct intermediates form and decay in time, single-wavelength kinetics measurements were carried out on the proteins. The glycerol-doped films were of superior optical quality, showing reduced light scattering even for the membrane-bound bR, due to quasi-matching of its refractive index with that of bR-containing purple membranes (Ormos et al., 2002).

For bR, four wavelengths were chosen to monitor the absorption changes in time, to get a comprehensive picture of the protein's photocycle. These wavelengths were 575 nm to observe the changes corresponding to the initial state's transient bleaching, 410 nm that corresponds to the absorption maximum of the M intermediate; and additionally 500 nm and 620 nm to gain spectral information for both the red- and blue-shifted side of the initial state's maximum. We found that the dry bR-glycerol sample's photocycle had a rate-limiting step of ca. 1 s relaxation time, which is considerably shorter than the rate-limiting steps

TABLE 1 | The measured TM and TE positions and the calculated refractive index values of bR and PYP samples.

	TM position (degree)	TE position (degree)	Refractive index	Thickness
Bare waveguide 1	15.989	19.111	n_f = 1.788	205.45 nm
bR film	18.392	20.270	n_{bR} = 1.427	>5 μm
Bare waveguide 2	15.777	19.164	n_f = 1.799	195.26 nm
PYP film	18.672	20.595	n_{PYP} = 1.460	>5 μm

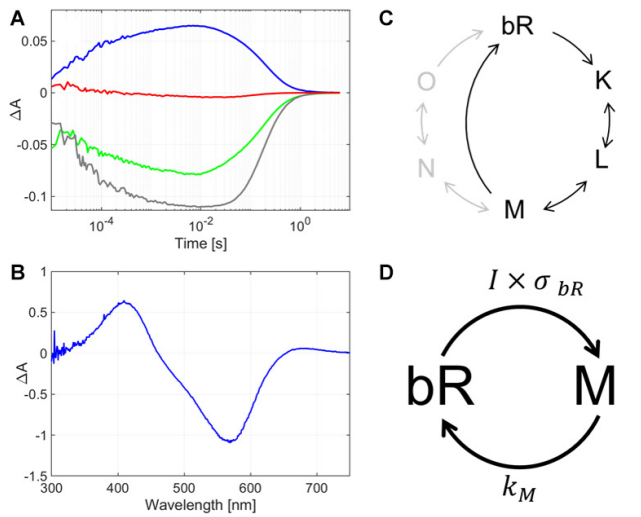

FIGURE 3 | (A) Absorption kinetics and **(B)** intermediate accumulation measurements taken on a glycerol-containing bR film. In panel **(A)**, the lines represent the change of absorption after light-excitation measured at 410 nm (blue line), 500 nm (green line), 575 nm (gray line) and at 620 nm (red line). In panel **(B)**, the difference absorption spectrum is shown, as measured after a 10-s excitation by subsequent laser pulses of a repetition rate of 2 Hz. **(C)** Schematic diagram of the full photocycle of a glycerol-containing bR film (black) and bR in water (gray). **(D)** Simplified diagram of the photocycle of the glycerol-containing bR film showing only the states relevant for our pulsed Z-scan measurements. *I* is the (average) light intensity exciting the sample, σ_{bR} is the absorption cross section of the bR molecule in the initial state, at the wavelength of excitation, and k_M is the rate constant of the M-decay.

in the dry bR film's photocycle (Tóth-Boconádi et al., 2011) (**Figure 3A**). The most probable reason for this phenomenon is that the glycerol-mediated wetting effect on the bR-conforming purple membranes dominates over viscosity effects, which were supposed to decelerate the decay of M intermediate (Beece et al., 1981). By also measuring the absorption difference spectrum after 10 s of CW excitation, we found that the majority of the bR molecules accumulate in the M intermediate state (**Figure 3B**). Compared to the flash duration and the interflash intervals of the Z-scan measurements, the decay of the photocycle is orders of magnitude slower, even at the lowest repetition rate. At 10 ms after excitation – which corresponds to the interflash interval at the lowest repetition rate in our Z-scan measurements –, the bR molecules are accumulated in the M intermediate state. Since the absorption cross section of bR in the M intermediate state is negligible at the wavelength of excitation (514 nm), and in dry samples the other long-living intermediates of the normal bR-photocycle (N and O) do not accumulate in considerable amounts (Tóth-Boconádi et al., 2011), the subsequent flashes hitting the sample will initiate photoreactions of the remaining ground-state molecules only. Hence, the exciting laser-flash train in the pulsed Z-scan experiments can be considered a quasi-CW illumination, while the sample can be considered to be in an average-intensity dependent dynamic equilibrium mixture of bR molecules in M intermediate and the initial state. **Figure 3C** shows the schematic representation of the photocycle of bR, where the most relevant part (marked with black color) corresponds to the glycerol-containing bR film. For the higher repetition rate measurements, hence the exciting laser-flash train in the pulsed Z-scan experiments can be considered quasi-CW illumination, while the sample can be considered to be in an average-intensity dependent dynamic equilibrium mixture of bR molecules in the M intermediate and the initial state. The corresponding simplified photocycle relevant for our Z-scan measurements, too, is illustrated in **Figure 3D**, indicating only the rate-limiting reactions. Here, $\boldsymbol{I}$ is the (average) light intensity exciting the sample, and $\boldsymbol{\sigma_{bR}}$ is the absorption cross section of the bR molecule in the initial state, at the wavelength of excitation. The product of the two, i.e., the probability of excitation, $\boldsymbol{I{\cdot}\sigma_{bR}}$, represents a virtual rate constant driving out the bR population from the initial state. Since the other transitions of the photocycle are much faster, practically only the M intermediate accumulates under (quasi-) steady state conditions, at an equilibrium concentration of $[\boldsymbol{bR}]_0 I\sigma_{bR}/(\boldsymbol{k_m} + I{\cdot}\sigma_{bR})$, where $\boldsymbol{[bR_0]}$ is the concentration of all the bR molecules (including the ones in the M and in the initial states), and $\boldsymbol{k_M}$ is the rate constant of the M-decay. The difference spectrum of such a sample is shown in **Figure 3B**, and the calculated $\boldsymbol{\Delta n}$ values are related to this steady state.

Similarly to bR, the wavelengths chosen for measuring the PYP's absorption kinetics represent the concentration development of different intermediates of the photocycle. The photocycle was monitored at three selected wavelengths: 430 nm, which is slightly blue-shifted from the initial state's maximum in order to limit the backscattering effect from the exciting light, while still gaining information about the initial state's concentration changes; 360 nm, to monitor the pB intermediate, and 470 nm for the pR intermediates. The rate-limiting step of the PYP-glycerol film's photocycle was found to be ca. 6 s (**Figure 4A**). Note that in PYP films devoid of glycerol, the photocycle does not take place at such low humidity, yet in our current measurements there is a clear indication of spectral changes in the wavelength range of the pR and pB intermediates, indicating a photocycle still being present in the glycerol-doped films (**Figure 4C**). Based on the glycerol concentration, the water activity in the sample was estimated to be the same as at 80% relative humidity without glycerol (Wheeler et al., 2012). Nevertheless, the photocycle is significantly slower than without glycerol (Krekic et al., 2019), which may be attributed to viscosity effects (Beece et al., 1981) rather than water-structure-mediated kosmotropic effects (Násztor et al., 2016), which should destabilize open conformations, such as pB, hence they should accelerate its decay (Kamikubo et al., 2007; Khoroshyy et al., 2013). Note that PYP is a water-soluble protein, unlike the membrane-protein, bR, so it is more exposed to solvent viscosity effects. The accumulation measurements (**Figure 4B**) are indicating a majority of the protein present in the pB state after excitation, hence, similarly to bR, we can suppose PYP is driven to a steady-state of pB and initial states, as indicated in **Figure 4D**, where their ratio is adjusted by the average exciting light intensity applied during pulsed Z-scan measurements (see similar argumentation above, for bR).

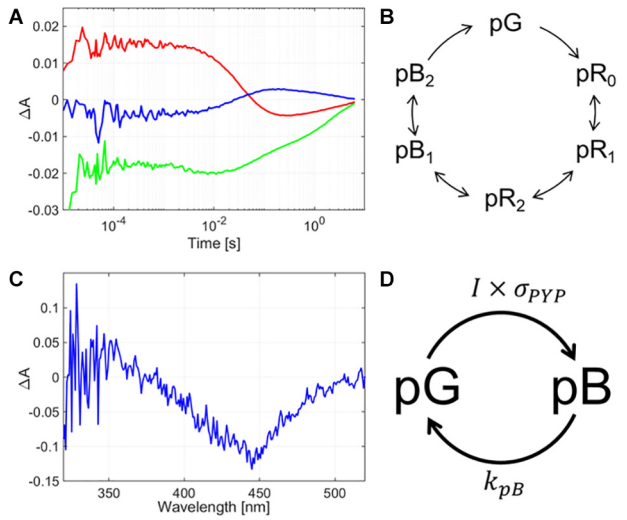

FIGURE 4 | (A) Absorption kinetics measurements and **(B)** intermediate accumulation measurements taken on a glycerol-containing PYP film. In subfigure **(A)**, the blue line represents the absorption spectrum measured at 360 nm, the green line at 430 nm, and the red line at 470 nm. In panel **(B)**, the difference absorption spectrum is shown, as measured after a 10-s excitation of the sample by a CW laser of 410 nm and 40 mW. **(C)** Schematic diagram of the full photocycle of a glycerol-containing PYP film. **(D)** Simplified diagram of the photocycle of the glycerol-containing PYP film showing only the states relevant for our pulsed Z-scan measurements. *I* is the (average) light intensity exciting the sample, σ_{PYP} is the absorption cross section of the PYP molecule in the initial state, at the wavelength of excitation, and k_{PB} is the rate constant of the pB-decay.

Z-Scan Measurements

Procedure for Separating Refractive Nonlinearities in Closed-Aperture Z-Scan Traces

Saturable absorption can drastically alter CA Z-scan traces even if the laser intensity does not significantly exceed the saturation intensity (cf. **Figure 5A**). Under such circumstances, the standard approach of dividing the CA trace by the corresponding OA trace is not sufficient to eliminate the effect of nonlinear absorption on the CA trace (cf. **Figure 5B**). Enabled by the use of a 2D camera in our Z-scan measurements, such effects can be removed using the following procedure. First, a 2D Gaussian spatial distribution is fitted on the measured beam profiles at each z position, and the position dependent beam waists, $w_x(z)$ and $w_y(z)$, and amplitudes, $A(z)$, are extracted. Then, the amplitudes are corrected assuming that the background-subtracted total signal count (E, energy) remains constant, i.e., independent of z. This constant is defined at a z position where nonlinear absorption is negligible,

$$E = A(|z| \gg z_0)\,\frac{w_x(|z| \gg z_0)\,w_y(|z| \gg z_0)\,\pi}{2} = constant. \tag{3}$$

The corrected amplitudes, $A'(z)$, constitute the corrected CA trace with an infinitesimally small aperture (cf. **Figure 5C**). In addition to separating nonlinear absorption effects from the CA traces, this correction procedure also reduces the fluctuations due to, e.g., sample inhomogeneity. All CA traces shown below are corrected traces based on this procedure.

Nonlinear Refractive Index of bR

Three laser repetition rates were used at 514 nm, 100 Hz, 1 kHz, and 100 kHz, to investigate the role of thermal effects and possible variation in the population distribution among various states in the photocycle of bR. CW measurements were also conducted at comparable intensities at 543 nm. Since the photocycle of bR is much longer than the laser repetition period (see section "Absorption Kinetics Spectroscopy"), the material is expected to be in a steady state, where a significant fraction of the molecules is in the M intermediate state (cf. **Figure 3D**). Also, the nonlinear response is expected to be driven by the average intensity rather than the peak intensity. In agreement, as shown in **Figure 6A**, we found that the magnitude of nonlinear refraction at an average intensity of 0.042 W/cm^2 was the same at a repetition rate of 100 Hz and 1 kHz despite an order of magnitude difference in peak intensity. At higher intensities, we found this to be still approximately true. The CA traces shown in **Figure 6B** were recorded at average intensities of 0.96 and 1.57 W/cm^2 at 100 Hz

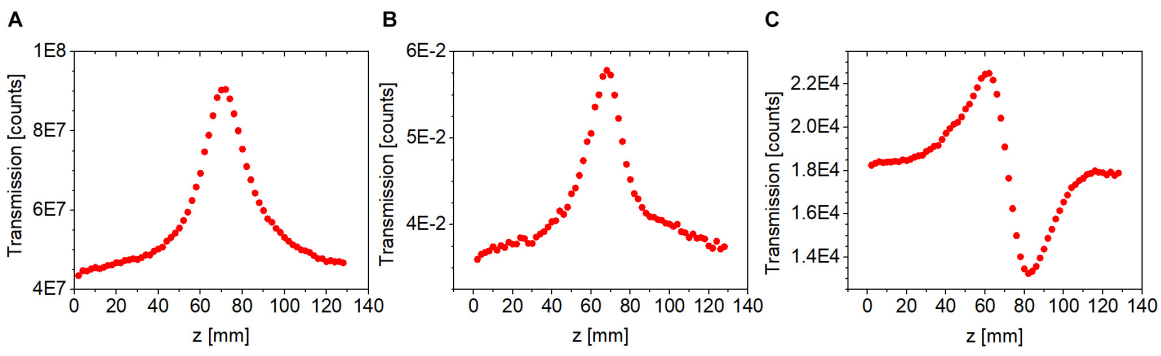

FIGURE 5 | Closed-aperture Z-scan traces measured using fs laser pulses at 514 nm for a bR sample at an average peak intensity of 0.13 W/cm^2. **(A)** Uncorrected closed-aperture trace. **(B)** Corrected closed-aperture trace obtained by dividing the uncorrected closed-aperture trace (cf. **A**) by the corresponding open-aperture trace. **(C)** Corrected closed-aperture trace obtained by applying our novel method described in Section "Procedure for Separating Refractive Nonlinearities in Closed-Aperture Z-Scan Traces."

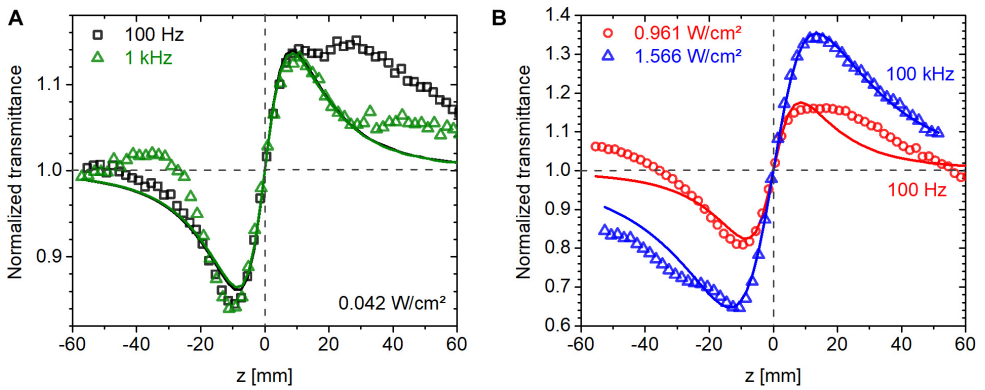

FIGURE 6 | Closed-aperture Z-scan traces measured on bR using fs laser pulses at 514 nm at average intensities of **(A)** 0.042 W/cm^2 and **(B)** around 1 W/cm^2. The symbols are measured data points obtained at various laser repetition rates, and the lines are fitted traces based on Eq. 1.

and 100 kHz, respectively. The ratio of ΔT_{P-V} (the difference between normalized peak and valley transmittance) of the 100-Hz and 100-kHz traces is 0.52, while the average intensity ratio is 0.61, i.e., only 18% higher than expected. In contrast, the ratio of peak intensities is 610.

To explore the saturable absorption behavior, we recorded open and closed-aperture Z-scan traces as a function of average intensity in the range of 0.04 and 0.42 W/cm^2 at a laser repetition rate of 1 kHz. The sample was 200 μm thick with an OD of 0.35 at 514 nm. Based on (Gu et al., 2006), we modeled the OA traces by assuming saturable absorption of a homogeneously broadened resonant transition characterized by an absorption coefficient,

$$\alpha(I) = \frac{\alpha_0}{1 + \frac{I}{I_s}}, \quad (4)$$

where $\boldsymbol{\alpha_0}$ is the linear absorption coefficient, and $\boldsymbol{I_s}$ is the saturation intensity. The results of the modeling are shown in **Figure 7A**. At the two lowest intensities, the fit is relatively good but it gets gradually worse at higher intensities. The extracted saturation intensities are shown in **Figure 7B** with a value approximately 0.1 W/cm^2 at an excitation intensity of 0.04 W/cm^2. The estimated error for the value of $\boldsymbol{I_s}$ at the lowest average intensity is ±20%, which includes uncertainty in the measured value of sample absorbance, thickness, and camera signal. The corresponding CA traces are shown in **Figure 7C**. At the two lowest intensities, the peak-to-valley distances are approximately the same with a value of $\sim\boldsymbol{2z_0}$, while at the highest intensity it is significantly larger. According to the Z-scan theory with cubic refractive nonlinearity (Sheik-Bahae et al., 1990), the peak-to-valley distance is $\sim\boldsymbol{1.7z_0}$ and it remains nearly constant at higher intensities with a small gradual decrease with increasing intensity. Therefore, at excitation intensities below 0.1 W/cm^2, we consider Eq. 1 a satisfactory model of nonlinear refraction of our bR samples.

In **Figures 8A,B**, the nonlinear refractive index, $\boldsymbol{n_2}$, is shown in a broad range of intensities. Although, we do not expect extracted $\boldsymbol{n_2}$ values to be consistent with the approximations implied by Eq. 1, our goal was to compare our measured $\boldsymbol{n_2}$ values with those in the literature and to provide for us benchmark values for the investigation of PYP (see section "Nonlinear Refractive Index of PYP"). Our measured $\boldsymbol{n_2}$ values in the average intensity range of 10^{-2} to 10^2 W/cm^2 fall in the range of 10^{-1} to 10^{-5} cm^2/W (**Figure 8A**) in agreement with the literature on bR excited in the green spectral range by CW lasers (Song et al., 1993; Kir'Yanov et al., 2000; Sifuentes et al., 2002; Banyal and Raghavendra Prasad, 2007). The increasing gap with increasing average intensity between the $\boldsymbol{n_2}$ values measured with a CW and a pulsed laser may suggest that further processes, other than a simple cubic nonlinearity are at play, such as thermal effects, thermally induced conformational changes, and refractive or absorptive nonlinearities of higher order. Our $\boldsymbol{n_2}$ data plotted as a function of peak intensity are also consistent with the literature on both bR and different retinal derivatives excited by pulsed lasers (Bezerra et al., 1997; Rakovich et al., 2013). In our peak intensity range of 10^8 to 10^{11} W/cm^2, the $\boldsymbol{n_2}$ values are in the range of 10^{-11} – 10^{-14} cm^2/W. These $\boldsymbol{n_2}$ values are many orders of magnitude smaller than the values obtained using CW lasers, which is typically not noted or discussed in the literature. As the average intensity is the main driving force behind the refractive nonlinearities of bR even at relatively low repetition rates (down to 100 Hz in our studies), we think that it is more relevant to determine and quote $\boldsymbol{n_2}$ values based on average intensities even for pulsed lasers. Interestingly, our $\boldsymbol{n_2}$ data closely follow an intensity dependence characterized by $\boldsymbol{I^{-1.075}}$, where $\boldsymbol{I}$ is the peak intensity (cf. solid line in **Figure 8B**). Importantly, the $\boldsymbol{n_2}$ data measured by our CW laser are also on this trend line. Accordingly, the corresponding change in refractive index, $\boldsymbol{\Delta n = n_2 I}$, in the whole intensity range is approximately constant with a value of 0.0009 to 0.0011 at 514 nm and around 0.0066 at 543 nm. This $\boldsymbol{\Delta n}$ value is in agreement with the refractive index change corresponding to the transition from the bR initial state to the M state (Song et al., 1993; Ormos et al., 2002; Fábián et al., 2015).

The saturable absorption behavior is also driven by average intensity rather than peak intensity. **Figure 8C** shows the relative change in the normalized transmission at $\boldsymbol{z = 0}$ as a function of average intensity approximately following the saturation behavior of a homogeneously broadened transition (solid line).

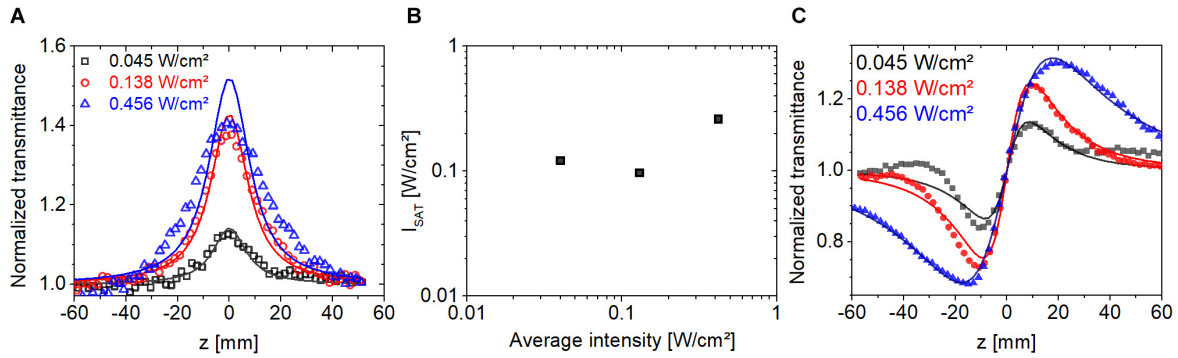

FIGURE 7 | (A) Open-aperture Z-scan traces measured on bR using fs laser pulses at 514 nm at three excitation intensities at a repetition rate of 1 kHz. **(B)** Saturation intensities extracted from the open-aperture traces in panel **(A)**. **(C)** Closed-aperture Z-scan traces obtained at 514 nm excitation corresponding to the curves in panel **(A)**. The symbols are the measured data points, and lines show the fitted traces.

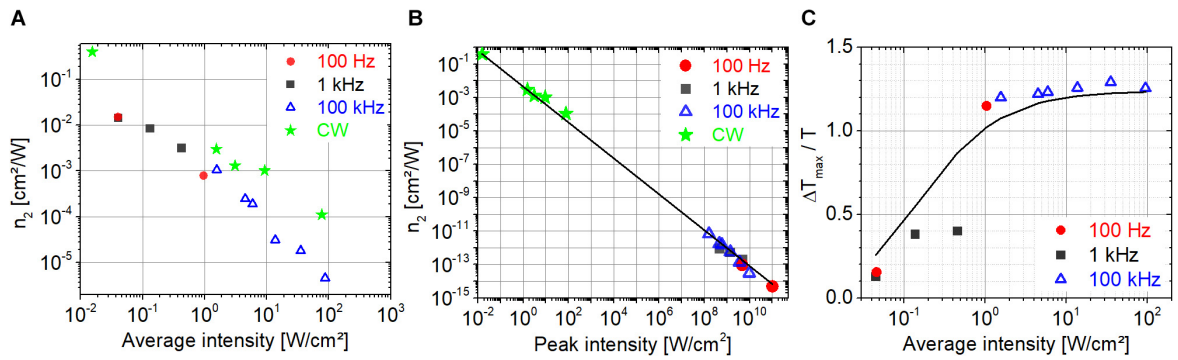

FIGURE 8 | Nonlinear refractive index of bR at 514 nm as a function of **(A)** average and **(B)** peak intensity. **(C)** The relative change in transmission as a function of average intensity. The solid line is a fit of a saturable absorption model on all measured data.

Obviously, the data do not follow a single trend when plotted as a function of peak intensity (not shown).

Nonlinear Refractive Index of PYP

In contrast to bR, excitation of the initial state of PYP (pG) at 514 nm is expected to lead to negligible linear absorption (see **Figure 4**). Therefore, the photocycle is not expected to be triggered at low excitation intensities. If the photocycle is initiated at laser repetition rates $\geq$1 kHz, it would lead to the accumulation of the pR intermediate state. Once the pR intermediate is produced, all the subsequent intermediates and also pR will linearly absorb at 514 nm.

We recorded Z-scan traces using pulsed-excitation at a repetition rate of 1 kHz and 100 kHz at 514 nm. **Figures 9A,B** show the CA traces measured at 1 kHz and 100 kHz, respectively, in the average intensity range of 10^{-1} and 10^{1} W/cm^2. Similarly to bR, the nonlinear response of PYP is also driven by the average intensity rather that peak intensity. In contrast to bR, the peak-to-valley configuration in the CA traces indicates a defocusing nonlinearity (i.e., negative $\boldsymbol{n_2}$). Note that the negative sign is in concert with the negative $\boldsymbol{\Delta n}$ measured at 633 nm in Krekic et al. (2019) and by Lee et al. (2018) between 470 nm and 570 nm. **Figure 9C** shows the CA traces measured at an average intensity of ~4.6 W/cm^2 at 1 kHz and 100 kHz. Despite of a factor of 100 larger peak intensity at 1 kHz than at 100 kHz, the $\boldsymbol{\Delta T_{P-V}}$ values are within ~30% suggesting that the excitation mechanism is not two-photon absorption but possibly a weak linear absorption process. In agreement, the OA traces show no sign of nonlinear absorption (cf. **Figure 9C** open symbols). With linear absorption, the photocycle can be started, and we expect the related refractive index changes to be larger than possible thermo-optical contributions.

The nonlinear refractive index of PYP extracted from the CA traces in **Figure 9** is shown in **Figures 10A,B**. The absolute value of our measured $\boldsymbol{n_2}$ data is also inversely proportional to the average intensity as in the case of bR (cf. **Figure 8A**), and these values fall in the range of 10^{-3} to 10^{-4} cm^2/W (**Figure 10A**) in the average intensity range of 0.1 to 1 W/cm^2. To the best of our knowledge, these are the first $\boldsymbol{n_2}$ values provided for PYP. If one extracts the $\boldsymbol{n_2}$ values from the $\boldsymbol{\Delta n}$ data provided in Vanhanen et al. (1998), the range of -2×10^{-2} to -9×10^{-3} cm^2/W is obtained for an average intensity between 3×10^{-3} and 2×10^{-2} W/cm^2 at 475-nm CW laser excitation. When plotted as a function of peak intensity, the $\boldsymbol{n_2}$ data points follow different power laws at different laser repetition rates (**Figure 10B**). The solid line was obtained by fitting the nonlinear refractive index

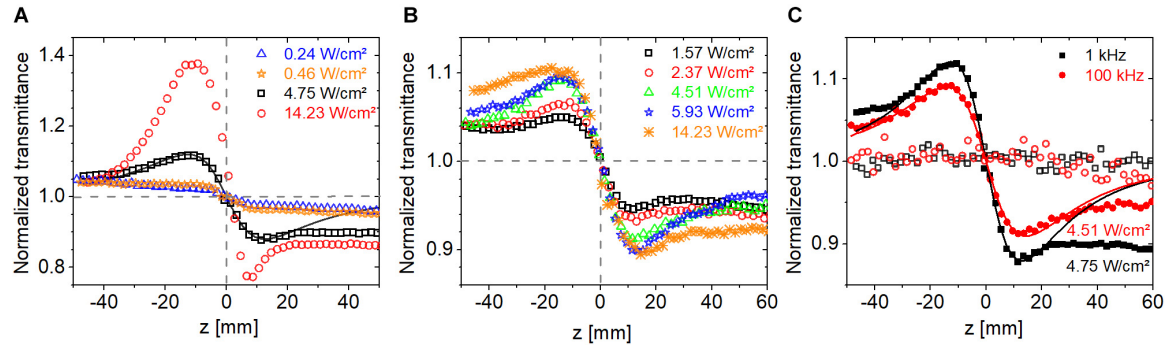

FIGURE 9 | Closed-aperture Z-scan traces measured on PYP using fs laser pulses at 514 nm at different excitation intensities at a repetition rate of **(A)** 1 kHz and **(B)** 100 kHz. **(C)** Comparison of the closed-aperture traces (filled symbols) and the open-aperture traces (hollow symbols) at a repetition rate of 1 kHz and 100 kHz, respectively, at ~4.6-W/cm^2 excitation intensity.

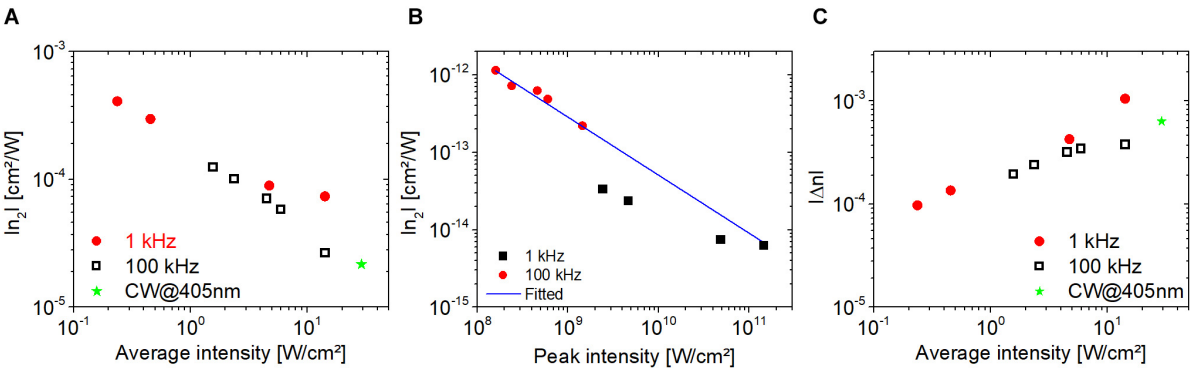

FIGURE 10 | Absolute value of the nonlinear refractive index of PYP at 514 nm as a function of **(A)** average and **(B)** peak intensity. **(C)** The absolute value of the change in the refractive index as a function of average intensity.

data points at 100 kHz. Clearly, the 1 kHz data points do not follow this trend. At both repetition rates, the dependence as a function of peak intensity is weaker than in the case of bR. The magnitude of the n_2 values of PYP in the peak intensity range of 10^8–10^{11} W/cm^2 are between 10^{-12} and 10^{-14} cm^2/W, which is a factor of 10 smaller range than that obtained with bR. Accordingly, the magnitude of the Δn values at the two repetition rates is not constant, but also increases as a function of average intensity, following a weak power law (cf. **Figure 10C**). In general, the Δn values obtained at a particular repetition rate and average intensity were of the same order of magnitude for both bR and PYP. However, in contrast to PYP, the dependence of the Δn values of bR as a function of average intensity is not monotonous and can be considered constant centered at 9×10^{-4} in a full range of 5×10^{-4} to 2×10^{-3} (not shown). The range of Δn values we obtained for PYP is in good agreement with the range obtained with 475-nm CW excitation, where the photocycle can unambiguously be initiated (Vanhanen et al., 1998).

Nonlinear Refraction as a Result of the Photocycle vs. Thermo-Optic Effects

Dealing with protein-containing samples, one should always consider the possibility of thermo-optic effects, reported for light-harvesting proteins, such as LHC complexes (Garab et al., 2002) or bR, too (Dancsházy et al., 1999). Such effects were shown to have a regulatory role in photosynthesis (Garab et al., 2002). In bR, it was demonstrated that high-energy flashes in the main absorption band of the protein can lead to permanent photobleaching of the sample. The effects were interpreted as a consequence of the transient increase of the temperature in the vicinity of the absorbing chromophore by more than 10 degrees, giving rise to temperature-induced conformational changes in the proteins. The dissipation of the heat packet was estimated to take place in the nanosecond time regime, and the effects showed a strongly nonlinear dependence on the peak intensity of the flash, attributed to a threshold phenomenon (Dancsházy et al., 1999). In the present measurements, however, we do not see such an effect as a function of peak intensity (this is why both the Δn and the n_2 dependences measured at different peak intensities could be reasonably unified to common curves on the time-averaged intensity scale), neither experienced we any photobleaching of the samples. Note, that the pulse energies were also much lower in our measurements than in Dancsházy et al. (1999). Of course, an effect of global heating of the sample at high average exciting energies cannot be excluded here, either, supporting our assumption that the

reliable values for these parameters are those in the low average power regime.

CONCLUSION

Our glycerol-doped thin films proved to be appropriate for optical applications: they allow to achieve a high protein concentration and optical quality, at the same time control the necessary water activity for the proteins to undergo a photocycle. They also show proper stability. A comprehensive study of the NLO properties of the protein-containing films was performed, by characterizing their absorption kinetics properties from the 10 μs to the 10 s time scale, and determining their linear and nonlinear refractive indices (n_0, Δn, and n_2 values).

The novel evaluation procedure we used for the Z-scan experiments could properly account for saturation effects that allows the determination of n_2 values for a Kerr material with much higher precision and reliability than before. At low average intensities, i.e., <0.1 W/cm^2, our obtained Δn values, $\sim 10^{-4}$ for PYP and $\sim 10^{-3}$ for bR, are comparable to those of the best solid-state materials. Importantly, our n_2 values, 4×10^{-4} cm^2/W for PYP and 10^{-2} cm^2/W for bR, are several orders of magnitude higher than those reported earlier for inorganic NLO materials (Adair et al., 1989; Kulagin et al., 2003; Eggleton et al., 2011), highlighting the potential utilization of these chromoproteins in special applications of photonics, where high Δn and n_2 are required. Some promising experiments have already been carried out in the fields of dynamic polarization holography (Hampp et al., 1990; Burykin et al., 2011), image filtering (Castillo et al., 2001), all-optical switching (Ormos et al., 2002; Topolancik and Vollmer, 2006; Fábián et al., 2010, 2011; Roy et al., 2010; Korposh et al., 2018) but a plethora of new applications can be envisaged in all-optical signal processing, utilizing the ultrafast transitions of the photocycle (Fábián et al., 2011), e.g., in multi-wave mixing, nonlinear mode-coupling in fibers (Xu et al., 2015), and wavelength multiplexing-demultiplexing in IO devices.

DATA AVAILABILITY STATEMENT

The raw data supporting the conclusions of this article will be made available by the authors, without undue reservation.

AUTHOR CONTRIBUTIONS

SK, ZH, MM, LZ, and AD created the research idea. ZH and MM designed the pulsed Z-scan measurements. SK, SV, LZ, and AD designed and conducted the CW Z-scan measurements, the OWLS, and kinetic experiments. TZ and ZG prepared the PYP protein while SK prepared all the thin protein film samples. The OWLS and kinetic data were analyzed by SK and AD, while the Z-scan measurements were analyzed and fitted by ZH and MM. SK, MM, ZH, and AD wrote the manuscript. All authors discussed and revised the article.

FUNDING

This study was funded by Deutsche Forschungsgemeinschaft (DFG) (GSC 1013 SALSA), National Research and Development Office, Hungary (NKFI-1 K-124922), Economic Development and Innovation Operative Programme of Hungary (GINOP-2.3.2-15-2016-00001), and German Academic Exchange Service (DAAD).

ACKNOWLEDGMENTS

ZH acknowledges funding by a Julia Lermontova Fellowship from DFG, No. GSC 1013 SALSA. We acknowledge support by the German Research Foundation (DFG) and the Open Access Publication Fund of Humboldt-Universität zu Berlin. SK acknowledges funding by the University of Szeged and the German Academic Exchange Service (DAAD). We are indebted to Prof. Hinorari Kamikubo for kindly providing the plasmid for PYP expression, and to Dr. Laszlo Fabian for helpful discussions.

REFERENCES

Adair, R., Chase, L., and Payne, S. A. (1989). Nonlinear refractive index of optical crystals. *Phys. Rev. B* 39:3337. doi: 10.1103/PhysRevB.39.3337

Adair, R., Chase, L. L., and Payne, S. A. (1987). Nonlinear refractive-index measurements of glasses using three-wave frequency mixing. *J. Optic. Soc. Am. B* 4, 875–881. doi: 10.1364/JOSAB.4.000875

Aranda, F. J., Rao, D. V., Wong, C. L., Zhou, P., Chen, Z., Akkara, J. A., et al. (1995). Nonlinear optical interactions in bacteriorhodopsin using Z-scan. *Optic. Rev.* 2, 204–206. doi: 10.1007/s10043-995-0204-x

Balashov, S. P. (1995). Photoreactions of the Photointermediates of Bacteriorhodopsin. *Israel J. Chem.* 35, 415–428. doi: 10.1002/ijch.19950 0040

Banyal, R. K., and Raghavendra Prasad, B. (2007). Measurements of photoinduced refractive index changes in bacteriorhodopsin films. *Pramana* 68, 435–441. doi: 10.1007/s12043-007-0046-0

Beece, D., Bowne, S. F., Czégé, J., Eisenstein, L., Frauenfelder, H., Good, D., et al. (1981). The effect of viscosity on the photocycle of bacteriorhodopsin. *Photochem. Photobiol.* 33, 517–522. doi: 10.1111/j.1751-1097.1981.tb05 454.x

Bezerra, A. G., Gomes, A. S. L., de Melo, C. P., and de Araújo, C. B. (1997). Z-scan measurements of the nonlinear refraction in retinal derivatives. *Chem. Phys. Lett.* 276, 445–449. doi: 10.1016/S0009-2614(97)00841-5

Boyd, R. W. (2003). "Chapter 4 - The intensity-dependent refractive index," in *Nonlinear Optics*, 2nd Edn, ed. R. W. Boyd (San Diego: Academic Press), 189–235. doi: 10.1016/b978-012121682-5/50005-5

Burykin, N., Stepanchikov, D., Dyukova, T., Savchuk, A., Balashov, S., and Korchemskaya, E. (2011). Real-time optical information processing through the use of low-saturable absorption in bacteriorhodopsin films. *Mol. Cryst. Liquid Cryst.* 535, 140–147. doi: 10.1080/15421406.2011.537966

Castillo, M. I., Sanchez-de-la-Llave, D., García, R. R., Olivos-Perez, L., Gonzalez, L. A., and Rodriguez-Ortiz, M. (2001). Real-time self-induced nonlinear optical Zernike-type filter in a bacteriorhodopsin film. *Optic. Eng. Bellingham Intern. Soc. Optic. Eng.* 40, 2367–2368. doi: 10.1117/1.1412425

Chai, Z., Hu, X., Wang, F., Niu, X., Xie, J., and Gong, Q. (2017). Ultrafast all-optical switching. *Adv. Optic. Mater.* 5:1600665. doi: 10.1002/adom.201600665

Clays, K., Van Elshocht, S., Chi, M., Lepoudre, E., and Persoons, A. (2001). Bacteriorhodopsin: a natural, efficient (nonlinear) photonic crystal. *JOSA B* 18, 1474–1482. doi: 10.1364/JOSAB.18.001474

Colonna, A., Groma, G. I., and Vos, M. H. (2005). Retinal isomerization dynamics in dry bacteriorhodopsin films. *Chem. Phys. Lett.* 415, 69–73. doi: 10.1016/j.cplett.2005.08.132

Dancsházy, Z., Tokaji, Z., and Dér, A. (1999). Bleaching of bacteriorhodopsin by continuous light. *FEBS Lett.* 450, 154–157. doi: 10.1016/S0014-5793(99)00487-1

Dér, A., and Keszthelyi, L. (2001). *Bioelectronic Applications of Photochromic Pigments*. Amsterdam: IOS Press.

Dini, D., Calvete, M. J. F., and Hanack, M. (2016). Nonlinear optical materials for the smart filtering of optical radiation. *Chem. Rev.* 116:13043. doi: 10.1021/acs.chemrev.6b00033

Draheim, J. E., and Cassim, J. Y. (1985). Effects of polyhydric alcohols on the conformational stability of the purple membrane. *J. Membr. Biol.* 86, 229–238. doi: 10.1007/BF01870602

Eggleton, B. J., Luther-Davies, B., and Richardson, K. (2011). Chalcogenide photonics. *Nat. Photon.* 5:141. doi: 10.1038/nphoton.2011.309

Fábián, L., Heiner, Z., Mero, M., Kiss, M., Wolff, E. K., Ormos, P., et al. (2011). Protein-based ultrafast photonic switching. *Optics Exp.* 19, 18861–18870. doi: 10.1364/OE.19.018861

Fábián, L., Mathesz, A., and Dér, A. (2015). New trends in biophotonics. *Acta Biol. Szegediensis* 59(Suppl. 2), 189–202.

Fábián, L., Wolff, E. K., Oroszi, L., Ormos, P., and Dér, A. (2010). Fast integrated optical switching by the protein bacteriorhodopsin. *Appl. Phys. Lett.* 97:023305. doi: 10.1063/1.3462940

Fitter, J., Lechner, R. E., and Dencher, N. A. (1999). Interactions of hydration water and biological membranes studied by neutron scattering. *J. Phys. Chem. B* 103, 8036–8050. doi: 10.1021/jp9912410

Garab, G., Cseh, Z., Kovács, L., Rajagopal, S., Várkonyi, Z., Wentworth, M., et al. (2002). Light-induced trimer to monomer transition in the main light-harvesting antenna complex of plants: thermo-optic mechanism. *Biochemistry* 41, 15121–15129. doi: 10.1021/bi026157g

Gu, B., Fan, Y.-X., Wang, J., Chen, J., Ding, J., Wang, H.-T., et al. (2006). Characterization of saturable absorbers using an open-aperture Gaussian-beam Z scan. *Phys. Rev. A* 73:065803. doi: 10.1103/PhysRevA.73.065803

Hales, J. M., Matichak, J., Barlow, S., Ohira, S., Yesudas, K., Brédas, J.-L., et al. (2010). Design of polymethine dyes with large third-order optical nonlinearities and loss figures of merit. *Science* 327, 1485–1488. doi: 10.1126/science.1185117

Hampp, N., Bräuchle, C., and Oesterhelt, D. (1990). Bacteriorhodopsin wildtype and variant aspartate-96 → aspargine as reversible holographic media. *Biophys. J.* 58, 83–93. doi: 10.1016/S0006-3495(90)82355-9

Hampp, N., and Juchem, T. (2001). Fringemaker-the first technical system based on bacteriorhodopsin. *Nato Sci. Ser. Sub. Ser. I Life Behav. Sci.* 335, 44–53.

Haque, S. A., and Nelson, J. (2010). Toward organic all-optical switching. *Science* 327, 1466–1467. doi: 10.1126/science.1188291

Heiner, Z., and Osvay, K. (2009). Refractive index of dark-adapted bacteriorhodopsin and tris (hydroxymethyl) aminomethane buffer between 390 and 880 nm. *Appl. Optics* 48, 4610–4615. doi: 10.1364/AO.48.004610

Hu, H.-J., Liu, C.-C., Zang, J.-Q., Zhu, C.-Y., and Luo, D.-B. (2017). Study the nonlinear optical property of pull/push type azo dye-doped polymer using 633 nm He-Ne laser. *J. Nonline. Optic. Phys. Mater.* 26:1750008. doi: 10.1142/S0218863517500084

Jeganathan, C., Sabari Girisun, T. C., Rao, S. V., and Thamaraiselvi, K. (2017). Variable ultrafast optical nonlinearity in bacteriorhodopsin achieved through simple chemical treatment. *J. Mater. Sci.* 52, 6866–6878. doi: 10.1007/s10853-017-0924-x

Joshi, C. P., Borucki, B., Otto, H., Meyer, T. E., Cusanovich, M. A., and Heyn, M. P. (2005). Photoreversal kinetics of the I1 and I2 intermediates in the photocycle of photoactive yellow protein by double flash experiments with variable time delay. *Biochemistry* 44, 656–665. doi: 10.1021/bi0481141

Kamikubo, H., Shimizu, N., Harigai, M., Yamazaki, Y., Imamoto, Y., and Kataoka, M. (2007). Characterization of the solution structure of the M intermediate of photoactive yellow protein using high-angle solution X-Ray scattering. *Biophys. J.* 92, 3633–3642. doi: 10.1529/biophysj.106.097287

Khoroshyy, P., Dér, A., and Zimányi, L. (2013). Effect of Hofmeister cosolutes on the photocycle of photoactive yellow protein at moderately alkaline pH. *J. Photochem. Photobiol. B Biol.* 120, 111–119. doi: 10.1016/j.jphotobiol.2012.12.014

Kir'Yanov, A., Barmenkov, Y. O., Starodumov, A., Leppanen, V.-P., Vanhanen, J., and Jaaskelainen, T. (2000). Application of the Z-scan technique to a saturable photorefractive medium with the overlapped ground and excited state absorption. *Opt. Commun.* 177, 417–423. doi: 10.1016/S0030-4018(00)00599-X

Korposh, S., James, S., Partridge, M., Sichka, M., and Tatam, R. (2018). All-optical switching based on optical fibre long period gratings modified bacteriorhodopsin. *Optics Laser Technol.* 101, 162–171. doi: 10.1016/j.optlastec.2017.11.021

Krekic, S., Nagy, D., Taneva, S. G., Fábián, L., Zimányi, L., and Dér, A. (2019). Spectrokinetic characterization of photoactive yellow protein films for integrated optical applications. *Eur. Biophys. J.* 48, 465–473. doi: 10.1007/s00249-019-01353-8

Kulagin, I. A., Ganeev, R. A., Kim, V. A., Ryasnyansky, A. I., Tugushev, R. I., Usmanov, T., et al. (2003). "Nonlinear refractive indices and third-order susceptibilities of nonlinear optical crystals," in *Proceedings of the Nonlinear Frequency Generation and Conversion: Materials, Devices, and Applications II*, San Jose, CA. doi: 10.1117/12.478999

Lanyi, J. K. (2004). Bacteriorhodopsin. *Annu. Rev. Physiol.* 66, 665–688. doi: 10.1146/annurev.physiol.66.032102.150049

Lee, K., Kim, Y., Jung, J., Ihee, H., and Park, Y. (2018). Measurements of complex refractive index change of photoactive yellow protein over a wide wavelength range using hyperspectral quantitative phase imaging. *Sci. Rep.* 8, 1–8. doi: 10.1038/s41598-018-21403-z

Leppanen, V., Haring, T., Jaaskelainen, T., Vartiainen, E., Parkkinen, S., and Parkkinen, J. (1999). The intensity dependent refractive index change of photochromic proteins. *Opt. Commun.* 163, 189–192. doi: 10.1016/S0030-4018(99)00141-8

Mathesz, A., Fábián, L., Valkai, S., Alexandre, D., Marques, P. V. S., Ormos, P., et al. (2013). High-speed integrated optical logic based on the protein bacteriorhodopsin. *Biosens. Bioelectron.* 46, 48–52. doi: 10.1016/j.bios.2013.02.022

Mero, M., Wang, L., Chen, W., Ye, N., Zhang, G., Petrov, V., et al. (2019). "Laser-induced damage of nonlinear crystals in ultrafast, high-repetition-rate, mid-infrared optical parametric amplifiers pumped at 1 μm," in *Proceedings of the Pacific Rim Laser Damage 2019 and Thin Film Physics and Applications*, Qingdao, China. doi: 10.1117/12.2540125

Meyer, T. E. (1985). Isolation and characterization of soluble cytochromes, ferredoxins and other chromophoric proteins from the halophilic phototrophic bacterium *Ectothiorhodospira halophila*. *Biochim. Biophys. Acta Bioenerget.* 806, 175–183. doi: 10.1016/0005-2728(85)90094-5

Meyer, T. E., Yakali, E., Cusanovich, M. A., and Tollin, G. (1987). Properties of a water-soluble, yellow protein isolated from a halophilic phototrophic bacterium that has photochemical activity analogous to sensory rhodopsin. *Biochemistry* 26, 418–423. doi: 10.1021/bi00376a012

Mihara, K., Hisatiomi, O., Imamoto, Y., Kataoka, M., and Tokunaga, F. (1997). Functional expression and site-directed mutagenesis of photoactive yellow protein. *J. Biochem.* 121, 876–880. doi: 10.1093/oxfordjournals.jbchem.a021668

Miller, D. A. (2010). Are optical transistors the logical next step? *Nat. Photon.* 4, 3–5. doi: 10.1038/nphoton.2009.240

Naskali, L., Huttunen, M. J., Virkki, M., Bautista, G., Deìr, A. S., and Kauranen, M. (2014). Microscopic determination of second-order nonlinear optical susceptibility tensors. *J. Phys. Chem. C* 118, 26409–26414. doi: 10.1021/jp509453b

Násztor, Z., Bogár, F., and Dér, A. (2016). The interfacial tension concept, as revealed by fluctuations. *Curr. Opin. Coll. Interf. Sci.* 23, 29–40. doi: 10.1016/j.cocis.2016.05.007

Nibbering, E. T. J., Franco, M. A., Prade, B. S., Grillon, G., Le Blanc, C., and Mysyrowicz, A. (1995). Measurement of the nonlinear refractive index of transparent materials by spectral analysis after nonlinear propagation. *Opt. Commun.* 119, 479–484. doi: 10.1016/0030-4018(95)00394-N

Nussenzveig, H. M. (1972). "Chapter 1: Casuality and dispersion relations," in *Mathematics in Science and Engineering*, ed. H. M. Nussenzveig (Amsterdam: Elsevier), 3–53. doi: 10.1016/s0076-5392(08)63161-6

Oesterhelt, D., and Stoeckenius, W. (1971). Rhodopsin-like Protein from the Purple Membrane of *Halobacterium halobium*. *Nat. New Biol.* 233, 149–152. doi: 10.1038/newbio233149a0

Oesterhelt, D., and Stoeckenius, W. (1973). Functions of a new photoreceptor membrane. *Proc. Natl. Acad. Sci. U.S.A.* 70, 2853–2857. doi: 10.1073/pnas.70.10.2853

Oesterhelt, D., and Stoeckenius, W. (1974). Isolation of the cell membrane of *Halobacterium halobium* and its fractionation into red and purple membrane. *Methods Enzymol.* 31, 667–678. doi: 10.1016/0076-6879(74)31072-5

Ormos, P., Fábián, L., Oroszi, L., Wolff, E. K., Ramsden, J. J., and Dér, A. (2002). Protein-based integrated optical switching and modulation. *Appl. Phys. Lett.* 80, 4060–4062. doi: 10.1063/1.1481197

Rakovich, A., Nabiev, I., Sukhanova, A., Lesnyak, V., Gaponik, N., Rakovich, Y. P., et al. (2013). Large enhancement of nonlinear optical response in a hybrid nanobiomaterial consisting of Bacteriorhodopsin and cadmium telluride quantum dots. *ACS Nano* 7, 2154–2160. doi: 10.1021/nn3049939

Ramsden, J. J. (1993). Review of new experimental techniques for investigating random sequential adsorption. *J. Statist. Phys.* 73, 853–877. doi: 10.1007/BF01052813

Roy, S., Prasad, M., Topolancik, J., and Vollmer, F. (2010). All-optical switching with bacteriorhodopsin protein coated microcavities and its application to low power computing circuits. *J. Appl. Phys.* 107:053115. doi: 10.1063/1.3310385

Sasikala, V., and Chitra, K. (2018). All optical switching and associated technologies: a review. *J. Optics* 47, 307–317. doi: 10.1007/s12596-018-0452-3

Schotte, F., Cho, H. S., Kaila, V. R. I., Kamikubo, H., Dashdorj, N., Henry, E. R., et al. (2012). Watching a signaling protein function in real time via 100-ps time-resolved laue crystallography. *Proc. Natl. Acad. Sci. U.S.A.* 109, 19256–19261. doi: 10.1073/pnas.1210938109

Sheik-Bahae, M., Said, A. A., Wei, T., Hagan, D. J., and Stryland, E. W. V. (1990). Sensitive measurement of optical nonlinearities using a single beam. *IEEE J. Q. Electron.* 26, 760–769. doi: 10.1109/3.53394

Sifuentes, C., Barmenkov, Y. O., and Kir'yanov, A. (2002). The intensity dependent refractive index change of bacteriorhodopsin measured by the Z-scan and phase-modulated beams techniques. *Optic. Mater.* 19, 433–442. doi: 10.1016/S0925-3467(02)00024-1

Song, Q. W., Zhang, C., Gross, R., and Birge, R. (1993). Optical limiting by chemically enhanced bacteriorhodopsin films. *Optics Lett.* 18, 775–777. doi: 10.1364/OL.18.000775

Stuart, J. A., Marcy, D. L., and Birge, R. R. (2001). Photonic and optoelectronic applications of bacteriorhodopsin. *Nato Sci. Ser. Sub. Ser. I Life Behav. Sci.* 335, 16–29.

Tenboer, J., Basu, S., Zatsepin, N., Pande, K., Milathianaki, D., Frank, M., et al. (2014). Time-resolved serial crystallography captures high-resolution intermediates of photoactive yellow protein. *Science* 346, 1242–1246. doi: 10.1126/science.1259357

Topolancik, J., and Vollmer, F. (2006). All-optical switching in the near infrared with bacteriorhodopsin-coated microcavities. *Appl. Phys. Lett.* 89:184103. doi: 10.1063/1.2372711

Tóth-Boconádi, R., Dér, A., and Keszthelyi, L. (2011). Optical and electric signals from dried oriented purple membrane of bacteriorhodopsins. *Bioelectrochemistry* 81, 17–21. doi: 10.1016/j.bioelechem.2010.12.003

Tóth-Boconádi, R., Dér, A., Taneva, S. G., and Keszthelyi, L. (2006). Excitation of the L intermediate of bacteriorhodopsin: electric responses to Test X-Ray structures. *Biophys. J.* 90, 2651–2655. doi: 10.1529/biophysj.105.068817

Tóth-Boconádi, R., Dér, A., Taneva, S. G., and Keszthelyi, L. (2010). Excitation of the M intermediates of wild-type bacteriorhodopsin and mutant D96N: temperature dependence of absorbance, electric responses and proton movements. *Theoret. Chem. Acc.* 125, 365–373. doi: 10.1007/s00214-009-0632-y

van der Horst, M. A., van Stokkum, I. H. M., Dencher, N. A., and Hellingwerf, K. J. (2005). Controlled reduction of the humidity induces a shortcut recovery reaction in the photocycle of photoactive yellow protein. *Biochemistry* 44, 9160–9167. doi: 10.1021/bi050237d

Vanhanen, J., Leppanen, V. P., Haring, T., Kettunen, V., Jaaskelainen, T., Parkkinen, S., et al. (1998). Nonlinear refractive index change of photoactive yellow protein. *Opt. Commun.* 155, 327–331. doi: 10.1016/S0030-4018(98)00395-2

Váró, G., and Keszthelyi, L. (1983). Photoelectric signals from dried oriented purple membranes of *Halobacterium halobium*. *Biophys. J.* 43, 47–51. doi: 10.1016/S0006-3495(83)84322-7

Vsevolodov, N. (2012). *Biomolecular Electronics: An Introduction via Photosensitive Proteins*. Berlin: Springer Science & Business Media.

Wheeler, M. J., Russi, S., Bowler, M. G., and Bowler, M. W. (2012). Measurement of the equilibrium relative humidity for common precipitant concentrations: facilitating controlled dehydration experiments. *Acta Crystallogr. Sect. F Struct. Biol. Crystalliz. Commun.* 68, 111–114. doi: 10.1107/S1744309111054029

Willner, A. E., Khaleghi, S., Chitgarha, M. R., and Yilmaz, O. F. (2014). All-Optical Signal Processing. *J. Lightwave Technol.* 32, 660–680. doi: 10.1109/JLT.2013.2287219

Wooten, F. (2013). *Optical Properties of Solids*. Cambridge, MA: Academic press.

Xu, J., Gordon, G. S., Wilkinson, T., and Peucheret, C. (2015). "Experimental observation of nonlinear mode conversion in few-mode fiber," in *Proceedings of the 2015 Conference on Lasers and Electro-Optics (CLEO)*, San Jose, CA. doi: 10.1364/CLEO_SI.2015.SM2L.3

Yeremenko, S., van Stokkum, I. H. M., Moffat, K., and Hellingwerf, K. J. (2006). Influence of the crystalline state on Photoinduced dynamics of photoactive yellow protein studied by ultraviolet-visible transient absorption spectroscopy. *Biophys. J.* 90, 4224–4235. doi: 10.1529/biophysj.105.074765

Conflict of Interest: The authors declare that the research was conducted in the absence of any commercial or financial relationships that could be construed as a potential conflict of interest.

Copyright © 2020 Krekic, Zakar, Gombos, Valkai, Mero, Zimányi, Heiner and Dér. This is an open-access article distributed under the terms of the Creative Commons Attribution License (CC BY). The use, distribution or reproduction in other forums is permitted, provided the original author(s) and the copyright owner(s) are credited and that the original publication in this journal is cited, in accordance with accepted academic practice. No use, distribution or reproduction is permitted which does not comply with these terms.

III. Petrovszki, D.; **Krekic, S.**; Valkai, S.; Heiner, Z.; Dér, A. All-Optical Switching Demonstrated with Photoactive Yellow Protein Films. *Biosensors* **2021**, *11* (11), 432. https://doi.org/10.3390/bios11110432. IF: 5.743

biosensors

MDPI

Communication

All-Optical Switching Demonstrated with Photoactive Yellow Protein Films

Dániel Petrovszki [1,2,†], Szilvia Krekic [1,2,†], Sándor Valkai [1], Zsuzsanna Heiner [3] and András Dér [1,*]

[1] Institute of Biophysics, Biological Research Centre, Eötvös Loránd Research Network, 6726 Szeged, Hungary; petrovszki.daniel@brc.hu (D.P.); krekic.szilvia@brc.hu (S.K.); valkai.sandor@brc.hu (S.V.)
[2] Doctoral School of Multidisciplinary Medical Sciences, University of Szeged, 6720 Szeged, Hungary
[3] School of Analytical Sciences Adlershof, Humboldt-Universität zu Berlin, 12489 Berlin, Germany; heinerzs@hu-berlin.de
* Correspondence: der.andras@brc.hu
† These authors contributed equally to this work: Dániel Petrovszki and Szilvia Krekic.

Abstract: Integrated optics (IO) is a field of photonics which focuses on manufacturing circuits similar to those in integrated electronics, but that work on an optical basis to establish means of faster data transfer and processing. Currently, the biggest task in IO is finding or manufacturing materials with the proper nonlinear optical characteristics to implement as active components in IO circuits. Using biological materials in IO has recently been proposed, the first material to be investigated for this purpose being the protein bacteriorhodopsin; however, since then, other proteins have also been considered, such as the photoactive yellow protein (PYP). In our current work, we directly demonstrate the all-optical switching capabilities of PYP films combined with an IO Mach–Zehnder interferometer (MZI) for the first time. By exploiting photoreactions in the reaction cycle of PYP, we also show how a combination of exciting light beams can introduce an extra degree of freedom to control the operation of the device. Based on our results, we discuss how the special advantages of PYP can be utilized in future IO applications.

Keywords: optical switching; integrated optics; photonics; photoactive yellow protein

check for updates

Citation: Petrovszki, D.; Krekic, S.; Valkai, S.; Heiner, Z.; Dér, A. All-Optical Switching Demonstrated with Photoactive Yellow Protein films. *Biosensors* **2021**, *11*, 432. https://doi.org/10.3390/bios11110432

Received: 1 September 2021
Accepted: 28 October 2021
Published: 31 October 2021

Publisher's Note: MDPI stays neutral with regard to jurisdictional claims in published maps and institutional affiliations.

Copyright: © 2021 by the authors. Licensee MDPI, Basel, Switzerland. This article is an open access article distributed under the terms and conditions of the Creative Commons Attribution (CC BY) license (https://creativecommons.org/licenses/by/4.0/).

1. Introduction

Integrated optics (IO) is a new alternative method of information transfer analogous to integrated electronics; however, the speed of the system at hand is dependent on the nonlinear optical (NLO) material that is applied as the active element of the IO circuit. Several materials are being developed and used in hybrid systems—mostly nonlinear crystals with π-conjugated electron systems [1,2]. It is among the long-term goals in optical telecommunication to find proper NLO materials that make possible all-optical IO switching at the proper efficiencies and speeds. Earlier works suggested the consideration of materials of biological origin for these purposes [3]. First, it was shown that (slow) spectral changes accompanying the photocycle of the chromoprotein bacteriorhodopsin (bR) are sufficient to achieve IO switching [4–6], making bR a promising candidate for IO applications. Eventually, it was also demonstrated that the primary events of the bR photocycle allow for ultrafast (sub-picosecond) switching as well [7].

The application of biological materials is appealing because of their easy availability and exceptional NLO properties [8]. Recently, another light-sensitive biomaterial, the photoactive yellow protein (PYP) [9,10], has garnered interest for IO applications because of its fast photocycle in solution and its large light-induced refractive index change in dried films [11]. PYP, being water-soluble and smaller than the bR membrane patches used previously, potentially enables its combination with special IO passive elements where the application of bR is not possible (e.g., in porous silicon structures). Based on our previous experiments, the PYP in film form could be a viable option for all-optical

switching experiments, as adding glycerol to the protein solution before drying the film helps maintain the integrity of the photocycle even in low humidity environments, allowing for the formation of the intermediate states [12], which accompanies refractive index changes of the film [11]. The photocycle of PYP consists of two main intermediates, the red-shifted pR and the blue-shifted pB (further distinguishing pR_1, pR_2, pB_1 and pB_2) [10]. By illuminating PYP with blue light, the photocycle takes place in a matter of milliseconds in solution. A study has shown that illuminating PYP during the photocycle's pB intermediate with violet light can cause a short circuit in the photocycle, making PYP return to the ground state via a faster route [13].

In this communication, our main motivation was to demonstrate that the spectral changes of the PYP photocycle can accompany refractive index changes sufficient for IO switching (similar to how it has been shown earlier for bR [4]), using the combination of a PYP film as an active NLO component and a proper integrated optical structure. Active IO elements can be implemented by utilizing a number of structures—interferometers [8,14], grating couplers [14,15], ring resonators [16], etc. The Mach–Zehnder interferometer (MZI) is one of the simplest IO passive devices, consisting of a bifurcated linear IO waveguide structure forming two arms. By adsorbing a transparent NLO material on top of the arms, adlayers are formed that can alter the effective refractive index, thus creating a phase difference between the arms joining at the output of the device, manifesting in intensity changes at the MZI's output. This principle is often used for biosensing applications, such as sensing bacteria or proteins in action, as well [17,18]. Hence, we performed all-optical switching experiments using an IO MZI, with a PYP adlayer as an active NLO component, for the first time. For the excitation of the sample, we used continuous illumination with two different laser wavelengths, targeting both the protein's pG ground state and pB intermediate state, demonstrating the different modalities of the switching capability of PYP-containing IO devices. Our results underpin that, besides bR, the chromoprotein PYP can also be considered as a promising NLO material for future, high-profile IO applications.

2. Materials and Methods

2.1. PYP Sample Preparation

The preparation method for PYP has been discussed elsewhere [10,11], but a brief summary will be given here as well. To prevent the cracking of the PYP films, 87% glycerol solution was added to the protein solution at 1:49 ratio. It was then allowed to dry in a laboratory environment (33% RH, 20 °C) for at least 24 h. By using glycerol as a ballast material, we secured the relative humidity inside the sample at ~80%, still allowing for the photocycle to take place [10,11].

2.2. IO Mach–Zehnder Interferometer Biosensor Fabrication

The fabrication method of the integrated optical Mach–Zehnder interferometer was based on the process used in one of our previous works [19], following the protocol of the manufacturer of the applied materials. The mentioned process was modified, considering the parameters used in several steps, to reach the desired thickness of the components of the device.

It should be kept in mind that MZIs have a sinusoidal transmission function (TMF), allowing for an approximate linear response of the device only in the vicinity of the inflexion points of the TMF and that this is where the bias point should be adjusted prior to the measurements. There are several methods to accomplish this task, in most cases via tuning the optical path length along one of the arms. Previously, we have used an optical solution [19]; however, here, controlled heating near one of the branches of the MZI was applied. By using a surface-sputtered heating wire close to the reference arm of the MZI, we can modify the environment's temperature and thus tune the device's bias point. According to our experience, the heating effects remained restricted to the area of the heating wire that was more than 1600 µm away from the proximal adlayer area (and even further away from the distal ones), leaving enough space for dissipation. This

solution resulted in an improved stability of the bias point during the measurements. In order to accomplish this task, a glass substrate covered by a gold heating wire structure was used, based on the method applied for surface electrode fabrication [19]. As a first step of the device fabrication, a 20 nm thick surface gold heating wire (1 kΩ resistance) capable of performing MZI's bias-point tuning was prepared on a microscope coverslip (Menzel-Gläser, Thermo Fisher Scientific, Waltham, MA, USA). Then, a rib waveguide stripe (SU-8 2002, MicroResist Technology GmbH., Berlin, Germany) of 2 × 2 µm was made on the mentioned glass substrate, forming the sensing optical interferometer structure in such a way that one of the arms was placed in the vicinity of the wire, as can be seen in Figure 1a.

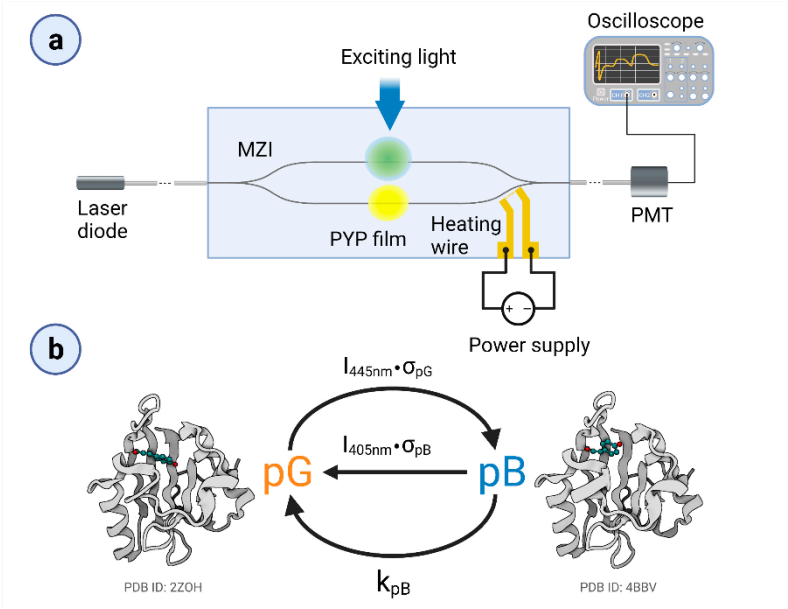

Figure 1. (**a**) Schematic representation of the measuring IO device, the MZI with the PYP adlayer and the heating wire for bias-point adjustment. (**b**) Simplified photocycle of the PYP film, with the ground state (pG) and the rate-limiting intermediate (pB). (Schematic PDB-structures are indicated for demonstration.) Long, continuous excitation with blue light results in the development of a pG–pB equilibrium. The figure was created by Biorender.com.

In the device's ready-to-use construction, the substrate was glued on a microscope slide (Menzel-Gläser, Thermo Fisher Scientific, Waltham, MA, USA) using NOA81 optical adhesive by exposing the layer with a mercury arc lamp (100W, HBO 100 Zeiss, Jena, Germany). To apply the tuning capability of the heating wire, electric wires were connected by droplets of conducting epoxy (CW2400 CircuitWorks® Conductive Epoxy, Chemtronics, Kennesaw, GA, USA) to the side contact pads of the gold structure. These were connected to the DC power supply (VLP 2403pro, Conrad Electronic, Hirschau, Germany), to perform the bias-point tuning.

2.3. Experimental Setup

A schematic representation of the experimental setup can be seen in Figure 1a. As a measuring light (referred to as a probe light), we used a green laser diode (532 nm, 50 mW, Roithner, Wien, Austria), which was coupled inside the single mode MZI by a single-mode optical fiber (S630-HP, Thorlabs GmbH, Lübeck, Germany). The fiber was positioned to the MZI's input with a micropositioner (DC-3K, Märzhäuser Wetzlar GmbH & Co. KG, Steindorf, Germany) and its optimal position was fixed with photopolymer glue (OP-66-LS, Dymax Europe GmbH, Wiesbaden, Germany). The same method was used for coupling the light out from the device. The stock solution of the PYP–glycerol mixture was pipetted on both arms of the interferometer, in ~1 mm diameter patches, before drying. To excite

and control the PYP photocycle, we used two different continuous laser beams (445 nm, 4/44 mW and 405 nm, 21.7 mW at the sample). The scheme of the simplified photocycle model is shown in Figure 1b. The duration of excitation was varied between 2 and 14 s. PYP films were deposited on both arms of the MZI but only one of them was excited at a time. For tuning the MZI's bias point, the voltage of the heating wire was varied between 0–4.6 V.

To measure the transfer characteristics of the MZI, its output was coupled to an optical fiber guiding the measuring light into a photomultiplier tube (H5783-01, Hamamatsu, Japan), from which the signal was transmitted to and recorded by a digital oscilloscope (LeCroy 9310-L, LeCroy, Chestnut Ridge, NY, USA). The voltage on the heating wire was controlled by a variable DC power supply (VLP 2403pro, Konrad Electronics, Hirschau, Germany). During each measurement, the ambient temperature was kept at 23 °C, with a relative humidity of 33%.

3. Results

3.1. Calibration of the MZI Bias Point

We first measured the transmission characteristics of our MZI by steadily increasing the voltage applied to the heating wire from 0 V to 3.5 V while detecting the intensity of the 633 nm probe light at the output of the interferometer (Figure 2). The heating caused a local thermal dilatation of the nearby waveguide area, resulting in an increase of the effective optical path length of the reference arm of the MZI, thereby introducing a phase difference between the light beams interfering with each other at the joint of the output side. The MZI's sensitivity is proportional to the first derivative of the sinusoidal transmission function, meaning that the sensitivity is smaller at the extremes, while it is the highest at the mean light intensity, compensated to an artificial zero output level by an offset voltage of the amplifier ("zero-intensity points" in Figure 2), where the derivative is the largest. By fine-tuning the power dissipated by the heating wire, one can adjust the bias point of the interferometer, before measurements, to one of these points of maximal sensitivity. One should note that changes in the ambient conditions (such as temperature and humidity) might cause a baseline drift (and an accompanying sensitivity change), so a careful control of these parameters is necessary to perform the experiments. In our case, the baseline drift could be kept on a negligible level during the time scale of the experiments (typically the 10-s to several minutes scale) by using the method of stationary local electric heating. The slight baseline drifts that still occurred during the present experiments could be attributed, rather, to local heating effects due to the several-second-long illumination of PYP films. Note that similar phenomena were observed while performing analogous experiments with bR, too [4]. Such effects, however, should play even less of role in future fast-switching experiments.

3.2. Demonstration of All-Optical Switching

To demonstrate all-optical switching, the intensity changes of the probe light were monitored, while PYP was excited by 405 nm continuous illumination. Prior to illumination, the bias point was properly adjusted to the "zero" level (Figure 2) by tuning the heating voltage to 4 V and keeping it constant during the whole period of detecting the output intensity of the MZI over time. The wavelength of the probe light was chosen to be 532 nm, so as to stay outside of the absorption range of the ground state and the intermediates of the PYP photocycle, respectively (Figure S2a), while still being in the high-refractive-index regime near the absorption peaks (Figure S2c). We used a 2 s long illumination and a subsequent 2 s break, during which no exciting light reached the sample. The significant changes of the measuring light level between the light and dark periods indicate that all-optical switching works properly (Figure 3) and that the bias point at 4 V heating voltage suffered only negligible drift. According to a brief interpretation of the observed phenomena based on a simplified reaction scheme of the PYP photocycle (Figure 1b), a steady-state equilibrium between the ground state (pG) and the rate-limiting

intermediate (pB) was formed about 2 s after excitation, in accordance with our earlier results [11], establishing a corresponding refractive index change of the protein-film adlayer (Figure S2c). After another 2 s of the dark period, most of the protein returned to the ground state, which, upon re-excitation, yielded the same signal as when exciting the sample for the first time (Figure 3), demonstrating the repeatability of switching. (A more detailed explanation of the effects is given below, in the Discussion section.)

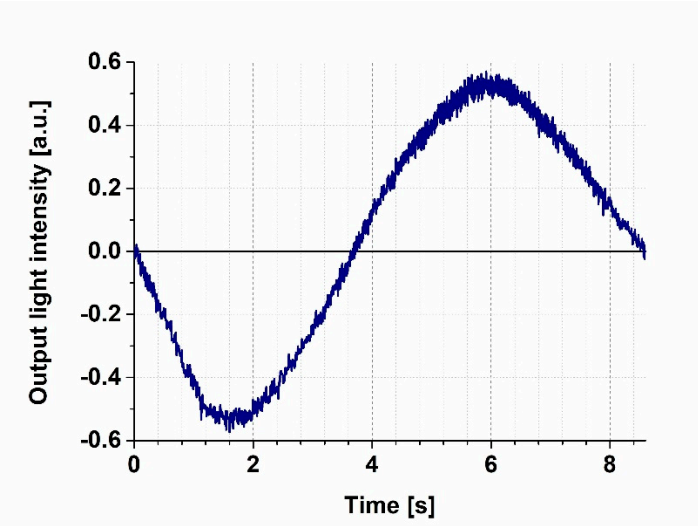

Figure 2. Transmission function of the MZI recorded by a 532 nm probe light, while increasing the heating voltage steadily from 0 to 4.6 V. Prior to each switching experiment, the bias point was adjusted to the zero level.

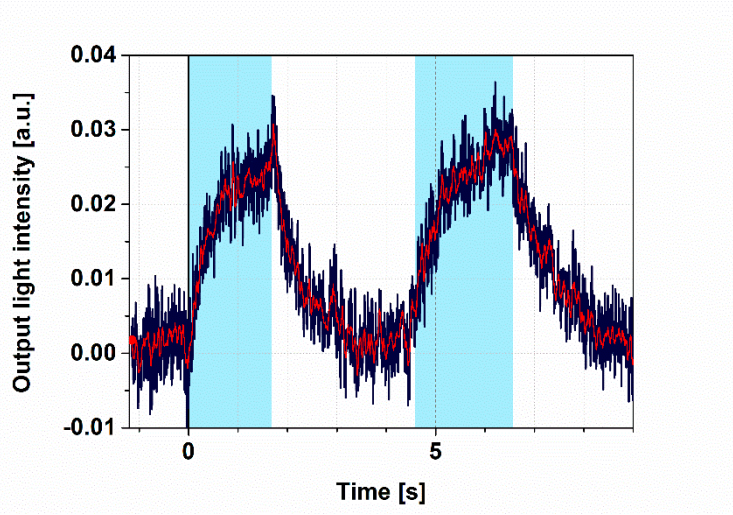

Figure 3. Demonstration of switching I. Light intensity measured at the MZI's output with two consecutive 4 s square-wave excitations. Excitation light: 445 nm, 4 mW; probe light: 532 nm; duty cycle: 50%; heating voltage: 4 V for adjusting the bias point. The blue line represents the original signal, while the red line corresponds to the filtered one. Cyan color shades indicate the periods of 445 nm illumination.

3.3. Controlling the Photocycle of PYP by Two Excitation Lights

The photocycle of PYP contains at least one light-induced shortcutting route, namely, a preferential excitation of pB drives back the molecule to the pG state [13], as shown schematically in Figure 1b. This phenomenon offers another degree of freedom to control PYP-based all-optical switching. Here, we demonstrate this opportunity by a combination of quasi-permanent illuminations.

First, we excited the PYP film with a weak (4 mW), 445 nm light for 3 s, which was followed by a relaxation in the dark, then another 3 s excitation at 405 nm (Figure 4a). Here, we can see that illuminations at both wavelengths were able to effectively excite the protein in the ground state and accumulate pB, as explained before, in agreement with its absorption spectrum (Figure S1a). The size difference of the two signals can be attributed to the much higher intensity of the 405 nm light (27 mW) that was overcompensating for the higher absorption cross section at 445 nm (4 mW).

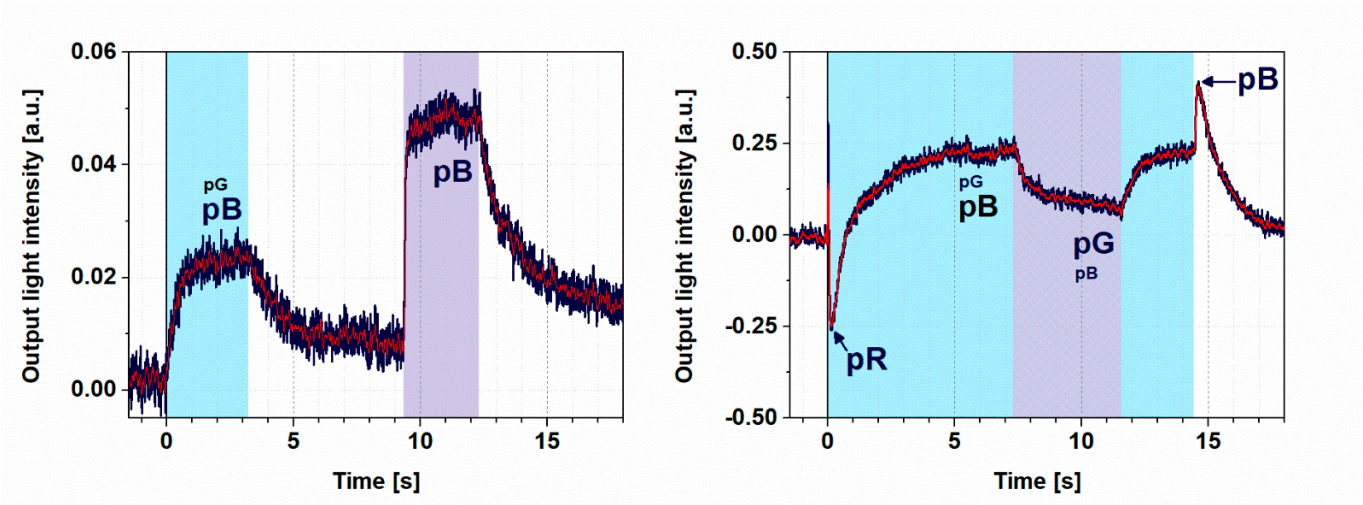

Figure 4. Demonstration of switching II. (**a**) Light intensity measured at output of the MZI, when the sample was first illuminated by a 445 nm (4 mW) excitation beam for 3 s. Then, after a dark period of 6 s, PYP was re-excited with a 405 nm illumination (27 mW) for 3 s. The bias voltage was set to 2.1 V. (**b**) Measured output signal of the MZI with 14 s excitation by a strong (44 mW) and continuous 445 nm light while, from 7 s, also exciting the film for 4 s by a 405 nm continuous light. The blue line represents the measured data, while the red is the filtered curve. The wavelength of the probe light propagating in the MZI was 532 nm in both cases. Color shades indicate the periods and wavelengths of illumination (cyan and violet for 445 nm and 405 nm, respectively, striped pattern for both). To facilitate understanding of the observed effects, we have now also indicated the states of the photocycle of PYP contributing to a greater or lesser extent (indicated by the size of the caption) to the actual effect, represented by different phases of the registered traces.

When, however, a strong 445 nm excitation was used (44 mW), a higher-level steady state was formed and the subsequently superimposed 405 nm excitation resulted in a quenching of the effect (Figure 4b), demonstrating that switching effects based on PYP films can be further controlled by a combination of illuminations. A more detailed explanation of the kinetic effects is given in the next section.

4. Discussion

4.1. Model Calculations

To interpret the registered kinetic traces, let us consider a typical scheme for photoexcitable disordered systems, where a primary absorption is followed by thermally driven processes, such as the stabilization of the light-induced conformational change and a subsequent relaxation [20–22]. While a single-photon absorption process is considered extremely fast, on the level of population of atoms or molecules the primary reaction is described by a rate constant that is proportional to the excitation light intensity (I) and an efficiency factor (σ), including the absorption cross section; on the other hand, the thermal processes are assumed to be light-independent [7,20–22]. This general scheme holds for light-driven chromoproteins as well; however, here, the thermally induced relaxation process is usually more complex than, e.g., in semiconductors [7]. (For PYP, such a complex, though not complete, model is shown in Figure S1 and the corresponding kinetic equations are shown

in Supporting Information.) Note, however, that in a first-order unidirectional reaction scheme, the slowest (rate-limiting) transitions dominate the kinetics. If, e.g., the $I \cdot \sigma$ for a light-driven reaction is much smaller than the rate constants of the subsequent thermal transitions, the contribution of the latter to the transient or equilibrium population of the intermediate states is negligible. Hence, at the relatively low light intensity levels provided by the continuous-wave lasers used in our experiments, we consider a simplified photocycle scheme, keeping only the ground state (pG) and the rate-limiting pB intermediate, accumulating to the largest extent under such circumstances (Figure 1b). (The differential equation system describing the kinetics is also reduced in this case, accordingly.) For the light-induced reactions under stationary illumination at 445 and 405 nm, we can introduce the quasi-first-order rate constants $I_{445nm} \cdot \sigma_{pG}$ and $I_{405nm} \cdot \sigma_{pB}$, respectively. (Here I_{445nm} and I_{405nm} denote the continuous blue and violet light intensities, while σ_{pG} and σ_{pB} include the absorption cross sections and the quantum efficiencies of the light-induced photocycle reactions at 445 and 405 nm, respectively.) The rate constant of the thermally induced decay of the pB intermediate is denoted by k_{pB}. Under continuous blue-light illumination (and in the absence of violet light), the equilibrium concentration of pG and pB can be expressed as follows:

$$[pB] = PG_0 \cdot I_{445nm} \cdot \frac{\sigma_{pG}}{I_{445nm} \cdot \sigma_{pG} + k_{pB}} \text{ and } [pG] = PG_0 \cdot I_{445nm} \cdot \frac{k_{pB}}{(I_{445nm} \cdot \sigma_{pG} + k_{pB})}, \quad (1)$$

where [pG] and [pB] are concentrations of the ground state and the pB intermediate, respectively, while $PG_0 = [pG] + [pB]$ and $d[pG]/dt = d[pB]/dt = 0$.

If both the blue and the violet lights are present, the photocycle scheme becomes somewhat more complex: the pG to pB transition will now be driven by the sum of two rate constants ($I_{445nm} \cdot \sigma_{pG} + I_{405nm} \cdot \sigma_{pG405}$), where σ_{pG405} stands for the absorption cross section of pG at 405 nm. The apparent rate constant of the pB to pG transition will be similarly modified to $I_{445nm} \cdot \sigma_{pB445nm} + I_{405nm} \cdot \sigma_{pG}$. It is, however, evident from Figure S2a, that $\sigma_{pG405} < \sigma_{pG}$, while on the other hand, $\sigma_{pB445nm} << \sigma_{pB}$. Being the blue and violet excitation light intensities of the same order of magnitude, we can end up with the following formula for the approximate concentrations of PYP states under two-color excitation:

$$[pB] = PG_0 \cdot I_{445nm} \cdot \frac{\sigma_{pG}}{(I_{445nm} \cdot * \sigma_{pG} + I_{405nm} \cdot \sigma_{pB} + k_{pB})}, \text{ and } [pG] = PG_0 \cdot I_{445nm} \cdot \frac{k_{pB}}{(I_{445nm} \cdot \sigma_{pG} + I_{405nm} \cdot \sigma_{pB} + k_{pB})}. \quad (2)$$

When exciting the pG ground state—which has an absorption maximum at 446 nm—with sufficiently high light intensity (i.e., if $I_{445nm} \cdot \sigma_{pG} >> k_{pB}$), a steady-state equilibrium between pG and pB is established according to (1), with the PYP primarily being in the pB state, since the $I_{445nm} \cdot \sigma_{pG}$ contribution is dominating the k_{pB} kinetic constant. From what we have seen in previous experiments, too [12], the steady state forms in the matter of a few seconds under such conditions, while the protein returns fully to the ground state after excitation ceases. If we use two different wavelengths for exciting the sample, choosing one to target, rather, pG, and another to target, rather, the pB intermediate, we can shift the concentration ratio of intermediates in the formed steady state. By introducing $I_{405nm} \cdot \sigma_{pB}$ into the rate equation we preferentially excite the dominant pB state, inducing a shortcut reaction back into pG [13]. The equilibrium concentration of pB and pG in this case are given by equation (2). The absorption spectra of the ground and intermediate states of the photocycle are shown in Figure S2a, from which, the corresponding difference absorption spectra can be determined (Figure S2b) and the refractive index difference spectra can be calculated according to the Kramers–Kronig relations [23] (Figure S2c).

The corresponding light-induced refractive index change of the PYP adlayer adsorbed on the MZI induces a phase shift in the measuring arm of the MZI, resulting in an intensity change at the output. The steady state, formed by using both excitation wavelengths simultaneously, has a different refractive index than that formed by illuminating the film at

only one wavelength. This phenomenon makes a detectable output intensity difference between the two states, which is utilized in our switching experiments. The transient positive and negative peaks in Figure 4b must have different routes. The latter we attribute to a transient accumulation of pR, a red-shifted photocycle intermediate (Figure S1), at high 445 nm intensities before decaying to pB, dominating the steady state [10]. On the other hand, the positive peak followed by the switch-off is probably due to a shortcutting effect of the 445 nm light itself, exciting the accumulating intermediate(s) at high intensities.

4.2. Evaluation of Kinetics

Although, in the equations presented in this chapter, we deal only with steady-state concentrations and did not intend to solve the complex, coupled differential equation system describing the photocycle kinetics (Supporting Information), some straightforward statements can still be made for the kinetics of rate-limiting reactions. In case of all transitions to the dark state after illumination, e.g., the slowest rate of the thermal reactions of the photocycle, namely, the pB to pG transition, is supposed to determine the time constant of relaxation. In fact, the results of the exponential fitting of these phases in Figures 3 and 4 all show a similar value within the estimated uncertainty limits of the experiments and evaluation (1.2 $\pm$ 0.2 s). This value is actually also congruent with the findings of earlier measurements on similar samples [12]. In the case of transitions to light-driven equilibria of various photocycle intermediates, on the other hand, the observed rates are always a mixture of virtual rate constants, due to the illumination driving the initial population towards a new equilibrium ($I^*\sigma$) and a thermal rate constant (k), i.e., $k_{virtual} = I^*\sigma + k$, as is discussed above, too. This means that these transitions should normally be faster than the ones discussed before. In fact, fitting the rising phases of the light-induced signals yields shorter time constants (τ_{rise}) than the ones corresponding to relaxations. In addition, the rates belonging to the same transitions normally increase by increasing intensity of excitation, as expected from the above equation (τ_{rise} = 600 $\pm$ 100 ms for the 4 mW excitation at 445 nm and τ_{rise} = 200 $\pm$ 40 ms for the 27 mW excitation at 405 nm. (Note that in the latter case, the higher intensity overcompensated the smaller absorption cross section (σ).) The kinetics of the PYP photocycle, however, get more complex when light-induced back-reactions are also involved, either due to a simultaneous excitation at two wavelengths, or to an excitation of more than one intermediate by the same excitation light (Figure 4b). The latter occurs, e.g., when a high-intensity illumination can compete with the pR to pB decay, resulting in the accumulation of pR. However, because of the highly overlapping spectra of pG and PR, the 445 nm excitation light drives back a considerable population of pR to pG before being able to get further to pB, following the normal pathway of the photocycle. This effect actually results in a slow-down of the formation of pB populations, even at high intensities of the excitation light. Right after switching off the strong 445 nm illumination (Figure 4b, near 14 ms), however, we see a fast rise (40 ms), which is due to the population of molecules that have been driven out from the ground state (pG) and, in the absence of a back-reaction, reach the pB state rapidly.

Although establishing a comprehensive model for the in-depth, quantitative description of the phenomena is beyond the scope of this short, application-oriented study, we could show that the PYP photocycle can be controlled by various illuminations. This allows for a sort of dynamic "programing" of PYP-based NLO materials by light, a potentially utilizable feature in future IO applications. According to our experiments, the light-induced intensity changes accompanying the PYP photocycle cover a major part of the full dynamic range of the Mach–Zehnder interferometer (Figures 2 and 4b), clearly proving the IO switching ability of PYP-based NLO films. Comparing the results with those of switching experiments carried out on a Mach–Zehnder interferometer structure doped by bR films also shows that the quality of the traces obtained by the two experiments are rather similar [4].

4.3. On the Opportunity of Increasing Switching Speed

Based on the present results and those of some recent publications [12,24], it can also be envisioned that, similarly to the case of bR, ultrafast all-optical switching by PYP films as NLO materials should be feasible. On the one hand, the kinetics analysis of our results under 4.2 implies that increasing the intensity of the excitation light increases the switching speed as well. However, we also saw that at higher light intensities, one should consider a more detailed photocycle scheme, including the faster-forming and decaying intermediates (Figure S1). On the other hand, Konold et al. have recently shown that large absorption changes occur in PYP samples after a strong, 50 fs excitation, still in the femtosecond time scale [24], where a blue-shifted intermediate (called "ES", after "excited state") develops. On the ns to μs time scale, it transforms to a red-shifted intermediate (pR) (Figure S1), which is known to transform later to a blue-shifted pB in the course of milliseconds [25] at room temperature (Figure S1). The absorption spectra of the pR and pB intermediates have been determined from kinetic experiments [25] (Figure S2a). From the Kramers–Kronig relations of optics, connecting the real and imaginary parts of the complex refractive index, one can then calculate the corresponding refractive index spectra [23] (Figure S2c). Although the full absorption spectrum of the ES intermediate has not been published yet, the relative sizes of the light-induced differential spectra of ES, pR and pB (Figure S2b) imply that the amplitude of the refractive index change associated to the pG to ES transition will most probably exceed those of the pG to pR and pG to pB transitions. Since the results of the present paper prove that refractive index changes associated with the pG to pB transition are sufficient for integrated optical switching, it can be safely stated that it should be also true for the pG to ES transition, which takes place on the femtosecond time scale, similar to the bR-I transition of bacteriorhodopsin [7]. Hence, it can be anticipated that an ultrafast integrated optical switching based on the primary phototransition of PYP should also be feasible to demonstrate at high-intensity short-pulse excitations with a proper femtosecond setup.

5. Conclusions and Outlook

Our results demonstrate that dried films of PYP can be used for all-optical IO switching because of the favorable nonlinear optical properties of the protein film. For PYP, being water-soluble and smaller than the bR membrane patches used previously theoretically enables its combination with special IO passive elements where the application of bR is not possible (e.g., with porous silicon—pSi—structures). According to a solid functionalization protocol developed for pSi structures, they can accommodate a variety of soluble proteins; as it has already been demonstrated for a couple of proteins of various sizes and compositions [26,27], so it is expected to be achievable for PYP as well.

The small size and water solubility are not the only properties that distinguish PYP from bR and allow for its unique applications. Another important feature is the different spectral range of the main absorption bands and refractive index changes, which are blue shifted in PYP by ca. 100 nm as compared to bR, making a complementary spectral range available for IO operations using biophotonic film as active, nonlinear optical materials.

For utilization in telecommunication, however, much faster switching procedures are usually required, since the present state of the art for solid-state NLO materials is in the subnanosecond range [28]. Similarly to the case of bacteriorhodopsin [7], the light-induced primary photocycle reactions of PYP [24] theoretically allow for such a short switching time regime, whose demonstration should be the subject of follow-up papers.

Supplementary Materials: The following are available online at https://www.mdpi.com/article/10.3390/bios11110432/s1, Figure S1. A simplified scheme of the PYP photocycle, including the light-induced and thermal reactions, represented by undulated and solid arrow lines with the corresponding rate constants, respectively. I and σ represent the light intensity and the absorption cross sections, pG stands for the ground-state pigment and ES is the blue-shifted first excited state forming on the 10 fs time scale at high I intensities and decaying to the red-shifted pR on the nanosecond to microsecond time scale (Konold et al.). pR decays further to the blue-shifted pB

on the 1 ms to 100 ms time scale (Khoroshyy et al., Krekic et al., 2019). Both pR and pB can be driven back by photoexcitation to pG. A differential equation system describing the kinetics of the concentrations of the photocycle intermediates is also presented. Figure S2. (a) Absorption spectra of the ground state (pG, black), an early intermediate (pR, red) and the rate-limiting intermediate (pB, blue) of the PYP photocycle, as determined from absorption kinetic experiments (Khoroshyy et al.). (b) Difference-absorption spectra of pR (red) and pB (blue), as compared to the ground state (pG). (c) Calculated change of the refractive index spectrum upon the rate-limiting pG → pB transition (underlying the effects described in the main body of the paper), using the Kramers–Kronig relations. For more details, see Fábián et al.

Author Contributions: A.D. created the research idea. The MZI was prepared by D.P. The measuring setup was designed and built by S.V., D.P. and A.D. The PYP sample was prepared by S.K. The measurements were done by D.P., S.K., S.V. and A.D. The quantitative evaluation of the measurements was done by Z.H. The manuscript was written by S.K., D.P., S.V., Z.H. and A.D. All authors have read and agreed to the published version of the manuscript.

Funding: National Research and Development Office, Hungary (NKFI-1 K-124922).

Data Availability Statement: The original data are available upon request from the corresponding author.

Acknowledgments: The authors are indebted to László Fábián and Gábor Sipka for helpful discussions and for providing the 445 nm laser, respectively.

Conflicts of Interest: The authors declare no conflict of interest or state.

References

1. Hales, J.M.; Matichak, J.; Barlow, S.; Ohira, S.; Yesudas, K.; Brédas, J.L.; Perry, J.W.; Marder, S.R. Design of polymethine dyes with large third-order optical nonlinearities and loss figures of merit. *Science* **2010**, *327*, 1485–1488. [CrossRef]
2. Hu, X.; Jiang, P.; Ding, C.; Yang, H.; Gong, Q. Picosecond and low-power all-optical switching based on an organic photonic-bandgap microcavity. *Nat. Photonics* **2008**, *2*, 185. [CrossRef]
3. Fábián, L.; Mathesz, A.; Dér, A. New trends in biophotonics. *Acta Biol. Szeged.* **2015**, *59* (Suppl. S2), 189–202.
4. Dér, A.; Valkai, S.; Fábián, L.; Ormos, P.; Ramsden, J.J.; Wolff, E.K. Integrated Optical Switching Based on the Protein Bacteriorhodopsin†. *Photochem. Photobiol.* **2007**, *83*, 393–396. [CrossRef]
5. Ormos, P.; Fábián, L.; Oroszi, L.; Wolff, E.K.; Ramsden, J.J.; Dér, A. Protein-based integrated optical switching and modulation. *Appl. Phys. Lett.* **2002**, *80*, 4060–4062. [CrossRef]
6. Roy, S.; Sethi, P.; Topolancik, J.; Vollmer, F. All-optical reversible logic gates with optically controlled bacteriorhodopsin protein-coated microresonators. *Adv. Opt. Technol.* **2012**, 727206. [CrossRef]
7. Fábián, L.; Heiner, Z.; Mero, M.; Kiss, M.; Wolff, E.K.; Ormos, P.; Osvay, K.; Dér, A. Protein-based ultrafast photonic switching. *Opt. Express* **2011**, *19*, 18861–18870. [CrossRef]
8. Mathesz, A.; Fábián, L.; Valkai, S.; Alexandre, D.; Marques, P.V.; Ormos, P.; Wolff, E.K.; Dér, A. High-speed integrated optical logic based on the protein bacteriorhodopsin. *Biosens. Bioelectron.* **2013**, *46*, 48–52. [CrossRef] [PubMed]
9. Meyer, T.E. Isolation and characterization of soluble cytochromes, ferredoxins and other chromophoric proteins from the halophilic phototrophic bacterium Ectothiorhodospira halophila. *Biochim. Et Biophys. Acta (BBA)-Bioenerg.* **1985**, *806*, 175–183. [CrossRef]
10. Meyer, T.E.; Yakali, E.; Cusanovich, M.A.; Tollin, G. Properties of a water-soluble, yellow protein isolated from a halophilic phototrophic bacterium that has photochemical activity analogous to sensory rhodopsin. *Biochemistry* **1987**, *26*, 418–423. [CrossRef]
11. Krekic, S.; Zakar, T.; Gombos, Z.; Valkai, S.; Mero, M.; Zimányi, L.; Heiner, Z.; Dér, A. Nonlinear Optical Investigation of Microbial Chromoproteins. *Front. Plant Sci.* **2020**, *11*, 1567. [CrossRef] [PubMed]
12. Krekic, S.; Nagy, D.; Taneva, S.G.; Fábián, L.; Zimányi, L.; Dér, A. Spectrokinetic characterization of photoactive yellow protein films for integrated optical applications. *Eur. Biophys. J.* **2019**, *48*, 465–473. [CrossRef]
13. Hendriks, J.; van Stokkum, I.H.; Crielaard, W.; Hellingwerf, K.J. Kinetics of and intermediates in a photocycle branching reaction of the photoactive yellow protein from Ectothiorhodospira halophila. *FEBS Lett.* **1999**, *458*, 252–256. [CrossRef]
14. Fábián, L.; Wolff, E.K.; Oroszi, L.; Ormos, P.; Dér, A. Fast integrated optical switching by the protein bacteriorhodopsin. *Appl. Phys. Lett.* **2010**, *97*, 023305. [CrossRef]
15. Korposh, S.; James, S.; Partridge, M.; Sichka, M.; Tatam, R. All-optical switching based on optical fibre long period gratings modified bacteriorhodopsin. *Opt. Laser Technol.* **2018**, *101*, 162–171. [CrossRef]
16. Topolancik, J.; Vollmer, F. All-optical switching in the near infrared with bacteriorhodopsin-coated microcavities. *Appl. Phys. Lett.* **2006**, *89*, 184103. [CrossRef]
17. Mathesz, A.; Valkai, S.; Újvárosy, A.; Aekbote, B.; Sipos, O.; Stercz, B.; Kocsis, B.; Szabó, D.; Dér, A. Integrated optical biosensor for rapid detection of bacteria. *Optofluid. Microfluid. Nanofluid.* **2015**, *2*, 15–21. [CrossRef]

18. Jankovics, H.; Kovacs, B.; Saftics, A.; Gerecsei, T.; Tóth, É.; Szekacs, I.; Vonderviszt, F.; Horvath, R. Grating-coupled interferometry reveals binding kinetics and affinities of Ni ions to genetically engineered protein layers. *Sci. Rep.* **2020**, *10*, 22253. [CrossRef]
19. Dér, A.; Valkai, S.; Mathesz, A.; Andó, I.; Wolff, E.K.; Ormos, P. Protein-based all-optical sensor device. *Sens. Actuators B Chem.* **2010**, *151*, 26–29. [CrossRef]
20. Abdulhalim, I. Model for Photoinduced Defects and Photorefractivity in Optical Fibers. *App. Phys. Lett.* **1995**, *66*, 3248–3250. [CrossRef]
21. Abdulhalim, I. Kinetic model for photoinduced and thermally induced creation and annihilation of metastable defects in hydrogenated amorphous silicon. *J. Appl. Phys.* **1995**, *77*, 1897–1901. [CrossRef]
22. Abdulhalim, I.; Gelbaor, M.; Klebanov, M.; Lyubin, V. Photoinduced phenomena in nano-dimensional glassy As2S3 films. *Opt. Mater. Express* **2011**, *1*, 1192–1201. [CrossRef]
23. Fábián, L.; Krekic, S.; Tóth-Boconádi, R.; Taneva, S.G.; Bálint, A.M.; Nánai, L.; Dér, A. Integrated optical investigation of two light-sensitive proteins. *AIP Conf. Proc.* **2017**, *1796*, 040001.
24. Konold, P.E.; Arik, E.; Weißenborn, J.; Arents, J.C.; Hellingwerf, K.J.; van Stokkum, I.H.; Kennis, J.T.; Groot, M.L. Confinement in crystal lattice alters entire photocycle pathway of the Photoactive Yellow Protein. *Nat. Commun.* **2020**, *11*, 4248. [CrossRef] [PubMed]
25. Khoroshyy, P.; Dér, A.; Zimányi, L. Effect of Hofmeister cosolutes on the photocycle of photoactive yellow protein at moderately alkaline pH. *J. Photochem. Photobiol. B Biol.* **2013**, *120*, 111–119. [CrossRef] [PubMed]
26. Hajdu, K.; Gergely, C.; Martin, M.; Zimányi, L.; Agarwal, V.; Palestino, G.; Hernádi, K.; Németh, Z.; Nagy, L. Light-harvesting bio-nanomaterial using porous silicon and photosynthetic reaction center. *Nanoscale Res. Lett.* **2012**, *7*, 400. [CrossRef]
27. Palestino, G.; Martin, M.; Agarwal, V.; Legros, R.; Cloitre, T.; Zimányi, L.; Gergely, C. Detection and light enhancement of glucose oxidase adsorbed on porous silicon microcavities. *Phys. Status Solidi C* **2009**, *6*, 1624–1628. [CrossRef]
28. Lin, G.R.; Su, S.P.; Wu, C.L.; Lin, Y.H.; Huang, B.J.; Wang, H.Y.; Tsai, C.T.; Wu, C.I.; Chi, Y.C. Si-rich SiNx based Kerr switch enables optical data conversion up to 12 Gbit/s. *Sci. Rep.* **2015**, *5*, 9611. [CrossRef]

IV. **Krekic, S.**; Mero, M.; Dér, A.; Heiner, Z. Ultrafast all-optical switching using doped chromoprotein films. *J. Phys. Chem. C* **2023**, *127* (3), 1499–1506. https://doi.org/10.1021/acs.jpcc.2c06232. IF: 4.177 (IF for 2021)

Pre-print reprinted with permission from *J. Phys. Chem. C* 2023, 127, 3, 1499–1506. Copyright 2023 American Chemical Society. The published article can be found on the website of **ACS Publications,** link: https://pubs.acs.org/doi/abs/10.1021/acs.jpcc.2c06232.

Ultrafast all-optical switching using doped chromoprotein films

Szilvia Krekic,[1,2,3] Mark Mero,[4] András Dér,[1]*, and Zsuzsanna Heiner[3]*

[1]Institute of Biophysics, Biological Research Centre, Temesvári krt. 62, 6726, Szeged, Hungary

[2]Doctoral School of Multidisciplinary Medical Sciences, University of Szeged, Dugonics tér 13, 6720, Szeged, Hungary

[3]School of Analytical Sciences Adlershof, Humboldt-Universität zu Berlin, Albert-Einstein-Straße 5-11, 12489 Berlin, Germany

[4]Max Born Institute for Nonlinear Optics and Short Pulse Spectroscopy, Max-Born-Straße 2a, 12489 Berlin, Germany

*Corresponding authors' e-mail addresses: heinerzs@hu-berlin.de, der.andras@brc.hu

Abstract

Next-generation communication networks require > Tbit/s single-channel data transfer and processing with sub-picosecond switches and routers at network nodes. Materials enabling ultrafast all-optical switching have high potential to solve the speed limitations of current optoelectronic circuits. Chromoproteins have been shown to exhibit a fast light-controlled refractive index change much larger than that induced by the optical Kerr effect due to a purely electronic nonlinearity, alleviating the driving energy requirements for optical switching. Here, we report femtosecond transient grating experiments demonstrating the feasibility of < 200-fs all-optical switching by hydrated thin films of photoactive yellow protein, for the first time, and compare the results with those obtained using bacteriorhodopsin. Possibilities for the practical utilization of the scheme in extremely high-speed optical modulation and switching/routing with nominally infinite extinction contrast are discussed.

Introduction

The exponential growth of Internet traffic carrying optically coded data trains (packets) requires telecommunication channels with Tbit/s rate and a corresponding sub-picosecond switching speed.[1–5] At Internet nodes, where high switching speed and repetition rate are especially important, currently so-called optical transceiver modules are used as electrical-optical interfaces with accompanying multiple conversions between optical and electric coding along an information channel. All-optical solutions are preferred to avoid any unnecessary delay in signal processing.[3,6] Modulation and routing can also utilize nonlinear optical (NLO) materials exhibiting large, rapid light-induced change in their absorption or refractive index.[7] Besides testing relatively well-known NLO solid-state materials, such as silicon, lithium-niobate[8], chalcogenide glasses,[9] and wide-bandgap semiconductor

waveguides[5], engineering of novel 2D materials[10] is also underway, but still far from practical applications. Another promising line of research is based on synthetic dyes of large, delocalized pi-electron systems showing high third-order polarizability typically without two-photon absorption losses, albeit with sensitivity or stability issues.[11,12] In contrast, natural pi-conjugated biomaterials with chromophores embedded in a stabilizing protein core exhibit high light sensitivity, long-term stability, and are readily available.[13–15] After photon absorption by the chromophore, the protein undergoes a cyclic reaction series called photocycle, where consecutive conformational changes occur through various intermediate states with characteristic absorption spectra before returning to the initial state. Since the first steps in the photocycle often proceed on a sub-picosecond time scale, they potentially can be exploited for ultrafast optical switching.

A nontrivial technical challenge in the application of chromoproteins as NLO materials in all-optical switching is the build-up of stable protein-substrate structures with controlled relative humidity that still allow the photocycle to take place. Doped chromoprotein films combined with passive integrated optical structures represent a convenient solution and have been shown to maintain stable optical properties for years.[16] Since the relative humidity in such hybrid structures affects the protein micro-environment, an in-depth characterization of the NLO properties and photocycle kinetics is mandatory.

One of the most thoroughly investigated chromoproteins for all-optical processing applications is the light-driven proton pump, bacteriorhodopsin (BR) - a membrane protein embedded in quasi-crystalline lipid-protein patches. BR has been used in a wide range of photonic and opto-electronic applications.[16–23] When used as the main adlayer component of integrated optical (IO) waveguides, thin films of BR were shown to be appropriate for photo-induced switching down to the sub-picosecond time domain.[24,25] Recently, photoactive yellow protein (PYP) has emerged as a candidate for all-optical switching applications.[26] In contrast to BR, PYP is a small, water-soluble protein offering much more straightforward incorporation into passive structures. Accordingly, the NLO properties of PYP films have recently been characterized[15,26] and shown promise for use in integrated optical modulators.[27] Nevertheless, utilization of the sub-picosecond photoreaction of the PYP photocycle[28,29] for ultrafast all-optical switching has not been accomplished so far.

The photocycles of BR and PYP in solution are depicted in Scheme 1, both showing fast, sub-picosecond to picosecond initial transitions. While the ultrafast kinetics of BR is well studied,[30–33] the ultrafast absorption kinetics of PYP in solution and crystalline form were only recently investigated.[28,34,35] At the same time, the role of environmental variables and structural details of newly engineered chromophore analogues on the ultrafast photocycle of PYP is still a subject of intensive research.[35–37] The existence of sub-picosecond initial transitions in dried, doped PYP films also needs confirmation.

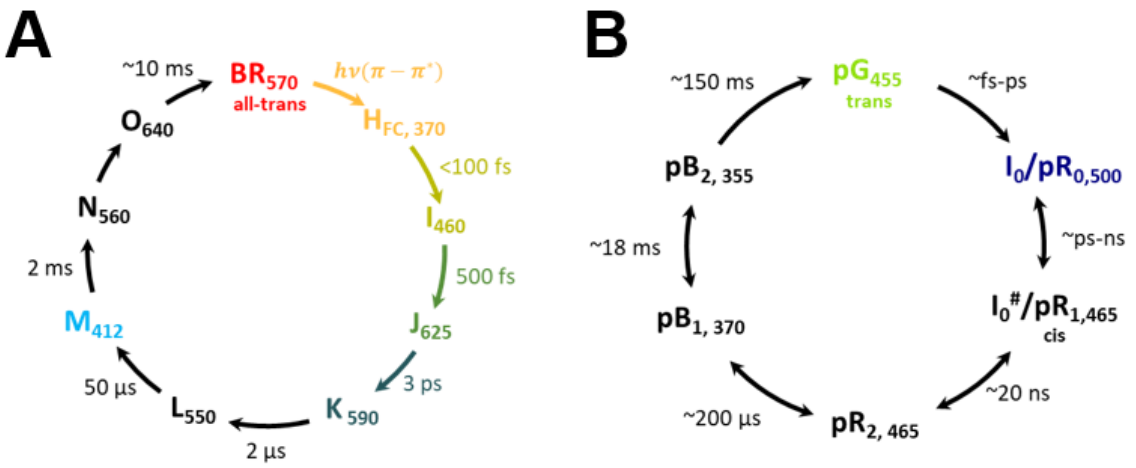

Scheme 1. Photocycle model of (A) bacteriorhodopsin and (B) photoactive yellow protein in solution based on Refs. [16,31,34,38–44].

Employing transient grating (TG) spectroscopy,[45,46] we show here that the photocycle of thin, doped PYP films with controlled humidity does contain a sub-picosecond initial step. We follow light-induced conformational changes over the first few ps after excitation, as revealed by the delay-dependent diffracted signal, and compare them with those obtained using thin, doped BR films. Harnessing the TG scheme itself, we successfully exploit the ultrafast kinetics of PYP films for the optical gating of a laser pulse with a rise and fall time down to < 200 fs depending on the film dopant material. The TG scheme naturally offers an arrangement for all-optical switching and modulation, where the diffracted signal represents the optically gated signal with an infinitely high nominal extinction ratio. Our experiments prove the feasibility of ultrafast all-optical switching using the early light-induced molecular transitions of PYP films. Further possibilities towards the practical utilization of such molecular transitions for ultrafast optical switching are briefly discussed.

Materials and methods

Sample preparation

For maintaining the water content of the thin protein films, polyacrylamide (PAM) and/or glycerol as doping materials were used. To reduce the cracking of the BR and PYP films, which occurs during the drying phase of the preparation, the protein solutions were first mixed with 87% glycerol as ballast material in various amounts, as explained in Ref[26]. Adding glycerol (GL) enables the creation of thin films in optical quality while also maintains the sample at an appropriate humidity, which is necessary for the integrity of the photocycle of the proteins. Adding glycerol to BR films secures the relative humidity inside the sample at 80-85%, based on our previous optical multichannel analyzer experiments.[26] During sample preparation with GL doping, the initial protein mixtures consisted of 10% volume ratio of glycerol for BR, and 2% for PYP. The solutions were sonicated for 1-2 minutes, then pipetted onto a 160-µm thick BK7 microscope cover slide. The samples were dried under an extractor fume for at least 12 hours before measurements, then they were sandwiched by using a 160-µm thick spacer between two slides to maintain appropriate sample thickness. The optical densities of the GL-doped films were 0.35 and 0.3 for BR and PYP film at our pump wavelength of 515 and 450

nm, respectively. The PAM-doped films were prepared based on a protocol published in Ref[47]. As a result, an 800-µm thick, 7.5 w/w % polyacrylamide layer containing the chromoprotein in high concentration was obtained and subsequently air-dried on a glass surface to form a 220-µm thick, optical-quality film (OD = 0.3 at 450 nm). All TG measurements were conducted at 23°C and at a relative humidity of 30-35%.

Experimental setup

For our ultrafast TG experiments, the visible optical pump and probe pulses were generated from the output of a commercial Yb laser/amplifier system, which delivered 180-fs laser pulses at a center wavelength of 1028 nm with a repetition rate tunable up to 100 kHz. Pulses at a center wavelength of 514 nm were obtained by second-harmonic generation from the Yb laser. Another portion of the 1028-nm pulses were used for pumping an optical parametric amplifier, which generated pump/probe pulses at wavelengths different from 514 nm. In the experiments discussed below, 450 nm and 480 nm pulses were employed. All pump and probe pulses had a pulse duration of 160 fs. Temporal pulse characterization was performed directly before the TG experiments based on the transient-grating frequency-resolved optical gating (TG-FROG) technique[48,49] by using the same TG setup with a 1-mm thick fused silica plate as the sample.

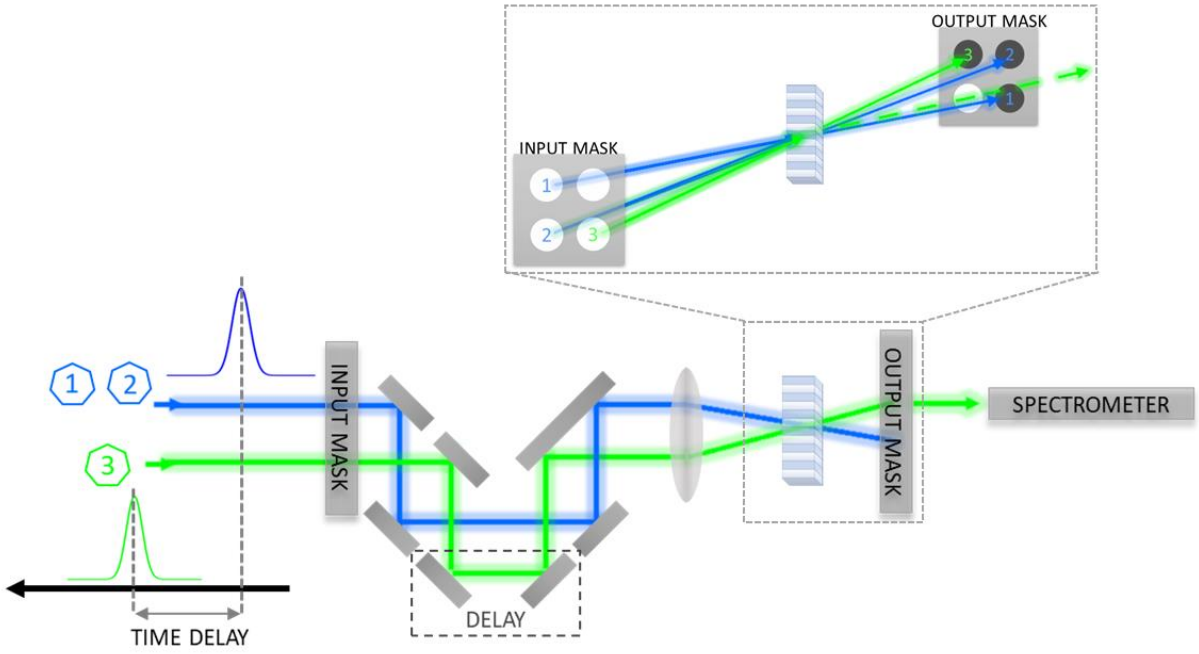

FIG. 1. Representative scheme and setup for the ultrafast transient grating experiments.

The schematics of the experimental method and setup are shown in Fig. 1. We used a simplified version[49] of the so-called folded BOXCARS geometry.[50,51] After beam expansion and spatial filtering (not shown), flat-top beams with a diameter of 2 mm were generated by sending up-collimated beams through an input mask. Beamlet 1 and 2 (pump) were derived from one of the expanded input beams and were reflected off the same mirrors securing identical arrival times at the sample. Beamlet 3 (probe) was obtained by transmitting the other input beam through a third hole on the mask and was delayed in time at 20-fs steps relative

to Beamlet 1 and 2. An *f* = 50-mm achromatic lens was used to spatially combine the three pulses (Beamlet 1-3) at the sample, which was placed in the focal plane. Depending on the experiment, the pulse energy per beamlet incident on the sample was 1-12.5 nJ at a repetition rate of 1 Hz. The diffracted signal was collected in the phase matching direction of $\vec{k}_1 - \vec{k}_2 + \vec{k}_3$, where $\vec{k}_{1-3}$ are the wave vectors of Beamlet 1-3, respectively. An output mask was used to spatially separate the diffracted signal from the incident beamlets, which was then detected by a miniature fiber optic spectrometer as a function of delay time. The pump and probe wavelengths were chosen to overlap with the absorption bands of the ground state and the fastest intermediates, respectively. Accordingly, 450-nm and 480-nm pump and 514-nm probe pulses were used for PYP, while 514-nm pump and 450-nm probe pulses were employed for BR (cf. Scheme 1). The two pump wavelengths of 450 and 480 nm in the case of PYP samples were used to test the hypothesis that the kinetics is different at these excitation wavelengths.[52] To induce ground state bleaching of the samples, i.e., creating a steady state that differs from the ground state, additional continuous wave (CW) excitation was used at 405 nm and 532 nm for PYP and BR, respectively.

Data were acquired in the delay range of -0.8 – 4 ps for BR and -0.8 – 10 ps for PYP samples. At each delay, only one single-shot spectrum was recorded and no averaging was performed for any of the time-dependent TG signal curves presented below. Pump-probe scans were repeated at least three times and showed high reproducibility. The background spectrum collected at a delay of -1.8 ps was subtracted from the data. The zero-delay was determined by generating a non-resonant Kerr-type diffraction signal from the uncoated glass substrate of the sample (i.e., no protein present), at an increased pump intensity. Since the spectral bandwidth of the pump and probe pulses was relatively narrow in this study, only a limited range of pixels were used and summed up at each delay to generate the time-dependent diffraction signal for further analysis.

Results and discussion

Bacteriorhodopsin

Glycerol-doped thin films of BR were used as our benchmark sample, since its photocycle is well known. The probe wavelength of 450 nm was chosen to fall close to the absorption peak of the I intermediate state of the protein (cf. Scheme 1A). Figure 2A shows the obtained diffracted probe intensity as a function of time (magenta line). The signal reaches its first maximum at the trailing edge of the excitation pulse and decays within 1 ps before it rises again. CW excitation of the sample at 532 nm almost completely diminishes the diffraction signal (cf. Fig. 2A, green line). Signal bleaching is due to the CW excitation creating a steady state population in the rate-limiting, blue-shifted M intermediate state (cf. Scheme 1) with an absorption maximum at 412 nm,[53] which does not have absorption at the applied pump wavelength of 514 nm.[54–56] Therefore, the bleached sample area cannot be excited by the pump laser and a diffraction grating cannot be formed.

To unravel the underlying dynamics, the time-dependent diffracted probe intensity was modelled using the known photocycle scheme for the early intermediates of BR.[25,31,57] Following a 160-fs excitation pulse at 514 nm, only the BR, H, I, J, and K coexisting

conformational states of the protein are formed within 4 ps. Accordingly, our model includes the intermediate states and transitions,

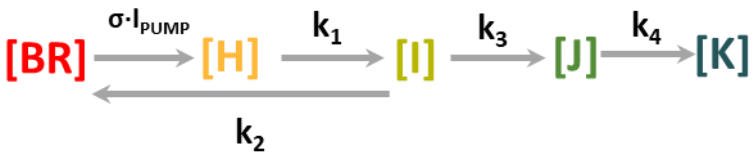

Scheme 2 Kinetic scheme for rate equations describing the initial steps of the photocycle of bacteriorhodopsin.

where [BR], [I], [J], and [K] represent the concentration of the intermediates, and [H] is the concentration of the Franck-Condon state,[31–33] $k_{1\text{-}4}$ are the rate constants, I_{PUMP} is the applied pump intensity, and σ is the absorption cross-section of the ground state.

The diffracted probe intensity, $\eta(t)$, was assumed to be proportional to the sum of the squares of the peak change in the real and the imaginary parts of the complex refractive index across the induced excited-state concentration grating, which in turn were assumed to be proportional to the concentration of the intermediate state normalized to the initial concentration of the ground state,[46,58]

$$\eta(t) \propto [a_i \sum_i \Delta n_i(t)]^2 + [a_i \sum_i \Delta \kappa_i(t)]^2 \propto \left[a_i \sum_i {}^{N_i(t)}/_{N_0}\right]^2, \quad (1)$$

where $\Delta n_i(t)$, $\Delta \kappa_i(t)$, and $N_i(t)$ are the change in the real and the imaginary parts of the complex refractive index, and the concentration of state *i*, respectively. Here, state *i* correspond to any state that contributes to the measured signal at the probe wavelength and a_i is a constant. N_0 denotes the dark-adapted concentration of the ground state. The time-dependent signal was modelled by calculating the sum of normalized concentration squared values for each time delay through solving the coupled differential equations for the concentrations and employing the least squares method. An absorption cross-section of $\sigma = 0.76\times10^{-16}$ cm^2 was assumed[25] and I_{PUMP} was calculated from experimental values. The rate constants were fitted starting from initial values obtained from the literature on BR.[25,31] The contribution of the J intermediate state to the diffracted signal was assumed to be negligible (i.e., $a \approx 0$ in Eq. (1)) due to the fact that the wavelength difference between the 625-nm absorption peak and the 450-nm probe wavelength is much larger than the width of the J-band. Figure 2B shows the so-obtained time-dependent concentrations, while the measured and modelled diffracted probe signals are presented in Fig. 2C.

The above results indicate a clear dominance of the BR-I transition in the measured signal within the first few 100 fs. On the other hand, after a delay of a few ps, the K intermediate state dominates. The rate constants we obtained by modeling the experimental data are k_1 = 1/100 fs^{-1}, k_2 = 1/1500 fs^{-1}, k_3 = 1/649 fs^{-1}, and k_4= 1/1787 fs^{-1}. These rate constant values are in good agreement with those published earlier.[25,30,31,59–64] Thus, the obtained transient grating signal can be fully reproduced by the standard photocycle model of BR (based on Scheme 2), confirming our hypothesis.

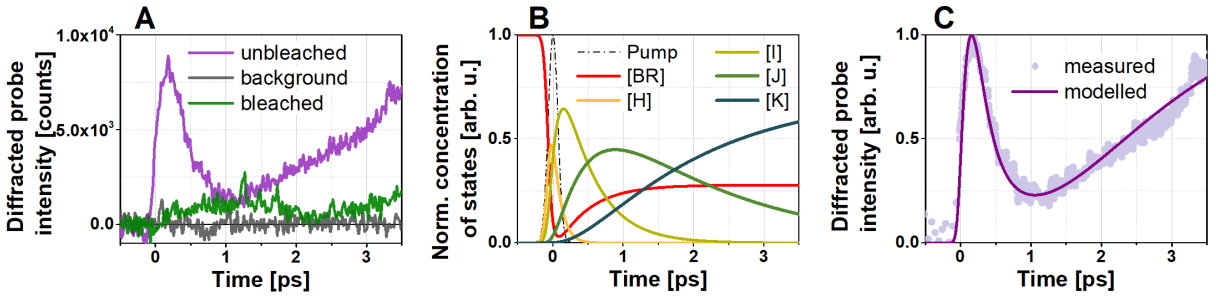

FIG. 2. Dynamics of glycerol-doped thin BR films. **(A)** Diffracted probe intensity as a function of time at a probe wavelength of 450 nm. The 160-fs pump pulses were centered at 514 nm. **(B)** Simulation of the normalized concentrations of the H, I, J and K intermediates after 160-fs photoexcitation at 514 nm. The temporal shape of the pump pulse is shown by the dash-dot line. **(C)** Measured and calculated diffracted probe intensity as a function of time.

Photoactive yellow protein

Measurement of the time-dependent diffraction signal was performed first on glycerol-doped PYP films pumped at 450 nm, which is an excitation wavelength at the peak of the ground state absorption and is most commonly used in the literature. In contrast to BR, the probe wavelength (i.e., 514 nm) was on the red wavelength side of the ground state, pG, to monitor the fastest known intermediate state, which exhibits an absorption peak near 500 nm. The corresponding measured diffraction signal up to a delay of 10 ps is shown in Fig. 3A (cf. orange line). The signal reaches its maximum at a delay of 140 fs and decays to 50% and 10% of its peak value at 520 fs and 1.6 ps, respectively, without any recovery over the measured delay range of 10 ps.

As in the experiments on BR, we attempted quenching of the diffracted transient grating signal by bleaching the ground state using CW excitation at 405 nm. While this quenching does, indeed, decrease the population of the ground state, at the same time, it increases the populations of all other states, including $pR_{0,1,2}$ and $pB_{1,2}$ states. Due to their smaller rate constants (longer decay times), mainly the blue-shifted pB states are expected to form as in the case of the M intermediate in the BR photocycle. Since the wavelength of the exciting laser is not totally outside of the absorption band of the pB states[65] (cf. Scheme 1), it can re-excite PYP molecules in the pB states, driving a portion of them back to the ground state.[66] Accordingly, the diffracted probe intensity decreased in proportion to the bleaching intensity but did not completely vanish, as shown in Fig. 3A (red, purple, blue lines). For example, at an average bleaching power of 30 mW, corresponding to an intensity of 1.0 W/cm², the diffracted signal decreased by 91 %. Using a different bleaching wavelength, for example, shifted more towards the red edge of the PYP ground state absorption, the diffraction is expected to be fully eliminated. Overall, our results here demonstrate sub-picosecond all-optical switching based on the NLO properties of PYP films and that the optical switching efficiency can be manipulated by creating a steady state of PYP intermediates.

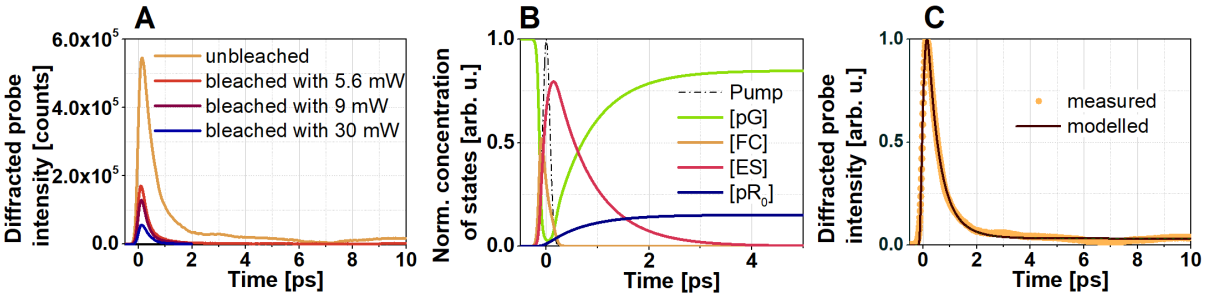

FIG. 3. Dynamics of glycerol doped thin PYP films. **(A)** Diffracted probe intensity as a function of time at a probe wavelength of 514 nm. The 120-fs pump pulses were centered at 450 nm. **(B)** Simulation of the normalized concentrations of the pG, FC, ES and pR_0 intermediates. The temporal shape of the pump pulse is shown by the dash-dot line. **(C)** Measured and calculated diffracted probe intensity as a function of time.

Based on the literature, only state pG and pR_0 contribute to the absorption change at 514 nm within the first 10-ps time frame.[28,34,52,67] However, using a model of the time-dependent diffracted probe intensity assuming only the presence of the two early intermediate states, pG and pR_0, the measured data could not be reproduced. Gradually extending the number of states in the model by adding a Franck-Condon and one or more excited states (similarly to that of the photocycle of PYP in liquid state[34,68]) and performing data regression based on the least squares method and Eq. (1), at least four states and four processes were needed for a satisfactory fit:

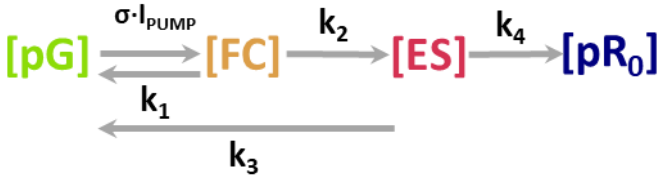

Scheme 3 Kinetic scheme for rate equations describing the initial steps of the photocycle of photoactive yellow protein.

Here, pG, FC, and ES correspond to the concentration of the ground state, the Franck-Condon state, and the excited state, respectively. Satisfactory fit is obtained when mainly states ES and pR_0 contribute to the diffracted signal. $k_{1\text{-}4}$ are the rate constants, I_{PUMP} is the applied pump intensity, and $\sigma = 1.682 \cdot 10^{-16}$ cm^2 is the absorption cross-section[68] of the ground state at 450 nm. Figure 3B shows the so-obtained time-dependent concentrations, while the measured and modelled diffracted probe signals are presented in Fig. 3C.

For the rate constants, we obtained k_1=1/42 fs^{-1}, k_2=1/96 fs^{-1}, k_3=1/876 fs^{-1}, and k_4=1/5364 fs^{-1}. Based on these results, we propose Scheme 3 for the early state of the photocycle model for thin, hydrated PYP films at an excitation wavelength of 450 nm.

The film dopant material had minor influence on the switching speed of PYP films. In contrast, shifting the excitation wavelength from the absorption peak of the pG state at 450 nm towards the red side, 480 nm, led to a drastic shortening of the switching time. With GL-doped films, the switched diffraction signal drops to 50% of its peak value at a delay 160 fs with 480-nm

excitation, as opposed to 520 fs obtained with a 450-nm pump. In addition, instead of a delayed buildup of the diffraction signal relative to the temporal peak of the excitation pulse as was seen with 450-nm pumping and glycerol doping (i.e., 140 fs), we obtained a negligible lag of 20 fs with 480-nm excitation. Figure 4A and 4B show the corresponding measured diffraction intensity up to a delay of 10 and 2 ps, respectively, summarizing these observations. Modelling of the time-dependent diffraction signal for the GL-doped film at a pump wavelength of 480 nm led to the rate constants, k_1=1/20 fs^{-1}, k_2=1/170 fs^{-1}, k_3=1/1500 fs^{-1}, and k_4=1/4040 fs^{-1} (cf. Fig. 4C). The rate values suggest that the much faster rise and decay time are due to the faster response of the Franck-Condon state at 480 nm than at 450 nm. We attribute the faster switching speed at 480 nm than at 450 nm to a higher stimulated emission cross section and concomitant emission, which forces the protein back to its ground state, as was also observed by Kuramochi et al[28].

The initial, few-100-fs and the final, 10-ps kinetics of the PAM-doped films followed closely that of the GL-doped films and showed somewhat slower decay components only on the intermediate few 100 fs – few ps time scale (cf. Fig. 4A and 4B, lines versus symbols). We tentatively attribute this difference between GL and PAM-doped films to a difference in the relative humidity and the protein structural heterogeneity.

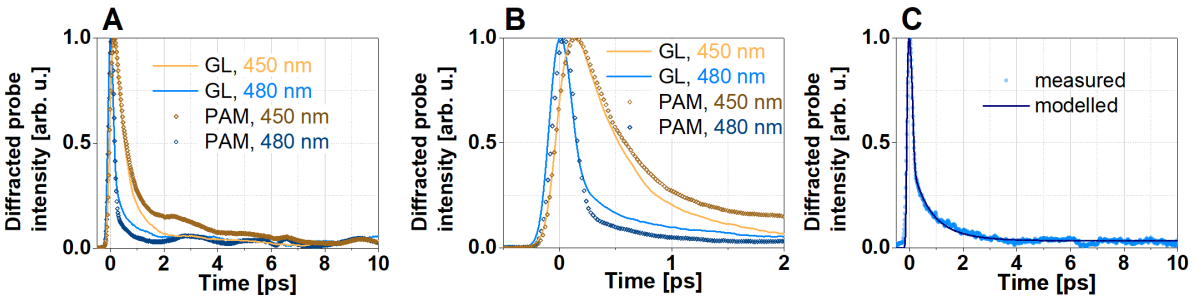

FIG. 4. Dynamics of PYP films. (A) Diffracted probe intensity as a function of time at a probe wavelength of 514 nm for GL-doped (solid lines) and PAM-doped (symbols) films. The excitation pulses were centered at 450 nm (yellow) or 480 nm (blue). (B) Zoomed-in version of (A) showing the temporal dependence up to 2 ps. (C) Measured and calculated diffracted 514-nm probe intensity as a function of time obtained for the GL-doped film with 480-nm, 160-fs excitation.

Summary and outlook

Employing the folded BOXCARS geometry of third-order nonlinear optical spectroscopy, we demonstrated ultrafast all-optical switching with doped PYP films for the first time, with a rise and fall time down to that of the 160-fs pump laser pulse depending on the excitation wavelength. We used glycerol and acrylamide as doping materials and monitored the temporal evolution of the laser-induced concentration grating in the films up to a delay of 10 ps. The film dopant material had minor influence on the switching speed of PYP films. In contrast, the excitation wavelength had a drastic effect on the switching time possibly due to the varying contribution of stimulated emission from the Franck-Condon to the ground state. Using coupled rate equations, we modelled the experimental time-dependent diffracted probe intensity and found that an extension of the early-state photocycle model of PYP was needed to obtain a better fit between experiment and theory. In contrast, our experimental

benchmark data on doped bacteriorhodopsin films could be fully explained using the known photocycle scheme for the known early intermediates. Our results show that an all-optical logic component based on PYP can be envisioned on the sub-ps timescale, enabling THz switching speed.

It is important to note that the ultrafast TG experiments, we report in this paper, go beyond our earlier results of all-optical on/off switching demonstrated by using bR films[25] and suggest the feasibility of a router-type all-optical packet switching by both chromoproteins (BR and PYP), as well, where data trains can be alternatively switched between different routes. While on/off switching can be used for encoding data, router-type switching is needed typically in Internet nodes, in order to deliver optically coded messages to the right address.[3,69] The latter requires a latching-type switch, where the on-rate should be extremely fast, and it should stay on during the transport of the whole data train ("packet").[3,69] In our experiments, the switch-on rate is following the duration of the excitation pulse (i.e., ca. 100 fs between 10% and 90% of maximal diffracted light intensity), while the switch stays in the "on" state until the "full" decay of the diffracted signal (for ca. 1 ps). We also showed that these switches can be temporarily inactivated by proper background CW illumination. It remains to be seen that the duration of the "on" state can be extended by using longer excitation pulses. Finally, the excited-state concentration grating employed in our scheme may also be used as an optically controlled diffractive element in future wavelength-selective switches (WSS).

For practical applications, the desirable high repetition rate remains to be demonstrated. Even though the repetition rate was limited by the duration of the photocycles of the chromoproteins in the present experiments, there are at least two straightforward solutions to the problem. One of them is utilizing the well-known photosensitivity of the intermediates in the photocycles of both BR and PYP,[39,66,70] namely, excitation of the intermediate states drives the proteins back to their ground-state conformations. In other words, the photocycles of both proteins are programmable by light. The other opportunity is a chemical modification of the chromophores. It has been demonstrated that both the retinal in bR and the p-coumaric acid in PYP can be removed by hydroxylamine treatment,[71–73] and the apoproteins can subsequently be reconstituted by non-isomerizable analogues of both chromophores.[36,74] In such chemically modified chromoproteins, only the Franck-Condon state and the quasi-stationary excited-state intermediate (I and ES, respectively) are allowed to be formed, because formation of the rest of the intermediates requires isomerization.[36,75] The I and ES excited states then spontaneously return to the ground states in the course of 10 ps (optimally suited for larger data packets).

Since the production of chromoproteins is cheap and they have high enough refractive index and absorption change, such proteins could be good candidates not only for light switching, but also for building holographic memories or image filtering.[76,77] In addition, BR and PYP have complementary advantages: BR works in a somewhat broader spectral range (between ca. 400 and 650 nm) as compared to PYP (between ca. 360 and 500 nm), while PYP, being a relatively small, water-soluble protein compared to BR that is available embedded in large membrane fragments, can be easily combined with nanostructured devices which makes it a suitable candidate as an active element in e.g., nanostructured IO devices.[27,78]

Acknowledgements

The authors are indebted to Prof. Hinorari Kamikubo for kindly providing the plasmid for PYP expression, and to Dr. Tomás Zakar for the protein preparation. The work has received funding from the National Research, Development and Innovation Office, Hungary (NKFI-1 K-124922), the Eotvos Lorand Research Network (ELKH KÖ-36/2021), and the Deutsche Forschungsgemeinschaft (DFG, No. GSC 1013 SALSA). Z. H. acknowledges funding by a Julia Lermontova Fellowship from DFG (GSC 1013 SALSA). S. K. acknowledges funding by the German Academic Exchange Service (DAAD) and the Eotvos Hungarian State Scholarship of Tempus Public Foundation funded by the Hungarian Government.

Author Declarations

The authors have no conflicts to disclose.

References

[1] Q. Cheng, M. Bahadori, M. Glick, S. Rumley, and K. Bergman, Optica **5**, 1354 (2018).
[2] P.C. Jain, in *2016 Int. Conf. Signal Process. Commun.* (2016), pp. 106–110.
[3] D.J. Blumenthal, Sci. Am. **284**, 96 (2001).
[4] E.N. Lallas, Opt. Switch. Netw. **31**, 22 (2019).
[5] D.J. Blumenthal, APL Photonics **5**, 020903 (2020).
[6] V. Kaushik and H. Saini, J. Opt. Commun. 000010151520200276 (2021).
[7] V. Sasikala and K. Chitra, J. Opt. **47**, 307 (2018).
[8] C. Monat and Y. Su, APL Photonics **5**, 020402 (2020).
[9] B.J. Eggleton, B. Luther-Davies, and K. Richardson, Nat. Photonics **5**, 141 (2011).
[10] H. Chen, C. Wang, H. Ouyang, Y. Song, and T. Jiang, Nanophotonics **9**, 2107 (2020).
[11] J.M. Hales, J. Matichak, S. Barlow, S. Ohira, K. Yesudas, J.-L. Brédas, J.W. Perry, and S.R. Marder, Science **327**, 1485 (2010).
[12] S.A. Haque and J. Nelson, Science **327**, 1466 (2010).
[13] P. Ormos, L. Fábián, L. Oroszi, E.K. Wolff, J.J. Ramsden, and A. Dér, Appl. Phys. Lett. **80**, 4060 (2002).
[14] A. Dér, S. Valkai, L. Fábián, P. Ormos, J.J. Ramsden, and E.K. Wolff, Photochem. Photobiol. **83**, 393 (2007).
[15] S. Krekic, D. Nagy, S.G. Taneva, L. Fábián, L. Zimányi, and A. Dér, Eur. Biophys. J. **48**, 465 (2019).
[16] J.A. Stuart, D.L. Marcy, and R.R. Birge, NATO Sci. Ser. SUB Ser. I LIFE Behav. Sci. **335**, 16 (2001).
[17] A. Dér and L. Keszthelyi, *Bioelectronic Applications of Photochromic Pigments* (IOS Press, Szeged, Hungary, 2001).
[18] N. Hampp and T. Juchem, NATO Sci. Ser. SUB Ser. I LIFE Behav. Sci. **335**, 44 (2001).
[19] N. Vsevolodov, *Biomolecular Electronics: An Introduction via Photosensitive Proteins* (Springer Science & Business Media, 2012).
[20] A. Mathesz, L. Fábián, S. Valkai, D. Alexandre, P.V.S. Marques, P. Ormos, E.K. Wolff, and A. Dér, Biosens. Bioelectron. **46**, 48 (2013).
[21] S. Roy, M. Prasad, J. Topolancik, and F. Vollmer, J. Appl. Phys. **107**, 053115 (2010).
[22] C.P. Singh and S. Roy, Opt. Commun. **218**, 55 (2003).
[23] Y.-T. Li, Y. Tian, H. Tian, T. Tu, G.-Y. Gou, Q. Wang, Y.-C. Qiao, Y. Yang, and T.-L. Ren, Sensors **18**, 1368 (2018).
[24] L. Fábián, E.K. Wolff, L. Oroszi, P. Ormos, and A. Dér, Appl. Phys. Lett. **97**, 142 (2010).
[25] L. Fábián, Z. Heiner, M. Mero, M. Kiss, E.K. Wolff, P. Ormos, K. Osvay, and A. Dér, Opt. Express **19**, 18861 (2011).
[26] S. Krekic, T. Zakar, Z. Gombos, S. Valkai, M. Mero, L. Zimányi, Z. Heiner, and A. Dér, Front. Plant Sci. **11**, 1567 (2020).
[27] D. Petrovszki, S. Krekic, S. Valkai, Z. Heiner, and A. Dér, Biosensors **11**, 432 (2021).
[28] H. Kuramochi, S. Takeuchi, K. Yonezawa, H. Kamikubo, M. Kataoka, and T. Tahara, Nat. Chem. **9**, 660 (2017).
[29] H. Kuramochi, S. Takeuchi, H. Kamikubo, M. Kataoka, and T. Tahara, J. Phys. Chem. B **125**, 6154 (2021).
[30] J. Briand, J. Léonard, and S. Haacke, J. Opt. **12**, 084004 (2010).
[31] O.A. Smitienko, T.B. Feldman, L.E. Petrovskaya, O. V. Nekrasova, M.A. Yakovleva, I. V. Shelaev, F.E. Gostev, D.A. Cherepanov, I.B. Kolchugina, D.A. Dolgikh, V.A. Nadtochenko, M.P. Kirpichnikov, and M.A. Ostrovsky, J. Phys. Chem. B **125**, 995 (2021).
[32] A. Yabushita and T. Kobayashi, Biophys. J. **96**, 1447 (2009).
[33] K.C. Hasson, F. Gai, and P.A. Anfinrud, Proc. Natl. Acad. Sci. **93**, 15124 (1996).
[34] P.E. Konold, E. Arik, J. Weißenborn, J.C. Arents, K.J. Hellingwerf, I.H.M. van Stokkum, J.T.M. Kennis, and M.L. Groot, Nat. Commun. **11**, 4248 (2020).
[35] S.-Y. Lu, T.J. Zuehlsdorff, H. Hong, V.P. Aguirre, C.M. Isborn, and L. Shi, J. Phys. Chem. B **125**, 12214 (2021).
[36] K. Kubota, T. Shingae, N.D. Foster, M. Kumauchi, W.D. Hoff, and M. Unno, J. Phys. Chem. Lett. **4**, 3031 (2013).
[37] Y. Kim, P. Ganesan, J. Jo, S.O. Kim, K. Thamilselvan, and H. Ihee, J. Phys. Chem. B **122**, 4513 (2018).

[38] J.K. Lanyi, Annu. Rev. Physiol. **66**, 665 (2004).
[39] S.P. Balashov, Isr. J. Chem. **35**, 415 (1995).
[40] Y. Imamoto and M. Kataoka, Photochem. Photobiol. **83**, 40 (2007).
[41] K.J. Hellingwerf, J. Hendriks, and T. Gensch, J. Phys. Chem. A **107**, 1082 (2003).
[42] L. Ujj, S. Devanathan, T.E. Meyer, M.A. Cusanovich, G. Tollin, and G.H. Atkinson, Biophys. J. **75**, 406 (1998).
[43] M.A. Cusanovich and T.E. Meyer, Biochemistry **42**, 4759 (2003).
[44] A.C. Terentis, L. Ujj, H. Abramczyk, and G.H. Atkinson, Chem. Phys. **313**, 51 (2005).
[45] K.A. Nelson, R. Casalegno, R.J.D.D. Miller, and M.D. Fayer, J. Chem. Phys. **77**, 1144 (1982).
[46] H.J. Eichler, P. Günter, and D.W. Pohl, *Laser-Induced Dynamic Gratings* (Springer-Verlag, Berlin, 1986).
[47] A. Dér, P. Hargittai, and J. Simon, J. Biochem. Biophys. Methods **10**, 295 (1985).
[48] J.N. Sweetser, D.N. Fittinghoff, and R. Trebino, Opt. Lett. **22**, 519 (1997).
[49] M. Li, J.P. Nibarger, C. Guo, and G.N. Gibson, Appl. Opt. **38**, 5250 (1999).
[50] A.C. Eckbreth, Appl. Phys. Lett. **32**, 421 (1978).
[51] J.A. Shirley, R.J. Hall, and A.C. Eckbreth, Opt. Lett. **5**, 380 (1980).
[52] L.T. Mix, E.C. Carroll, D. Morozov, J. Pan, W.R. Gordon, A. Philip, J. Fuzell, M. Kumauchi, I. Van Stokkum, and G. Groenhof, Biochemistry **57**, 1733 (2018).
[53] A. Dér, L. Oroszi, Á. Kulcsár, L. Zimányi, R. Tóth-Boconádi, L. Keszthelyi, W. Stoeckenius, and P. Ormos, Proc. Natl. Acad. Sci. **96**, 2776 (1999).
[54] L. Fábián, S. Krekic, R. Tóth-Boconádi, S.G. Taneva, A.M. Bálint, L. Nánai, and A. Dér, in *AIP Conf. Proc.* (2017), p. 040001.
[55] L. Zimányi, J. Phys. Chem. B **108**, 4199 (2004).
[56] C. Gergely, L. Zimányi, and G. Váró, J. Phys. Chem. B **101**, 9390 (1997).
[57] G.I. Groma, A. Colonna, J.-L. Martin, and M.H. Vos, Biophys. J. **100**, 1578 (2011).
[58] K.A. Nelson, R. Casalegno, R.J.D. Miller, and M.D. Fayer, J. Chem. Phys. **77**, 1144 (1982).
[59] A. Colonna, G.I. Groma, and M.H. Vos, Chem. Phys. Lett. **415**, 69 (2005).
[60] R.A. Mathies, C.H. Brito Cruz, W.T. Pollard, and C. V Shank, Science **240**, 777 (1988).
[61] S. Ruhman, B. Hou, N. Friedman, M. Ottolenghi, and M. Sheves, J. Am. Chem. Soc. **124**, 8854 (2002).
[62] A. V Sharkov, A. V Pakulev, S. V Chekalin, and Y.A. Matveetz, Biochim. Biophys. Acta - Bioenerg. **808**, 94 (1985).
[63] J. Dobler, W. Zinth, W. Kaiser, and D. Oesterhelt, Chem. Phys. Lett. **144**, 215 (1988).
[64] H. Kandori, K. Yoshihara, H. Tomioka, H. Sasabe, and Y. Shichida, Chem. Phys. Lett. **211**, 385 (1993).
[65] P. Khoroshyy, A. Dér, and L. Zimányi, J. Photochem. Photobiol. B Biol. **120**, 111 (2013).
[66] C.P. Joshi, B. Borucki, H. Otto, T.E. Meyer, M.A. Cusanovich, and M.P. Heyn, Biochemistry **44**, 656 (2005).
[67] P. Changenet-Barret, P. Plaza, M.M. Martin, H. Chosrowjan, S. Taniguchi, N. Mataga, Y. Imamoto, and M. Kataoka, Chem. Phys. Lett. **434**, 320 (2007).
[68] C.N. Lincoln, A.E. Fitzpatrick, and J.J. van Thor, Phys. Chem. Chem. Phys. **14**, 15752 (2012).
[69] A. Hamori, M. Serényi, A. Dér, K. Ferencz, and S. Kökenyesi, in (Proceedings of the European Microwave Association, 2008), pp. 221–225.
[70] R. Tóth-Boconádi, A. Dér, S.G. Taneva, and L. Keszthelyi, Biophys. J. **90**, 2651 (2006).
[71] D. Oesterhelt, M. Meentzen, and L. Schuhmann, Eur. J. Biochem. **40**, 453 (1973).
[72] Y. Imamoto, T. Ito, M. Kataoka, and F. Tokunaga, FEBS Lett. **374**, 157 (1995).
[73] Y. Kim, P. Ganesan, J. Jo, S.O. Kim, K. Thamilselvan, and H. Ihee, J. Phys. Chem. B **122**, 4513 (2018).
[74] M. Sheves, N. Friedman, A. Albeck, and M. Ottolenghi, Biochemistry **24**, 1260 (1985).
[75] T. Ye, N. Friedman, Y. Gat, G.H. Atkinson, M. Sheves, M. Ottolenghi, and S. Ruhman, J. Phys. Chem. B **103**, 5122 (1999).
[76] E. Korchemskaya, N. Burykin, S. Bugaychuk, O. Maksymova, T. Ebrey, and S. Balashov, Photochem. Photobiol. **83**, 403 (2007).
[77] D. Dini, M.J.F. Calvete, and M. Hanack, Chem. Rev. **116**, 13043 (2016).
[78] K. Hajdu, C. Gergely, M. Martin, L. Zimányi, V. Agarwal, G. Palestino, K. Hernádi, Z. Németh, and L. Nagy, Nanoscale Res. Lett. **7**, 400 (2012).

V. **Krekic, S.**; Mero, M.; Kuhl, M.; Balasubramanian, K.; Dér, A.; Heiner, Z. Photoactive yellow protein adsorption at hydrated polyethyleneimine and poly-L-glutamic acid interfaces. Submitted for publication to *Molecules* on April 7, **2023**. *Not yet published*. https://doi.org/10.26434/chemrxiv-2023-zmtk4. IF: 4.927 (IF for 2021)

Attached pre-print.

Photoactive yellow protein adsorption at hydrated polyethyleneimine and poly-L-glutamic acid interfaces

Szilvia Krekic[1,2,3], Mark Mero[4], Michel Kuhl[1,5], Kannan Balasubramanian[1,5], András Dér[2], and Zsuzsanna Heiner[1]*

[1] School of Analytical Sciences Adlershof, Humboldt-Universität zu Berlin, Berlin, Germany

[2] Institute of Biophysics, Biological Research Centre, Szeged, Hungary

[3] Doctoral School of Multidisciplinary Medical Sciences, University of Szeged, Szeged, Hungary

[4] Max Born Institute for Nonlinear Optics and Short Pulse Spectroscopy, Berlin, Germany

[5] Department of Chemistry and IRIS Adlershof, Humboldt-Universität zu Berlin, Berlin, Germany

*Correspondence: heinerzs@hu-berlin.de

Abstract

Chiral and achiral vibrational sum-frequency generation (VSFG) spectroscopy was performed in the 1400-1700 and 2800-3800 cm^{-1} range to study the interfacial structure of photoactive yellow protein (PYP) adsorbed on polyethyleneimine (PEI) and poly-L-glutamic acid (PGA) surfaces. Nanometer-thick polyelectrolyte layers served as the substrate for PYP adsorption, with 6.5-pair layers providing the most homogeneous surfaces. When the topmost material was PGA, it acquired a random coil structure with a small number of β_2-fibrils. Upon adsorption on oppositely charged surfaces, PYP yielded similar achiral spectra. However, the VSFG signal intensity increased for PGA surfaces with a concomitant redshift of the chiral C^{α}-

H and N-H stretching bands suggesting increased adsorption for PGA compared to PEI. At low wavenumbers, both the backbone and the side chains of PYP induced drastic changes to all measured chiral and achiral VSFG spectra. Decreasing ambient humidity led to the loss of tertiary structure with a re-orientation of α-helixes, evidenced by a strongly blue-shifted chiral amide I band of the β-sheet structure with a shoulder at 1654 cm^{-1}. Our observations indicate that chiral VSFG spectroscopy is not only capable of determining the main type of secondary structure of PYP, i.e., β-scaffold, but is also sensitive to tertiary protein structure.

Keywords: polyelectrolyte, vibrational sum frequency generation spectroscopy, photoactive yellow protein, polyethyleneimine, poly-L-glutamic acid, layer-by-layer deposition

1. Introduction

The interior of cells is far from being a pure electrolyte, as it contains a lot of solvated macromolecules and cytoskeletal components [1,2]. Under such circumstances, biochemical reactions are dominated by macromolecular interactions taking place at charged interfaces between proteins or nucleic acids and supramolecular assemblies (composed of protein biopolymers, planar or cubic lipid phases, etc.), inside a dynamic, aqueous environment [3–7]. It has been shown that the dynamics of a model peptide at the interface significantly deviates from that observed in the bulk [8], implying that proper characterization of the behavior of peptides and proteins at macromolecular interfaces, including their reversible adsorption to surfaces, is a prerequisite for understanding fundamental physiological processes stemming from intracellular reactions [9]. Upon adsorption, proteins self-assemble into viscoelastic 2D nanolayers [10,11], depending on the overall conditions at the interfaces, such as material surface parameters, surface charge, pH, concentration of proteins, etc. [12–15]. However, the adsorption of a protein is also highly influenced by its amino acid sequence and its higher-order structure.

A detailed knowledge about these complex phenomena, dominated by electrostatic, van der Waals, and hydrophobic interactions, is also crucial when designing biomaterials for

implants, medical devices, and bioelectronics. On the other hand, photosensitive coatings based on biomolecules are attractive due to their biodegradability and easy manufacturability for the conversion of light to electrical energy [16], and for integrated optics [17–19]. In such applications, controlled immobilization of proteins is needed to create well-ordered protein layers with high optical quality.

All-in-all, understanding and controlling macromolecular interactions with biocompatible surfaces at the nanoscale, in their nearly natural, aqueous environment, is necessary from the point of view of both basic biochemistry and the development of advanced functional biomaterials and biosensors. *In situ* determination of the orientation and secondary structure of the adsorbed biomolecules at interfaces would be required, but the atomic-level description of the interacting macromolecular interfaces is also still to come.

To this end, methods of measurement based on physical principles (e.g., infrared and Raman-techniques, CD-spectroscopy, neutron scattering, micro-calorimetry, electron microscopy, and evanescent-wave based techniques, such as OWLS and interferometry) are widely used [20–26], but combined chemical and surface specificity is usually missing. Vibrational sum-frequency generation (VSFG) spectroscopy is a powerful, label-free technique, which is especially suited for such investigations, as it is sensitive only to anisotropic molecular structures that are characteristic to the immediate vicinity of macromolecular interfaces, and, at the same time, it retains the chemical sensitivity of infrared spectroscopy [27–31]. In addition to surface specificity and structural information, the VSFG technique is also capable of revealing molecular chirality [32–34] and secondary structure of proteins [30,35,36], in a very similar manner to the methods based on vibrational circular dichroism (VCD) [37,38] and Raman optical activity (ROA) [39–41].

Photoactive yellow protein (PYP) is a molecule with a high potential for photosensitive coating applications. PYP is a water-soluble light-sensing protein from the microorganism *Halorhodospira halophila*. PYP is a hydrophilic, 14 kDa protein consisting of 125 amino acids and its structure often serves as a model for understanding biologically important

photoreceptors, such as rhodopsins, and receptor activation in biological signal transduction processes [42–44]. Recently, PYP received more attention due to its possible application in bioelectronics and integrated optics [18,19,45–47]. PYP belongs to the group of globular proteins and is the model structure for the PAS- (Per–Arnt–Sim) domain superfamily, which is a signal transduction α/β pathway structure commonly found in prokaryotic and eukaryotic organisms [48]. PAS domains are key components in sensory and signaling proteins, and they are an integral part of the protein-protein interactions taking place during signaling. The α/β pathway structure of PYP consists of a central β-sheet with five strands and helical connectors on both sides. On the sides of the β-sheet, the PYP molecule has two hydrophobic cores [49–51]. The molecular surface of PYP includes several patches which have both negative and positive electrostatic potential since mostly polar amino acids can be found on the outer side that interact with solvents via dipole-dipole interactions. Being a highly soluble protein, PYP has all its important hydrophilic parts outside, forming a water shell. Therefore, hydrogen bonds as driving forces play a determinative role besides ionic interactions. In contrast, the apolar amino acids sit in the interior part of the protein but are also expected to play a role in conformational changes assumed to accompany the adsorption process [52].

In this paper, we report on a model study carried out by using high-spectral-resolution, 100-kHz VSFG spectroscopy [53,54] on photoactive yellow protein and its adsorption on self-assembled layers of biopolymers of different electric charge. The macromolecular surface interacting with PYP was built up from polyethyleneimine (PEI) and poly-L-glutamate (PGA) chains via layer-by-layer (LbL) deposition, forming positively and negatively charged layers on the surface of a CaF_2 substrate, respectively [55]. LbL-deposition is a versatile self-assembly technique where materials with complementary interactions are used in an alternating fashion to build up multilayer structures at the nanoscale [56,57]. This self-assembly process is most often driven by electrostatic interactions between polyelectrolytes (e.g., PEI; poly-L-lysine, PLL; PGA; polyacrylic-acid, PAA, polydiallyldimethylammonium chloride, PDDA; and polystyrene sulfonate, PSS, etc.), where the alternating layers carry opposite net charge [10,55,58–61]. The secondary structure of the topmost layer of the films strongly affects the

conformation of species adsorbed onto the surface, for example, the β-sheet structure at the interfaces in nanoscale films supports cell spreading [62]. Here, we extensively characterize the conformational changes taking place upon the interaction of our model protein, PYP, with positively charged PEI and negatively charged PGA interfaces at the molecular level, by applying a self-developed VSFG setup. Chiral- and achiral-mode spectra also reveal orientational information of both the adsorbed protein and the water molecules at the interface. The results enable deeper insight into protein interaction processes at biological interfaces, and their generalizable implications for basic and applied sciences are briefly discussed.

2. Results and discussion

2.1 VSFG spectra of hydrated PYP films

To determine the VSFG spectrum of PYP without the effects of the charged polyelectrolyte layers, PYP films were created on top of plasma-treated CaF_2 slabs. These slabs were kept at constant humidity and temperature during the experiments. VSFG spectra measured for a high-humidity (RH > 85%) environment are shown in Figure 1. The spectra of the hydrated thin protein films were acquired in different chiral and achiral polarization combinations with the spectral range of the broadband mid-infrared (MIR) laser beam tuned to either 2800-3500 cm^{-1} or 3000-3800 cm^{-1}, to cover the C-H, N-H, and O-H stretching regions. The VSFG spectra recorded in the two cases were joined at 3500 cm^{-1} (cf. Figure 1).

In achiral polarization combinations (PPP and SSP), intense C-H stretching bands are visible between 2800 and 3000 cm^{-1} that can be assigned to the C^{α}-H, CH_2, and CH_3 vibrational modes of the protein (cf. Figure 1a). The most intense bands, the CH_3 symmetric and asymmetric stretching modes, appear at 2883 and 2958 cm^{-1}, respectively, together with the Fermi resonance of the methyl group at 2945 cm^{-1}, i.e., a resonance between the symmetric methyl stretching and bending overtone. The high obtained intensity of the vibrational modes

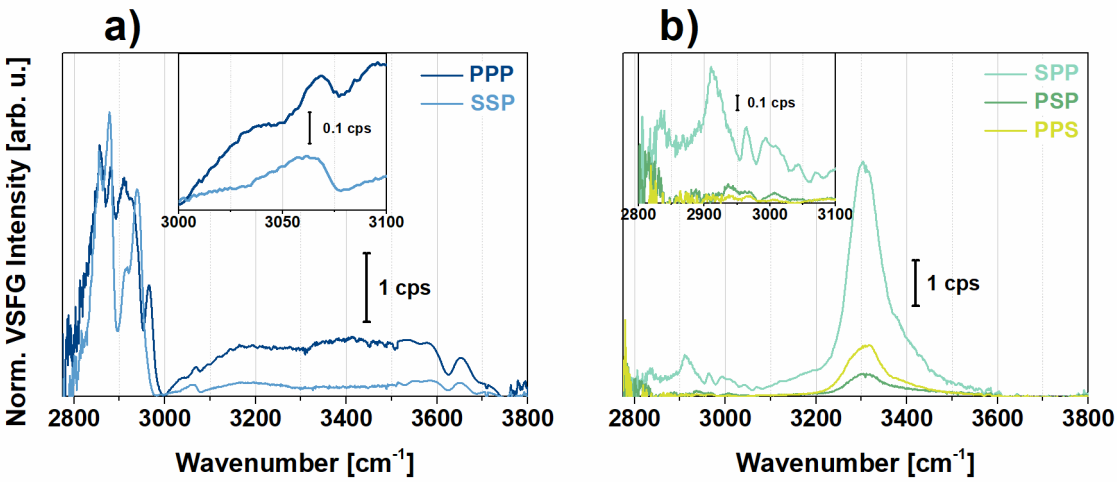

Figure 1. (a) *Achiral (SSP, PPP) and* ***(b)*** *chiral (SPP, PSP, PPS) VSFG spectra of a hydrated thin film of PYP on CaF_2. The spectra were interlinked at 3500 cm^{-1} from two measurement sets between 2800-3500 and 3000-3800 cm^{-1}. The insets show the zoomed-in view in the 3000-3100 cm^{-1} (a) and the 2800-3100 cm^{-1} range (b).*

of the methyl group correlates not only with their large number in the side chains of the protein but also with their highly ordered arrangement at the air-protein interface. The high conformational order of the methyl groups is due to their hydrophobic nature leading them to point more upwards in the direction of the vapor. The contribution of the symmetric (2850 cm^{-1}) and asymmetric (2930 cm^{-1}) stretching mode, and the Fermi resonance (2910 cm^{-1}) of the methylene group is relatively small. These observations are in good agreement with previous studies at hydrophilic silica surfaces [63] and at the air-water interface [33,64] for globular proteins. The C^{α}-H stretching band appears at 2984 cm^{-1} and shows a large vibrational amplitude in PPP as well as in all chiral polarizations, while it is almost undetectable in the SSP polarization combination. Between 3000 and 3100 cm^{-1}, three C-H stretching modes of aromatics, at 3030, 3050, and 3067 cm^{-1}, and the overtone of the symmetric bending mode of the NH_3^+ groups from the side chains are present. We can see interference effects between the aromatic C-H stretching and the overtones of NH_3^+ modes of the side chains (Figure 1a).

The water molecules contributing to the spectrum in the O-H region are organized in two extreme arrangements: the tetrahedrally coordinated (“ice-like”, ~3200 cm^{-1}) and asymmetrically bonded (“liquid-like”, ~3450 cm^{-1}) state. At ~3600 cm^{-1}, the band belongs to a weakly oriented O-H group, which originates from the interaction with the ester groups of the sidechains of PYP. The narrow bands found at ~3660 and 3700 cm^{-1} can be assigned to the

non-hydrogen-bonded, “free” O-H stretching mode of water molecules. The “free” O-H stretching band is usually a narrow, single vibrational mode. Nevertheless, at the air-protein interface in our study, two distinct groups of interfacial water molecules with H atoms protruding into the vapor phase may be found exhibiting different average dipole orientations and O-H bond lengths at the interface.

At chiral polarization combinations (SPP, PSP, and PPS, cf. Figure 1b), four C-H stretching modes at 2945, 2970, 2984, and 2998 cm^{-1} appear. The methylene stretching band is also visible at 2910 cm^{-1} in SPP polarization, which may be a contribution from the $C^{\beta}H_2$ groups of sidechains. At 3300 cm^{-1}, we can see bands associated with N-H stretches, which are virtually nonexistent at achiral polarizations. This observation of chiral N-H stretching features is in accordance with previously assigned bands with respect to the secondary structure of antiparallel β-sheet or α-helix structures [35]. Around 3200 and 3400 cm^{-1}, chiral O-H stretching vibrations are clearly visible as shoulders on the N-H stretching band, which can be attributed to water. This shows that the orientation of the interfacial water molecules is strongly influenced by the polar sidechains of the protein. Previous studies concluded that this water reorientation occurs within an interaction distance of about < 10 Å at the air-water interface [65]. This chiral signature of interfacial water is coupled to the chiral N-H stretching modes of the backbone indicating that the secondary structure of PYP at the air-water interface is well-ordered and the interfacial water molecules that are H-bonded to the backbone or interacting with the polar sidechains are following the ordering of the N-H dipoles. Since the chirality of the C^{α}-H group governs the symmetry of the N-H moiety [32], we likely see here the well-ordered β-sheet part of PYP. This β-scaffold motif stands at the end of the protein from the 88^{th} to the 125^{th} amino acid, where most of the side chains (22 out of 38) are polar or charged. The same chiral feature we observed here was previously assigned in the literature to the C-H and N-H groups of the backbone of an antiparallel β-sheet (model peptide of LK_7) also influencing the orientation of nearby water molecules [65]. From an analysis based on the maximum entropy method (MEM) [66,67] performed on our measured homodyne

VSFG spectra (cf. Figure S1), we can assume that the anti-parallel β-sheet part of PYP, i.e., β-scaffold, is more likely oriented parallel to the surface.

2.2. VSFG spectra of hydrated PEI and PEI+PGA at the air-CaF_2 interface

Figures 2a-d show achiral (PPP, SSP) and chiral (SPP, PSP) spectra of PEI and PEI+PGA polyelectrolytes at the air-water interface in the spectral range from 2800 to 3600 cm^{-1}. While the achiral spectra are dominated by C-H and O-H stretching modes, the chiral features correspond mostly to C-H vibrational modes. In order to collect more comprehensive information, first, the imaginary part of $\chi^{(2)}$ was calculated based on MEM from which the number of vibrational modes and the sign of their amplitudes can be fixed for further analysis. In the next step, each of the normalized VSFG spectra was fitted by a sum of Lorentzian functions based on Equation (1), where the number and sign of the amplitudes of the resonances were taken from the previous MEM analysis. We employed a global fitting procedure (based on Equation (1)) on the VSFG spectra in PPP and SSP, as well as SPP and PSP polarizations. The resulting curves are also shown in Figures 2a-d.

In the achiral spectra obtained for PEI (Figure 2a), characteristic CH_2 vibrational modes are visible. The bands at 2840, 2856, and 2873 cm^{-1} correspond to methylene symmetric stretching modes for variously hydrated forms of PEI (i.e., anhydrate, hemihydrate, and dihydrate) for which the asymmetric stretching modes appear at 2890-2900, 2914, 2925 cm^{-1}. Between 2940 and 2990 cm^{-1} two broad features can be extracted with a resonance wavenumber of 2950 and 2980 cm^{-1}. Since the bandwidth of both resonances is ~25-40 cm^{-1}, we assign them to the Fermi resonances of the methylene modes. In the O-H stretching range, two broad vibrational bands at 3120 and 3450 cm^{-1} are observed with damping factors of 150 and 100 cm^{-1}, respectively. The red-shifted mode at 3120 cm^{-1} shows strong, tetrahedral H-bonding interactions with PEI which can originate from the interaction of interfacial water with the tertiary or secondary amine groups via Coulombic forces. Similar results were observed earlier in the VSFG spectra of various cationic polymers at interfaces [68,69]. The blue-shifted O-H

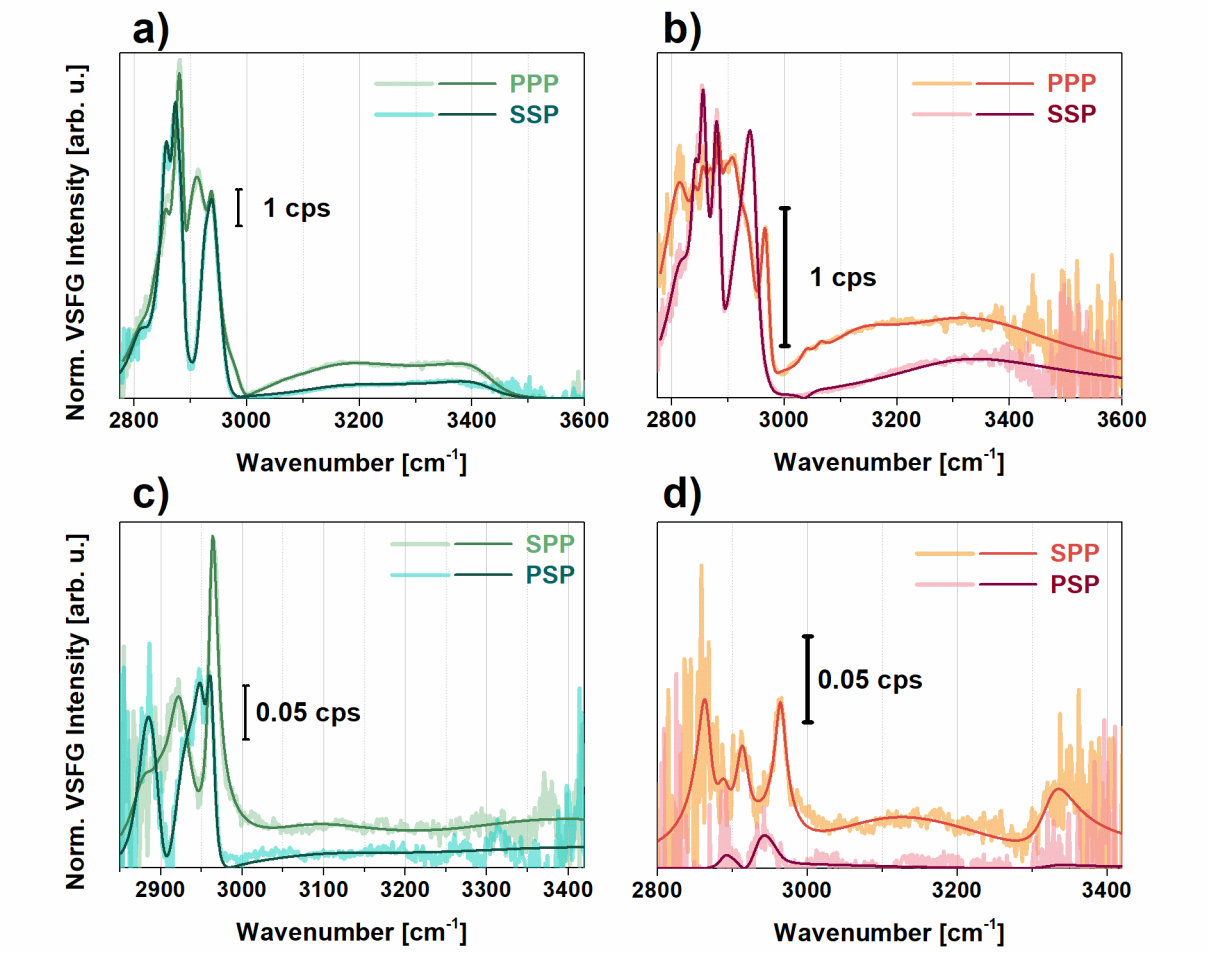

Figure 2. *Measured and fitted VSFG spectra of PEI on CaF_2* ***(a)*** *and* ***(c)****, and PGA on PEI-CaF_2* ***(b)*** *and* ***(d)****. Figures on the top represent the achiral VSFG spectra in PPP and SSP polarizations, on the bottom correspond to the chiral SPP and PSP polarization combinations. The fitted curves are based on Equation (1).*

stretching mode at 3450 cm^{-1} corresponds to the asymmetrically bonded, i.e., less than tetrahedral, group of water molecules, most probably near the primary amine groups since this group has more flexibility in space and this group induces an H-up ordering of water molecules associated with a positive amplitude in the imaginary part of χ^2 (cf. Figure S2a). In the chiral VSFG spectra of PEI (Figure 2c), C-H stretching bands appear at 2890, 2900, 2925, and 2950 cm^{-1} suggesting that the hydrated layer contains secondary structural elements in the chain, i.e., double helix conformational parts [70]. Around 3070, 3270, and 3320 cm^{-1}, N-H and O-H stretching modes with small amplitudes are observable which can be linked to the chiral C-H groups. The lower N-H stretching frequency indicates a strong N-H···N hydrogen bond.

In the achiral VSFG spectra of PGA (cf. Figure 2b) between 2800 and 2950 cm^{-1}, several symmetric, asymmetric CH_2 stretching, and Fermi resonance modes appear, indicating that the methylene groups are in both trans and cis form. We can observe a very strong band at 2933 cm^{-1} and a doublet at 2952 and 2962 cm^{-1} which can be associated with the C-H stretching modes of the methylene groups. These observed CH_2 vibrational modes are in good agreement with previous FT-Raman studies [71]. A valley detected at 2991 cm^{-1} can be assigned to the antisymmetric stretch of CH_2. A weak vibrational mode appears at 3056 cm^{-1} corresponding to the symmetric bending overtone of the NH_3^+ group which was also obtained earlier by using polarized Raman and FTIR spectroscopy on L-glutamine [20]. The appearance of this vibrational mode is more likely due to the charged primary amine groups of branched PEI which are interacting with the side chains of PGA. For interfacial water, the lower-frequency vibrational band around 3150 cm^{-1} (FWHM ~ 110 cm^{-1}) corresponds to strongly H-bonded interfacial water, namely, it reveals the Coulombic/ionic interaction between the COO^- group and $H^{\cdots}O$-H. In Figure S2, this band shows a negative amplitude in the imaginary part suggesting an H-down orientation on the top of PGA. The broad vibrational band at ca. 3350 cm^{-1} (FWHM ~ 200 cm^{-1}) is the overtone of the OH bending mode. Such a broad feature comes from a broad orientational distribution of interfacial water [72] which is most probably embedded in and between the backbone of PGA. Near 3500 cm^{-1}, a Fano-shape resonance is shown which can be linked to the stretching overtone of the C=O group. Since the stretching frequency of this group is very sensitive to the intramolecular H-bonding, we may also see here the interaction of some C=O groups with water molecules.

At chiral polarizations (cf. Figure 2d), C-H vibrational bands of PGA are identified at 2890, 2934, and 2970 cm^{-1}. We attribute the first and third vibrational bands to the out-of-plane and in-plane C^{α}-H stretching modes, respectively, governing chirality in amino acids. This doublet was also obtained in the Raman spectra of alcohols [21]. Above 3000 cm^{-1}, a very weak signal with broad bandwidth was detected in both SPP and PSP polarizations suggesting that PGA does not form well-ordered β-sheet or α-helical arrangements since the characteristic chiral N-H stretch at ~3300 cm^{-1} is missing. Instead, PGA most probably lies parallel to the surface of

PEI in a random coil structure given that the chiral N-H stretching signal is forbidden in random coil and disordered structures [35]. We found that the overall VSFG signal decreased when PGA was adsorbed on PEI which is most likely due to destructive interference between the methylene modes of PEI and PGA.

Since the homogeneity of the PEI and PEI+PGA layers can be improved by creating several pairs of oppositely charged layers [58,61,73], we studied how the VSFG spectra of the topmost layer of PGA changed when 0.5 versus 6.5 pairs of layers were built up. The results are summarized in Figure S3. In each of the applied polarization combinations (PPP, SSP, SPP) we observed a much (factor of two) higher signal for 6.5-pair layers due to the higher surface homogeneity. Importantly, the red-shifted O-H stretching mode in each polarization shows a higher signal which can be attributed to a well-ordered interfacial water structure near the charged side chains of amino acids.

2.3. PYP adsorption at air-polyelectrolyte interfaces

Figure 3a-d show the VSFG spectra of adsorbed PYP on PEI and PEI+PGA layers in the range of 2800 and 3600 cm^{-1} obtained in SSP and SPP polarization combinations. For comparison, the spectra acquired for the polyelectrolyte layers and the hydrated PYP film separately are also plotted. As shown in Figure 3, the adsorption of PYP on the polyelectrolyte layers of PEI and PEI+PGA led to significant spectral changes. The C^{α}-H stretching feature shows up as a shoulder at 2980 cm^{-1} in both achiral and chiral polarizations. This has been observed previously by other groups on various types of proteins (e.g., $LK_7\beta$, pepsin). While strong stretching modes of methylene groups are observed from the polyelectrolytes, almost every C-H stretching mode is shifted when PYP is adsorbed on the polyelectrolyte surfaces. These shifts are due to the vibrational modes of methyl groups from the nonpolar side chains of PYP, similar to what was shown in the case of hydrated PYP on CaF_2. The vibrational modes centered at 2860, 2885, 2915, and 2945 cm^{-1} are previously assigned (in the case of hydrated PYP) to the CH_2 and CH_3 symmetric stretch, CH_2 asymmetric stretch, and the Fermi resonance of the CH_3 group, respectively. Between 3000-3100 cm^{-1}, characteristic aromatic C-H stretching modes interfere with the symmetric bending overtone of the NH_3^+ group derived

from PYP side chains. The VSFG spectra obtained for PYP and adsorbed PYP on both surfaces show a marked difference. The bands at 3030, 3050, and 3070 cm^{-1} appear in chiral polarization clearly without interference for each PYP sample, while in achiral polarizations the adsorbed PYP shows a valley at 3030 cm^{-1} with narrow bands at 3070 and 3085 cm^{-1} due to the interference between the aromatics C-H stretching with the amide B mode.

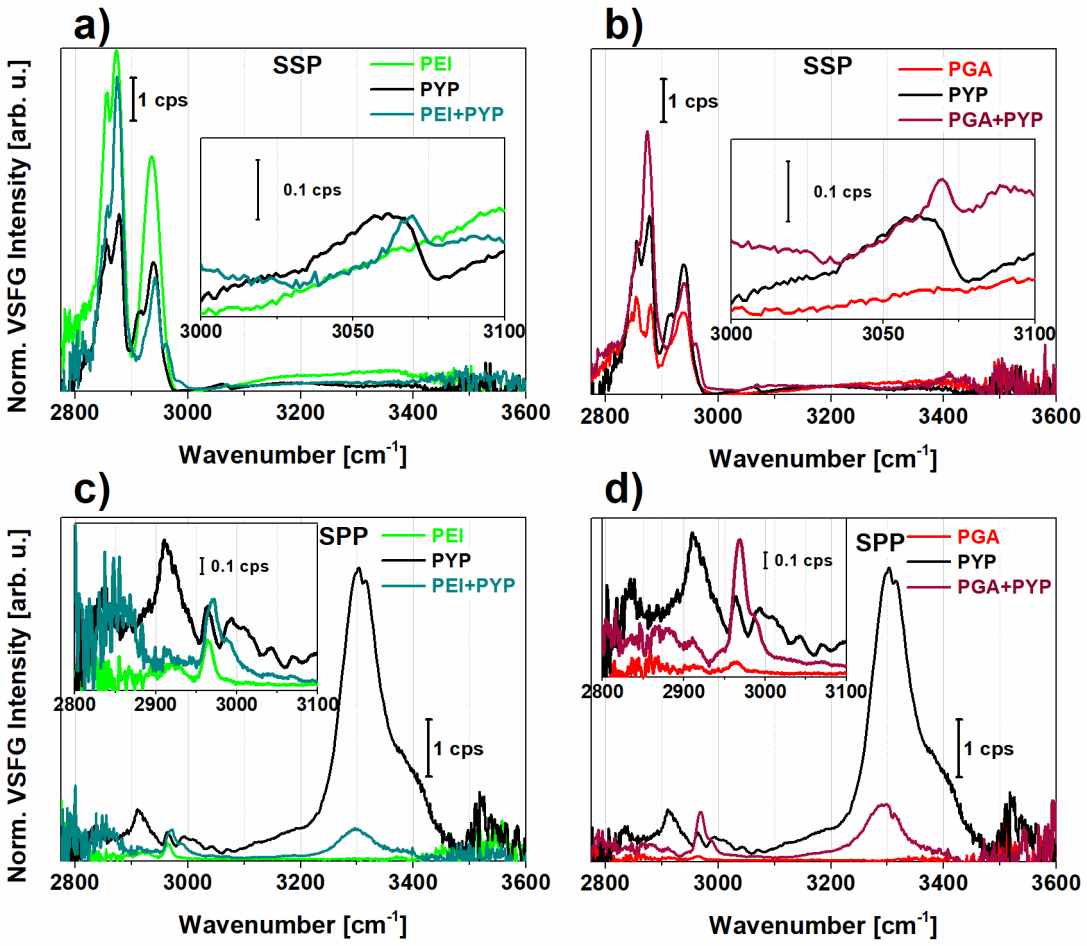

Figure 3. *Normalized VSFG spectra of photoactive yellow protein (PYP) adsorbed on PEI* ***(a,c)****, PGA* ***(b,d)*** *polyelectrolyte layers prepared by the LbL method. For comparison, the corresponding spectrum of PYP film (black) is also shown. Panel (a,b) and (c,d) show achiral and chiral VSFG spectra, respectively.*

The imaginary part of $\chi^{(2)}$ was calculated from the acquired VSFG spectra (cf. Figure S2) to provide additional information about the interfacial orientation of certain molecular groups. A positive/negative sign of the broad O-H stretching band in the imaginary part of $\chi^{(2)}$ above 3000 cm^{-1} represents a net hydrogen-up/down orientation [74,75]. Thus, the bands at 3150 cm^{-1} for PEI and 3200 cm^{-1} for PGA suggest that water above/on the top of the polyelectrolyte

layers exhibits an H-down orientation. Since PGA is negatively charged, such an H-down orientation at the surface is expected through electrostatics, however, an H-down orientation at the PEI surface is not. Although PEI is positively charged at physiological pH, only an amount of ~30% of branched PEI amines are protonated at a pH of ~7.4 [76,77], which can be responsible for the deduced orientation of interfacial water. On the other hand, PEI is a weak hydrophobic polymer due to its ethylene-rich backbone which further controls the orientation of the surrounding water molecules. Upon PYP adsorption on PEI, the O-H orientation flips to H-up most probably due to the side chains of PYP.

In the chiral spectra in Figures 3c and 3d, adsorption of PYP on both PEI and PGA lead to the emergence of characteristic bands at 2943, 2958, 2976, and 2990 cm^{-1}, in accordance with the presence of C^{α}-H and CH_3 groups of various amino acids in PYP. The valley at 2958 cm^{-1} and the local peak at 2976 cm^{-1} can be attributed to C^{α}-H stretching. These bands show opposite signs in the imaginary χ^2 spectra (Figure S2) suggesting that the C^{α}-H stretch exhibits the same chirality and orientation as the N-H stretch at ~3300 cm^{-1}. From this information, we can conclude that these chiral vibrational modes can be connected to the antiparallel β-sheets with hydrogen bonds between C═O···H–N which are lying on the plane of the surface. The appearance of the spectral shoulder at 2990 cm^{-1} is an indication of a C^{α}-H bond from other amino acids, most often assigned to lysine [32,78]. In the structure of the β-scaffold motif of PYP, lysine can be found in the highest number. The β-sheet structure is also supported by the well-ordered N-H stretching and the presence of a strong chiral amide I vibrational mode (cf. Figure 4b). We observed only small differences in the VSFG spectra of PYP adsorbed on PEI versus PGA. However, the higher overall VSFG intensity obtained for PYP on PGA than on PEI suggests that a larger amount of PYP was adsorbed on the PGA surface possibly due to the random coil structure of PGA facilitating better PYP adhesion. The vibrational bands corresponding to C^{α}-H and N-H stretching modes are red-shifted for PGA+PYP, indicating stronger interaction, i.e., shorter bond lengths. At 2990 cm^{-1}, the sign of the vibrational mode is opposite, positive for PEI+PYP and negative for PGA+PYP.

Next, the effect of the improved structural homogeneity of the topmost PGA layer in multilayer stacks on the adsorption of PYP was studied. Investigations of the multilayer structures using atomic force microscopy (AFM) revealed a very homogeneous surface for PEI+(PGA+PLL)$_{6.5}$ and an increase in surface roughness upon PYP adsorption (cf. Figure S4). A densely packed surface was clearly discernible when PYP was adsorbed onto the PGA layer with a concomitant decrease in interfacial stiffness. This decrease is consistent with the formation of a relatively soft protein layer, which was found to be very homogeneous over several microns. In Figure 4, the acquired VSFG spectra of the polyelectrolyte multilayer, PEI+(PGA+PLL)$_{6.5}$, with and without PYP adsorption is shown in the vibrational region between 1380 and 1720 cm^{-1}, and between 1500 and 1700 cm^{-1} for achiral and chiral polarization combinations, respectively. This region is suitable to study not only the amide I and II modes, but also the side-chain vibrations. The tables in the supplementary material summarize the assignments of the achiral (Table S1 and S3) and chiral (Table S2 and S4) vibrational modes of the multilayer structures without and with PYP, respectively, obtained from fitting Lorentzian line profiles based on Equation (1) onto the spectra.

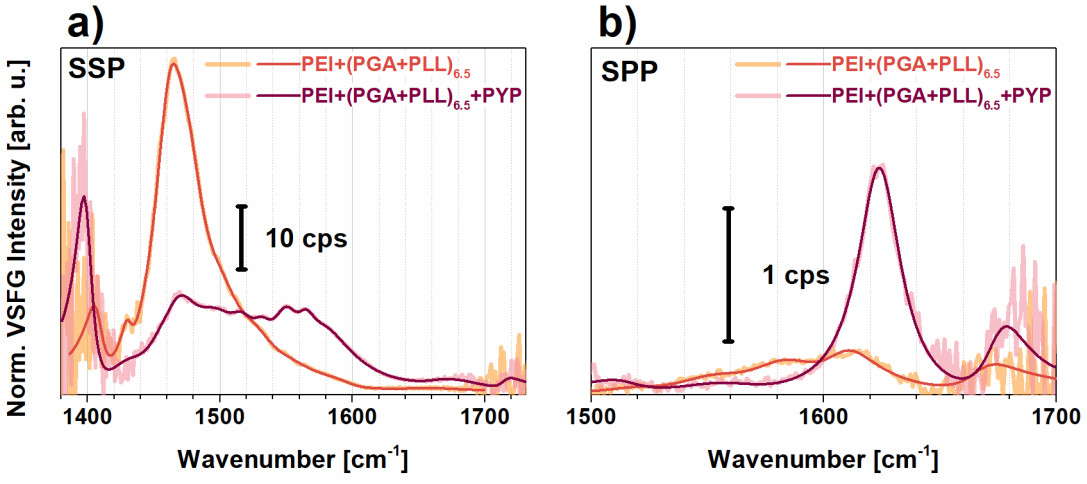

Figure 4. *Achiral **(a)** and chiral **(b)** spectra of (PGA-PLL)$_{6.5}$ (light red) and (PGA-PLL)$_{6.5}$+PYP (dark red) in the amide I region. The relative humidity of the films was ~80%.*

At 1402 cm^{-1}, the symmetric COO$^-$ stretch from aspartate and glutamate units can be seen in the PYP spectrum, while it shifts to 1408 cm^{-1} on the polymer interface (cf. Figure 4a). Without PYP, huge CH_2 deformation bands of polymers appear at 1425-1475 cm^{-1}, which are more intense and can be seen at lower frequencies (i.e., 1425 cm^{-1}) when next to a C=O moiety.

Upon PYP adsorption, these deformation modes decrease and broaden, suggesting that the methylene groups of PYP have random orientational distribution. The asymmetric deformation mode of CH_3 is around 1445-1480 cm^{-1}, while the symmetric and asymmetric bending modes of the NH_3^+ group lie at 1527 and 1625 cm^{-1}, respectively, and each one is observed for both with and without PYP. When PGA is the topmost layer, the NH_3^+ bending modes more likely appear from the Lys layer under the PGA. For PYP, the ring mode near 1517 cm^{-1} was detected which is usually very characteristic in protein absorption spectra from the Tyr side chain. At 1583 cm^{-1}, a band appears in chiral polarization when the topmost layer is PGA, which can be assigned to asymmetric COO^- stretching. For PYP, bands at 1590 and 1610 cm^{-1} are detected. The lower frequency band belongs to the COO^- stretching mode of Glu/Asp side chains that are red-shifted during the interaction of PYP with the PGA surface. Since the stretching frequency of COO^- moiety is very sensitive to the local environment, it may shift ± 40-60 cm^{-1} [79]. A chiral band at 1610 cm^{-1} is found both with and without PYP due to a bifurcated H-bonding to −COOH groups on the protonated Glu side chain which reflects very strong H-bonding [80,81]. Interestingly, ROA studies of polylysine, polyglutamic acid, and some proteins also showed a negative/positive signal at 1610/1626 cm^{-1} for β-sheet structures [82] which were later linked to the formation of β_2-fibrils [83].

In the achiral spectra, the weak vibrational bands at 1640 cm^{-1} and 1665 cm^{-1} can be assigned to the amide I B_2 and B_1 mode of the antiparallel β-sheets, respectively. In the chiral spectrum of PYP, these amide I modes are enhanced and red-shifted, while the amide II band near 1560 cm^{-1} is also characteristic. Our observations on the chiral N-H stretching together with the chiral amide I and II modes confirm that chiral VSFG spectroscopy is capable of determining the type of secondary structure with the highest abundance of PYP, i.e., β-scaffold in this case.

Figure 5 shows the chiral spectra of PYP adsorbed on the $PEI+(PGA+PLL)_{6.5}$ multilayer structure in the spectral range from 1400 to 1700 cm^{-1} at a relative humidity of 3% and 100%. Tables S5 and S6 contain the assignments of the corresponding vibrational modes of the

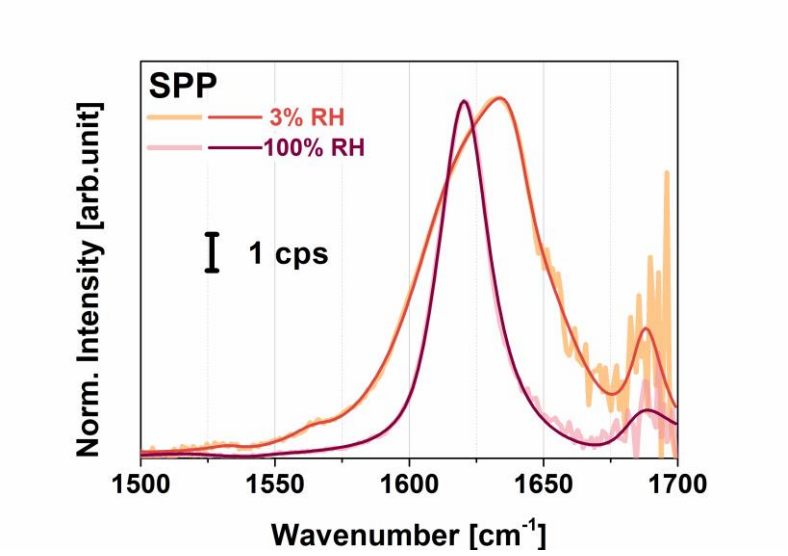

Figure 5. *Chiral VSFG spectra of PEI+(PGA+PLL)$_{6.5}$+PYP multilayer in different relative humidity environments, orange corresponding to low (3%) and dark red corresponding to high (100%) relative humidity.*

multilayer structures without and with PYP, respectively, obtained from fitting based on Equation (1) onto the spectra. The characteristic amide I B_1 and B_2 modes at high humidity are very narrow with damping factors lying between 8 and 11 cm^{-1}, respectively, indicating a narrow orientational distribution of the peptide bonds in the β-scaffold part of PYP. The B_2 mode of the β-sheet structure lies at 1621 cm^{-1}, where the low frequency value can be explained by very strong H-bonds. When the humidity decreased, no broadening of the chiral B_1 and B_2 vibrational modes was observed. However, the B_2-mode blue-shifted to 1640 cm^{-1} (almost the highest frequency attainable to a B_2 band) and a new peak arose at 1654 cm^{-1}, which we assigned to the amide I mode for an α-helix secondary structure. Yan and co-workers obtained no chiral amide I signal for rhodopsin, pHLIP, and LKα14 model systems [35] suggesting that the chiral amide I mode is silent for helical structures. In contrast, Ishibashi's group found a small but significant chiral amide I band for BSA with a secondary structural content of 67% α-helix and 10% β-turn [33]. The fact that we could resolve the shoulder at 1654 cm^{-1} was made possible by the high spectral resolution (~3 cm^{-1}) of our home-built VSFG spectrometer and its high sensitivity thanks to the employed 100-kHz laser system. Since globular proteins easily undergo denaturation, we expect that PYP loses the hydrogen shell at low humidity. Therefore, a partial loss of its tertiary structure was likely detected, which changed the orientation of α-helixes and β-sheets and also weakened their H-bond structure.

Detailed calculations of molecular orientation for polyelectrolyte-PYP interfaces are in progress.

3. Materials and Methods

3.1. Sample preparation

To prepare the polyelectrolyte layers, we used branched polyethyleneimine, poly-L-glutamic acid, and poly-L-lysine by utilizing the layer-by-layer method. All three polyelectrolytes were purchased from Sigma-Aldrich and have a molecular weight of 600,000-1,000,000 (branched PEI solution, concentration of ~50% in H_2O), 50,000-100,000 (PGA sodium salt), and >30,000 (PLL hydrochloride). The applied PEI stock solution had a concentration of 5 mg/ml, while the concentration of PGA and PLL was 1 mg/ml. First, PEI was sprayed onto an oxygen plasma-cleaned CaF_2 window to fully coat the substrate and provide a base for subsequent layers. The deposited PEI layer was left for a minute, then the residue was thoroughly washed off with distilled water. In the following step, a layer of PGA was added and left to adsorb for 20 seconds with the residue then washed off. The PGA layer was followed by adding and similarly washing a layer of PLL. We continued to add PGA and PLL layers up to a total of six and a half pairs as this resulted in a very homogeneous surface [58,61,73]. A layer of PYP was added to the topmost polyelectrolyte layer by pipetting the PYP stock solution of 0.28 mM on top and letting it set for 5 minutes, then washing it off similarly to the case of the previous layers. After preparation, the samples were left to equilibrate for at least 10 minutes before collecting VSFG spectra. The measurements were done on PEI, PEI+PGA, and six-and-a-half pairs of PGA+PLL layers on PEI (denoted as PEI+$(PGA+PLL)_{6.5}$). Additionally, PYP was adsorbed on top of PEI, PEI+PGA, and PEI+$(PGA+PLL)_{6.5}$ samples. While repeating the measurements, the samples were held in a hydrated state by keeping them in a >80% relative humidity environment.

3.2 Vibrational sum-frequency generation (VSFG)

The VSFG setup was described in detail elsewhere [53,54]. Here, only a brief account is given. The pump laser employed in the VSFG spectrometer is a Yb:$KGd(WO_4)_2$ laser oscillator-

amplifier system operating at a center wavelength of 1028 nm with a repetition rate of 100 kHz. The pump pulses were split into two parts. One part was forwarded into a home-built spectral compressor which generated narrowband visible pulses at 514 nm, while the other part of the beam was used to generate tunable MIR laser pulses in the spectral ranges of 2800-3800 cm^{-1} and 1400-1700 cm^{-1} via optical parametric amplification. On the path of the infrared pulses, a home-made purging-enclosure system was used to minimize absorption by atmospheric water vapor and CO_2. The energy of the visible pulses was kept at 4 μJ per pulse, while the pulse energies of the mid-infrared pulses centered at wavenumbers of 1267, 2980, and 3455 cm^{-1} were 0.2, 0.7, and 0.7 μJ respectively. All listed pulse energies refer to the incident values on target. The visible and infrared pulses were focused onto the sample and overlapped temporally and spatially. The angles of incidence for the pulses were 68° and 57°, respectively. The VSFG signal was collected by a spectrometer equipped with a Peltier-cooled, deep-depletion charge-coupled device. The spectral resolution of the VSFG spectrometer was ~3 cm^{-1}.

The polarization for the input beams was controlled by using zero-order half-waveplates, while an additional polarizer with a half-waveplate was employed at the entrance of the spectrometer for the SFG beam. Spectra in the C-H, N-H, and O-H stretching regions were collected in PPP, SSP, SPP, PSP, and PPS polarization combinations (the order of polarizations corresponds to SFG, visible and infrared beams, respectively), while spectra in the amide I region were collected in SSP and SPP polarization combinations. The acquisition times ranged from 10 s to 120 s – shorter times were applied in the C-H, N-H, and O-H stretch regions, while longer times were used in the amide I region. All measurements were repeated at least 3 times and at different sample positions to minimize and account for the effect of the environment on the acquired spectra. The measurements were carried out at room temperature (23 °C) and controlled relative humidity.

The VSFG spectra were frequency calibrated using a 50-μm-thick polystyrene film, which was inserted into the MIR beam. Difference spectra were calculated by subtracting the background spectrum from each measurement (the spectrum without infrared excitation). To

convert spectral intensity into count-per-second, the difference spectra were divided by the acquisition time. The non-resonant spectrum measured at a silver surface was normalized to one and then corrected by multiplying it by the measured infrared intensity at the sample's surface for the absolute comparison of the different spectral regions. The VSFG difference spectra were then normalized by this corrected non-resonant spectrum. Finally, the normalized spectra were fitted by the sum of Lorentzian functions that describe the resonant part of the obtained signal and a non-resonant additional part using the following equation:

$$I_{VSFG}(\omega) \propto \left| P_{NR} e^{i\Phi} + \sum_{i=1}^{\nu} \frac{Q_\upsilon}{\omega - \omega_\nu - i\Gamma_\upsilon} \right|^2 , \quad (1)$$

where Q_ν, ω_ν, *and* Γ_ν are the strength, frequency, and damping factor of the ν^{th} Lorentzian peak. The first element of the sum accounts for the non-resonant contribution with amplitude P_{NR} and phase Φ making it possible to describe both constructive and destructive interference.

3.3 Atomic Force Microscopy (AFM)

AFM images were obtained on a Bruker/JPK NanoWizard 4 operating in Quantitative Imaging (QI) mode. In this mode, force spectra are collected at every point in a given image area, from which several nanomechanical parameters such as height, stiffness and adhesion are extracted. The height is estimated from a setpoint force chosen during the experiment, while the stiffness is estimated as the slope of the approach curve. The images were obtained using Nanosensors PPP-NCH probes.

4. Conclusions

Chiral and achiral VSFG spectroscopy was performed to study the adsorption properties of photoactive yellow protein on positively and negatively charged, self-assembled polyelectrolyte surfaces and layer stacks. We demonstrated that homodyne VSFG spectroscopy is a viable technique for the structural study of nm-scale multilayers, where the orientational information is extracted by employing the maximum entropy method (MEM) and the standard global fitting procedure on the VSFG spectrum in conjunction. We found that the multilayer stack leads to a much more homogenous top layer when 6.5 layers are

employed than in the 0.5-layer case. Structural homogeneity was revealed by increasing vibrational band amplitudes and decreasing bandwidths which were further confirmed by AFM studies. Our data suggest that while PEI shows helical structural elements, PGA forms mostly random coil arrangement with a small amount of β_2-fibril structure at the interface at physiological pH, and these structures do not change when more pairs of layers are applied.

Due to our high spectral resolution, the C^{α}, C^{β}, and C^{γ} signals can also be spectrally resolved during the buildup of polymer layer structures, which can be used to follow the cis-trans changes of methylene groups. If the protein is adsorbed, the methylene modes become less informative as a result of interference effects. Nevertheless, the methyl groups become well-ordered in this case due to the air-layer interface giving a strong CH_3 stretch signal. Acquiring chiral spectra revealed details about the β-scaffold portion of PYP, while the achiral signal of the hydrated PYP layer was not specific to the protein. However, upon PYP adsorption on charged surfaces, the C^{α}-H, aromatics C-H, and side-chain N-H vibrational bands, characteristic of proteins, also appear in achiral polarization combinations making achiral signals also surface specific.

Chiral VSFG spectra of adsorbed PYP contain a wealth of information: the homodyne N-H stretch signal shows a redshift for negatively charged PGA+PYP compared to PEI+PYP, which is also confirmed by the spectra extracted using the MEM procedure. The relative redshift in the PGA+PYP case suggests that PYP keeps its tertiary structure to a higher degree when interacting with PGA than with PEI. The AFM characterization has shown that an intact PYP layer is formed on the PGA-terminated surface, as evidenced by an increase in surface roughness and a homogenous reduction in interfacial stiffness. We also found that both the chiral and achiral VSFG spectra obtained in the spectral region of 1400-1700 cm^{-1} exhibit significant differences when PYP adsorbed at the interface which can be linked to the amide I and II modes and side chain vibrations. The changes in the amide I and II bands suggest that PYP loses its external hydrogen shell at low humidity in spite of a stable beta-sheet secondary structural motif. At the same time, some minor denaturation, i.e., partial loss of tertiary structure, was also detectable. Our results corroborate that chiral VSFG spectroscopy can

determine the secondary structure of proteins which has the highest abundance and is additionally very sensitive to the tertiary structure of proteins.

Supplementary Materials: Figure S1: Imaginary part of the chiral VSFG spectra of PYP in the C-H, N-H, and O-H stretch region calculated from the observed SPP spectrum via the MEM algorithm.; Figure S2: Calculated imaginary part of $\chi^{(2)}$ of PEI and PEI+PYP (a, c), and PGA and PGA+PYP (b, d) in SSP and SPP polarizations, respectively.; Figure S3: Achiral (a, b) and chiral (c) VSFG spectra of one pair of PEI+PGA (light red) and PEI+$(PGA+PLL)_{6.5}$ (dark burgundy) multilayers in the C-H, N-H, and O-H stretch region. The topmost layer contains PGA in each case. Table S1: Vibrational mode assignments and corresponding VSFG wavenumbers, spectral widths, and amplitudes of PEI+$(PGA+PLL)_{6.5}$, i.e., topmost layer is PGA, in the spectral region between 1400 and 1700 cm^{-1} at a relative humidity of 80%. Table S2: Vibrational mode assignments and corresponding VSFG wavenumbers, spectral widths, and amplitudes of PEI+$(PGA+PLL)_{6.5}$+PYP, i.e., topmost layer is PYP, in the spectral region between 1400 and 1700 cm^{-1} at a relative humidity of 80%. Table S3: Chiral vibrational mode assignments and corresponding VSFG wavenumbers, spectral widths, and amplitudes of PEI+$(PGA+PLL)_{6.5}$, i.e., topmost layer is PGA, in the spectral region between 1500 and 1700 cm^{-1} at a relative humidity of 80%. Table S4: Chiral vibrational mode assignments and corresponding VSFG wavenumbers, spectral widths, and amplitudes of PEI+$(PGA+PLL)_{6.5}$+PYP in a relative humidity of 80% in the spectral region between 1500 and 1700 cm^{-1}. Table S5: Vibrational mode assignments and corresponding VSFG wavenumbers, spectral widths, and amplitudes of PEI+$(PGA+PLL)_{6.5}$+PYP in a relative humidity (RH) of 3% in the spectral region between 1500 and 1700 cm^{-1}. Table S6: Vibrational mode assignments and corresponding VSFG wavenumbers, spectral widths, and amplitudes of PEI+$(PGA+PLL)_{6.5}$+PYP in a relative humidity (RH) of 100% in the spectral region between 1500 and 1700 cm^{-1}. Figure S4: AFM images of PEI+$(PGA+PLL)_{6.5}$ multilayers without and with PYP. Figure S5: Histogram of stiffness values from AFM images without and with PYP.

Funding: This work has received funding from the National Research, Development and Innovation Office, Hungary (NKFI-1 K-124922), the Eotvos Lorand Research Network (ELKH KÖ-36/2021), the Deutsche Forschungsgemeinschaft (DFG, no. GSC 1013 SALSA), German

Academic Exchange Service (DAAD) and the Eotvos Hungarian State Scholarship of Tempus Public Foundation funded by the Hungarian Government.

Acknowledgments: The authors are grateful to Prof. Hinorari Kamikubo for providing the plasmid for PYP expression and to Dr. Tomás Zakar for preparation of the protein. Z.H. acknowledges funding by a Julia Lermontova Fellowship from DFG (GSC 1013 SALSA). S.K. acknowledges funding by a short-term scholarship provided from the German Academic Exchange Service (DAAD) and the Eotvos Hungarian State Scholarship of Tempus Public Foundation funded by the Hungarian Government. K.B. acknowledges funding from the DFG for major instrumentation via grant INST 276/754-1. The protein structure in the graphical abstract generated with ChimeraX [84].

References

1. Zimmerman, S.B.; Trach, S.O. Estimation of Macromolecule Concentrations and Excluded Volume Effects for the Cytoplasm of Escherichia Coli. *J. Mol. Biol.* **1991**, *222*, 599–620, doi:10.1016/0022-2836(91)90499-V.

2. Goodsell, D.S. Inside a Living Cell. *Trends Biochem. Sci.* **1991**, *16*, 203–206, doi:10.1016/0968-0004(91)90083-8.

3. Ellis, R.J. Macromolecular Crowding: Obvious but Underappreciated. *Trends Biochem. Sci.* **2001**, *26*, 597–604, doi:10.1016/S0968-0004(01)01938-7.

4. Dér, A.; Kelemen, L.; Fábián, L.; Taneva, S.G.; Fodor, E.; Páli, T.; Cupane, A.; Cacace, M.G.; Ramsden, J.J. Interfacial Water Structure Controls Protein Conformation. *J. Phys. Chem. B* **2007**, *111*, 5344–5350, doi:10.1021/jp066206p.

5. Násztor, Z.; Bogár, F.; Dér, A. The Interfacial Tension Concept, as Revealed by Fluctuations. *Curr. Opin. Colloid Interface Sci.* **2016**, *23*, 29–40, doi:10.1016/j.cocis.2016.05.007.

6. Bogár, F.; Bartha, F.; Násztor, Z.; Fábián, L.; Leitgeb, B.; Dér, A. On the Hofmeister Effect: Fluctuations at the Protein–Water Interface and the Surface Tension. *J. Phys. Chem. B* **2014**, *118*, 8496–8504, doi:10.1021/jp502505c.

7. Kincses, A.; Santa-Maria, A.R.; Walter, F.R.; Dér, L.; Horányi, N.; Lipka, D. V.; Valkai, S.; Deli, M.A.; Dér, A. A Chip Device to Determine Surface Charge Properties of Confluent Cell Monolayers by Measuring Streaming Potential. *Lab Chip* **2020**, *20*, 3792–3805, doi:10.1039/d0lc00558d.

8. Laaser, J.E.; Skoff, D.R.; Ho, J.-J.; Joo, Y.; Serrano, A.L.; Steinkruger, J.D.; Gopalan, P.; Gellman, S.H.; Zanni, M.T. Two-Dimensional Sum-Frequency Generation Reveals Structure and Dynamics of a Surface-Bound Peptide. *J. Am. Chem. Soc.* **2014**, *136*, 956–962, doi:10.1021/ja408682s.

9. Minton, A.P. The Influence of Macromolecular Crowding and Macromolecular Confinement on Biochemical Reactions in Physiological Media. *J. Biol. Chem.* **2001**, *276*, 10577–10580, doi:10.1074/jbc.R100005200.

10. Ladam, G.; Gergely, C.; Senger, B.; Decher, G.; Voegel, J.-C.; Schaaf, P.; Cuisinier, F.J.G. Protein Interactions with Polyelectrolyte Multilayers: Interactions between Human Serum Albumin and Polystyrene Sulfonate/Polyallylamine Multilayers. *Biomacromolecules* **2000**, *1*, 674–687, doi:10.1021/bm005572q.

11. Mezzenga, R.; Fischer, P. The Self-Assembly, Aggregation and Phase Transitions of Food Protein Systems in One, Two and Three Dimensions. *Reports Prog. Phys.* **2013**, *76*, 046601, doi:10.1088/0034-4885/76/4/046601.

12. Santa-Maria, A.R.; Walter, F.R.; Valkai, S.; Brás, A.R.; Mészáros, M.; Kincses, A.; Klepe, A.; Gaspar, D.; Castanho, M.A.R.B.; Zimányi, L.; et al. Lidocaine Turns the Surface Charge of Biological Membranes More Positive and Changes the Permeability of Blood-Brain Barrier Culture Models. *Biochim. Biophys. Acta - Biomembr.* **2019**, *1861*, 1579–1591, doi:10.1016/j.bbamem.2019.07.008.

13. Kovacs, B.; Saftics, A.; Biro, A.; Kurunczi, S.; Szalontai, B.; Kakasi, B.; Vonderviszt, F.; Der, A.; Horvath, R. Kinetics and Structure of Self-Assembled Flagellin Monolayers on Hydrophobic Surfaces in the Presence of Hofmeister Salts: Experimental Measurement of the Protein Interfacial Tension at the Nanometer Scale. *J. Phys. Chem. C* **2018**, *122*, 21375–21386, doi:10.1021/acs.jpcc.8b05026.

14. Brash, J.L.; Horbett, T.A. Proteins at Interfaces. In; American Chemical Society: Washington, 1995; pp. 1–23 ISBN 0841233047.

15. Lyklema, J.; Norde, W. Interfacial Behaviour of Biomacromolecules. In *Interfaces, Surfactants and Colloids in Engineering*; Jacobasch, H.-J., Ed.; Steinkopff: Darmstadt, 1996; Vol. 101, pp. 9–17 ISBN 978-3-7985-1664-9.

16. Stieger, K.R.; Ciornii, D.; Kölsch, A.; Hejazi, M.; Lokstein, H.; Feifel, S.C.; Zouni, A.; Lisdat, F. Engineering of Supramolecular Photoactive Protein Architectures: The Defined Co-Assembly of Photosystem i and Cytochrome: C Using a Nanoscaled DNA-Matrix. *Nanoscale* **2016**, *8*, 10695–10705, doi:10.1039/c6nr00097e.

17. Fábián, L.; Heiner, Z.; Mero, M.; Kiss, M.; Wolff, E.K.; Ormos, P.; Osvay, K.; Dér, A. Protein-Based Ultrafast Photonic Switching. *Opt. Express* **2011**, *19*, 18861, doi:10.1364/OE.19.018861.

18. Petrovszki, D.; Krekic, S.; Valkai, S.; Heiner, Z.; Dér, A. All-Optical Switching Demonstrated with Photoactive Yellow Protein Films. *Biosensors* **2021**, *11*, 432, doi:10.3390/bios11110432.

19. Krekic, S.; Mero, M.; Dér, A.; Heiner, Z. Ultrafast All-Optical Switching Using Doped Chromoprotein Films. *J. Phys. Chem. C* **2023**, *127*, 1499–1506, doi:10.1021/acs.jpcc.2c06232.

20. Dhamelincourt, P.; Ramirez, F.J. Polarized Micro-Raman and FT-IR Spectra of L-Glutamine. *Appl. Spectrosc.* **1993**, *47*, 446–451, doi:10.1366/0003702934335083.

21. Chen, L.; Zhu, W.; Lin, K.; Hu, N.; Yu, Y.; Zhou, X.; Yuan, L.-F.; Hu, S.-M.; Luo, Y. Identification of Alcohol Conformers by Raman Spectra in the C–H Stretching Region. *J. Phys. Chem. A* **2015**, *119*, 3209–3217, doi:10.1021/jp513027r.

22. Szalontai, B.; Nagy, G.; Krumova, S.; Fodor, E.; Páli, T.; Taneva, S.G.; Garab, G.; Peters, J.; Dér, A. Hofmeister Ions Control Protein Dynamics. *Biochim. Biophys. Acta - Gen. Subj.* **2013**, *1830*, 4564–4572, doi:10.1016/j.bbagen.2013.05.036.

23. Zsiros, O.; Ünnep, R.; Nagy, G.; Almásy, L.; Patai, R.; Székely, N.K.; Kohlbrecher, J.; Garab, G.; Dér, A.; Kovács, L. Role of Protein-Water Interface in the Stacking Interactions of Granum Thylakoid Membranes—As Revealed by the Effects of Hofmeister Salts. *Front. Plant Sci.* **2020**, *11*, doi:10.3389/fpls.2020.01257.

24. Petrovszki, D.; Walter, F.R.; Vigh, J.P.; Kocsis, A.; Valkai, S.; Deli, M.A.; Dér, A. Penetration of the SARS-CoV-2 Spike Protein across the Blood–Brain Barrier, as Revealed by a Combination of a Human Cell Culture Model System and Optical Biosensing. *Biomedicines* **2022**, *10*, 188, doi:10.3390/biomedicines10010188.

25. Ramsden, J.J. OWLS: A Versatile Technique for Sensing with Bioarrays. *Chimia (Aarau).* **1999**, *53*, 67, doi:10.2533/chimia.1999.67.

26. Horvath, R.; Cottier, K.; Pedersen, H.C.; Ramsden, J.J. Multidepth Screening of Living Cells Using Optical Waveguides. *Biosens. Bioelectron.* **2008**, *24*, 799–804, doi:10.1016/j.bios.2008.06.059.

27. Nagasawa, D.; Azuma, T.; Noguchi, H.; Uosaki, K.; Takai, M. Role of Interfacial Water in Protein Adsorption onto Polymer Brushes as Studied by SFG Spectroscopy and QCM. *J. Phys. Chem. C* **2015**, *119*, 17193–17201, doi:10.1021/acs.jpcc.5b04186.

28. Meister, K.; Paananen, A.; Speet, B.; Lienemann, M.; Bakker, H.J. Molecular Structure of Hydrophobins Studied with Site-Directed Mutagenesis and Vibrational Sum-Frequency Generation Spectroscopy. *J. Phys. Chem. B* **2017**, *121*, 9398–9402, doi:10.1021/acs.jpcb.7b08865.

29. Strazdaite, S.; Meister, K.; Bakker, H.J. Orientation of Polar Molecules near Charged Protein Interfaces. *Phys. Chem. Chem. Phys.* **2016**, *18*, 7414–7418, doi:10.1039/C5CP06372H.

30. Hosseinpour, S.; Roeters, S.J.; Bonn, M.; Peukert, W.; Woutersen, S.; Weidner, T. Structure and Dynamics of Interfacial Peptides and Proteins from Vibrational Sum-Frequency Generation Spectroscopy. *Chem. Rev.* **2020**, *120*, 3420–3465, doi:10.1021/acs.chemrev.9b00410.

31. Yesudas, F.; Mero, M.; Kneipp, J.; Heiner, Z. High-Resolution and High-Repetition-Rate Vibrational Sum-Frequency Generation Spectroscopy of One- and Two-Component Phosphatidylcholine Monolayers. *Anal. Bioanal. Chem.* **2019**, *411*, 4861–4871, doi:10.1007/s00216-019-01690-9.

32. Hu, X.-H.; Fu, L.; Hou, J.; Zhang, Y.-N.; Zhang, Z.; Wang, H.-F. N–H Chirality in Folded Peptide LK 7 β Is Governed by the C α –H Chirality. *J. Phys. Chem. Lett.* **2020**, *11*, 1282–1290, doi:10.1021/acs.jpclett.9b03470.

33. Okuno, M.; Ishibashi, T.A. Heterodyne-Detected Achiral and Chiral Vibrational Sum Frequency Generation of Proteins at Air/Water Interface. *J. Phys. Chem. C* **2015**, *119*, 9947–9954, doi:10.1021/acs.jpcc.5b01937.

34. Okuno, M.; Ishibashi, T. Chirality Discriminated by Heterodyne-Detected Vibrational Sum Frequency Generation. *J. Phys. Chem. Lett.* **2014**, *5*, 2874–2878, doi:10.1021/jz501158r.

35. Yan, E.C.Y.; Fu, L.; Wang, Z.; Liu, W. Biological Macromolecules at Interfaces Probed by Chiral Vibrational Sum Frequency Generation Spectroscopy. *Chem. Rev.* **2014**, *114*, 8471–8498, doi:10.1021/cr4006044.

36. Guo, W.; Lu, T.; Gandhi, Z.; Chen, Z. Probing Orientations and Conformations of Peptides and Proteins at Buried Interfaces. *J. Phys. Chem. Lett.* **2021**, *12*, 10144–10155, doi:10.1021/acs.jpclett.1c02956.

37. Stephens, P.J. Theory of Vibrational Circular Dichroism. *J. Phys. Chem.* **1985**, *89*, 748–752, doi:10.1021/j100251a006.

38. Keiderling, T.A. Structure of Condensed Phase Peptides: Insights from Vibrational Circular Dichroism and Raman Optical Activity Techniques. *Chem. Rev.* **2020**, *120*, 3381–3419, doi:10.1021/acs.chemrev.9b00636.

39. Barron, L.D.; Zhu, F.; Hecht, L.; Tranter, G.E.; Isaacs, N.W. Raman Optical Activity: An Incisive Probe of Molecular Chirality and Biomolecular Structure. *J. Mol. Struct.* **2007**, *834–836*, 7–16, doi:10.1016/j.molstruc.2006.10.033.

40. Blanch, E. Vibrational Raman Optical Activity of Proteins, Nucleic Acids, and Viruses. *Methods* **2003**, *29*, 196–209, doi:10.1016/S1046-2023(02)00310-9.

41. Zajac, G.; Kaczor, A.; Pallares Zazo, A.; Mlynarski, J.; Dudek, M.; Baranska, M. Aggregation-Induced Resonance Raman Optical Activity (AIRROA): A New Mechanism for Chirality Enhancement. *J. Phys. Chem. B* **2016**, *120*, 4028–4033, doi:10.1021/acs.jpcb.6b02273.

42. Meyer, T.E. Isolation and Characterization of Soluble Cytochromes, Ferredoxins and Other Chromophoric Proteins from the Halophilic Phototrophic Bacterium Ectothiorhodospira Halophila. *Biochim. Biophys. Acta - Bioenerg.* **1985**, *806*, 175–183, doi:10.1016/0005-2728(85)90094-5.

43. Meyer, T.E.; Yakali, E.; Cusanovich, M.A.; Tollin, G. Properties of a Water-Soluble, Yellow Protein Isolated from a Halophilic Phototrophic Bacterium That Has Photochemical Activity Analogous to Sensory Rhodopsin. *Biochemistry* **1987**, *26*, 418–423, doi:10.1021/bi00376a012.

44. Hellingwerf, K.J.; Hendriks, J.; Gensch, T. Photoactive Yellow Protein, A New Type of Photoreceptor Protein: Will This “Yellow Lab” Bring Us Where We Want to Go? *J. Phys. Chem. A* **2003**, *107*, 1082–1094, doi:10.1021/jp027005y.

45. Krekic, S.; Zakar, T.; Gombos, Z.; Valkai, S.; Mero, M.; Zimányi, L.; Heiner, Z.; Dér, A. Nonlinear Optical Investigation of Microbial Chromoproteins. *Front. Plant Sci.* **2020**, *11*, 1567, doi:10.3389/fpls.2020.547818.

46. Khoroshyy, P.; Dér, A.; Zimányi, L. Effect of Hofmeister Cosolutes on the Photocycle of Photoactive Yellow Protein at Moderately Alkaline PH. *J. Photochem. Photobiol. B Biol.* **2013**, *120*, 111–119, doi:10.1016/j.jphotobiol.2012.12.014.

47. Krekic, S.; Nagy, D.; Taneva, S.G.; Fábián, L.; Zimányi, L.; Dér, A. Spectrokinetic Characterization of Photoactive Yellow Protein Films for Integrated Optical Applications. *Eur. Biophys. J.* **2019**, *48*, 465–473, doi:10.1007/s00249-019-01353-8.

48. Pellequer, J.-L.; Wager-Smith, K.A.; Kay, S.A.; Getzoff, E.D. Photoactive Yellow Protein: A Structural Prototype for the Three-Dimensional Fold of the PAS Domain Superfamily. *Proc. Natl. Acad. Sci.* **1998**, *95*, 5884–5890, doi:10.1073/pnas.95.11.5884.

49. Van Beeumen, J.J.; Devreese, B. V.; Van Bun, S.M.; Hoff, W.D.; Hellingwerf, K.J.; Meyer, T.E.; Cusanovich, M.A.; Mcree, D.E. Primary Structure of a Photoactive Yellow Protein from the Phototrophic Bacterium Ectothiorhodospira Halophila , with Evidence for the Mass and the Binding Site of the Chromophore. *Protein Sci.* **1993**, *2*, 1114–1125, doi:10.1002/pro.5560020706.

50. Hoff, W.D.; van Stokkum, I.H.; van Ramesdonk, H.J.; van Brederode, M.E.; Brouwer, A.M.; Fitch, J.C.; Meyer, T.E.; van Grondelle, R.; Hellingwerf, K.J. Measurement and Global Analysis of the Absorbance Changes in the Photocycle of the Photoactive Yellow Protein from Ectothiorhodospira Halophila. *Biophys. J.* **1994**, *67*, 1691–1705, doi:10.1016/S0006-3495(94)80643-5.

51. Baca, M.; Borgstahl, G.E.O.; Boissinot, M.; Burke, P.M.; Williams, D.R.; Slater, K.A.; Getzoff, E.D. Complete Chemical Structure of Photoactive Yellow Protein: Novel Thioester-Linked 4-Hydroxycinnamyl Chromophore and Photocycle Chemistry. *Biochemistry* **1994**, *33*, 14369–14377, doi:10.1021/bi00252a001.

52. Graham, D..; Phillips, M.. Proteins at Liquid Interfaces. *J. Colloid Interface Sci.* **1979**, *70*, 415–426, doi:10.1016/0021-9797(79)90049-3.

53. Heiner, Z.; Petrov, V.; Mero, M. Compact, High-Repetition-Rate Source for Broadband Sum-Frequency Generation Spectroscopy. *APL Photonics* **2017**, *2*, 066102, doi:10.1063/1.4983691.

54. Heiner, Z.; Wang, L.; Petrov, V.; Mero, M. Broadband Vibrational Sum-Frequency Generation Spectrometer at 100 KHz in the 950-1750 Cm^{-1} Spectral Range Utilizing a LiGaS 2 Optical Parametric Amplifier. *Opt. Express* **2019**, *27*, 15289, doi:10.1364/OE.27.015289.

55. Debreczeny, M.; Ball, V.; Boulmedais, F.; Szalontai, B.; Voegel, J.-C.; Schaaf, P. Multilayers Built from Two Component Polyanions and Single Component Polycation Solutions: A Way To Engineer Films with Desired Secondary Structure. *J. Phys. Chem. B* **2003**, *107*, 12734–12739, doi:10.1021/jp035037v.

56. Schönhoff, M. Self-Assembled Polyelectrolyte Multilayers. *Curr. Opin. Colloid Interface Sci.* **2003**, *8*, 86–95, doi:10.1016/S1359-0294(03)00003-7.

57. Zhao, S.; Caruso, F.; Dähne, L.; Decher, G.; De Geest, B.G.; Fan, J.; Feliu, N.; Gogotsi, Y.; Hammond, P.T.; Hersam, M.C.; et al. The Future of Layer-by-Layer Assembly: A Tribute to ACS Nano Associate Editor Helmuth Möhwald. *ACS Nano* **2019**, *13*, 6151–6169, doi:10.1021/acsnano.9b03326.

58. Panayotov, I. V.; Collart-Dutilleul, P.-Y.; Salehi, H.; Martin, M.; Végh, A.; Yachouh, J.; Vladimirov, B.; Sipos, P.; Szalontai, B.; Gergely, C.; et al. Sprayed Cells and Polyelectrolyte Films for Biomaterial Functionalization: The Influence of Physical PLL-PGA Film Treatments on Dental Pulp Cell Behavior. *Macromol. Biosci.* **2014**, *14*, 1771–1782, doi:10.1002/mabi.201400256.

59. Nagy, K.; Pilbat, A.-M.; Groma, G.; Szalontai, B.; Cuisinier, F.J.G. Casein Aggregates Built Step-by-Step on Charged Polyelectrolyte Film Surfaces Are Calcium Phosphate-Cemented. *J. Biol. Chem.* **2010**, *285*, 38811–38817, doi:10.1074/jbc.M110.151167.

60. Richardson, J.J.; Cui, J.; Björnmalm, M.; Braunger, J.A.; Ejima, H.; Caruso, F. Innovation in Layer-by-Layer Assembly. *Chem. Rev.* **2016**, *116*, 14828–14867, doi:10.1021/acs.chemrev.6b00627.

61. Michel, M.; Toniazzo, V.; Ruch, D.; Ball, V. Deposition Mechanisms in Layer-by-Layer or Step-by-Step Deposition Methods: From Elastic and Impermeable Films to Soft Membranes with Ion Exchange Properties. *ISRN Mater. Sci.* **2012**, *2012*, 1–13, doi:10.5402/2012/701695.

62. Sergeeva, Y.N.; Huang, T.; Felix, O.; Jung, L.; Tropel, P.; Viville, S.; Decher, G. What Is Really Driving Cell–Surface Interactions? Layer-by-Layer Assembled Films May Help to Answer Questions Concerning Cell Attachment and Response to Biomaterials. *Biointerphases* **2016**, *11*, 019009, doi:10.1116/1.4943046.

63. Kim, J.; Somorjai, G.A. Molecular Packing of Lysozyme, Fibrinogen, and Bovine Serum Albumin on Hydrophilic and Hydrophobic Surfaces Studied by Infrared−Visible Sum Frequency Generation and Fluorescence Microscopy. *J. Am. Chem. Soc.* **2003**, *125*, 3150–3158, doi:10.1021/ja028987n.

64. Perets, E.A.; Videla, P.E.; Yan, E.C.Y.; Batista, V.S. Chiral Inversion of Amino Acids in Antiparallel β-Sheets at Interfaces Probed by Vibrational Sum Frequency Generation Spectroscopy. *J. Phys. Chem. B* **2019**, *123*, 5769–5781, doi:10.1021/acs.jpcb.9b04029.

65. Perets, E.A.; Konstantinovsky, D.; Fu, L.; Chen, J.; Wang, H.-F.; Hammes-Schiffer, S.; Yan, E.C.Y. Mirror-Image Antiparallel β-Sheets Organize Water Molecules into Superstructures of Opposite Chirality. *Proc. Natl. Acad. Sci.* **2020**, *117*, 32902–32909, doi:10.1073/pnas.2015567117.

66. Sovago, M.; Vartiainen, E.; Bonn, M. Determining Absolute Molecular Orientation at Interfaces: A Phase Retrieval Approach for Sum Frequency Generation Spectroscopy. *J. Phys. Chem. C* **2009**, *113*, 6100–6106, doi:10.1021/jp810123g.

67. de Beer, A.G.F.; Samson, J.-S.; Hua, W.; Huang, Z.; Chen, X.; Allen, H.C.; Roke, S. Direct Comparison of Phase-Sensitive Vibrational Sum Frequency Generation with Maximum Entropy Method: Case Study of Water. *J. Chem. Phys.* **2011**, *135*, 224701, doi:10.1063/1.3662469.

68. York, R.L.; Holinga, G.J.; Somorjai, G.A. An Investigation of the Influence of Chain Length on the Interfacial Ordering of L -Lysine and L -Proline and Their Homopeptides at Hydrophobic and Hydrophilic Interfaces Studied by Sum Frequency Generation and Quartz Crystal Microba. *Langmuir* **2009**, *25*, 9369–9374, doi:10.1021/la900654m.

69. Lott, G.A.; King, M.D.; Hill, M.W.; Scatena, L.F. Effects of Relative Humidity on the Surface and Bulk Structures of Linear Polyethylenimine Thin Films. *J. Phys. Chem. C* **2014**, *118*, 17686–17698, doi:10.1021/jp504321r.

70. Hashida, T.; Tashiro, K. Structural Investigation on Water-Induced Phase Transitions of Poly(Ethylene Imine), Part IV: Changes of Intra- and Intermolecular Hydrogen Bonds in the Hydration Processes as Revealed by Time-Resolved Raman Spectral Measurements. *Polymer (Guildf).* **2007**, *48*, 7614–7622, doi:10.1016/j.polymer.2007.10.031.

71. Navarrete, J.T.L.; Hernández, V.; Ramírez, F.J. Vibrational Study of Aspartic Acid and Glutamic Acid Dipeptides. *J. Mol. Struct.* **1995**, *348*, 249–252, doi:10.1016/0022-2860(95)08635-9.

72. Livingstone, R.A.; Zhang, Z.; Piatkowski, L.; Bakker, H.J.; Hunger, J.; Bonn, M.; Backus, E.H.G. Water in Contact with a Cationic Lipid Exhibits Bulklike Vibrational Dynamics. *J. Phys. Chem. B* **2016**, *120*, 10069–10078, doi:10.1021/acs.jpcb.6b07085.

73. Picart, C.; Ladam, G.; Senger, B.; Voegel, J.C.; Schaaf, P.; Cuisinier, F.J.G.; Gergely, C. Determination of Structural Parameters Characterizing Thin Films by Optical Methods: A Comparison between Scanning Angle Reflectometry and Optical Waveguide Lightmode Spectroscopy. *J. Chem. Phys.* **2001**, *115*, 1086–1094, doi:10.1063/1.1375156.

74. Nihonyanagi, S.; Mondal, J.A.; Yamaguchi, S.; Tahara, T. Structure and Dynamics of Interfacial Water Studied by Heterodyne-Detected Vibrational Sum-Frequency Generation. *Annu. Rev. Phys. Chem.* **2013**, *64*, 579–603, doi:10.1146/annurev-physchem-040412-110138.

75. Nojima, Y.; Suzuki, Y.; Yamaguchi, S. Weakly Hydrogen-Bonded Water Inside Charged Lipid Monolayer Observed with Heterodyne-Detected Vibrational Sum Frequency Generation Spectroscopy. *J. Phys. Chem. C* **2017**, *121*, 2173–2180, doi:10.1021/acs.jpcc.6b09229.

76. Nagaya, J.; Homma, M.; Tanioka, A.; Minakata, A. Relationship between Protonation and Ion Condensation for Branched Poly(Ethylenimine). *Biophys. Chem.* **1996**, *60*, 45–51, doi:10.1016/0301-4622(95)00143-3.

77. Ziebarth, J.D.; Wang, Y. Understanding the Protonation Behavior of Linear Polyethylenimine in Solutions through Monte Carlo Simulations. *Biomacromolecules* **2010**, *11*, 29–38, doi:10.1021/bm900842d.

78. Perets, E.A.; Videla, P.E.; Yan, E.C.Y.; Batista, V.S. Chiral Inversion of Amino Acids in Antiparallel β-Sheets at Interfaces Probed by Vibrational Sum Frequency Generation Spectroscopy. *J. Phys. Chem. B* **2019**, *123*, 5769–5781, doi:10.1021/acs.jpcb.9b04029.

79. Barth, A. The Infrared Absorption of Amino Acid Side Chains. *Prog. Biophys. Mol. Biol.* **2000**, *74*, 141–173, doi:10.1016/S0079-6107(00)00021-3.

80. Fulara, A.; Dzwolak, W. Bifurcated Hydrogen Bonds Stabilize Fibrils of Poly(l -Glutamic) Acid. *J. Phys. Chem. B* **2010**, *114*, 8278–8283, doi:10.1021/jp102440n.

81. Xie, A.; Kelemen, L.; Hendriks, J.; White, B.J.; Hellingwerf, K.J.; Hoff, W.D. Formation of a New Buried Charge Drives a Large-Amplitude Protein Quake in Photoreceptor Activation. *Biochemistry* **2001**, *40*, 1510–1517, doi:10.1021/bi002449a.

82. McColl, I.H.; Blanch, E.W.; Gill, A.C.; Rhie, A.G.O.; Ritchie, M.A.; Hecht, L.; Nielsen, K.; Barron, L.D. A New Perspective on β-Sheet Structures Using Vibrational Raman Optical Activity: From Poly(L-Lysine) to the Prion Protein. *J. Am. Chem. Soc.* **2003**, *125*, 10019–10026, doi:10.1021/ja021464v.

83. Tobias, F.; Keiderling, T.A. Role of Side Chains in β-Sheet Self-Assembly into Peptide Fibrils. IR and VCD Spectroscopic Studies of Glutamic Acid-Containing Peptides. *Langmuir* **2016**, *32*, 4653–4661, doi:10.1021/acs.langmuir.6b00077.

84. Pettersen, E.F.; Goddard, T.D.; Huang, C.C.; Meng, E.C.; Couch, G.S.; Croll, T.I.; Morris, J.H.; Ferrin, T.E. UCSF ChimeraX: Structure Visualization for Researchers, Educators, and Developers. *Protein Sci.* **2021**, *30*, 70–82, doi:10.1002/pro.3943.